Magnetic Resonance Strategies for Tracking Immune Cells

Submitted by
David Cohen

Thesis submitted to the University of Nottingham for the degree of
Doctor of Philosophy

September 2024

Abstract

Currently, understanding of immune response is derived from tissue destructive techniques, such as immunohistochemistry. These techniques, whilst sensitive, do not provide a full picture of complex physiological processes as they only visualise discrete timepoints. Macrophages undergo contextual polarisation towards either pro-inflammatory (M1) or anti- inflammatory (M2) polarisation states, making them useful indicators of local immune state. Cell targeted molecular magnetic resonance imaging (MRI) represents one of the most promising approaches for visualisation of cell activity *in-vivo.* There is a need to develop sensitive, imaging approaches which can resolve immune cell activity at a molecular level. To address these key unmet research needs, three *in vitro* strategies were developed to exploit high-field MRI/MRS allowing visualisation of both unique cell populations through their distinct cell surface marker expression, metabolic fingerprints, and propensity for drug uptake, chiefly through models of macrophage polarisation. Positive identification of macrophage subpopulations was achieved through cell surface marker labelling using targeted iron oxide nanoparticles. In addition, macrophage subpopulations could be further identified by their unique metabolic fingerprints, through visualising turnover of deuterium labelled substrates. Building upon the imaging probe development and screening approaches, efficacy of drug-contrast agent conjugates were used to investigate the uptake of drug complexes in glioblastoma cell lines. Beyond the initial results from these *in vitro* studies, the development of cell targeted MRI strategies *in vivo* will help inform clinical interventions and development of further research tools for the non-invasive understanding of cell biology.

Acknowledgments

This thesis and the work described within it would not have been possible without the support and guidance of several people.

To my supervisors –

Thank you first and foremost to my primary supervisor Pete Harvey. Pete has gone above and beyond to support me through the PhD process. My project would not have been possible without him.

Secondly, I would like to extend my thanks to my co-supervisors Amir Ghaemmaghami and Morgan Alexander for their guidance and expertise.

Chapter 3 & 5 would not have been possible without the kind, patient help of Malcolm Prior.

Chapter 4 would have been impossible without the training and expertise of Huw Williams and Kevin Butler. Working on the 800 MHz spectrometer was a highlight of my PhD.

Thank you to Ian Ward and Sébastien Serres for their advice, training and support.

A special thanks goes the Harvey Lab: Charlotte Gidman, Christian Smith, Georgia Aspinall, Cam Devine, Loyan Salah, Katie Nichols, Xiwen Ma, Milo Hollingworth, Sakaorna Jeyanathan, Hannah Sedgwick and Patricia Jensen for their valued input and friendship.

Thanks also to everyone in the Immunology and Immuno-bioengineering group : Qiran, Lisa, Karen, Leanne, Consu, Reem, Zeynep, Majed, Kate, Shirin, Sari, Walaa, Babatunde, Harie, George, Charlie, Mo, Scott, Arsalan, Edi, Mitchell and Reece. You have all been so kind and welcoming.

To my family and friends

My parents, Debbie and Graham. Thank you for everything you have done to support me.

Ali for encouraging me to do a PhD. Dan and Luke for making frequent trips to Beeston/Melbourne.

Thank you to Hazel, Edna and Lola for their emotional support.

Lastly, thank you to Rachel for supporting me through everything. Love you lots.

Table of Figures

Glossary of Terms

ATP – Adenosine triphosphate
BBB – Blood brain barrier
CEST – chemical exchange saturation transfer
COX – Cyclooxygenase
CT – Computed tomography
DNP – Dynamic nuclear polarisation
DOX - Doxorubicin
FDG - Fluorodeoxyglucose
GLUT – Glucose transporter
GM-CSF – Granulocyte-macrophage colony-stimulating factor
HP – Hyperpolarised
IFNγ– Interferon gamma
IL10 – Interleukin 10
IL4 – Interleukin 4
IL6 – interleukin 6
iNOS – Nitric oxide synthase
LPS – lipopolysaccharide
M-CSF – Macrophage colony-stimulating factor
M1 – Proinflammatory macrophage
M2 – Anti-inflammatory macrophage
MACS – Magnetic activated cell sorting
MRI – Magnetic resonance imaging
MRS – Magnetic resonance spectroscopy
NMR – Nuclear magnetic resonance
NO – Nitric oxide
NSAID – Non-steroidal anti-inflammatory
OXPHOS – oxidative phosphorylation
PBMCs – Peripheral blood mononuclear cells
PET – Positron emission tomography
PFC - Perfluorocarbons
PMA - Phorbol 12-myristate 13-acetate
R_1 – $1/T_1$ (relaxation rate)
R_2- $1/T_2$ (relaxation rate)
SNR – Signal to noise ratio
SPIONs – superparamagnetic iron oxide nanoparticles
T_1 – longitudinal relaxation time
T_2 – transverse relaxation time
TAMs – Tumour-associated macrophages
TCA – Tricarboxylic acid (cycle)
TE – Echo time
TMZ – Temozolomide
TNFα – Tumour necrosis factor alpha
TR – Repetition time
VEGF – vascular endothelial growth factor

Table of Contents

Chapter 1 - General Introduction

1.1 Introduction

Cell morphology, localisation, migration, proliferation, and metabolism within tissue are highly sensitive to the tissue microenvironment in which they reside. Cell behaviour within tissue can reveal information relating to disease, immune response and therapy response (or lack thereof). For the most part, information related to cell behaviour has been limited to invasive tissue destructive approaches including tissue or blood biopsy immunohistochemistry. Cell tracking is a process which utilises a non-invasive imaging modality to label specific cell populations and visualise their activity through space and time.[1,2] Non-invasive imaging modalities, such as magnetic resonance imaging (MRI) and positron emission tomography (PET), offer new opportunities to track and monitor cell behaviour in real time.[2,3] Non-invasive tracking of cells has multiple downstream applications for *in vivo* investigations. In particular, tracking of inflammatory cells could provide a wealth of information relating to disease progression, therapy response and host rejection. This thesis explores three different approaches to exploit magnetic resonance imaging to visualise and label cells for translational applications. The first, described in *Chapter 3*, is a cell surface imaging approach, employing a modular antibody and iron oxide nanoparticle based platform to label macrophages based off their unique surface marker expression. The second, described in *Chapter 4*, is a metabolic imaging approach, using deuterium isotopes to identify the metabolic fingerprints of different macrophage polarisation states. The third, described in *Chapter 5*, is a small molecule therapy-diagnostic (theranostic) platform approach, using DNA intercalators bound to contrast agents to visualise glioblastoma drug uptake.

1.2 Inflammation – Immune Cells as Targets for Cell Tracking

Inflammation is a core, yet complex, hallmark of tissue injury and disease including cancer,[4] neurological diseases,[5] autoimmune response,[6] infection[7] and allograft rejection.[8] Inflammation

can be triggered by many factors such as pathogens, damage to cells and toxic compounds.[7] Inflammatory processes are highly conserved and carefully orchestrated. The process can be surmised by the following steps: initial inflammation, inflammatory resolution, and tissue neovascularisation with tissue remodelling.[1–4] From a cell labelling perspective, targeting inflammatory processes, especially behaviour of immune cells within a given environment, could reveal a large amount of information relating to disease progression and therapy response. Macrophages play an essential role in inflammatory response, making them ideal subjects for targeted molecular imaging of the inflammatory processes.

1.3 Structure and Function of Macrophages

1.3.1 Role of Macrophages

Macrophages are a critical host defence mechanism and are key players of inflammatory processes. They play key roles in tissue development, homeostasis, wound healing and immune response.[10] They show a both a high degree of heterogeneity and plasticity, which facilitates their multiple functions.[10]

1.3.2 Macrophage as Inflammatory Indicators

Macrophages serve as a core molecular hub for immune response to tissue injury.[11] Macrophages undergo functional, morphological and metabolic changes in response to stimuli in their local microenvironment.[11,12] Broadly, resting macrophages (M0) undergo contextual adaptations, in response to either a pro-inflammatory or anti-inflammatory stimuli to give rise to pro-inflammatory (M1) or anti-inflammatory (M2) macrophages, in a process called macrophage polarisation. The ability of macrophages to undergo polarisation in response to anti- or pro-inflammatory stimuli, is critical to tissue homeostasis.[13] The M1/M2 paradigm of macrophage activation was first conceptualised by Mills and colleagues, who demonstrated macrophages from

two different mouse strains (C57Bl/6 and Balb/c) had a preferential metabolism of arginase for either synthesis of nitric oxide (NO) (M1 polarised) or ornithine (M2 polarised) following lipopolysaccharide (LPS) stimulation (see *figure 1.1*).[12,14]

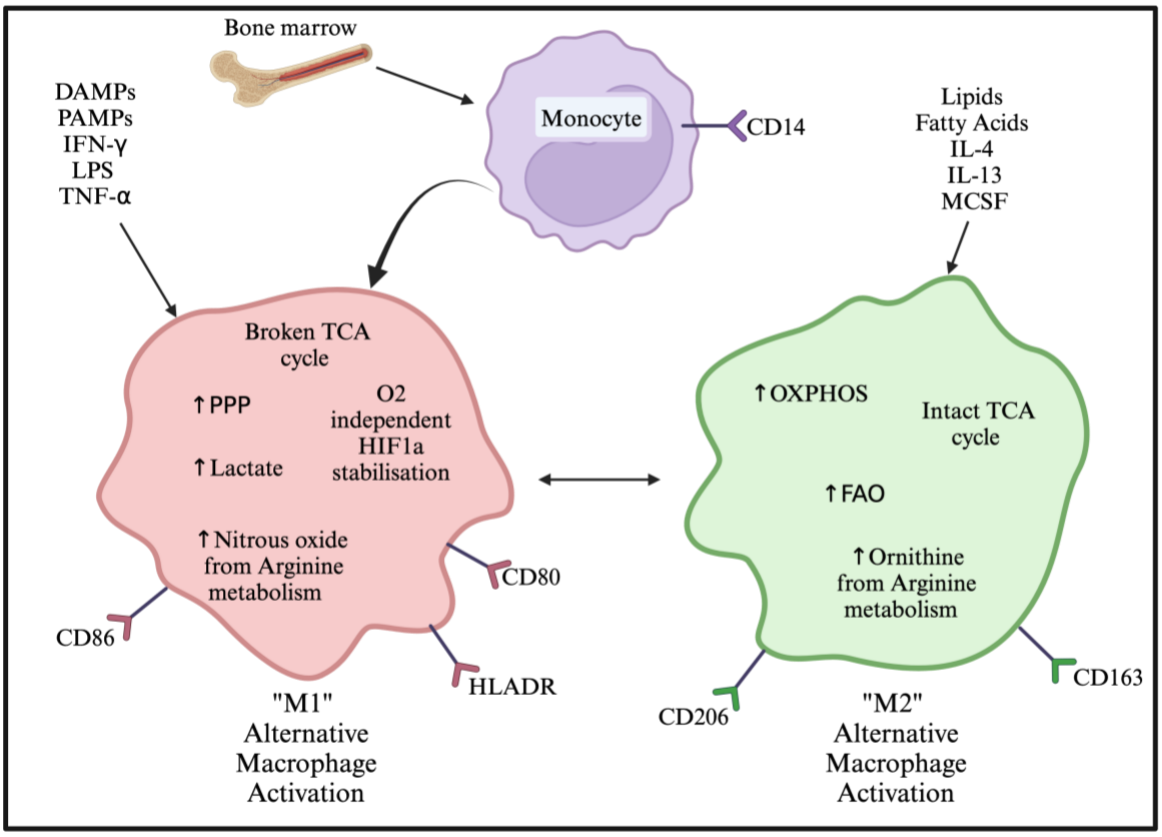

Figure 1.1 – Schematic showing classical macrophage (M1) and alternative (M2) macrophage activation from a monocyte precursor. M1 macrophages are activated by damage-associated molecular patterns (DAMPs), pathogen-associated molecular patterns (PAMPs), interferon gamma (IFN- γ), LPS and tumour necrosis factor alpha (TNF-α). In a feed forward mechanism, these M1 macrophages display a marked increase in synthesis of pro-inflammatory type signal mediators, including TNF-α, nitric oxide synthase (iNOS), interlukin-1 (IL-1), interlukin-6 (IL-6), and interlukin-10 (IL-10). Upregulation of these factors leads to killing of intracellular pathogens, tumour resistance and perpetuation of immune response.[15] In addition to their pro-inflammatory functions, macrophages can be alternatively activated (M2), having significant anti-inflammatory and tissue repair roles.[15] M2 activation is stimulated by lipids, interleukin-4 (IL-4), interleukin-13 (IL-13), and macrophage colony stimulating factor (MCSF) M2 macrophages are characterised by upregulation of vascular endothelial growth factor (VEGF), along with increased oxidative phosphorylation (OXPHOS) and increased fatty acid oxidation (FAO). Anti-inflammatory signalling molecules including interleukin 1 receptor (IL-1R), decoy IL-1 type II and interleukin-10 (IL-10) are also upregulated in the M2 phenotype. Together, the upregulation of these factors leads to increased synthesis of extracellular matrix (ECM), increased angiogenesis and increased phagocytic capacity.[16] Drawn using Biorender. Image adapted from Wynn and Vannella., 2016.[17]

Macrophage's differential metabolism of arginine determines their role in tissue homeostasis. Depending on their activation, macrophages display preference for arginine metabolism by either

iNOS to NO, or arginase to ornithine.[11] Production of either NO or ornithine in macrophages leads to vastly different polarisation states. NO synthesis is predominantly characterised by the cessation of cell proliferation, whereas ornithine synthesis leads to macrophage cell proliferation and repair.[13] Functionally, M1 macrophages are effector cells, constituting a first line of defence and are activated by pro-inflammatory cytokines, including tumour necrosis factor (TNF-α), interferon gamma (IFN-γ) and bacterial derived lipopolysaccharide (LPS).[18] M1 macrophages display a high degree of phagocytic activity towards pathogens, dead cells, foreign bodies and tumour cells, effectively sanitizing the local microenvironment.[18–20] M1 macrophages can further potentiate M1 polarisation by secreting high concentrations of pro-inflammatory cytokines.[21,22] Distinct from M1 macrophages, M2 macrophages exert their function through anti-inflammatory cytokine signalling, and are heavily involved in the repair and remodelling or tissue architecture and dampening of immune response.[18]

Whilst macrophage polarisation can serve as a useful signature for healthy physiological response to tissue insult and damage, the dysregulation of normal macrophage response is heavily implicated in many disease states including cancer and chronic inflammatory diseases.[23–27] Tumour-associated macrophages (TAMs) are one such example, which are macrophages widely present in a number of tumour types and contribute to the formation of the tumour microenvironment. [28] In particular, M2-TAMs potentiate tumour angiogenesis, promote tumour recurrence, dampen T-cell anti-tumoral responses and increase metastatic potential.[28–31] The presence of TAMs, both in terms of M1-TAMs and M2-TAMs, have key clinical prognostic value for patient survival.[32,33] Fundamentally, macrophages and their polarisation states serve as useful indicators for physiological state, including disease progression and therapeutic response.

Evidently, the identification of macrophage polarisation state can hold significant clinical value, such as the case for TAMs, moreover a cell tracking approach that could both identify and track these macrophage populations could further illuminate the role of macrophages in inflammatory responses.

Table 1.1 – Current Macrophage Targeted Molecular Imaging Approaches

Macrophage Labelling Approach	**Exemplified Probes**	**Mechanism**	**Modality**	**Advantages**	**Disadvantages**	**Citation**
Macrophage Targeted Gadolinium Contrast Agent	PG-Gd-NIR813, GBCA-HDL, TMV-Gd-DOTA	Targeted mediated either direct conjugation of targeting moiety or by encapsulating agent in targeted carrier such as a liposome or lipid nanoparticle	MRI	Easy functionalisation, moderate sensitivity.	Metal ion leaching and Nephrotoxicity concerns	[34–36]
Iron Oxide Nanoparticles	SPIONs	Typically approaches exploit macrophage phagocytosis of nanoparticles.	MRI, Multimodal	Moderate sensitivity, generally good biocompatibility, easy functionalisation with targeting moieties, long circulation times.	Hypointense imaging due to T2 contrast enhancement	[37–41]
^{19}F Probes	Perfluoro-19-crown-5-ether	Phagocytosis by immune cells	MRI	High specificity due to low background.	Long scan times due to low sensitivity relative to proton MRI.	[42,43]
Macrophage Fluorescent Labelling	CDr17, Fluorescent labelled SPIONs (e.g SPION-Fluoprobes-565)	Typically targeting surface receptors, or preferential uptake of species such as a glucose	Optical, Multimodal	High sensitivity, multiplex imaging.	Generally low depth penetration and high signal attenuation.	[39,44–46]
Metabolic MRS	^{13}C-Pyruvate, endogenous ^{13}C-compounds	Facilitated diffusion	MRS	Multiple options for MR active nuclei to enrich probes. Often highly biocompatible analogues.	Lower sensitivity	[47–50]
Mass spectrometry	N/A	N/A	Mass Spec	High sensitivity, can detect a wide range of compounds to produce detailed fingerprints	Sample destructive	[51,52]
PET radiotracers	Fluorodeoxyglucose, ^{124}I-DPA-713, ^{18}F-GE-180	Facilitated diffusion or cell surface marker labelling	Positron emission tomography	High sensitivity	Low spatial resolution, single channel, ionising radiation	[53,54]

1.4 Imaging Modalities for Cell Tracking

There are several imaging modalities available to clinicians, each with their own advantages and limitations. Conventional imaging modalities capable of cell tracking include magnetic resonance imaging (MRI), positron emission tomography (PET), optical imaging, computed tomography (CT) and ultrasound. *Table 1.2* summarises the parameters of each modality. The two main modalities for cell tracking with the most translational potential are MRI and PET (highlighted in yellow in *Table 1.2*).

Table 1.2 - Summary of widely available imaging modalities and their parameters. Highlighted in yellow are the two main imaging modalities that are currently being used to develop translational cell tracking approaches, PET and MRI. Adapted from Cheng et al., 2023.[2]

Modality	**Spatial Resolution**	**Depth Penetration**	**2D/3D**	**Sensitivity threshold to contrast agent**	**Signal duration**
MRI	0.1-1 mm	Unlimited	3D	10^{-3}-10^{-5} M	days
PET	5-10 mm	Unlimited	3D	10^{-10}-10^{-12} M	minutes
Optical	2-5 mm	Cannot pass bone/air	2D	10^{-9}-10^{-12} M	days
CT	0.5 mm	Unlimited	3D	10^{-2} M	days
Ultrasound	1 mm	< 2 cm	2D	10^{0} M	days

Generally, successful cell tracking modalities should address the following challenges:

i. depth penetration – the whole sample should be imaged.

ii. contrast sensitivity – the imaging modality should allow for discrimination between different structures, functional units and cell types.

iii. spatial resolution/3D-imaging – better spatial resolution helps to contextualise the location and environment surrounding the cell.

1.4.1 Depth Penetration in Cell Tracking Modalities

There are several parameters to consider when designing a cell tracking imaging modality. Modalities such as MRI, PET and CT have unlimited depth penetration, making these approaches more practical for tracking labelled cells through complex tissue structures. Cell tracking via optical imaging suffers from signal attenuation as a result of light scattering and absorption by biomolecules such as haemoglobin and water.[55] Realistically, optical imaging is only achieved either in thin, exposed tissue sections or small *in vivo* models.

1.4.1.1 Sensitivity to Contrast in Cell Tracking Modalities

In diagnostics, sensitivity is defined as the probability of an observed positive result, in a patient truly positive for the tested disease. As described in point (ii) above, a cell tracking imaging modality should allow for discrimination between different structures, functional units and cell types. One of the most prevalent cell targeted imaging modalities with high sensitivity is 2-fluorodeoxyglucose-PET (FDG-PET), visualised in *figure 1.2*. FDG is a glucose analogue that serves as a substrate for glucose transporters. FDG enters cells with high metabolic turnover, such as tumours, cardiac and brain tissue. Spontaneous decay of the ^{18}F nuclide into a ^{18}O stable nuclide results in positron emission, leading to collisions with electrons in neighbouring tissue. This decay leads to an annihilation event, lasting ~125 picoseconds, resulting in the emission of two 511 keV photons in opposite directions. These photons are detected by coincidence detectors, which will localise the annihilation event along the line joining the two detectors. PET, including FDG-PET, is a successful and highly sensitive cell tracking imaging modality, however FDG-PET can only visualise glucose uptake. Following phosphorylation by hexokinase to FDG-6-phosphate, FDG-

6P becomes terminally entrapped within cells and cannot be further metabolised. MRI offers good sensitivity to contrast with minimum detection of contrast enhanced tissues within the picomolar range.

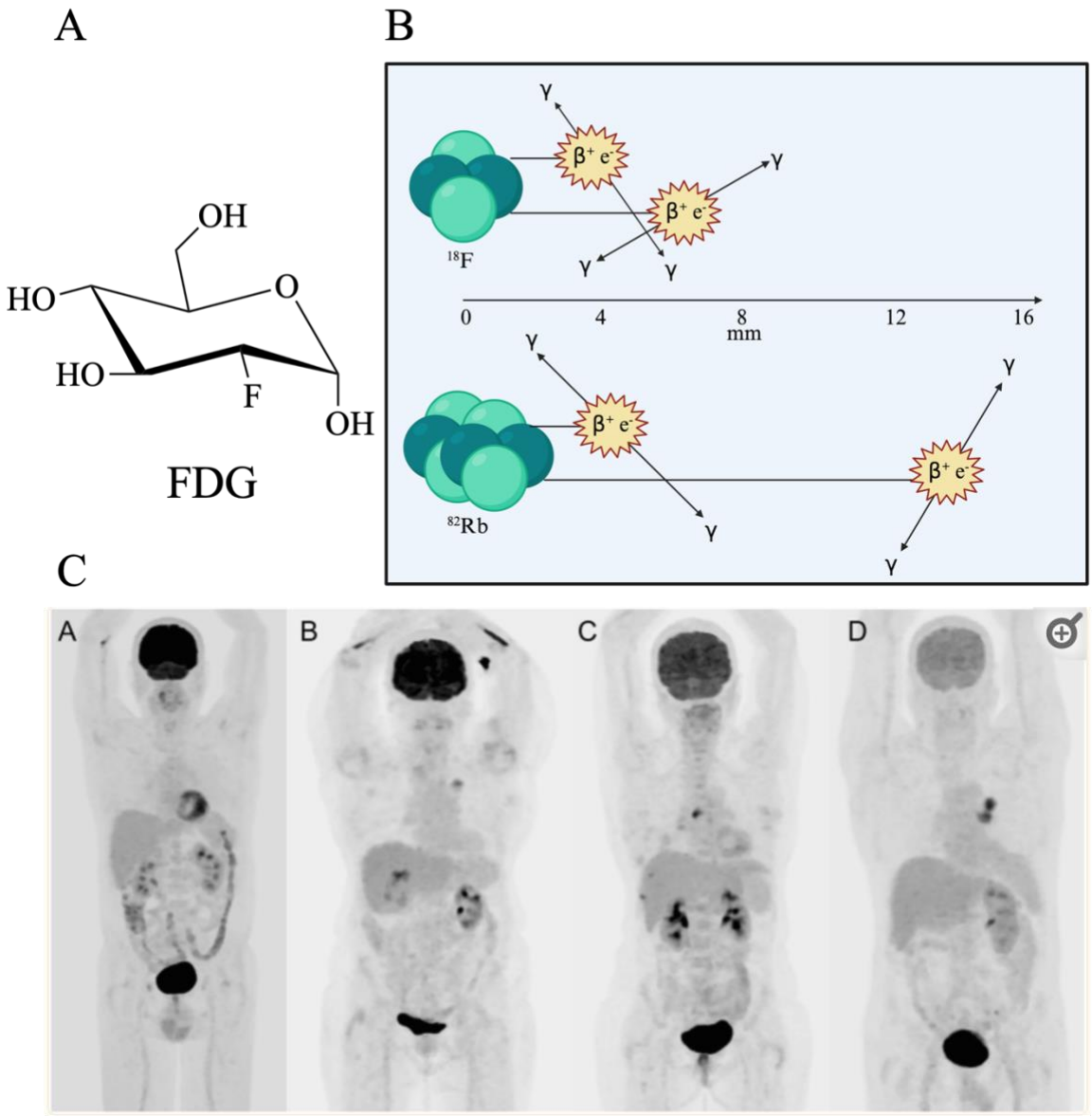

Figure 1.2 - For PET imaging, spatial resolution is limited by a number of factors including the detector size, range of the positron and non-collinearity. **A**. ^{18}F-Fluorodeoxyglucose (FDG), a PET probe used to image glucose uptake. **B.** In PET imaging a positron is emitted as a result of beta decay from a positron emitting nuclide. The positron collides with electrons in neighbouring tissues in an annihilation event, giving rise to two 511 keV photons with equal energy in opposing directions. **C.** FDG-PET whole body images of healthy patients from different glycaemia groups. High FDG signal (dark) is visualised in tissue with high metabolic activity including the brain and cardiac tissue. Often PET is combined with another imaging modality (MRI or CT) to address the lack of spatial resolution. Image from Sprinz et al., 2018[56]

1.4.1.2 Spatial Resolution for Cell Tracking Modalities

Spatial resolution is another consideration, with imaging approaches such as MRI offering excellent soft tissue detail. Spatial resolution refers to the minimum distance at which two points within an image can be distinguished. Imaging of minute structures is more easily achieved by modalities with better resolution, allowing for facile identification of lesions. An MR image is made up of voxels, which is a 3-dimensional unit of a pixel. In a given image, each voxel has a specific intensity that is proportional to the number of nuclei in each voxel. In MRI, voxel intensity is also affected by the relaxation rates and pulse sequences employed. PET is notable for having poor spatial resolution, compared to modalities such as MRI and CT. Conversely CT has excellent spatial resolution of around 0.5 mm.

1.4.1.3 Why MRI as a Modality for Cell Tracking?

For cell tracking applications, MRI can be exploited in a number of ways. MRI provides excellent images of the whole body, including highly detailed projections of internal organs. Magnetic resonance spectroscopy (MRS) can also be used to analyse metabolic information of different sites within a given tissue. MRS is capable of detecting any nuclei with a magnetic moment, and compounds containing those nuclei, if they are at a high enough local concentration. MRS has previously been used to target various metabolites containing ^{1}H, ^{2}H, ^{13}C and ^{31}P, giving rise to unique fingerprint spectra. For example, N-acetyl-aspartate (NAA), creatine (Cr) and choline (Cho) are detectable by proton MRS. Deuterated glycolytic metabolites including ^{2}H-glucose, ^{2}H-lactate, ^{2}H-glutamine/glutamate, ^{2}H-fumarate and deuterium oxide are all visible within deuterium MRS spectra. ^{13}C labelled compounds such as glucose and pyruvate, both from enriched and naturally occurring sources are equally detectable via natural abundance or hyperpolarised ^{13}C MRS.

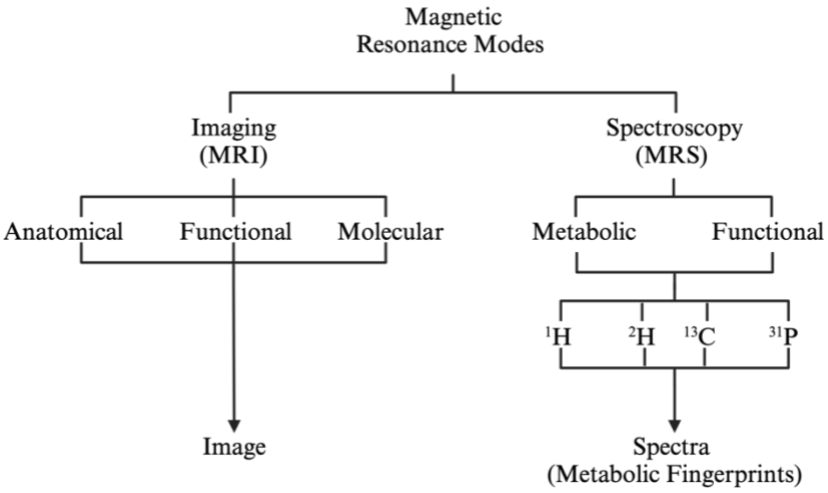

Figure 1.3 - Schematic displaying the diverse functionality of magnetic resonance approaches. MR approaches transcend the requirements for cell tracking applications. MRI and magnetic resonance spectroscopy (MRS) are the two broad modes for which MR can be used for cell tracking. MRI provides excellent anatomical functional and molecular information. MRS provides voxel by voxel metabolic fingerprint information. Figure from So et al. [57]

1.5 Principles of Magnetic Resonance Imaging

Magnetic resonance imaging (MRI) is a non-invasive imaging technique used widely in both pre-clinical and clinical settings. The contribution of MRI to the field of medical imaging has been significant. Since the clinical capabilities of the technique were first demonstrated by Mansfield and Lauterbur in the 1970s, for which they won the 2003 Nobel Prize for Medicine,[58] MRI has become a near ubiquitous medical imaging approach. MRI provides users with excellent soft tissue contrast (*see figure 1.4).* Standard MR images are generated from the intense ^{1}H nuclear magnetic resonance (NMR) signal of water. Fundamentally, the basis of MRI is rooted in the physics of nuclear magnetic resonance (NMR) spectroscopy, first experimentally demonstrated by Bloch and Purcell in 1946.[59,60]

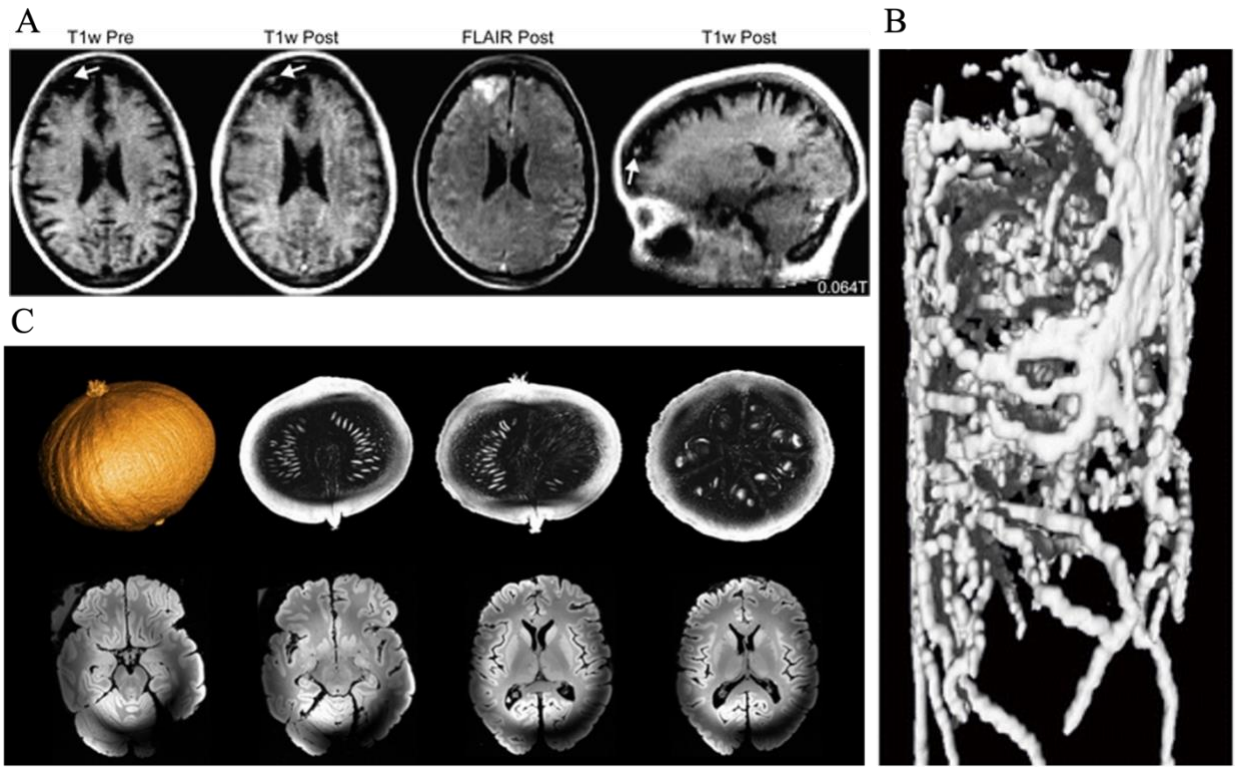

Figure 1.4 **-** ^{1}H MRI images at different fields**. A.** pre- and post- gadolinium contrast *T1*w scan and fluid-attenuated inversion recovery imaging of brain tumour patient at 0.064 T. [61] **B.** MRI of *Phaseolus vulgaris L*. plant root system at 4.7 T.[62] **C.** MRI of pumpkin and *ex vivo* brain at 11.7 T.[63]

1.5.1 NMR Principle and Signal Generation in MRI

Atomic nuclei that possess an odd mass number display the quantum property of nuclear spin, which means they exhibit dipole behaviour when in the presence of an applied magnetic field (B_0). Spin active nuclei in the presence of a B0 field precess about the field with an angular frequency called Larmor frequency. The Larmor frequency is a product of the gyromagnetic ratio of the nuclei and the magnitude of the magnetic field. This can be surmised using the following equation:

$$\omega = \gamma B_0$$

Where ω is the Larmor frequency, γ is the gyromagnetic ratio and B_0 is the magnetic field. An applied radiofrequency (RF) pulse at the Larmor frequency of a given nuclei can cause the misalignment of nuclear spins from the axis of the B_0 field. Following excitation by an RF pulse,

the precession of nuclear spins back to the lower energy ground state, B_0, results in generation of RF signals. The environments in which spin active nuclei reside will impact spectral readouts.

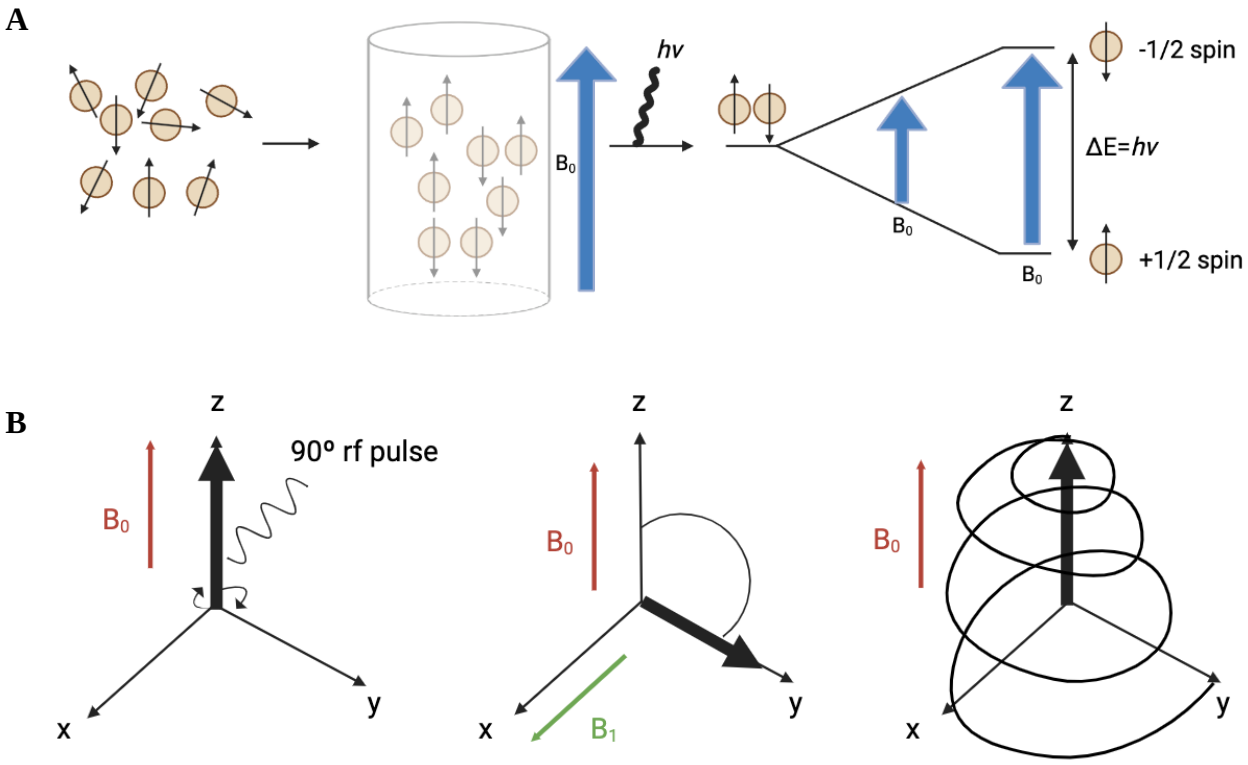

Figure 1.5 – A. Schematic showing an MRS experiment. Nuclei possess random spins, however in the presence of applied magnetic field B_0, causes these spins to display dipole behaviour and align parallel or anti-parallel to the axis of the B_0 field. In a standard MRS experiment, an applied radiofrequency pulse (RF) leads to the excitation of nuclear spins to the excited state. Magnetic resonance of a given nuclei occurs when the external RF is approximately the same as the Lamor frequency of the nuclei. B. Schematic demonstrating precession of nuclear spin following excitation of nuclei by RF pulse. Broadly, the net magnetisation vector (M) is displaced from the z-axis to the transverse plane following RF pulse excitation of nuclei. The recovery of M back to equilibrium occurs as precession relative to the direction of B_0. Free induction decay (FID), generated as a result of this phenomena is processed by Fourier transform, giving rise to interpretable NMR spectra. Drawn using Biorender.com

MRI active isotopes exhibit nuclei spin, where hydrogen protons show the most favourable parameters for imaging. *Table 1.3* describes the key parameters of common MR active isotopes relevant for applications in biomedical imaging, including natural abundance of the isotope and overall concentration in human tissue. These values are key in terms of both intrinsic sensitivity and for concentration detection limits with externally applied contrast agents. The gyromagnetic

ratio is a fundamental property of each nuclei that relates to the sensitivity of the isotope – the higher the value the more sensitive the isotope for MR applications.

Table 1.3 - Table showing MR parameters for notable isotopes.

Nucleus	**Spin**	**Gyromagnetic Ratio MHz.T^{-1}**	**Natural Abundance (%)**	**Larmor Frequency (MHz) at 7.0 T**	**Concentration of Isotope in Human Tissue**
^{1}H	1/2	42.58	~100	298.06	88 M
^{2}H	1	6.53	< 0.1	45.71	12 mM
^{23}Na	3/2	11.26	~100	78.82	80 mM
^{31}P	1/2	17.24	~100	120.68	75 mM
^{19}F	1/2	40.05	~100	280.35	4 mM
^{17}O	5/2	-5.77	0.04	40.39	16 mM

Table 1.4 - Table showing T_1 and T_2 relaxation rates for different tissue types [64]

Tissue	**T_1 (msec) at 3.0T**	**T_2 (msec) at 3.0T**
Muscle	1420 ± 38.1	31.7 ± 1.90
Cartilage	1240 ± 107	36.9 ± 3.81
Subcutaneous fat	371 ± 7.94	133 ± 4.43
Marrow fat	365 ± 9.0	133 ± 6.14

1.5.2 T_1 vs T_2 Imaging

Classical ^{1}H MRI exploits the signal generated from the ^{1}H-proton spin of water molecules *in vivo*, allowing for excellent spatiotemporal resolution of soft-tissue. The classic approach to generate

MRI images is to utilise the relaxation properties of hydrogen nuclei of water, which generates contrast between different tissues. Longitudinal relaxation (T_1) is the process by which the net magnetization vector realigns from the M_{xy} plane to the M_z plane, where the Mz plane is the . Conversely, transverse relaxation (T_2) is the loss of signal coherence observed in the M_{xy} plane as the net magnetisation vector realigns to the M_z plane. Longitudinal (T_1) and transverse (T_2) relaxation rates of water protons differ depending on the tissue in which they reside. *Figure 1.6* below details differences between T_1 and T_2 relaxation rates in both fat and water. T_1 recovery of fat is much faster than that of water. Low molecular tumbling rate of fat that is equivalent to the Lamor frequency results in rapid exchange between hydrogen nuclei and surrounding lattice. T_1 recovery of water is slower than fat. Water is more disordered and has non-equivalent molecular tumbling rate/Lamor frequency resulting in less efficient energy exchange between the hydrogen nuclei and adjacent lattice. For T_1 weighted images, repetition time (TR) is the largest contributing factor. TR is the time gap between successive pulse sequences. The greatest difference in T_1 values between different tissues (water and fat) occurs at shorter TRs, meaning T_1 -weighted images employ short TRs to achieve the greatest contrast. T_2 decay in fat is rapid as energy exchange is highly efficient in ordered tissue. T_2 decay in water is slower than fat. For T_2 weighted images, echo time (TE) is the largest contributing factor. TE is the time between the centre of radiofrequency pulse and centre of the echo peak. The greatest difference in T_2 values between different tissues (water and fat) occurs at longer TEs, meaning T_2 -weighted images employ long TEs to achieve the greatest contrast.

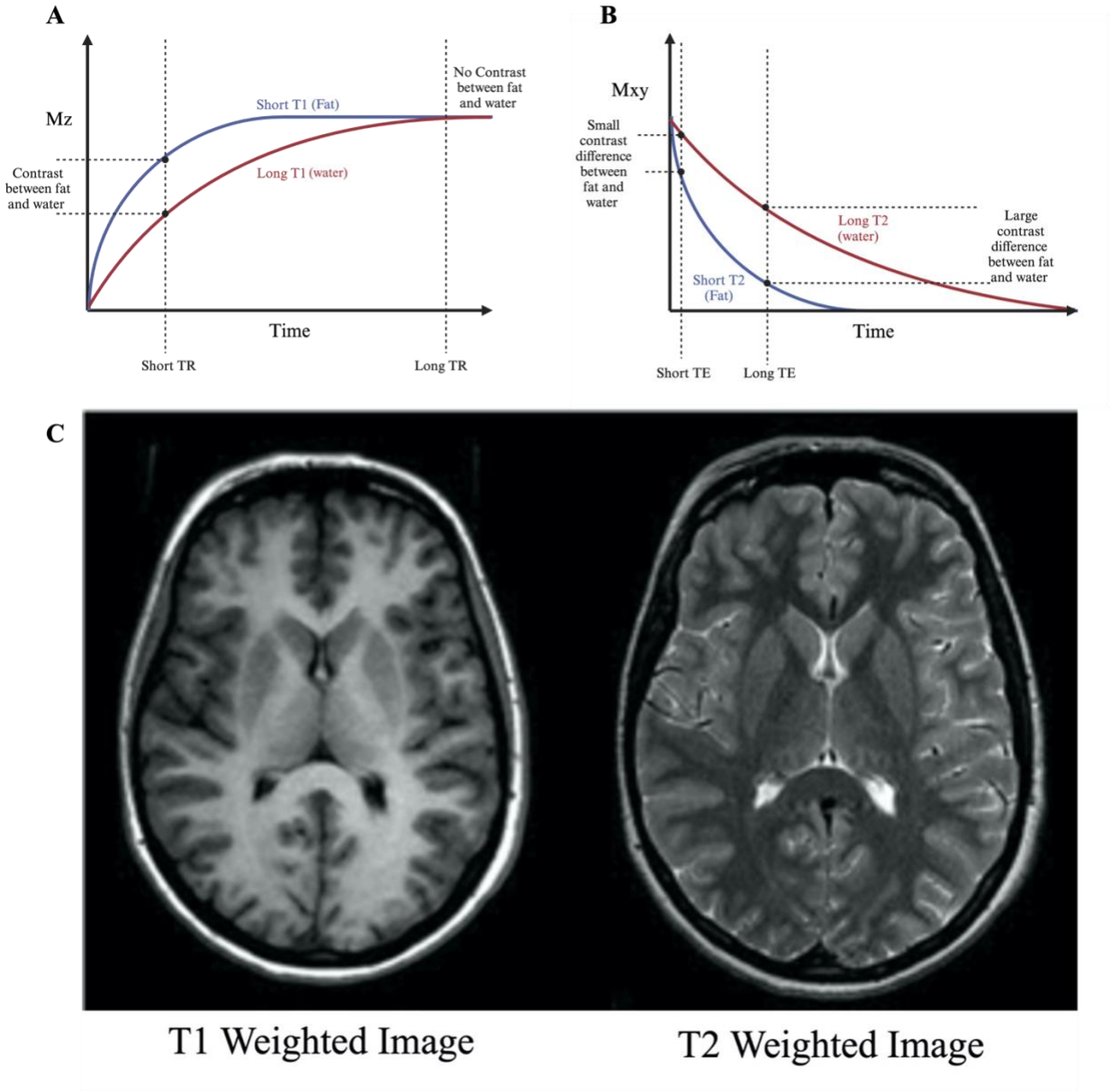

Figure 1.6 **-** T_1 and T_2 differences. **A**. Schematic depicting differences in T_1 recovery between water (red) vs fat (blue). **B.** T_2 decay in water (red) vs fat (blue). **C.** T_1 vs T_2 weighted image of brain

1.5.3 Relaxation Times

The reciprocal of relaxation times T_1 and T_2, gives the relaxation rate, and are denoted as R_1 and R_2 respectively. In T_1-weighted images, signal intensity increases with a higher R_1 rate ($R_1 = 1/T_1$) and decreases with an increased R_2 rate ($R_2 = 1/T_2$). Conversely for T_2-weighted images, the opposite occurs. The relaxation rates R_1 and R_2 can be enhanced by the presence of contrast agents,

allowing for greater signal difference between tissues in both T_1 and T_2 weighted images. Contrast agents are paramagnetic or superparamagnetic compounds, which greatly alter the behaviour of adjacent water protons, increasing both the R_1 and R_2 relaxation rates. This indirect water response means that, unlike iodinated CT or X-ray contrast agents, MRI contrasts are not directly observed. Broadly, contrast agents can be subdivided into T_1- and T_2-weighted contrast agents, depending on how impactful the response is on the particular relaxation mechanism. For example, T_1-weighted contrast agents predominantly affect T_1 relaxation, resulting in increased signal intensity.

The most common T_1 contrast agents are gadolinium (Gd^{3+}) chelates, which are used in approximately a 1/3 of clinical MRI scans. Other paramagnetic ions, such as Mn^{2+} and Fe^{3+}, however, can also be used. T_2 contrast agents include superparamagnetic iron oxide nanoparticles (SPIONs), which cause a reduction in signal intensity.

1.6 MRI Contrast Agent Choice

For MRI, there are multiple strategies that can be employed to label cells. These strategies can generally be subdivided into direct and indirect labelling methods. Direct labelling methods include using gadolinium chelates, superparamagnetic iron oxide nanoparticles, manganese chelates, ^{19}F agents, and CEST/ParaCEST agents. To achieve selective cell labelling, these agents are generally conjugated to a targeting moiety, such as an antibody or peptide.

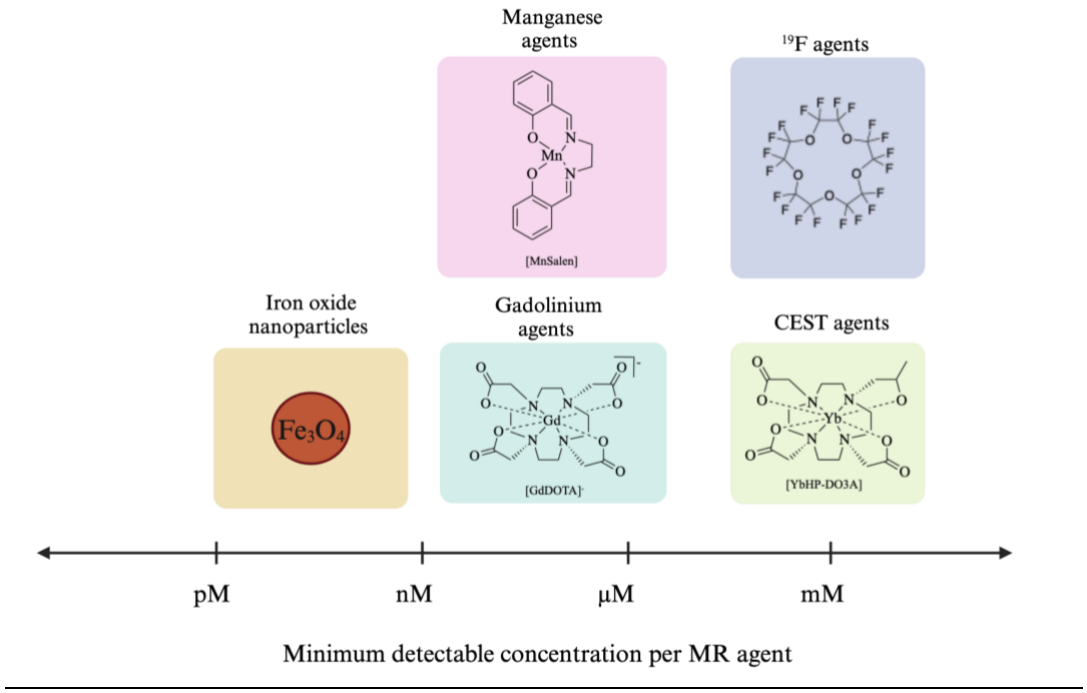

Figure 1.7 - Schematic of MRI contrast agents for cell tracking organised by minimal detectable concentration..[65]

Gadolinium (Gd^{3+}) chelates are paramagnetic contrast agents which predominately affect the spin lattice relaxation time, or T_1 (see *figure 1.6*). Water protons proximal to Gd^{3+} complexes exchange rapidly leading to a marked reduction in T_1 relaxation, resulting in positive contrast.[1] Gadolinium based imaging approaches are used in approximately 400 million scans per year, accounting for 50 tonnes of gadolinium.[66] Unlike perfluorocarbons (PFC) and iron oxide based CAs, gadolinium chelates are not readily phagocytosed by macrophages.[67] Therefore, targeting molecules such as antibodies must be incorporated within the design of gadolinium CAs to achieve targeted imaging.[67]

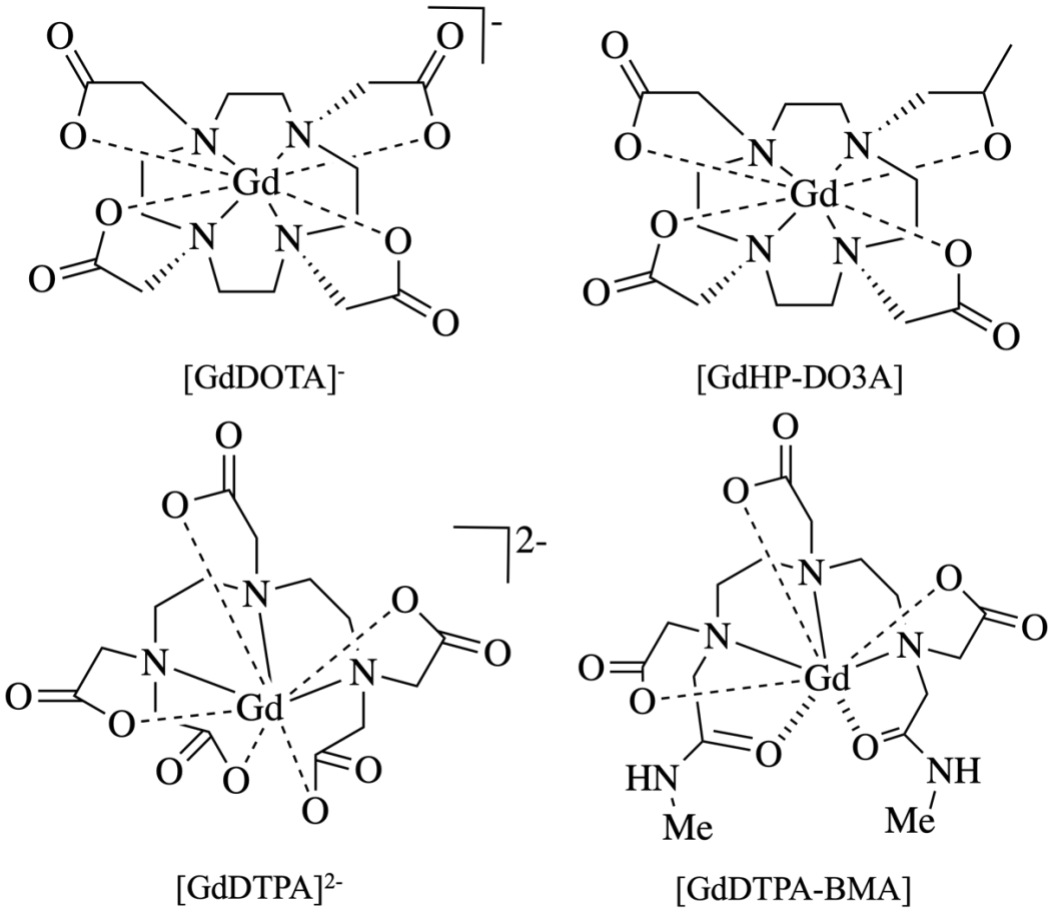

Figure 1.8 – Examples of macrocyclic and linear gadolinium based contrast agents that have been clinically approved. Macrocyclic agents: Gadoterate meglumine $[GdDOTA]^-$ (Dotarem®); Gadoteridol [GdHP-DO3A] (Prohance®). Linear agents: Gadopentetate dimeglumine $[GdDTPA]^{2-}$ (Magnevist®); Gadodiamide [GdDTPA-BMA] (Omniscan®).

Unchelated gadolinium is toxic to most biological systems, due to the fact that gadolinium has a similar ionic radius to that of Ca^{2+}.[25] This property means that free Gd^{3+} can interfere with calcium binding proteins, including calmodulin and Ca^{2+} channels. Of the clinically approved GBCAs the most common chelate systems are based on either DTPA (diethylenetriaminepentaacetic acid) or DOTA (1,4,7,10- tetraazacyclododecane-N,N,N,N-tetraacetic acid). Examples of clinically approved DTPA-based gadolinium contrast agents include GdDTPA and GdDTPA-BMA as displayed in *figure 1.8.* GdDTPA is a complex of the $Gd3^+$ metal ion and the $DTPA^{5-}$ ligand. The Gd^{3+} ion has a coordination number of 9, The multidentate $DTPA^{5-}$ ligand is coordinated with 5

carboxylate donor groups and 3 nitrogen donor groups. The Gd-DTPA complex displays conformational flexibility, with its 9th coordination site being occupied by one water molecule. Gd-DTPA-BMA is a derivative of GdDTPA, where two of the 5 carboxylate donors have been replaced with 2-methylamide groups, giving an overall neutral charge. Water exchange rate is a major factor influencing ligand choice. The water exchange rate describes how quickly water molecules in the inner sphere are replaced with water in the second sphere. A slow exchange rate means that water coordinated to the inner sphere does not exchange rapidly, which in turn has a negative impact on the ability of the contrast agent to effect relaxivity. Similarly if the water exchange is too fast, the overall effect on relaxation is similarly diminished. Factors including overall negative charge, stearic hindrance and conformational flexibility of the ligand all significantly affect the water exchange rate. GdDTPA has a conformationally flexible ligand and an overall negative charge, which are factors which support faster water exchange. Macrocyclic GBCAs include GdDOTA and GdDO3A. GdDOTA has an overall negative charge and is coordinated by 4 carboxylate donors and 4 nitrogen donors. GdDO3A similarly features coordination to the metal ion by 4 oxygen donor groups and 4 nitrogen donor groups, where a water molecule occupies the final coordination site. Macrocyclic GBCAs have less conformational flexibility, relative to their linear counterparts coupled with lower dissociation rates. Water exchange rate in macrocyclic ligands can be impacted by the geometry of the molecule. GdDOTA exists in two different isomeric forms; square anti-prismatic (SAP) and inverted anti-prismatic (TSAP) isomers. Due to differences in stearic compression, TSAP isomers can display water exchange rates between 50-500 times faster than SAP isomers. [68]

Whilst GBCAs are effective, there are several off target effects associated with their use. GBCA administration is linked to both nephrotoxicity and nephrogenic systemic fibrosis.[69,70] In fact,

approved GBCAs have been shown to display upregulation of inflammation even at low systematic concentrations.[71] In 2017, the European Medicines Agency (EMA) restricted the use of linear GBCAs, including Magnevist and Omniscan (*see figure 1.8*). Typically, linear chelators, including DTPA, display increased dissociation of Gd^{3+} relative to macrocyclic chelators. The poor thermodynamic and kinetic stability of linear GBCAs risks chelate transmetallation, with endogenous cations including Ca^{2+} and Zn^{2+}.[72] Macrocyclic GBCAs, including those with DOTA and DO3A chelators, offer better safety profiles whilst maintaining comparable relaxivity.[73] Due to the minimized risk of metal ion leaching, macrocyclic chelate systems have become the favoured choice for clinical imaging.

1.7 MRI Cell Tracking Using GBCAs

1.7.1 Non-Targeted Labelling of Cells with Gadolinium Based Agents.

Targeted imaging approaches with GBCAs normally involve using small molecule or antibody modifications to the linear or macrocyclic chelate complexes. With this approach, GBCAs have been specifically developed to target surface antigens of both immune cells and cancers.[74] Gadolinium-based contrast agents may be used for either targeted or non-specific image enhancement for T_1 weighted images. Within the context of inflammation, GBCAs have been developed to target both specific macrophage subpopulations and other markers of inflammation.

1.7.2 Cell tracking with Small Molecule-GBCAs

One example of this is [GdDOTA]-mef (see *figure 1.9*), which is gadolinium chelates modified with a mefenamic acid.[75] Mefenamic acid is a non-steroidal anti-inflammatory drug (NSAID), which specifically inhibits cyclooxygenase 1 and 2 (COX1 and COX2). It functions by inhibiting prostaglandin-endoperoxide synthase, leading to prevention of prostaglandin formation. Interestingly, the contrast agents displayed low cytotoxicity toward HeLa cells, with high uptake

in glioma cell lines (U87), relative to Gd-DOTA.[75] Scans with [GdDOTA]-mef showed enhanced T_1 contrast in both the glioblastoma and arthritic models tested (see *figure 1.9*). Use of small molecule targeting, such as with mefenamic acid, represent one method that could be used to label macrophage subpopulations with GBCAs.

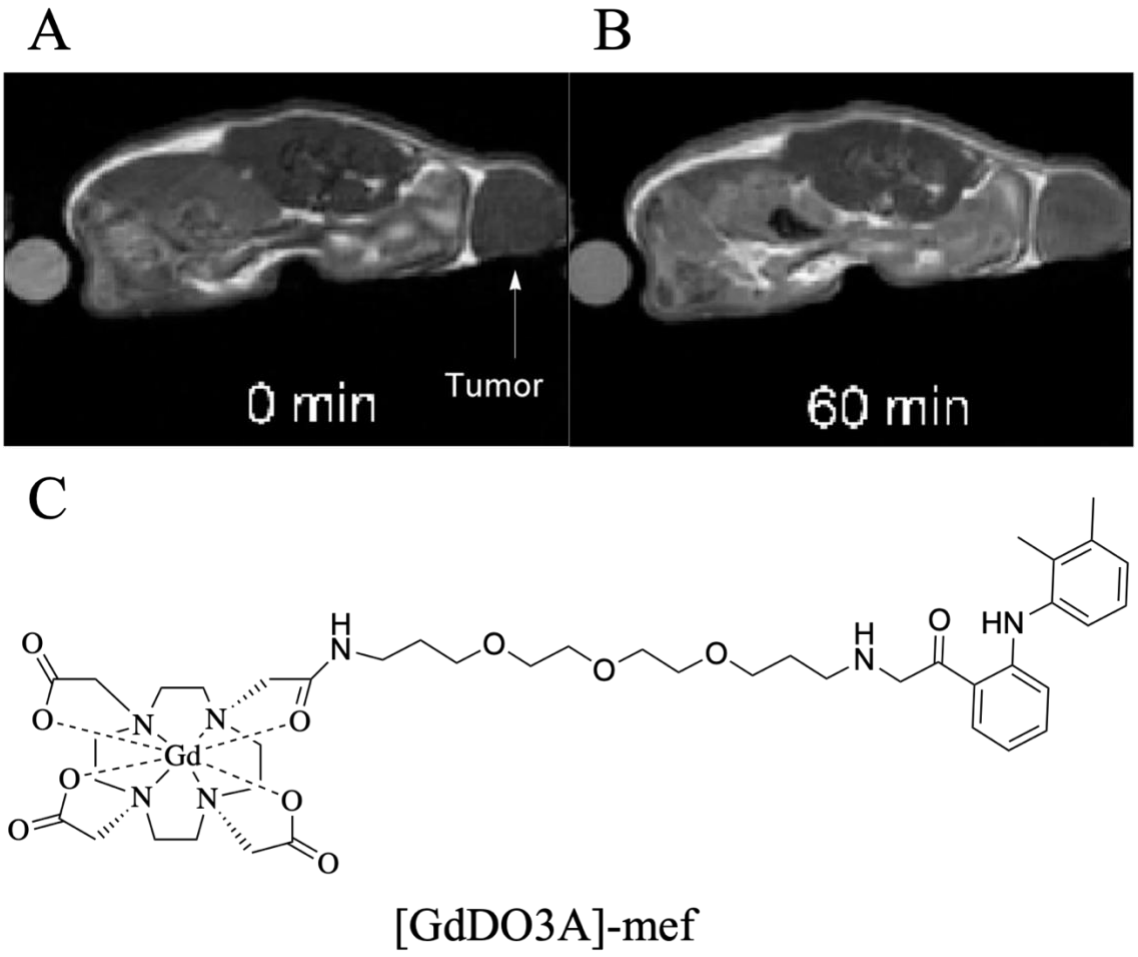

Figure 1.9 **-** [GdDO3A]-mef developed by Leung et al., 2014.[75] **A.** T_1 weighted MR image of U87 xenograft nude mouse pre-[GdDO3A]-mef. **B.** T_1 weighted MR image of U87 xenograft nude mouse 60 mins after [GdDO3A]-mef tail vein injection. **C.** Chemical structure of [GdDO3A]-mef.

Translocator protein (TSPO) antigen is upregulated in activated macrophages and has previously been used as a macrophage imaging marker in positron emission tomography (PET) investigations.[76] One study generated a TSPO targeted GBCA. TSPO ligand CB86 was used to guide gadolinium chelates, allowing for visualisation of inflamed regions in rheumatoid arthritis

mouse models.[77] Use of synthetically derived protein peptidomimetics to target GBCAs has become a popular strategy. One example of this is an $\alpha_v\beta_3$ integrin targeted GBCA [GdDOTA]-IAC developed by Kim et al.[78]

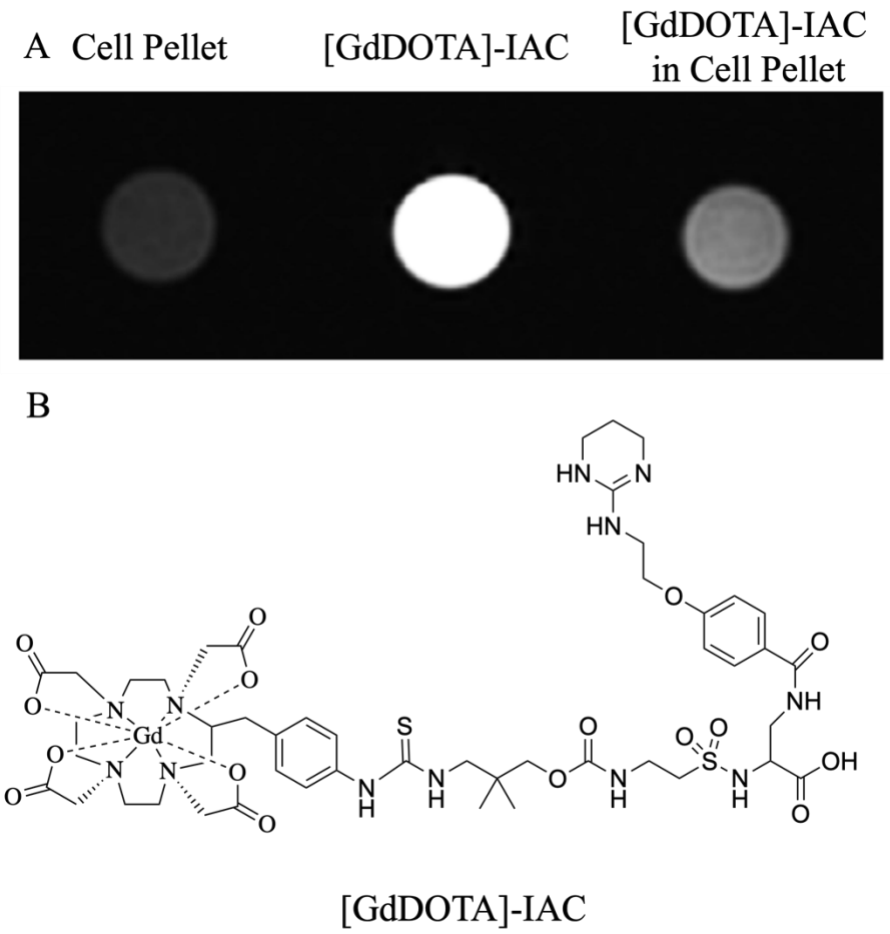

Figure 1.10 **- A.** *T1*-weighted MRI of M21 cell pellet, [GdDOTA]-IAC and [GdDOTA]-IAC labelled M21 cell pellet. **B**. Chemical structure of [GdDOTA]-IAC. Figure adapted from Kim et al., 2015[78]

As visualised in *figure 1.10* above, the [GdDOTA]-IAC displayed a visible improvement to T_1 signal when imaged with cell pellet (M21 melanoma), compared to the cell pellet alone. Conjugation of peptidomimetics and [Gd-DOTA] is relatively straightforward and easily achieved through peptide deprotection and coupling strategies. One particular limitation of this is study is that controls were limited to binding within melanoma cell lines, meaning that binding could be due non-specific interactions between the peptidomimetic attachment and general cell factors. This

study could have been improved by demonstrating that this agent does not bind to healthy cell lines. Cytokine receptors, including the interlukin-6 receptor (IL6R), have also been targeted with similar approaches. [Gd-DOTA]-Lys(rhodamine)-(Leu-Ser-Leu-Ile-Thr-Arg-Leu) was developed as a GBCA to target the IL-6 receptor.[79] The targeting molecule is a peptidomimetic for the IL-6 receptor binding domain. Whilst the imaging application for this compound has mainly been focused on cancer, IL-6 upregulation is also seen in macrophage subpopulations.

Ayat *et al* develop an extra domain-B fibronectin (EDB-FN) targeted macrocyclic GBCA, named ZD2-N_3-Gd[HP-DO3A], as a theranostic for triple negative breast cancer (see *figure 1.10*).[80] EDB-FN is a matrix protein, which is highly upregulated in triple negative breast cancer and is thought to be a key mediator of angiogenesis and endothelial cell proliferation. Hallmarks which are also consistent with processes of inflammation. This targeting mechanism displayed high tumour contrast enhancement at low doses (0.02 mmol Gd/Kg), and outperformed clinically approved [Gd(HP-DO3A].[80]

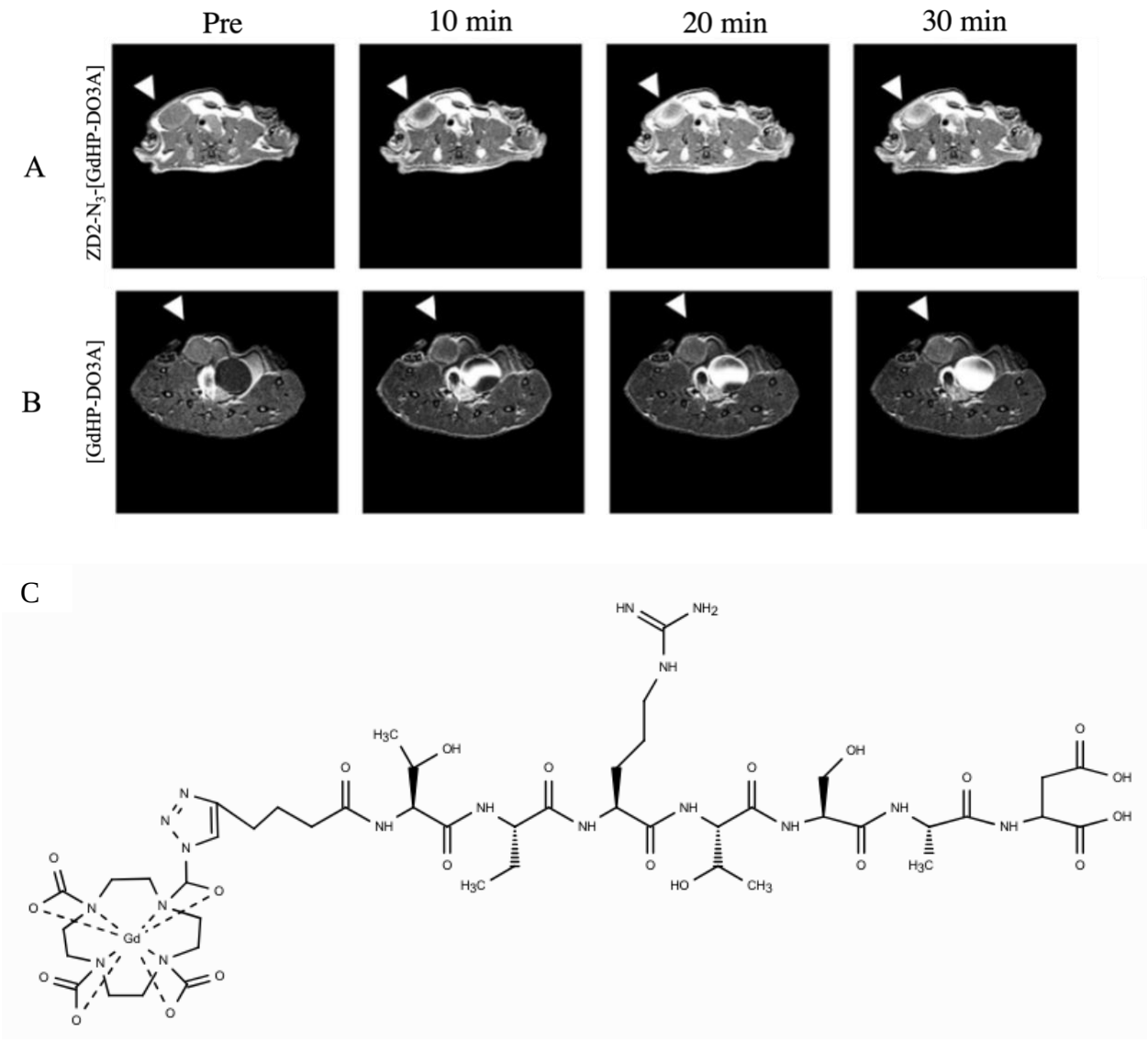

Figure 1.11 - **A**. *T_1* weighted imaging of MDA-MB-231 (triple negative breast cancer) tumours in mice, pre and 0-30 min post injection with ZD2-N3-[GdHP-DO3A]. **B**. *T_1* weighted imaging of MDA-MB-231 (triple negative breast cancer) tumours in mice, pre and 0-30 min post injection with [GdHP-DO3A]. **C.** Chemical structure of ZD2-N3-[GdHP-DO3A]. Images from Ayat et al., 2019.[80]

1.7.3 Antibody Targeting with GBCAs

Antibody targeting methods have also been applied to target tumours via GBCAs. Tumour targeting through an anti-EGFR single domain antibody conjugated to an arginine-glycine-aspartic acid (iRGD) peptide was developed by Xin et al.[81] This targeting moiety was then coupled to a Gd-DTPA imaging agent.

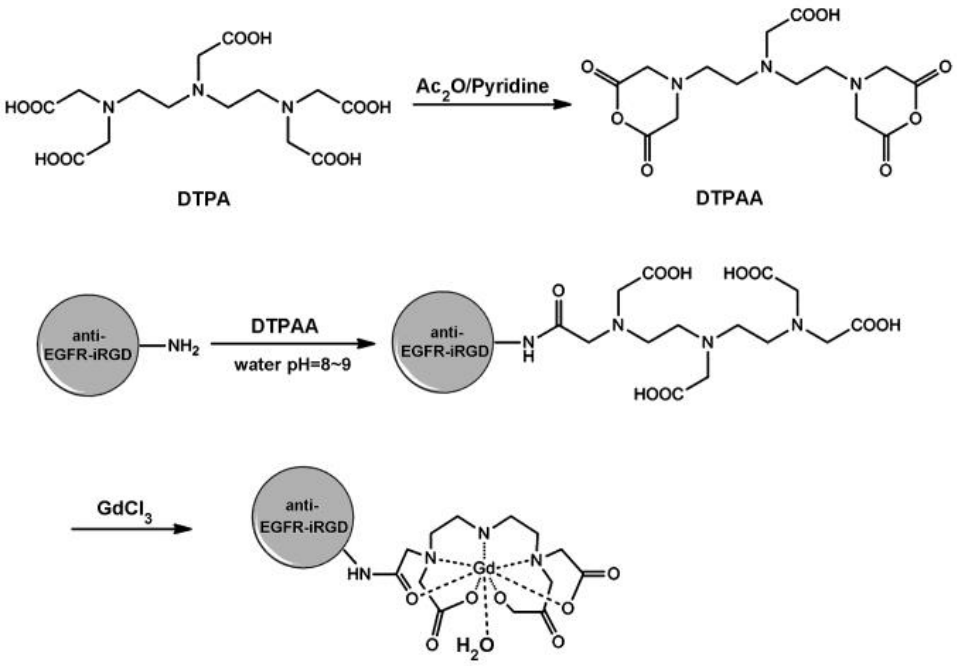

Figure 1.12– *Synthesis for anti-EGFR-iRGD-GdDTPA from Xin et al., 2016.* [59]

Alone, RGD peptides have been used for tumour penetration and are known to bind with high affinity to the αvβ3-integrin receptor.[81] The GBCA [GdDTPA]-antiEGFR-iRGD displayed higher T_1 relaxivity and increased tumour targeting as seen in *figure 1.13*.[81]

In addition, agents such as [GdDTPA]-antiVEGF receptor 2 have proved highly effective for imaging neovascularisation in cancer models.[82] VEGF upregulation is a promising target for MDI related inflammation, where potentially a VEGF targeted GBCA could provide insight into early stages of the inflammatory process. This approach could potentially be improved through the use of a DOTA or DO3A chelate system, to avoid off-target effects of gadolinium ion leaching.

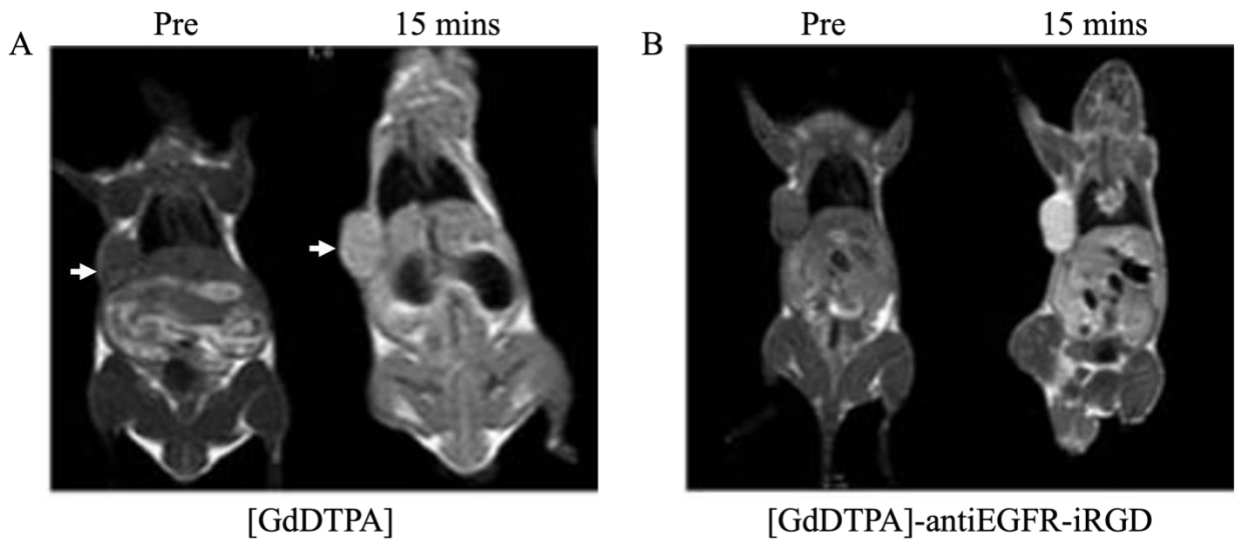

***Figure 1.13* – A.** T_1 weighted images of BGC-823 xenograft mice (gastric cancer) before and 15 minutes after tail vein injection of [GdDTPA] **B.** T_1 weighted images of BGC-823 xenograft mice (Gastric cancer) before and 15 minutes after tail vein injection of [GdDTPA]-antiEGFR-iRGD.

1.7.4 Using Liposomes and Micelles with GBCAs

A popular targeting mechanism for GBCA delivery is through the use of liposomes. Liposomes are spherical vesicles made up of phospholipid bilayers, which encapsulate molecules for drug delivery. Liposome vectors can be modified using several targeting molecules to specifically deliver contrast agents, including GBCAs where they colocalise with intended cellular targets. One such example is gadolinium-containing phosphatidylserine liposomes, which have been used to image atherosclerotic plaques.[83] Phosphatidylserine (PS) residues in apoptotic cells trigger macrophage phagocytosis via the macrophage scavenger receptor pathways.[83] Liposomes containing Gd-DTPA-PS, which is a linear GBCA functionalised with rhodamine, were injected into ApoE-/- mouse models of atherosclerosis and analysed by 11.7 T T_1 weighted MRI and fluorescence imaging. The Gd-liposome system displayed enhancement to atherosclerotic plaques and Gd colocalization with macrophages.[83]

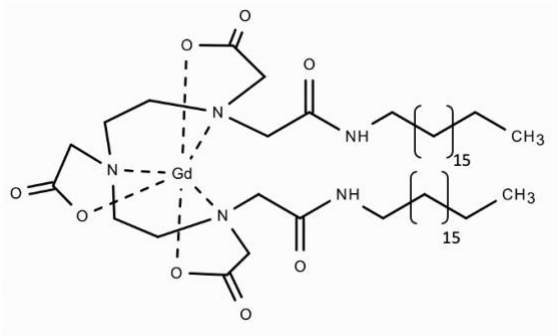

***Figure 1.14** – Figure of Gd-DTPA-PS (Maiseyeu et al., 2009)*

Liposomes, targeted by a GBI-10 aptamer have been developed to deliver gadolinium contrast agents. Both showed increased accumulation of gadolinium chelates at the tumour periphery in glioma. These methods of targeting could be applied to surface antigens of activated macrophages. In addition, micelles loaded with GBCAs such as Gd-DTPA-conjugated PGG-PTX, have been developed to target lung cancers.[84]

1.7.5 Targeting Macrophages with GBCAs

Macrophages and their activity are highly reliable indicators of inflammation, as detailed in the introduction of this review. Importantly, the distinction between macrophage polarisation states can confer information about the state of inflammation within specific tissue.[34] GBCAs conjugated with synthetically derived high density lipoproteins, can selectively target macrophage uptake.[34] Significantly, these modifications with high-density lipoprotein moieties do not affect the MR parameters. This system represents a promising small molecule approach to target macrophages *in vivo.*[34] Silica coated Gd(DOTA)-loaded protein nanoparticles have been shown to target macrophages when functionalised with a tobacco mosaic virus (TMV).[36]

Multimodal gadolinium probes have also been developed such as PG-Gd-NIR813, which is a magneto-optical probe used to delineate M2 polarised TAMs.[31,25,85] PG-Gd-NIR813 exhibits positive contrast and, as a multimodal contrast agent, fluoresces at 813 nm. [35] This design of contrast agent represents a promising approach for multimodal diagnostic imaging, whereby both

MRI and fluorescence imaging can be used in parallel. Interestingly, PG-Gd-NIR813 was found to have colocalised with macrophages (CD68+) within the tumoral peri-necrotic region but, however, did not co-localise with macrophages (CD163+) at the tumour periphery.[35] This result potentially suggests that PG-Gd-NIR813 distribution within the tumour is dependent on activated tumour-infiltrating macrophages, which function to clear necrotising tumour cells.[35]

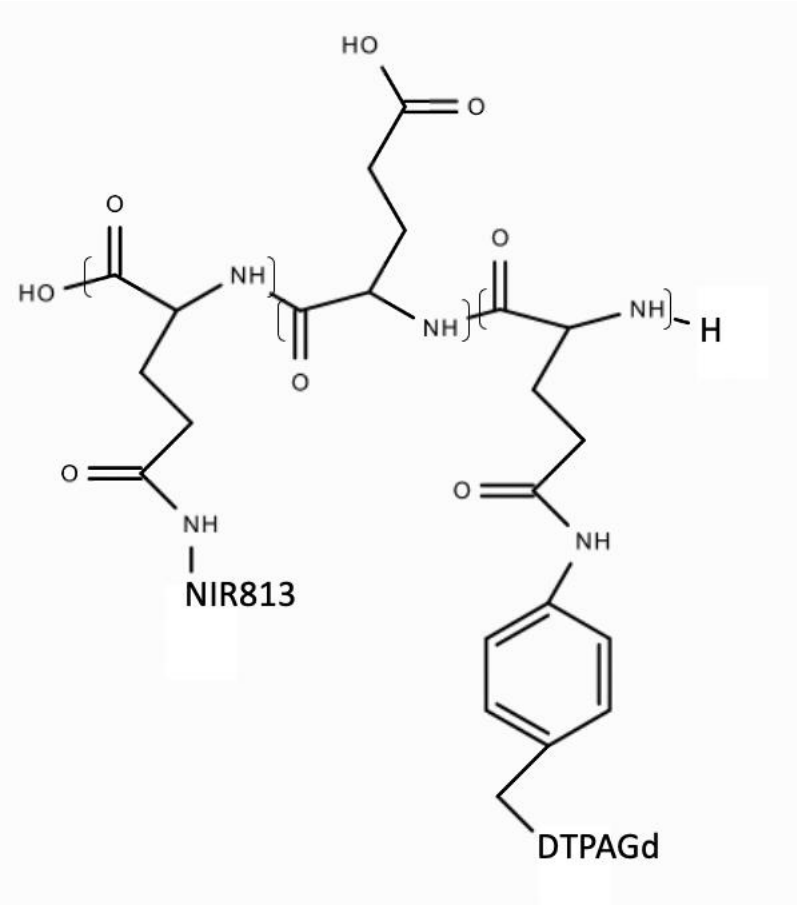

Figure 1.15 – *Figure of PG-Gd-NIR813 (Melancon et al., 2010).*[65]

1.7.5.1 Further Considerations of GBCAs

Linear GBCAs, such as Gd-DTPA displayed increased brain retention following repeated administration, suggesting that neuroinflammation is a potential contraindication for linear GBCA use.[86] The poor thermodynamic and kinetic stability of the linear DTPA ligand system means that Gd^{3+} is more likely to undergo transmetallation events leading to the deposition of free, highly toxic Gd^{3+}. Design of future GBCAs should consider several factors, including tissue retention, off-target effects and use of macrocyclic systems. Evidently, DOTA and DO3A chelate systems represent safer approaches, and functionalisation with targeting molecules is readily achieved.

1.8 Fe-MRI Approaches

Iron-oxide based nanoparticles (IONPs) used for molecular MRI are superparamagnetic and generally fall under three categories: superparamagnetic iron oxide nanoparticles (SPIONs); ultrasmall superparamagnetic iron oxide nanoparticles (USPIONs) or micrometer sized iron oxide nanoparticles (MPIONs).[87] IONPs comprise of small iron oxide particles (FeO-Fe_2O_3) which have a very strong magnetic moment, capable of perturbing the local magnetic field. In MRI acquisitions, SPIONS reduce T_2 signal intensity in tissue which absorb the contrast agents, resulting in negative contrast.[87] Ferumoxytol, which is an FDA approved intervention for iron deficiency in adults with chronic kidney disease, has been developed as contrast agent for patients who are otherwise contraindicated for GBCAs or iodinated contrasted agents.[88]

Generally, monitoring inflammation via Fe-MRI exploits macrophage's phagocytic behaviour toward IONPs. Macrophage phagocytosis of administered SPIONS leads to shortening of T_2 and T_2*. Where T_2 relaxation times refer to "natural" transverse relaxation, T_2* reflects the decay of transverse magnetisation caused by spin-spin relaxation and magnetic field inhomogeneity.[89] It is

highly important to understand the roles that individual macrophage subpopulations play in inflammation resolution, especially in the context of therapeutic design and delivery.[42]

1.8.1 Targeted Fe-MRI

Phenotyping of specific macrophage subtypes has helped steer development of targeted experimental contrast agents. Contrast agents including iron oxide nanoparticles can be modified with various targeting moieties, including antibodies and small molecules. IONPs are typically modified with a diverse set of biocompatible coatings, including dextran, PEG, amino acids and other metals including gold and gadolinium. For example, iron oxide nanoparticles may be coated with either temperature or pH responsive coatings, including poly-(N-isopropylacrylamide) and poly-(acrylic acid).[90] This approach is a particularly advantageous from drug delivery perspective, where parameters such as temperature and pH may differ under disease states.

1.8.2 Antibody Targeting in Fe-MRI

IONPs of different sizes have been used for antibody targeting of immune cells. One method of localising IONPs to target sites is through modifying with antibodies. An example of this is vascular cell adhesion protein 1 (VCAM-1) targeted IONP imaging. VCAM-1 is responsible for cell adhesion of monocytes and lymphocytes to vascular endothelium and has been shown to be upregulated in neuroinflammation, making it an attractive marker for imaging inflammation.[91] VCAM-1 targeted antibodies, conjugated to micrometre sized iron oxide particles (MPIONs) have been developed for MR imaging of multiple sclerosis.

Similarly, matrix metalloproteases (MMPs) have been targeted by nanoparticle conjugates. MMP-12 is highly elevated in peripheral neuroinflammation, which make it an attractive target for imaging studies. Husain et al developed an MMP targeted SPION, which showed favourable results for imaging spinal nerve lesions as seen in figure 1.16 Below .[92] Khurana *et al* demonstrated

successful MR visualisation of CD25(+) regulatory T cells, by labelling with CD25 targeted magnetic activated cell sorting (MACs) microbeads, which despite their name are actually 50 nm SPIONs.[93]

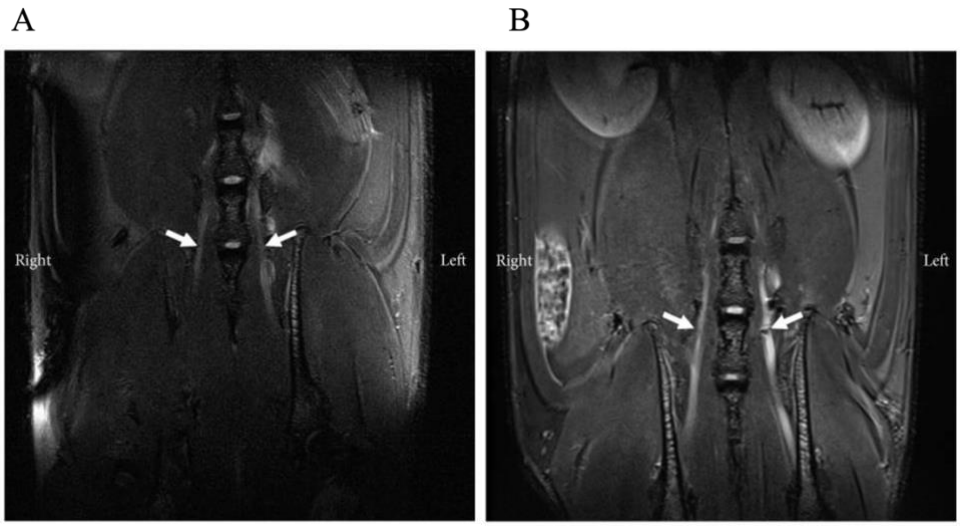

Figure 1.16 – *Figure from adapted from Husain et al., 2019. T2 weighted image of (A) sham and (B) spinal nerve lesion mice following injection with MMP-12 targeted SPION. Signal loss induced by iron oxide nanoparticle accumulation is observed in image (B) at the approximate lesion site denoted by the white arrows.*

1.8.3 Cell Tracking using Fe-MRI

The *in vivo* capabilities of MRI allow for real time cell tracking. Contrast agent enhancement has facilitated mapping of individual cell types. Macrophage mapping following nerve damage has previously been investigated using SPIONs and USPIONs.[37] Signal loss due to the paramagnetic effect of SPIONs/USPIONs was correlated to an increased presence in macrophages.[37] This loss of signal, however can also occur in the event of proximal haemorrhages and passive diffusion of SPIONS across a disrupted blood nerve barrier.[94,95] Recently, the focus on Fe-MRI, especially within the context of cell migration studies, has shifted to the use of MPIONs, due to their increased sensitivity relative to USPIONs and SPIONS.[96]

Macrophage infiltration following allograft rejection has been visualised by MRI, where USPION contrast agents have been used for image enhancement. Iron labelled macrophages at lesion sites are positively correlated to tissue rejection[97]. SPIONS have been of particular interest in renal imaging studies as GBCAs are associated with kidney damage and splenic enlargement.[38] SPIONs have been used to label and map macrophages to sites of kidney damage in mice. MR images showed a distinct signal loss after 2 days.[38]

1.8.4 Multimodal Approaches of Fe-MRI

Fe-MRI has frequently been used in conjunction with several other imaging modalities. Multimodal nanoparticle-based approaches have been used in studies of GBM. Lee et al developed a multimodal approach of water dispersible, near infrared fluorescent silica coated iron oxide nanoparticles (NFSPIONs), which allowed for *in vivo* imaging of cancer.[46] Potentially, the use of these MR and fluorescent active multimodal agents allows for delineation of tumour margins, through the targeting of surface markers of TAMs during GBM resection. Allowing for an improvement of outcomes.[46] NFSPIONs have also been used to label and track macrophages throughout myocardical infarct. Rats were injected with nanoparticles, where activity of resting monocytes and macrophages were monitored via both MRI and optical imaging. [39] Myocardial infarction was then induced, where monocyte and macrophages were tracked to sites of inflammation. Localisation of monocytes and macrophages correlated well to histological findings and *ex vivo* MR analyses.[39]

Labelling with SPIONS prior to inducing myocardial infarct meant that presence of iron in the lesion was solely due to infiltration of monocytes and macrophages. Experiments where SPIONS are loaded prior to lesion formation do not allow for differentiation between macrophages that phagocytose extravasated iron or recently loaded monocytes.[96] Fluorescent SPIONS allow for

multimodal imaging, where it can serve as a MR contrast media and cellular localisation via fluorescence microscopy.[39] This technology can provide prognostic information relating to other therapies which are provided concomitantly.

This concomitant approach has been applied experimentally using anti-CCL5. CCL5 is a chemokine which facilitates leukocyte recruitment to inflammatory lesions. Following administration of anti-CCL5 to myocardial infarct lesion sites, a decrease in monocyte/macrophage infiltration was observed via MR, resulting in less severe infarct.[39] Potentially targeting endogenous chemokines such as CCL5 could provide better insight into the inflammatory status of an tissue around an MDI, than just imaging contrast enhanced macrophage activity alone. Selt *et al* employed a multimodal imaging approach whereby SPIONS were used for spatiotemporal localisation of macrophages via MRI and cell survival via bioluminescence imaging.[40] Monocyte and macrophage viability is largely unaffected by SPION phagocytosis, where even under increased iron concentration at 50µg Fe/mL actually saw an increase in cell viability.[40] Iron deposition is an existing phenotypic attribute of TAMs. Contrast-agent free MRI can detect these TAMs as a result of endogenous iron accumulation.[98] Endogenous hemosiderin iron deposition has been used as a biomarker for TAMs *in vivo* and used both iron MRI and iron histology methods to map TAM activity in prostate and breast metastatic models of cancer.[98] TAM iron deposits have shown to be correlated with positive response to CSF1R breast cancer immunotherapy, the spatiotemporal activity of iron deposition in TAMs is conserved across both human and murine breast cancer. This attribute allows for differentiation between microenvironments in human breast cancer.[98] Iron(+) macrophages displayed M1 like inflammatory behaviours, where they chelate endogenous iron to avoid situations of iron depletion, such as that in haemmorahge.[98] This behaviour of iron deposition in TAMs may cause some

differences to T_2 signals, which may affect performance of administered IONPs. In a study by Leftin and colleagues, iron(III) chelation is shown as potential oncotherapy that functions by decreasing the bioavailability of iron(III) in proliferating tumour cells.[99] This study showed that short term iron(III) chelator deferiprone administration does not lead to perturbation of non-haem iron whilst maintaining anti-tumour effects. The same cannot be said for long term administration.[99] MRI visualisation via T_2 mapping showed increased iron-labelled infiltrating macrophages at lesion sites was correlated with decreased anti-tumour chelation therapeutic response. This finding implied that mapping macrophages with respect to their iron status serves as a surrogate biomarker for immune status and tumour prognosis.[99]

MRI markers of disease are predominantly indirect parameters including oedema, gliosis and blood brain barrier leakage. Cross-linked iron oxide nanoparticles (CLIOs) were shown to be taken up to a lesser degree in adaptive immune cells, meaning that imaging via nanoparticles was a marker for innate immunity. Infiltrating macrophages (CD11b+) showed a greater propensity for uptake of CLIOs than both T and B cells. A proposed mechanism for nanoparticle uptake is via micropinocytosis.[100] A limitation of contrast agents, nanoparticles in particular, is the feasibility of clinical translation. Although macrophage activity is an important prognostic factor, other key players including B cells and T cells are additional targets which should be considered, where SPION functionality is limited.[100]

IONP approaches as described above are generally well tolerated and are suitable for macrophage labelling, either nanoparticle via endocytosis or via cell surface antigen targeting. Certainly, there are multiple avenues to further develop IONPs for macrophage and inflammation monitoring via ^{1}H MRI. Additionally, IONP approaches could be used in conjunction with GBCA approaches to achieve target enhancement in both T_1 and T_2.

1.9 ^{19}F Approaches

One MRI approach to monitor the behaviour of macrophages *in vivo* is through ^{19}F MRI. ^{19}F MRI commonly involves the use of emulsified perfluorocarbons (PFCs) containing ^{19}F isotopes. PFC probes are biochemically inactive, meaning they are not metabolised whilst maintaining a high number of ^{19}F moieties.[42] ^{19}F MRI has a high degree of specificity and an excellent signal to noise ratio due to lack of background ^{19}F signal in biological systems (see *figure 1.17*).[42,101,102] Emulsified perfluorocarbons (PFCs) are commonly used as they are phagocytosed by macrophages.[42]

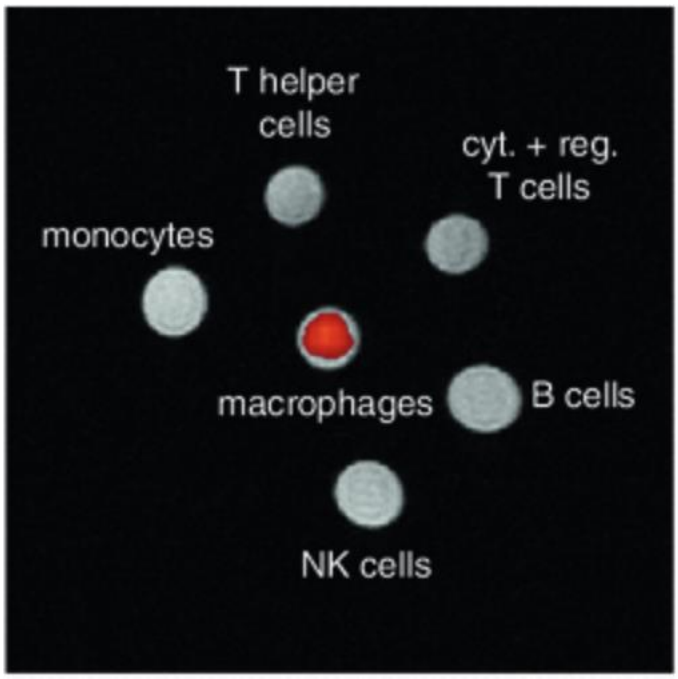

Figure 1.17 **-** ^{19}F/^{1}H MRI of immune cell subpopulations. Individual immune cell types were sorted into in 200µL microfuge tubes. These cell pellets were then stained with PFCs, and subsequently washed to remove non-specific ^{19}F signal. Overall anatomical detail is provided by the ^{1}H MRI and is shown in grey ^{19}F signal (seen in red) was only observed in macrophages and dendritic cells, indicating that PFCs only labelled macrophages and dendritic cells. Figure from Jacoby *et al*., 2014[103]

PFC labelling of cells follows different principles to labelling with paramagnetic contrast agents. Crucially, paramagnetic agents interact with water protons, having an effect on T_1, T_2 and T_2*

relaxation times.[104] An advantage of ^{19}F MRI and the use of PFCs is the fact that they do not have significant interactions with proton spins of water molecules. This is of particular significance, as it allows for parallel ^{1}H MRI imaging. The gyromagnetic ratio, which is the ratio of magnetic moment to the angular momentum, of ^{19}F is similar to that of ^{1}H, differing by only 6% (see *table 1.3*).[104] These parameters make ^{19}F MRI a favourable imaging modality to be used alongside conventional ^{1}H MRI, where image co-registration allows for concomitant resolution of soft tissue and of PFC stained cells.[94,101] In essence, a ^{1}H-MRI acquisition would provide spatial resolution of tissues, whilst ^{19}F-MRI provides spatial information on PFC labelled cells.

1.9.1 Classification of PFC Agents $^{1}H/^{19}F$ MRI

PFCs have been clinically approved as a blood substitute. Significantly, different PFCs have unique ^{19}F chemical shifts, which effectively allow for quantification of inflammation via spin density weighted image acquisition.[105,106] Notably, chemical shift of ^{19}F is unchanged within cells.[104,105] There are 5 main categories of PFC agents, these being: aromatic and unsaturated PFCs, linear saturated PFCs, saturated ring systems, perfluoroamines, and perfluoroethers.[104] An example of a common PFC, perfluoro-15-crown-5 ether (depicted in *figure 1.18 below)*, has particularly desirable ^{19}F molecular resonance parameters. It has 20 chemically equivalent ^{19}F fluorine atoms, and only displays as a single resonance signal. However, it has a long clearance time and will accumulate in both the spleen and liver, meaning it is not suitable for clinical translation into humans.[107] A potential alternative is through the use of perfluorooctyl bromide, which offers superior clearance times but, however, is a less sensitive MRI agent.[107] This decreased sensitivity is attributed to its complex magnetic resonance spectrum.[107]

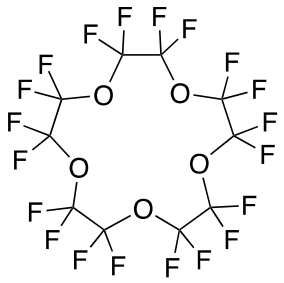

Figure 1.18 – Chemical structure of perfluoro-15-crown-5 ether.

1.9.2 Myocardial infarct and PFC Macrophage Labelling

Several studies have utilised ^{19}F MRI to monitor inflammation following myocardial infarction. Events following myocardial infarction involve complex inflammatory processes, where macrophages play key regulatory roles.[95] Parallel $^{19}F/^{1}H$ MRI has been carried out to map macrophage and monocyte distribution following myocardial infarct.[95] ^{19}F signals following myocardial infarct showed a strong correlation for regions where intramyocardial haemorrhage had occurred, indicating monocyte and macrophage infiltration. This effect was further confirmed by histological analysis.[95] Consequently, $^{19}F/^{1}H$ MRI also revealed a distinct absence of macrophage activity in regions of microvascular obstruction. A key limitation of this investigation is the unknown fate of PFC molecules following macrophage apoptosis. Macrophage apoptosis, following infiltration to sites of myocardial infarct, could lead to false positive macrophage mapping.[95]

1.9.3 Cancer and PFC Macrophage Labelling

Macrophage activity is, especially within the context of macrophage polarisation, a highly important prognostic factor in many diseases such as cancer.[101] Tumour associated macrophages (TAMs) have been shown to co-option infiltrating macrophages, leading to an increase in tumour proliferation, neo-angiogenesis and metastases.[101] ^{19}F MRI has also been used to monitor macrophage activity in cancer. Presence of tumour associated macrophages are a key prognostic

factor in tumours. MRI has increasingly become a key approach to monitor and assess the role of TAMs in cancer. [108]

An investigation into macrophage recruitment in head and neck cancer revealed local recruitment of macrophages to lymphatic vessels.[43] Macrophages within the tumour microenvironment, as shown by ^{19}F MRI analysis, showed TAMs play a key role in the metastatic co-optioning of lymphatic vasculature.[43] The study demonstrated increased macrophage recruitment to lesion sites in models of squamous cell carcinoma (double hit/cal27 cell lines).[43] Being a unique diagnostic for both macrophage infiltration and metastases, this ^{19}F approach is highly promising for macrophage tracking .[43] Macrophage tracking via ^{19}F MRI has previously been used to investigate macrophage infiltration and tumour associated activation of macrophages to the TAM phenotype following high intensity focused ultrasound ablation (HIFU).[101] HIFU is a treatment that functions to destroy tumour cells with ultrasound waves and has generally been applied for treatment of prostate cancer.[109]

A key consideration when developing MRI diagnostics is sensitivity of the approach. In the Ahrens *et al* study they determined dendritic cell detection sensitivity to be within 10^5 cells, which is on the upper end of current ^{19}F MRI sensitivity limits.[110] PFC labelling can drive cells to divide mitotically, which can lead to a change in phenotype for dendritic cells. Specificity issues are also an issue with ^{19}F approaches, which currently do not allow for discrimination between macrophage subpopulations. This limitation, however, is a consistent issue across all contrast agent approaches. From an oncology perspective, the ability to discriminate between macrophage subtypes including TAMs is a highly important prognostic feature. The lack of specificity means that macrophages

are generally labelled by PFCs. Critically, not all macrophages are pro-tumorigenic, making the requirement for improved contrast approaches even more meaningful.[108]

1.9.4 Cell Tracking of MSCs using PFCs

Beyond monitoring macrophage activity, PFCs can be used to pre-label cells ahead of administration. Tracking of therapeutic mesenchymal stem cells (MSCs) is particularly relevant. Targeted ^{19}F labelling approaches, such as those used to label macrophages, can readily be translated to therapeutic payload delivery tracking. Insight into their activities following transplantation allows for insight into different methods of therapeutic administration and success of transplant.[111] Significantly, Ribot *et al* showed that PFC labelling of MSCs did not impede cell viability.[111] Like all contrast agents, minimal cell toxicity is highly desirable, which is demonstrated by PFCs.

1.9.5 Feasibility of ^{19}F MRI

To summarise, whilst PFC based investigations provide valuable insight into macrophage infiltration, there are several limitations with clinical translation, specifically relating to the slow clearance of PFCs and large systemic dosages (approximately 1-5 g/kg for PFCs) required for appropriate contrast.[101,102] Additionally, there are further limitations with cell density, and tumour volume analyses with ^{19}F-MRI. Due to sensitivity limitations, 1000s of cells per voxel are needed to detect PFC labelled cells, whereas iron based methods have higher sensitivity.[112] ^{19}F-MRI efficacy is further hindered by relatively poor agent uptake. This relatively poor uptake by macrophages can potentially be overcome through the implementation of transfection reagents including FuGENE^{HD}, which is a non-liposomal transfection system originally designed to transfect DNA into a variety of cell lines.[102]

1.10 Manganese (Mn^{2+}/Mn^{3+}) agents for cell tracking

As previously mentioned, GBCA administration has been directly correlated to nephrotoxicity and nephrogenic systemic fibrosis, which has prompted further interest into alternatives to GBCAs. Mn^{2+} is an alternative paramagnetic metal ion, capable of producing contrast enhancement in MRI. Early Mn^{2+} approaches for cell labelling involved application of $MnCl_2$ to natural killer cells and cytotoxic T cells.[113] More recently this approach has been applied to tracking transplanted mesenchymal stem cells.[114] Chelators including porphyrins, EDTA and salen have all attracted interest for manganese contrast agents, offering increased stability and reduced toxicity.[115]

1.11 CEST/ParaCEST MRI

Proton density of tissue and relaxation properties of protons in a given tissue are two major factors contributing to image contrast in MRI. Standard contrast agents in MRI function by shortening either the T_1 or T_2 relaxation times of protons in their local vicinity. Chemical exchange saturation transfer (CEST) is a MRI approach which introduce image contrast in a fundamentally distinct way from conventional contrast agents.[116] A critical limitation for cell tracking in T_1- and T_2-weighted contrast enhanced MRI is that the visualisation of more than one labelled cell population is not possible.[117] CEST imaging approaches are capable of detecting low concentrations of compounds with high sensitivity, which is achieved by indirect detection of signal reduction of endogenous solvent water after saturation with RF pulses.[118–120] Magnetization is transferred from other molecules to the bulk water, meaning that the saturation effect that was from the target molecule, can be observed via the water signal.[118] CEST agents work to selectively reduce the magnetization of the water signal. Paramagnetic lanthanide chelates (PARACEST) induces a large shift in resonance of local nuclei.[117] This means that two different PARACEST agents with different lanthanides could be selectively irradiated to large, distinct shifts. This could allow for

labelling and visualisation of two different cell populations. From a cell tracking perspective, cells can be directly labelled with PARACEST agents and administered *in vivo*.[2] There are a limited examples of cell tracking using PARACEST, mainly due to relatively poor spatial resolution (>2 mm) and lower SNR than that of T_1 and T_2 imaging. However, CEST agents [Yb-HPDO3A] and [Eu-HPDO3A] have been used to visualise different populations of murine macrophages and melanoma cells.[121]

1.12 Magnetic Resonance Spectroscopy (MRS)

Changes to metabolism reflect some of the earliest adaptation to tissues in disease pathogenesis.[122–124] As previously mentioned in *figure 1.3,* biomedical applications of NMR approaches broadly fall under two general modes, MRI and MRS. The clear distinction between MRI and MRS is their output, with MR signal being used to encode different information.[125] The output of MRI is an image, whether that be of the whole organism, individual organs or the smaller tissue structures. MRS is an analytic approach, which confers chemical information about a given tissue. For MRS, a spectra is generated instead of an image for biological molecules containing atoms with spin active nuclei.[126] The main signal generated from proton MRS is water, as it is the main ^{1}H compound in tissue at ~40 M. Metabolites of interest are normally at concentrations less than 10 mM, so water suppression is required to distinguish metabolic peaks.[127] *In vivo*, natural abundance ^{1}H MRS facilitates the detection of various metabolites and has been used to study metabolism of various tissues, including the brain.[127–129] In addition to ^{1}H MRS, there are numerous MRS approaches that exploit other spin active nuclei, either using isotope enriched probes or by natural abundance detection. These include ^{13}C and more recently ^{2}H MRS.

1.12.1 ^{1}H MRS for Inflammation Detection

^{1}H MRS is capable of detecting a diverse range of neurometabolites including N-acetylaspartate (NAA), glutamate (Glu) myoinositol (MI), choline (Cho) and creatine (tCr). Changes in the concentrations of these metabolites can reflect several pathologies. Neuroinflammation with reactive astrocytosis and activated microglia is correlated to raised MI. Whereas a decreased NAA concentration is correlated to neuronal damage.[130] ^{1}H MRS ratiometric detection of these metabolites, normalised to housekeeping reference peak such as water or creatine, have been used to assess several neurodegenerative disorders, traumatic brain injury and brain tumours.[127,131–135] Direct detection of inflammation by ^{1}H MRS *in vivo* is technically challenging. It is difficult to determine the cellular origin of metabolites from natural abundance ^{1}H MRS measurements. *In vitro* ^{1}H MRS experiments were carried out on macrophages in the early 1990s by King and colleagues, giving initial insight into the ^{1}H MRS metabolic fingerprint of IFN-γ stimulated macrophages.[136] ^{1}H MRS based metabolomic approaches have provided useful insight into metabolism of different macrophage polarisation states.[47,49,137] Furthermore, ^{1}H MRS provides fingerprints for steady state concentrations of metabolites in tissue, however it is not well suited to measuring metabolic flux.[138] ^{1}H MRS cannot distinguish between endogenous and introduced ^{1}H species, meaning the approach is better suited to steady state acquisitions. Relative to contemporary spectroscopic approaches such as hyperpolarised ^{13}C MRS, ^{1}H MRS requires long, if not multiple acquisitions to achieve appropriate resolution.

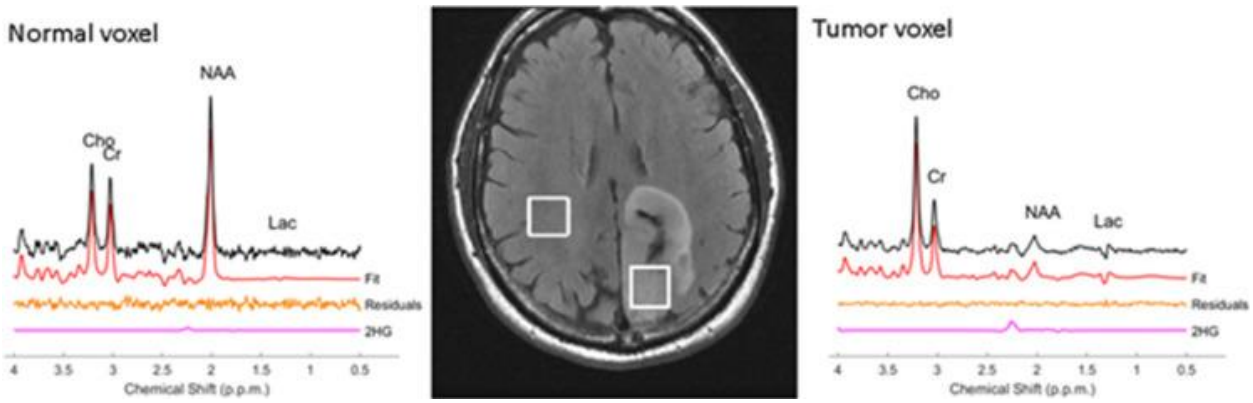

Figure 1.19– *in vivo* single voxel localized PRESS ^{1}H MRS spectra of an astrocytoma patient at 3 T with ^{1}H MRS of normal brain tissue and tumour, depicting a changes in NAA signal intensity. Figure from Laino et al., 2020[135]

1.12.2 ^{13}C MRS for inflammatory imaging

^{13}C is a spin active nuclei that is commonly used for MRS experiments. ^{13}C MRS has relatively low sensitivity by comparison to ^{1}H MRS, with ^{13}C 1.59% compared to 100% sensitivity in ^{1}H MRS (paired with low natural abundance of 0.017%) meaning that endogenous ^{13}C MRS can only be carried out for biomolecules at very high concentrations. ^{13}C MRS has a much larger chemical shift range (~250 ppm) versus proton (~15 ppm).[139] ^{13}C enriched probes have been extensively studied have been used for visualising metabolic processes such as glycolysis and the Krebs cycle in real time. Enrichment with ^{13}C is an effective way to increase SNR. SNR of ^{13}C resonances can be massively improved by proton decoupling (irradiating the entire ^{1}H NMR absorption range), leading to ^{13}C singlet with enhancement from nuclear Overhauser effect. One of the first clinical applications of ^{13}C MRS was used to evaluate and measure glycogen synthesis using [^{13}C]-glucose as a probe for these measurements.[140] However, low sensitivity meant ^{13}C MRS was not widely adopted in the clinic, until sensitivity was improved by pre-polarisation of ^{13}C substrates via hyperpolarisation (HP) techniques such as dynamic nuclear polarisation (DNP).[141–144] There are several ^{13}C enriched probes that have been investigated for a wide range of pathologies including tumours, diabetes and inflammation.[145–150] The most common probe used in HP ^{13}C MRS is [1-

^{13}C]-pyruvate, which has been applied extensively to *in vitro* and *in vivo* cancer models, visualising dynamic changes to production of downstream [1-^{13}C]-lactate.[126,144,146,151–154]

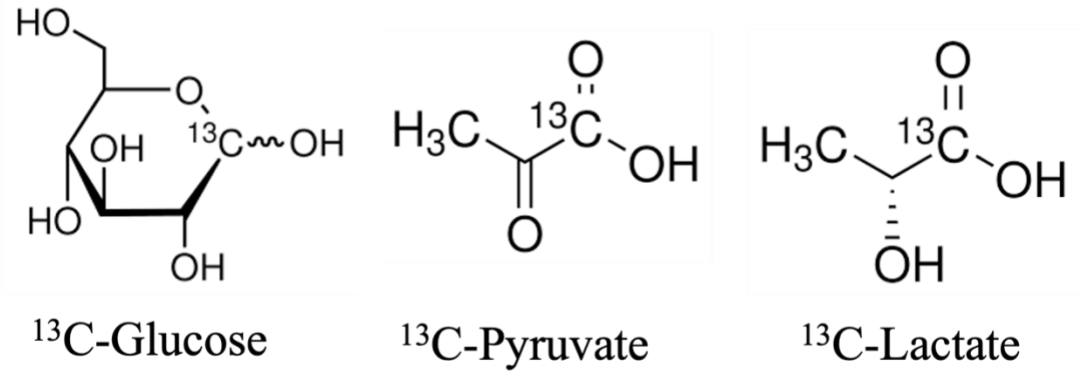

Figure 1.20- Chemical structures for ^{13}C glucose, ^{13}C-pyruvate and ^{13}C-Lactate

1.12.2.1 HP ^{13}C MRS to Detect Tissue Inflammation via Monitoring Changes to Immune Cell Metabolism

Immune cells display distinct metabolic adaptations in response to inflammatory stimuli. For example, M1 macrophages display aerobic glycolysis characterised by increased production of lactate, whereas M2 macrophages display an increased dependence on oxidative phosphorylation to satisfy their ATP requirements.[155,156] *In vitro* the application of HP ^{13}C MRS to inflammatory imaging has been investigated using several probes, including HP [1-^{13}C]-pyruvate, HP [6-^{13}C]-arginine and HP [1-^{13}C]dehydroascorbic acid.[48,150,157,158] Qiao and colleagues demonstrated that both HP [1-^{13}C]-pyruvate and [1-^{13}C]dehydroascorbic acid could be used to non-invasively identify both M1 and M2 macrophages by their ^{13}C MRS metabolic fingerprints.[48] Similarly, Sriram and colleagues showed similar results for new probes including HP [6-^{13}C]-arginine to target arginase activity in myeloid-derived suppressor cells *in vitro*.[150] Critically, Najac and colleagues demonstrated that [6-^{13}C]-arginine can be hyperpolarised, and successfully showed that turnover of the probe to [^{13}C]-urea was highly corelated to myeloid-derived suppressor. *In vivo*

HP [1-^{13}C]-pyruvate has been used for metabolic imaging of inflammatory response following myocardial infarct.[159] An intense [1-^{13}C]-lactate peak as visible in following myocardial infarct in both rodent and pig models.[159] However, for translation to *in vivo* applications, hyperpolarised probes require long T_1 relaxation to lengthen the signal lifetime. Furthermore, hyperpolarisation techniques are technically demanding and require specialised equipment and staff, limiting the translational potential of HP ^{13}C MRS.

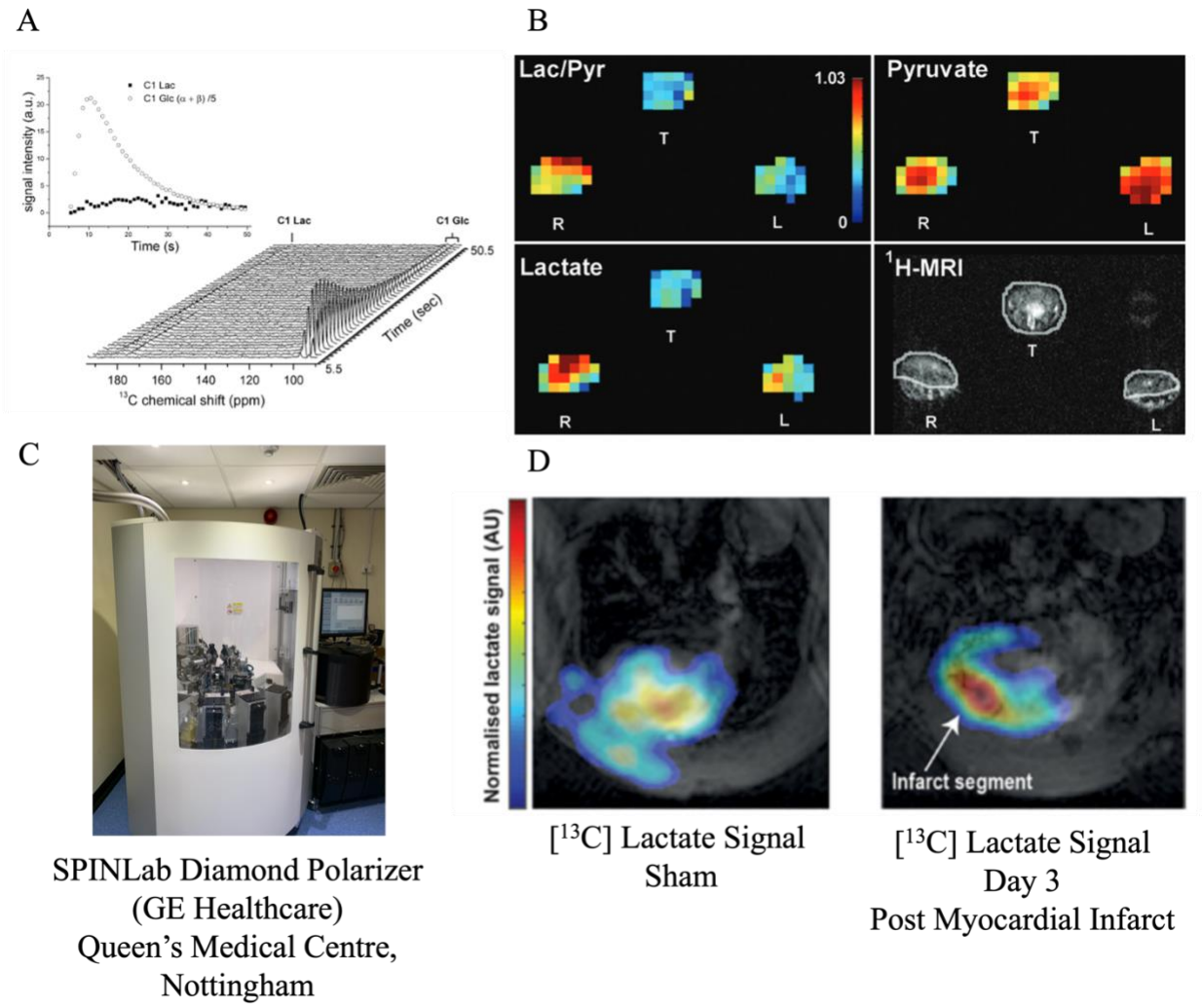

***Figure 1.21* – A.** *In vivo* metabolism visualised by HP ^{13}C MRS of [U-$^{2}H_7$,U-$^{13}C_6$]-D-glucose to [^{13}C]-lactate over 45 seconds in mouse head. (Figure from Mishkovsky et al., 2017).[160] **B.** HP ^{13}C MRS metabolic maps of arthritic paw (R), control paw (L) and tail (T) following injection of HP [^{13}C]-pyruvate. (Figure from MacKenzie et al., 2011)[161] **C.** SPINLab Diamond Polarizer (GE Healthcare) in Queen's Medical Centre, Nottingham. Highlighting the additional equipment required to achieve hyperpolarisation. **D.** HP ^{13}C MRS metabolic maps

of [^{13}C]-lactate, following myocardial infarct and injection of HP [^{13}C]-pyruvate. (Figure from Lewis et al., 2018).[159]

1.12.3 ^{2}H MRS for Cell Identification

Whilst FDG-PET and HP [1-^{13}C]-pyruvate MRS have successfully been used to visualise metabolism in brain tumour *in vivo*, neither technique can measure glycolytic flux through the complete glycolytic pathway.[162] Deuterium (^{2}H) is another spin active isotope that has recently regained popularity as a probe for MRS. ^{2}H has a very low natural abundance (0.01%) meaning the detection of ^{2}H enriched probes is feasible with very low background.[163] ^{2}H MRS does have a few limitations, mainly in that low gyromagnetic ratio ^{2}H contributes to poor sensitivity. However, the short T_1 relaxation times of ^{2}H substrates allows for rapid signal acquisition.[138] A key benefit of ^{2}H MRS over ^{13}C MRS is that it avoids the requirement for technically challenging, short lived HP to achieve adequate sensitivity for *in vivo* imaging. Not requiring hyperpolarisation affords ^{2}H probes greater temporal resolution (seconds for HP ^{13}C MRS and minutes to hours for ^{2}H MRS) for metabolite tracking, compared to HP ^{13}C MRS.[138,163,164] Several deuterium enriched substrates have been used to investigate metabolism *in vivo* in both healthy and brain tumour patients, including D_2O, [6,6'- $^{2}H_2$]-glucose (see *figure 1.22*), [$^{2}H_3$]-acetate, [$^{2}H_9$]-choline and [2,3-$^{2}H_2$]-fumarate.[162,165–170] There is only one example in the literature of ^{2}H MRS being used to identify inflammation, where LPS Matrigel plugs were implanted into mice, and [6,6'- $^{2}H_2$]-glucose was used to monitor metabolism of infiltrating immune cells. To date no studies have investigated deuterium based probes for differentiation of macrophage phenotypes, highlighting a distinct research gap.

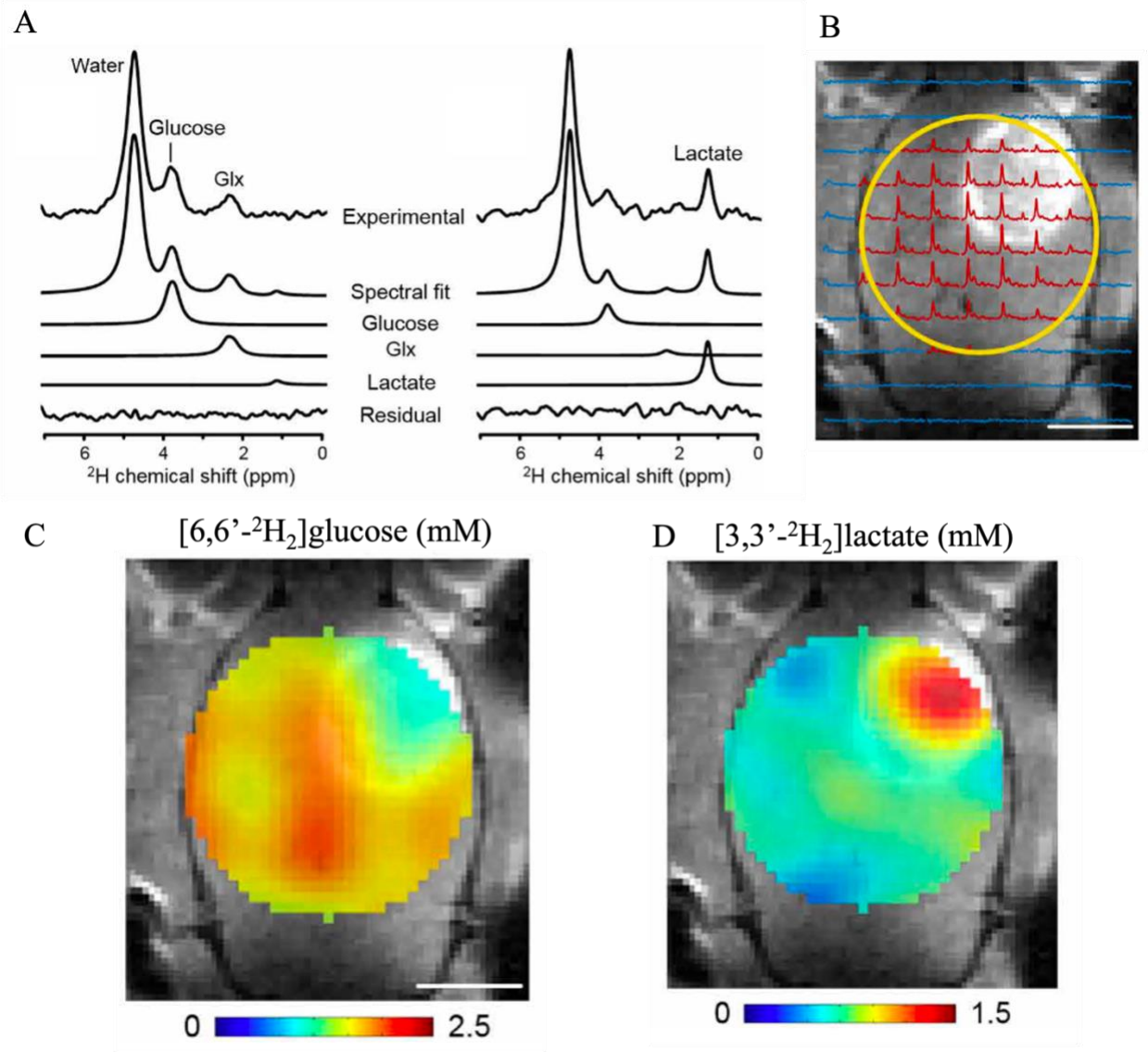

Figure 1.22 – DMI experiments in RG2 glioma rat brain from De Feyter et al., 2018.[170] **A.** ^{2}H MRS spectra following [6,6'$^{2}H_2$]glucose infusion from normal brain and tumour lesion. **B.** TICE MR image of RG3 glioma rat brain, with overlayed 2x2x2 mm^3 voxel ^{2}H MRS spectra. **C.** ^{2}H MRS metabolic maps of [6,6'$^{2}H_2$]glucose in RG3 glioma rat brain. **D.** ^{2}H MRS metabolic maps of [3,3'$^{2}H_2$]lactate in RG3 glioma rat brain.

1.13 Implementation of Imaging Macrophage Polarisation at a Clinical Level

Highlighted at the beginning of this thesis, macrophage polarisation is a powerful indicator of inflammatory state. *in situ* detection of macrophage polarisation state, at clinical level has the potential to provide clinicians with valuable information relating to disease progression and

treatment response. The capability to identify proinflammatory response in a transplanted organ or tissue could aid identification of transplant rejection, expediting surgical intervention. Equally, detecting immune cell presence within the tumour microenvironment could inform therapeutic decision making. However, clinical implementation would require regulatory approval, significant financial investment, and both patient and clinician buy-in. It is therefore reasonable to assume that molecular imaging approaches with highest potential at clinical level display the following characteristics:

1. Low Toxicity
    i. Gadolinium based contrast agents are implicated in acute nephrogenic toxicity.
    ii. Biocompatible imaging probes might include those that are biomimetic such as ^{13}C – or ^{2}H- glucose; or naturally occurring compounds such as iron.
2. High sensitivity and specificity
    i. Molecular imaging probes should match or improve upon the sensitivity of clinically available probes. Iron oxide nanoparticles have a lower detection limit relative to gadolinium agents.
    ii. Targeting moieties should be able to selectively target macrophage subtype with low non-specific activity.
    iii. macrophage's sensitivity to undergo contextual adaptations to stimuli within their environment, new imaging probes should not perturb 'true' macrophage activity.
3. Short scan times
    i. Approaches that require long scan times are inefficient and are more susceptible to patient movement and discomfort.
4. Low capital expenditure requirements

i. Sensitivity boosting approaches such as hyperpolarisation require expensive equipment, operated by specially trained individuals.
ii. Approaches that exploit existing infrastructure may improve chances of clinical adoption.

For macrophage imaging at a clinical level, approaches such as deuterium metabolic imaging and iron oxide based approaches are especially promising. Both iron oxide and deuterium based approaches are low toxicity approaches, relative to GBCAs. In general, iron oxide nanoparticles display lower minimum detection than GBCAs. Whilst deuterium metabolic imaging requires higher field strengths to achieve appropriate SNR, scanner modifications are relatively straightforward. Deuterium metabolic imaging does not require costly and technical hyperpolarisation, to achieve sensitivity requirements.

1.14 Project Aims

The aim of this work is to develop translational cell tracking tools and strategies to visualise both macrophage behaviour and tumour cells via MRI/MRS. The ability to distinguish these macrophage subpopulations *in situ* by their unique surface marker expression would provide a clear understanding to the type of inflammation within a given tissue, avoiding the requirement for invasive, tissue destructive biopsy. The first strategy is to target cell surface marker expression with superparamagnetic iron oxide nanoparticle (SPION) contrast agents. Targeting cell surface markers should allow for positive selection of target cell populations, with SPIONs providing adequate sensitivity for detection by MRI. SPIONs demonstrate the lowest minimum detection per agent for any MR contrast agent, meaning that they provide the best option for labelling and identifying cell populations.

Macrophage polarisation states have unique metabolic fingerprint, with metabolic shifts being one of the earliest physiological adaptations in macrophage polarisation. Metabolic imaging of macrophage polarisation state would allow for long term tracking of these early metabolic adaptations. The second strategy in this thesis to target the metabolic niche of macrophage polarisation states using ^{2}H MRS. ^{2}H MRS of different macrophages subpopulations supplied with ^{2}H enriched glucose should provide an insight into the different metabolic traits of macrophage polarisation states, and whether these can be used for inflammatory imaging applications. ^{2}H MRS was selected as a metabolic imaging modality as it does not require hyperpolarisation to achieve the required sensitivity for detection. Furthermore it allows for tracking of dynamic information relating to metabolic flux, through the entire glycolytic pathway. This is impossible in FDG-PET and ^{1}H MRS, Conveniently ^{2}H MRS can be carried out alongside standard ^{1}H MRI/MRS measurements making it a highly attractive spectroscopic approach.

Whilst detection of macrophage polarisation state *in situ* is an overarching aim of this thesis, the development of imaging platforms with sufficient sensitivity to distinguish cell types has unrealised benefits beyond inflammatory assessment. Mechanistic understanding of drug dynamics *in vivo* remain poorly understood, especially within the context of hard to access tissues such as the brain. The development of sensitive molecular imaging probes at cellular scale, will provide a window into drug dynamics of chemotherapy agents, helping to inform treatment regimens. The third strategy in this thesis is to use contrast-agent therapeutic platforms to investigate theranostic labelling of glioblastoma cells. This should allow for the non-invasive tracking of cytotoxic drug dynamics including uptake and localisation within tissue. It is envisioned, that these methods could provide a wealth of information relating to inflammation, drug dynamics, uptake and therapeutic response.

Chapter 2 - General Methods

2.1 Fluorescent Imaging

Fluorescent screening was employed to visualise expression of both surface antigens on target cell populations and presence of fluorescent active contrast agents within cells. Fluorescent imaging allows for highly sensitive detection of molecular targets, providing insight into biodistribution and expression levels of specific target biomolecules. Labelling strategies for immunofluorescent imaging can be broadly subdivided in two, direct and indirect immunofluorescence, depicted in figure below. In both approaches, primary antibodies are used to label target antigens with high specificity. The direct labelling approach involves a one incubation step. The indirect method is a modular two stage protocol which involves an initial primary antibody incubation and a fluorophore conjugated secondary antibody. Given the modularity of the approach, the antibodies, both primary and secondary, can be tailored to imaging requirements. The indirect method also displays superior SNR versus direct immunofluorescence, as multiple secondary antibodies are capable of labelling with a given primary antibody.

A third approach which has been employed within this project involves utilising a biotinylated primary antibody and streptavidin-linked fluospheres (see *figure 2.1*). The binding of biotin and streptavidin is the strongest known non-covalent interaction, with a dissociation constant of 10^{-15}M. Fluospheres (ThermoFisher), are fluorescent beads which can serve as fluorescently active analogues to nanoparticle contrast agents. The biotin-streptavidin labelling system is highly modular, allowing for facile modification and can be used in conjunction with secondary antibody staining.

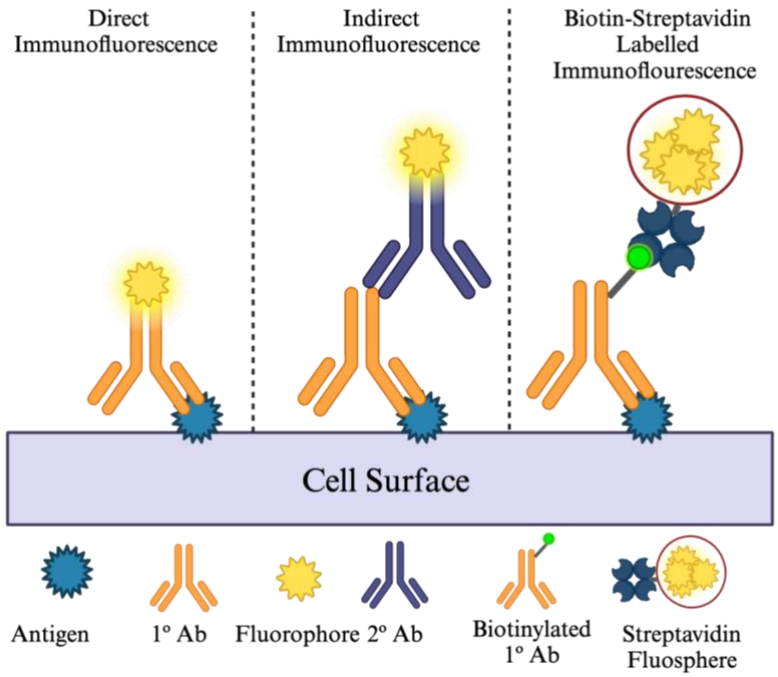

Figure 2.1 - *Immunofluorescent labelling strategies. Direct immunofluorescence involves the selective binding of an primary antibody to a target antigen*, where a fluorophore is directly conjugated to the primary antibody. Indirect immunofluorescence is a two-step process whereby a primary antibody selectively binds to a target antigen. A fluorophore conjugated secondary antibody (selective for the species of primary antibody) then binds to primary antibody. Biotin-streptavidin mediated immunofluorescences exploits the biotin-streptavidin non-covalent bond strength. Biotin labelled primary antibody selectively binds to the target antigen. Subsequent incubation with streptavidin linked fluorescent particles leads to a strong non-covalent interaction between the antibody linked biotin and the fluorescent particle linked streptavidin.

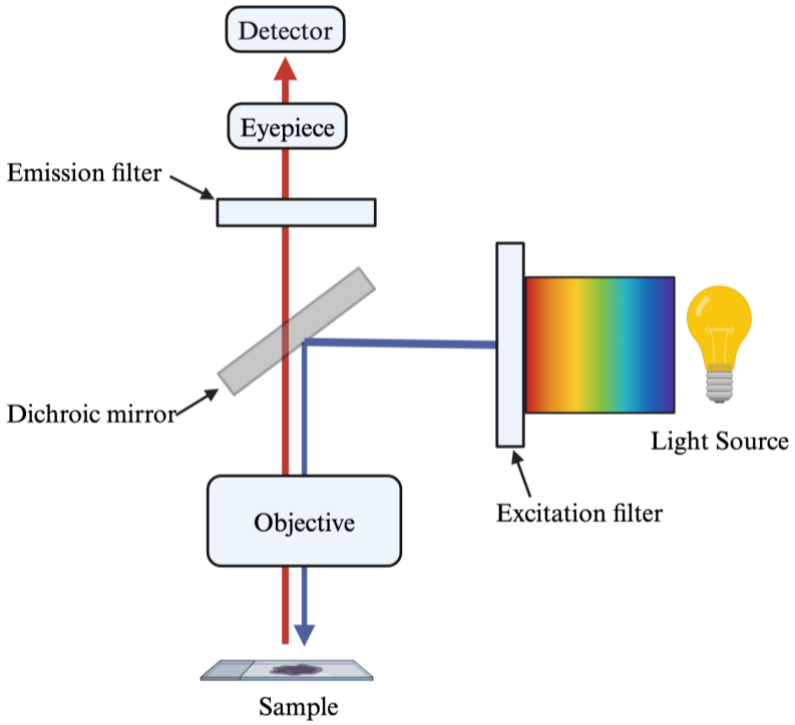

Figure 2.2 - *Schematic of widefield fluorescent imaging.* Widefield fluorescent imaging was used for screening fluorescently labelled cells. Fluorophores present at labelling sites absorb specific wavelengths of light (photon) which leads to excitation of electrons from the ground state to the excited state. Electrons rapidly contract back to their ground state, emitting photons at a different wavelength. In the case of fluorescent widefield imaging, Wavelengths of light are selectively beamed through the excitation filter to excite a chosen fluorophore, and the excited wavelength are subsequently passed through the emission filter to be detected.

2.2 Buffy Coat

Primary derived monocytes were extracted via magnetically labelled positive selection from donor whole blood. Blood samples are separated by centrifugation with Ficoll resulting in phase separation of the constituent blood parts. The PBMC containing buffy coat layer, illustrated in the figure below, is carefully separated from the other phases. Monocytes are selected out by labelling with CD14 targeted magnetic beads, which facilitate the positive selection of labelled cells.

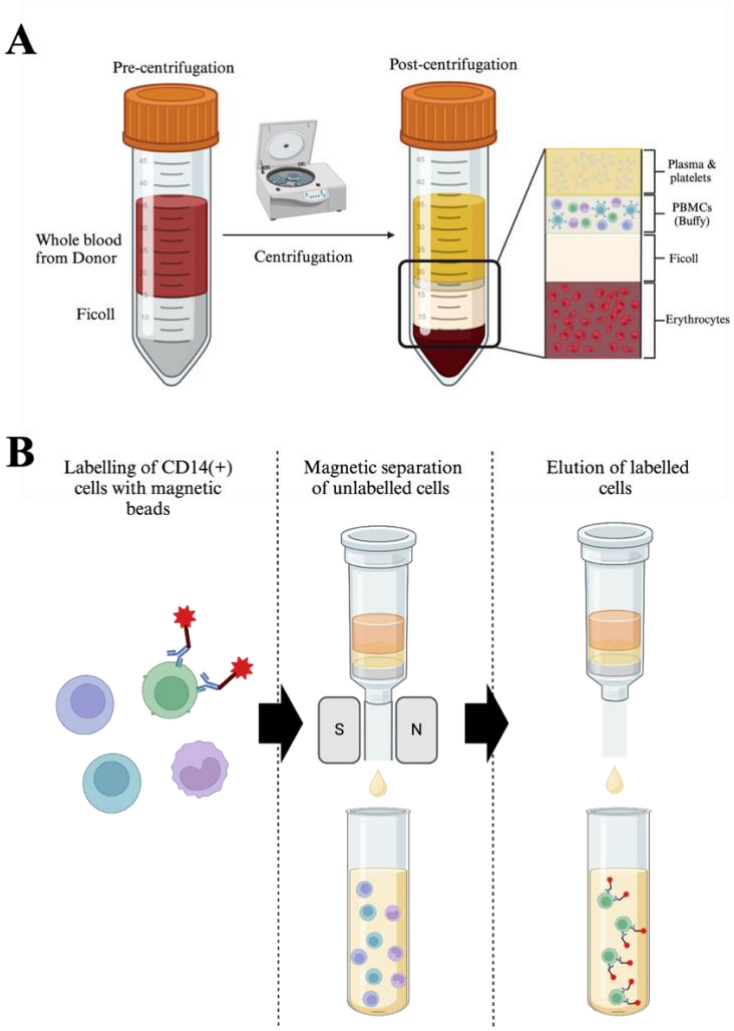

Figure 2.3 - *Schematic for buffy coat isolation from whole blood. A. Whole blood is decanted into ficoll, a hydrophilic polysaccharide solution. Following successive centrifugation steps, whole blood is separated into separate phases of erythrocytes, buffy coat (PBMCs), and the plasma layer. The buffy coat layer is carefully isolated from the solution. B. Positive selection of CD14+ monocytes from buffy coat. Following isolation, buffy coat cells are incubated with magnetic beads targeted towards CD14 antigen, expressed on monocytes. In the presence of a magnetic field, non-labelled mononuclear cells are eluted through, where labelled CD14+ monocytes are retained within the elution column. In the absence of the magnetic field, CD14+ labelled monocytes are then eluted, resulting in a crop of positive selected cells.*

2.3 Live/Dead Toxicity Assay

Live/Dead staining was used to determine toxicity of compounds towards various cell types. Cells were seeded in a 96 well plate at high confluency, and exposed to labelling condition. After 24 hrs of incubation cells were washed 3 times with PBS. For ‘dead’ controls, cells were treated with 100% ethanol (30 mins, r.t). Following PBS washes, a working solution of calcien-AM/ethidium

dimer was added to each well and left to incubate (30 mins, r.t). Cells following incubation cells are visualised using a GloMax® Explorer fluorescent plate reader.

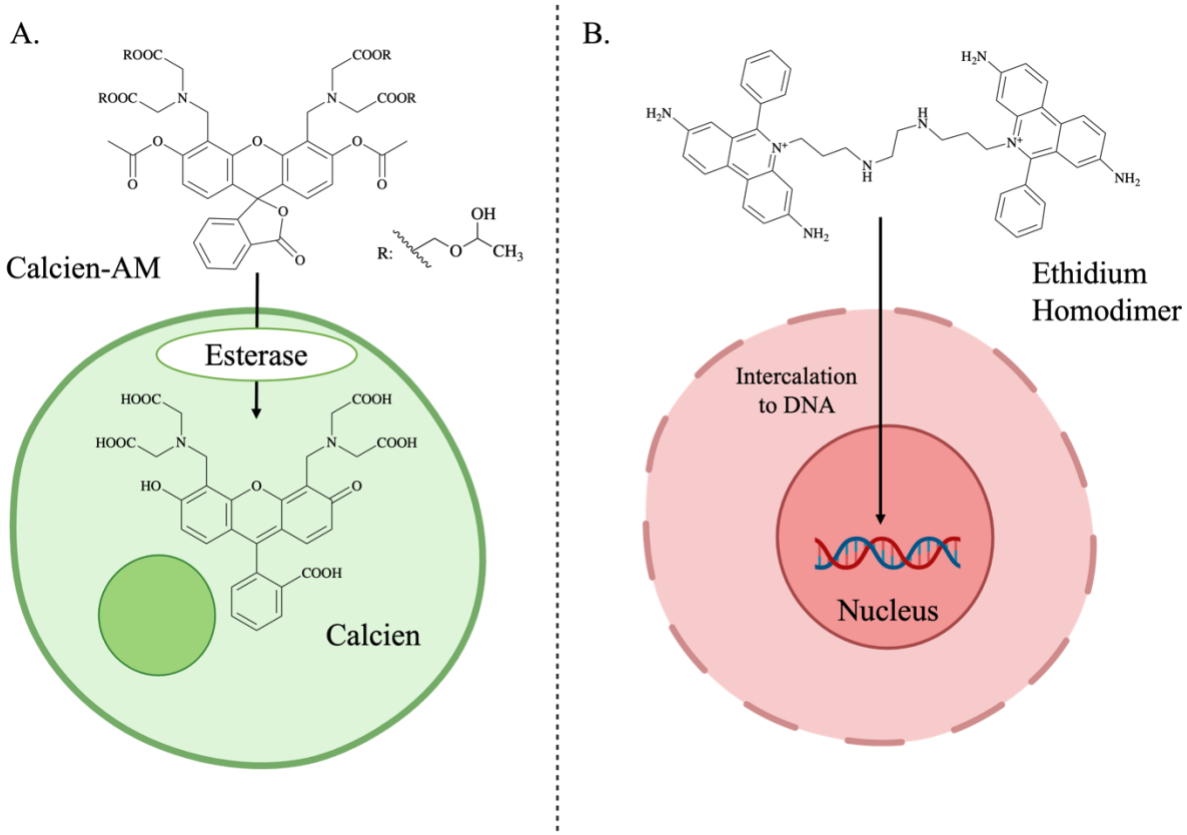

Figure 2.4 - *Schematic of LIVE/DEAD Staining using Calcien-AM and Ethidium Homodimer (EthD-1).* ***A.*** *In live cells, have high intracellular esterase activity, catalysing the conversion of non-fluorescent calcien acetoxymethyl (calcien AM) to highly fluorescent calcien, which is retained within the live cell.* ***B.*** *Ethidium homodimer (EthD-1) is a DNA intercalator which enters damaged or dead cells and displays red fluorescent activity when bound to DNA.*

Confirmation of Calcien/EthD1 was further confirmed by fluorescent microscopy. Figure below displays the expected fluorescent characteristics from Calcien/EthD1 staining in live and dead controls.

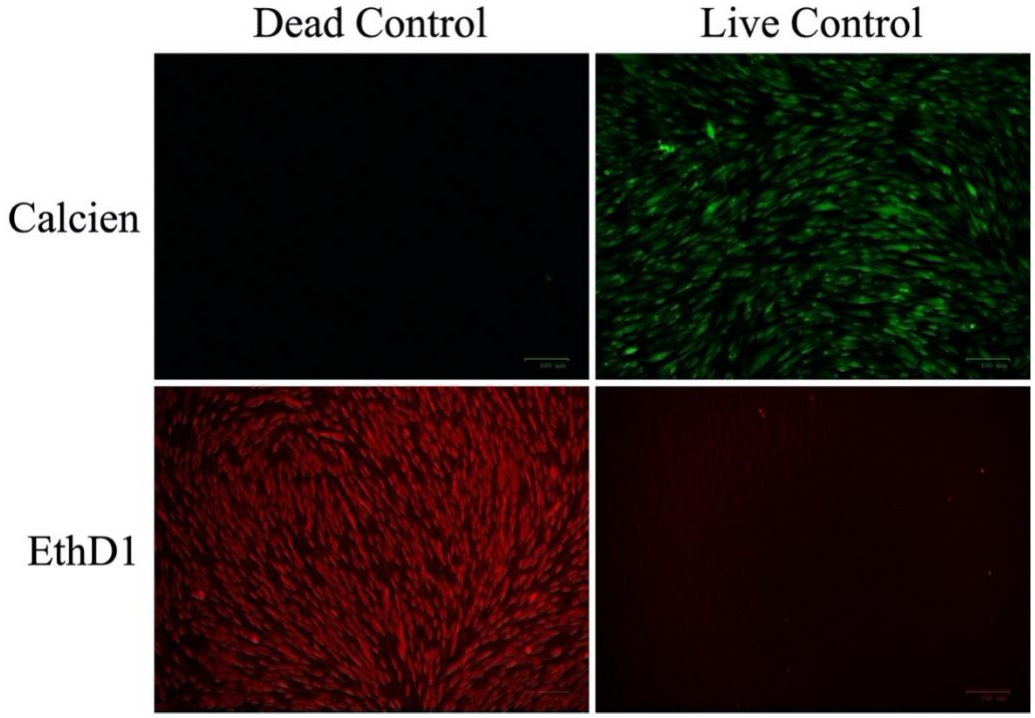

Figure 2.5 - *LIVE/DEAD assay, visualised using ZOE fluorescent microscope. Live control is U251 cells in complete DMEM media, stained with 2µM Calcien/ 4µM EthD1 working solution for 30 minutes.. Dead control is U251 cells, treated with 100% ethanol (30 mins, r.t) prior to incubation with Calcien/EthD1 working solution.*

Chapter 3 - *In vitro* Distinction of Macrophage Polarisation State Using Cell Surface Marker Labelling.

3.1 Introduction

Currently, understanding of inflammation is mostly derived from tissue destructive techniques, such as immunohistochemistry, which do not provide a full picture of complex physiological processes. There is a need to develop sensitive, *in-vivo* methods that can resolve immune activity at a molecular level. A clear objective is to develop novel molecular imaging methods to track specific immune responses in real-time. Macrophages are critical innate immune cells that are essential to maintaining tissue homeostasis.[171–173]. They are ubiquitous to every tissue, and play a crucial role in the detection, ingestion and degradation of pathogens, dead cells, tumour cells and foreign bodies.[174–176] Macrophages undergo contextual polarisation towards either pro-inflammatory (M1) or anti-inflammatory (M2) subpopulations, making them useful indicators of local immune state.[13,177,178] Cell targeted molecular magnetic resonance imaging (MRI) represents one of the most promising approaches for visualisation of immune activity in-vivo.[1,2,179] Throughout this chapter, macrophages have been generated either by the immortalised monocytic cell line, THP1 or from primary blood derived monocytes. Both approaches have previously been described as models for macrophage polarisation, allowing for facile fabrication of neutral, M1 and M2 macrophages.[180–183] An initial aim is to visualise macrophages through labelling their phenotype specific cell surface markers. The modular proof of concept approach employed in this chapter (see *figure 3.1*) uses a streptavidin biotin linkage between monoclonal antibodies selective for macrophage surface markers and MR T_2 active superparamagnetic iron oxide nanoparticle (SPION) contrast agents. Magnetic nanoparticles are an increasingly studied class of contrast agent.[90,184–186] Presently, clinically approved contrast agents are dominated by gadolinium-based T_1 agents.[87,187] By comparison to gadolinium chelates, superparamagnetic iron oxide nanoparticles (SPIONs) display higher sensitivity and have enhanced biocompatibility.[179,188] In non-targeted

labelling of mesenchymal stem cells, SPIONs were four times more sensitive than gadolinium chelates, with a detection threshold of 12,500 cells at 3 T.[188] Magnetic nanoparticles display magnetic anisotropy, giving rise to two distinct antiparallel orientations. If in the absence of applied magnetic field, B_0, nanoparticle net magnetisation averages to 0, the nanoparticles are superparamagnetic.

In short, SPIONs display high magnetisation within an applied field (B_0), which is diminished when absent from the given B0 field.[189] SPIONs are generally T_2 agents, and will impact the rate of R_2 ($1/T_2$) relaxation in tissues where they have accumulated. Effective T_2 agents will demonstrate short T_2, resulting in dark hypointense signal.[190] SPIONs also have well established surface chemistry. SPIONs may be functionalised for a variety of applications, including for targeting, therapeutic, immunomodulatory and immune evasive purposes.[191,192] This functionality paired with favourable R_2, makes SPIONs attractive candidates for targeted labelling of cellular surface markers.

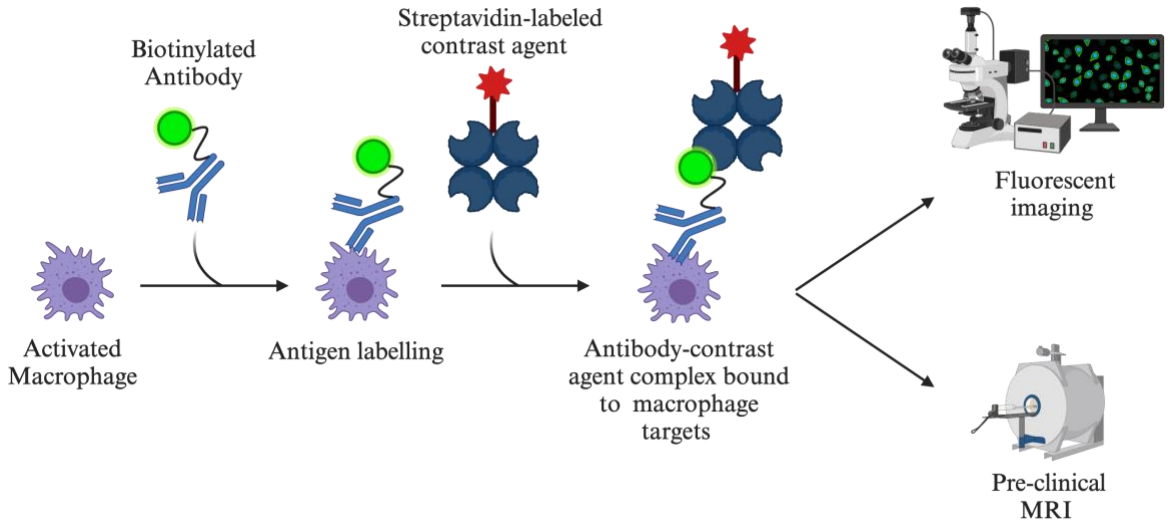

Figure 3.1 - Schematic depicting the modular streptavidin-biotin cell surface marker labelling system. Polarisation state specific surface markers are targeted via biotinylated antibody. Streptavidin-linked iron oxide

nanoparticles selectively bind to the biotin tag and increase the rate of transverse relaxation in subsequent MR imaging or fluorescent imaging experiments.

This approach allows for delineation of desired subpopulations of macrophage cells at 7 T. A bespoke contrast agent library targeted toward macrophage subtype surface antigens will allow for real time monitoring of inflammatory processes, with high translational potential. It is envisaged that these probes could be used to monitor immune cell behaviour following clinical interventions including allograft transplant, biomaterial implantation and administration of therapeutics for diseases such as cancer and fibrosis.

3.1.1 Experimental Design

3.1.1.1 Macrophages as a Molecular MRI Imaging Targets

THP1 is derived from monocytic myeloid leukaemia and minimizes donor to donor variability.[183,193] It is, therefore, a useful platform for optimisation of cell surface imaging. The ultimate goal is to develop a cell surface imaging platform that can selectively label individual subpopulations of macrophages. One strategy is to target the unique surface markers which are expressed by macrophage subpopulations. There are, however, a few limitations with using THP1 as our chosen model. THP1 is a cancer derived cell line and so less representative of immune cells than primary derived monocytes/macrophages. Equally, THP1 does not express classical cell surface markers of M2-like macrophages, including CD163.[183] Interestingly, a classical marker for M2 macrophages, CD206, shows no significant difference in expression between THP1 derived M0, M1 or M2 macrophages.[183] THP1 does, however, provide excellent control over expression of M1-like macrophage cell surface markers, such as HLADR.[182]

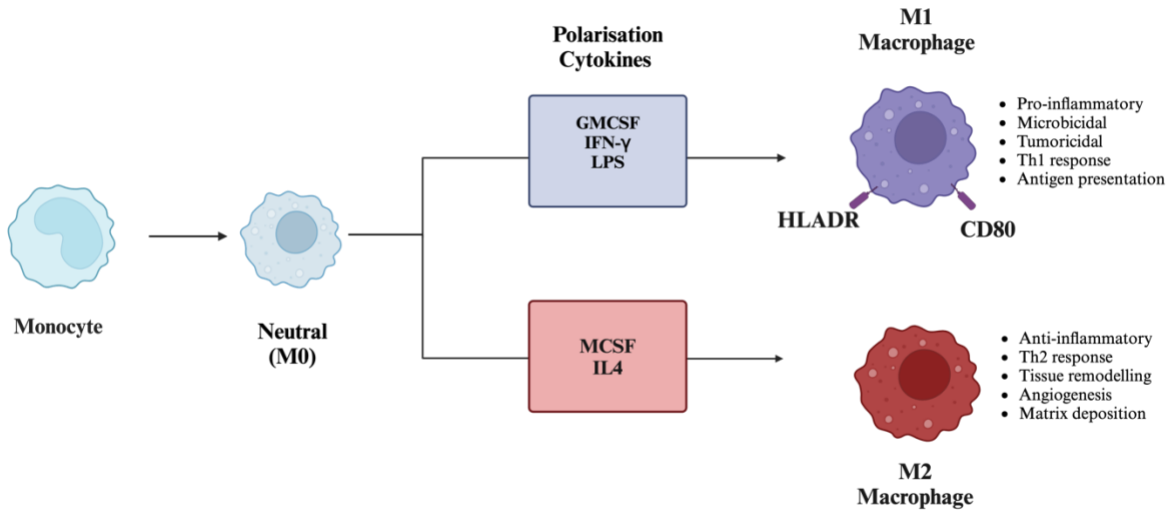

Figure 3.2 - General overview of THP1 macrophage polarisation. Monocytes are conditioned with polarisation cytokines over prolonged periods of time to give two general polarisation states, M1 and M2. HLADR and CD80 are two markers which have demonstrated increased expression in IFN-γ/LPS (M1) treated THP1 relative to M0 and M2 polarisation conditions.[194]

3.1.2 Iron Oxide Nanoparticles as T_2 agents For Direct Cell Labelling

In this chapter, an antibody/SPION modular platform is used to selectively distinguish between macrophage polarisation states using MRI and the following hypothesis was tested.

I hypothesis that the antibody-biotin streptavidin-SPION system can be used to discriminate between macrophage surface markers via MRI. I will test this hypothesis with the following aims:

a. Investigate the suitability of THP1 as a model for fabrication of macrophages with distinct surface marker expression profiles at the fluorescent level.
b. Investigate the suitability of the streptavidin-biotin modular labelling platform (described in *figure 3.1)* for selectively delivering nanoparticles to macrophage surface markers.
c. Investigate different phantom approaches for imaging labelled macrophage systems.

The feasibility of iron oxide nanoparticles for imaging macrophage cell surface markers will be achieved using the modular screening approach described in figure 3.1. Effectively, appropriate

cell surface markers will be identified via initial fluorescent screening. Following this, cell phantoms containing polarised macrophage subpopulations will be labelled using the streptavidin biotin system. Efficacy of labelling and performance of SPIONs will be assessed through imaging labelled phantoms, to determine the R_2 relaxation rate of iron oxide targeted cells relative to non-targeted cell phantoms.

3.2 Methods and Materials

3.2.1 THP1 Cell Culture

THP-1 (ATCC® TIB-202) cells were cultured in RPMI-1640 (Gibco) with 10% heat inactivated fetal bovine serum (FBS, Gibco). The medium was supplemented with glucose (4500 mg/L ,Gibco), 1% glutamax (Gibco), HEPES (10 mM, Gibco) sodium pyruvate (1 mM, Gibco), 1% penicillin-streptomycin (Sigma Aldrich) and 2-mercaptoethanol (0.05 mM, Sigma Aldrich). Differentiation: To differentiate THP1 to M0-like THP1, complete RPMI was doped with phorbol 12-myristate 13-acetate (PMA) (50 ng/mL, Sigma Aldrich) and left to incubate for 6 hrs. Following this, the PMA containing media was removed and replaced with fresh RPMI-1640 and left to incubate for 18 hours (5% CO_2, 37º C, relative humidity).

3.2.1.1 THP1 Differentiation and Polarisation

To polarise M0-like THP1 to M1-like THP1, complete RPMI-1640 was doped with granulocyte-macrophage colony-stimulating factor (GM-CSF)(50ng/mL) (Miltenyi), lipopolysaccharide (LPS) (100 ng/mL) (Sigma) and interferon gamma (IFN-γ) (20 ng/mL) (R&D systems) and left to incubate for 72 hours (5% CO_2, 37º C, relative humidity). To polarise M0-like THP1 to M2-like THP1, complete RPMI-1640 was doped with macrophage colony stimulating factor (M-CSF) (50 ng/mL) (Miltenyi) and interleukin-4 (IL-4) (20 ng/mL) (Miltenyi) left to incubate for 72 hours (5% CO_2, 37º C, relative humidity).

3.2.2 Isolation Human Peripheral Blood Mononuclear Cells (PBMCs)

Blood was obtained from healthy donors (National Blood Service, Sheffield, UK) after informed written consent and following ethics committee approval (Research Ethics Committee, School of Medicine, University of Nottingham). PBMCs were separated via density gradient centrifugation with histopaque (Sigma Aldrich), and CD14+ monocytes were positively selected using MACS CD14 isolation kit (Miltenyi Biotec, UK). PBMCs were twice washed with MACS buffer (2 mM EDTA with 0.5% FBS in PBS) and then incubated with CD14+ targeted magnetic beads (15 mins, 4º C). Following incubation, labelled cells were then selected using LS columns (Miltenyi). CD14+ bound cells were washed using MACS buffer, three times and then eluted. CD14+ monocytes were then cultured in RPMI-1640 media supplemented with 10% fetal FBS, 1% penicillin/streptomycin (v/v) and 1% L-glutamine (v/v).

3.2.2.1 Preparation of Macrophages from PBMCs

To generate naïve-like monocytes (M0), RPMI-1640 media was further supplemented with M-CSF (10 ng/mL). To generate proinflammatory macrophages (M1) RPMI-1640 media was further supplemented with IFN- γ (20 ng/mL) and GM-CSF (50 ng/mL). To generate anti-inflammatory macrophages, RPMI-1640 media was further supplemented with IL4 (20 ng/mL) and M-CSF (50 ng/mL). Cells were cultured under sterile conditions (37º C, 5% CO_2, relative humidity) for 6 days, with media changes at day 3 of the polarisation procedure.

3.2.3 Streptavidin-biotin based modular system for screening phenotype specific cell surface markers.

For surface marker contrast agent screening at both fluorescent and magnetic resonance levels, a modular labelling platform was employed. Primary antibodies were modified with a biotin tag. Primary antibodies used for labelling: anti-HLADR-biotin, anti-CD14-biotin, anti-CD206-biotin,

anti-CD163-biotin and anti-CD86-biotin were all supplied ThermoFisher and were used at a concetration of 5 µg/mL. 30 nm Iron oxide nanoparticles (Thermofisher) were modified with a streptavidin linker. Red (580/605) Neutravidin 40 nm fluospheres (Invitrogen) were used as a fluorescent analogue for iron oxide nanoparticles.

3.2.4 Fluorescent Imaging and Image Analysis

3.2.4.1 Immunofluorescent Staining of THP1 Macrophage Populations Using Streptavidin-Biotin Modular Labelling System

Cells were fixed in 4% paraformaldehyde (10 mins, r.t) and subsequently washed in PBS (3 times, r.t). Cells were then blocked using 5% goat serum in PBS [v/v] (1 hr, r.t). Cells were then washed 3 times using PBS (10 mins, r.t). All primary antibodies (unless otherwise stated) were diluted into 5% goat serum for staining. Cells were incubated with primary antibody at 2 hours at room temperature or overnight at 4ºC. Cells were then washed with PBS 3 times, 10 mins, r.t). Cells were then incubated (1 hrs, r.t, protected from light) with an goat anti-mouse AlexaFluor-488 secondary antibody (495/519 nm excitation/emission wavelength), suspended in 5% goat serum/PBS. Cells were washed 3 times using PBS (10 mins, r.t.). Cells were then counterstained with DAPI (Invitrogen) (359/461 nm excitation/emission wavelength, 10 mins, r.t, protected from light). All data acquired from fluorescent imaging is expressed as a mean ± the column standard deviation. One- or two- way ANOVA and Tukey's post hoc analysis was used to calculate statistical significance, where $p < 0.05$ is considered to be statistically significant.

3.2.5 Screening using widefield immunofluorescent microscopy

3.2.5.1 THP1 Screening in 96 well plates

THP1 cells were seeded into 96-well plates (Corning) at a density of 50,000 cells per well. Following differentiation and polarisation (as described above), media was removed from cells

and 4% PFA was added to each well for 10 minutes. Cells were then stained and imaged using an EttaLuma widefield fluorescent microscope 10x and 40x objectives.

3.2.5.2 PBMC Derived Macrophage Screening in 96-well plates

CD14+ selected primary monocytes were seeded into 96-well plates at a density of 50,000 cells per well. Following differentiation and polarisation (as described above), media was removed from cells and 4% PFA was added to each well for 10 minutes. Cells were then stained and imaged using an EttaLuma widefield fluorescent microscope using 10x and 40x objectives.

3.2.5.3 Screening via Confocal Immunofluorescent Microscopy Using Neutravidin Fluospheres

40 nm red neutravidin fluospheres (580/605nm) (Invitrogen) were used as a fluorescent analogue for streptavidin-linked iron oxide nanoparticles. Neutravidin fluospheres were suspended into 5% goat serum at 200,000 nanoparticles per cell. Number of microspheres per/mL were calculated using the following:

$$\text{Number of microspheres/ mL} = \frac{6C \times 10^{12}}{\rho \times \pi \times \phi^3}$$

Where: C = concentration of suspended beads in g/mL
(0.02 g/mL for a 2% suspension)
ϕ = diameter of microspheres in µm
ρ = density of polymer in g/mL (1.05 for polystyrene)

Cells were then washed again with 3 times with PBS for 15 minutes. The cells were counterstained with DAPI (ThermoFisher). Cells were stained with primary antibody as described above.

3.2.6 Magnetic Resonance Imaging and Analysis

MRI measurements were acquired on a 7 T Bruker BioSpin MR scanner with a Bruker Avance III Console (Bruker BioSpin, Ettlingen, Germany). For transverse relaxation rates (R_2), a multiscan-

multiecho MSME sequence protocol were used to generate T_2 maps of the phantoms. FIJI/Image J was used to reconstruct images and relaxation times were calculated by fitting image intensity data from the T_2 image to the exponential equation:

$$Sn = S_0 \exp\left(-\frac{TEn}{T2}\right)$$

The MRI analysis calculator fitting tool was developed as a plugin tool by Karl Schmidt. All MRI experiments were carried out using a 30 cm bore Bruker Biospec 70/30 7 T MR scanner with a Bruker Avance III Console (Bruker BioSpin, Ettlingen, Germany).

All data acquired from phantom imaging is expressed as a mean ± the column standard deviation. One- or two- way ANOVA and Tukey's post hoc analysis was used to calculate statistical significance, where $p < 0.05$ is considered to be statistically significant.

3.2.6.1 MR Imaging Parameters

Live staining phantom: Labelled cells were transferred to a 100 µL PCR tube. Each PCR tube contained 1mn cells. PCR tubes were then arranged within a Styrofoam tube holder and placed within the MRI scanner. 4 x 1 mm slices were imaged in a coronal orientation through the centre of each PCR tube with data matrices of 256 x 256 with a field of view of 8.0 x 8.0 cm. T_2 relaxation times were calculated with a MSME pulse sequence (flip angle = 90 º) with 30 TEs ranging from 14 to 420 ms. *Cell pellet phantom:* Labelled cells were transferred to a 100 µL PCR tube. Each PCR tube contained 1mn cells. PCR tubes were then arranged within a Styrofoam tube holder and placed within the MRI scanner. 6 x 1 mm slices were imaged in a coronal orientation through the centre of each PCR tube with data matrices of 256 x 256 with a field of view of 3.81 x 3.81 cm. T_2 relaxation times were calculated with a MSME pulse sequence (flip angle = 90 º) with 16 TEs ranging from 11 to 176 ms. *PCR tube agarose phantom:* Labelled cells were transferred to a 100 µL PCR tube. Each PCR tube contained 1.5 mn cells and were suspended in 100µL of 1% agarose.

PCR tubes were then arranged within a Styrofoam tube holder and placed within the MRI scanner. 4 x 1 mm slices were imaged in a coronal orientation through the centre of each PCR tube with data matrices of 256 x 192 with a field of view of 7.5 x 5.8 cm. T_2 relaxation times were calculated with a MSME pulse sequence (flip angle = 90 º) with 16 TEs ranging from 7.76 to 124.18 ms. *Coverslip phantom:* Coverslips were transferred to a 30 mL universal holder. Coverslips were then suspended in 1% agarose. Universal holders were placed inside a tube holder within the MRI scanner. 60 x 1 mm slices were imaged in axial orientation through the centre of each universal holder with data matrices of 256 x 256 with a field of view of 3.0 x 3.0 cm. T_2 relaxation times were calculated with a MSME pulse sequence (flip angle = 90 º) with 16 TEs ranging from 14 to 210 ms. 24 x 1 mm slices were imaged in sagittal orientation through the centre of each universal holder with data matrices of 512 x 256 with a field of view of 8.0 x 4.0 cm. T_2 relaxation times were calculated with a MSME pulse sequence (flip angle = 90 º) with 30 TEs ranging from 15.5 to 467.6 ms. *Cell droplet phantom:* Droplets were transferred to a 30 mL universal holder suspended in 1% agarose. Universal holders were placed inside a tube holder within the MRI scanner. 21 x 1 mm slices were imaged in axial orientation through the centre of each universal holder with data matrices of 256 x 205 with a field of view of 7.5 x 6.0 cm. T_2 relaxation times were calculated with a MSME pulse sequence (flip angle = 90 º) with 16 TEs ranging from 7.7 to 124.1 ms.

3.2.7 Magnetic Resonance Imaging Macrophage Phantom Preparation

3.2.7.1 Live Staining with Primary Antibodies

THP1 cells were seeded into T75 flasks (Corning) at a density of $8x10^6$ cells per flask. Cells were polarised and cultured as per the 6-day protocol described above. Cells were detached by TrypLE

(ThermoFisher) enzymatic detachment. Media was removed and the flasks were washed using sterile PBS.

3.2.7.2 Cell Pellet MRI Phantom

THP1 cells were seeded into T75 flasks at a density of $8x10^6$ cells per flask. Cells were polarised and cultured as per the 6 day protocol described above. Cells were detached by TrypLE enzymatic detachment. Media was removed and the flasks were washed using sterile PBS. TrypLE solution was then added to the flask containing cells and then left to incubate (20 mins, 37º C, 5% CO_2, relative humidity). Following incubation, detachment was confirmed via light microscopy. Solution containing cells was removed from the flask and placed within a 50mL falcon tube and pelleted by centrifugation (350 g, 5 mins). Supernatant was then removed, leaving only the cell pellet. The cell pellet was then resuspended in 4% PFA in PBS and left to fix for 10 minutes. PFA was then removed and cells were washed using PBS (3 times, 5 mins). Cells were labelled as described above. Labelled cells were then dispensed into 0.2 mL PCR tubes at $1.5x10^6$ cells per tube, and centrifuged using a benchtop microcentrifuge (350 g, 5 mins).

3.2.7.3 Cell PCR Tube Agarose Phantom

THP1 cells were blocked, and labelled as per the conditions described above. Agarose phantoms were fabricated using 1% agarose in distilled water. Agarose (Sigma Aldrich) was melted into distilled water using a microwave oven. 1% agarose solution was then agitated using a stirring hotplate (150º C, 200 rpm). Labelled cells were then dispensed into 0.2 mL PCR tubes at different densities, and centrifuged using a benchtop microcentrifuge to remove excess supernatant (350 g, 5 mins). Cells were resuspended 100 µL of agarose and allowed to set at room temperature.

3.2.7.4 Cell Coverslip Phantom

THP1 cells were seeded on to coverslips and polarised as described above. Media was removed and cells were fixed using 4% PFA (5 mins). Cells were washed using PBS (3 times, 5 mins, r.t). Cells were blocked and labelled as described above. Coverslips were removed from the well plates and suspended into 1% agarose in a 30 mL universal holder (Corning).

3.2.7.5 Cell Droplet Phantom

For cell drop phantoms, antibody/iron oxide labelled fixed cells were suspended into 50 µL 1% agarose droplets. Agarose/cell suspensions were dispensed onto a petri dish lid and suspended as a hanging droplet. Agarose cell suspension droplets were then left to form at room temperature for 20 minutes. Once formed, agarose droplet were detached and resuspended in liquid 1% agarose in a 30 mL universal holder.

3.3 Results

3.3.1 Fluorescent Labelling of THP1 Macrophage Cell Surface Markers

THP1 was selected as a cell line for cell surface labelling platform optimisation. THP1 is an acute myeloid leukaemia (AML) derived cell line which is routinely used as an *in vitro* cell model for both monocyte and macrophages. Macrophage subpopulations are fabricated from THP1 cell suspension, first by the differentiation of THP1 monocytes to M0-like macrophages via addition of phorbol 12-myristate 13-acetate (PMA) to the cell culture media. Macrophage polarisation, towards M1- and M2-like subpopulations is then achieved by the addition of specific cytokine cocktails to the cell culture media. The M1 THP1 is generated by the addition of granulocyte-macrophage colony-stimulating factor (GM-CSF), interferon gamma (IFN-γ) and lipopolysaccharide (LPS), whereas the M2 THP1 is generated via macrophage colony-stimulating factor (M-CSF) and interleukin 4 (IL4). Stimulation of monocytes by cytokines signals to the

different macrophage polarisation results in expression of polarisation state specific cellular markers, which have been extensively reviewed.[13,15,18,195] Previous studies have highlighted several surface markers which are differentially expressed under different cytokine condition.[182,194] One marker, human leukocyte antigen – DR isotype (HLADR) is reported to be highly expressed in IFN-γ/LPS stimulated THP1 monocytes. [182,194,196] HLADR is a cell surface receptor which functions to present foreign antigens to immune cells including T-cells, in order to stimulate an immune cascade. HLADR is typically expressed in antigen presenting cells including macrophages, B-cells or dendritic cells. The differences in HLADR expression between THP1 macrophage polarisation states represent an attractive biomarker target for identifying M1-like macrophages over M2. Immunofluorescent staining using an anti-HLADR antibody revealed a high level of HLADR expression in M1 THP1 macrophages. Incidentally, the M0 and M2 subpopulations of THP1 displayed negligible HLADR expression at the cell surface. Given the high degree of control afforded by THP1 and high expression of a surface marker (HLADR) for a given subpopulation (M1), this target was selected for further cell labelling optimisation experiments. Figure 3.3a depicts representative fluorescent imaging of M0 and M1 (IFN-γ/LPS stimulated) THP1 macrophages stained with anti-HLADR-biotin and goat anti-mouse Alexa488 secondary antibody (495/519 nm). high green intensity seen in the M1 indicates presence of the HLADR surface receptor. Interestingly, HLADR+ cells only represent a minority fraction of cells within the bulk population of M1 macrophages. Evidently, HLADR is expressed at a higher level in M1, relative to M0 and M2. Figure 3.3b highlights the difference in relative fluorescent intensity (RFI) between polarisation states, green signal integrated density normalised to cell number is significantly higher in M1 cells (49.74 a.u., ****$p<0.0001$) than M0 (1.00 au) and M2 (0.42 a.u).

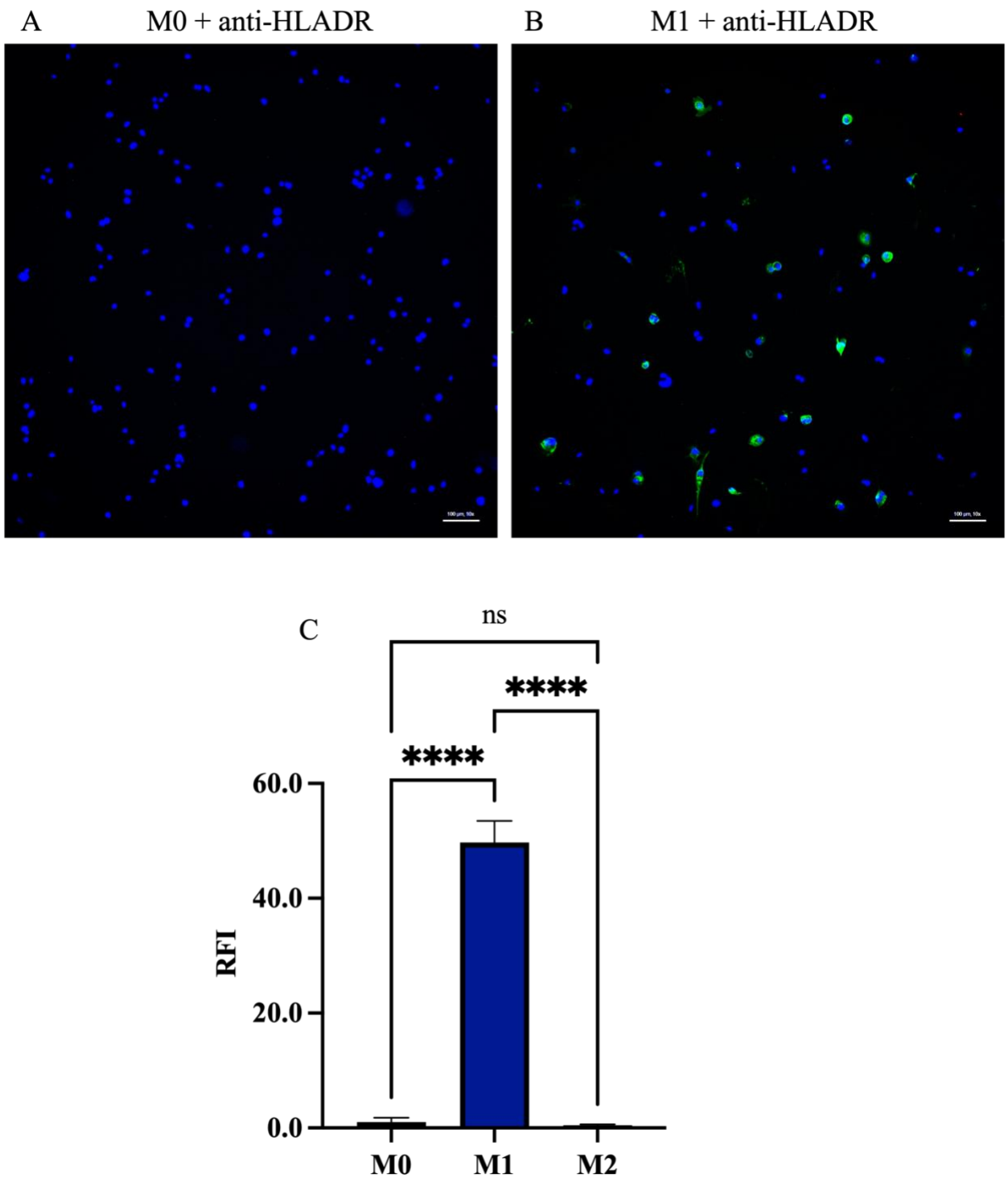

Figure 3.3 - Representative widefield fluorescent images of M0-like and M1-like THP1 stained with anti-HLADR (green, Alexa-488) and DAPI nuclear stain (blue). Images acquired using a 10x objective. **B.** Relative fluorescent intensity (RFI) of HLADR labelling in M0, M1 and M2 THP1. RFI was quantified by measuring the integrated density of HLADR(+) cells, normalised to the total cell count. *p<0.05, **p<0.01, ***p<0.001, ****p<0.0001

3.3.2 Platform Optimisation

3.3.2.1 Labelling HLADR+ M1 THP1 with Neutravidin Fluospheres

Following screening of THP1 and the identification of HLADR as an appropriate target for streptavidin-biotin labelling optimisation, the next objective is to qualify the streptavidin-biotin as a cell surface labelling approach. Given the contrast agent of choice (SPIONs) for labelling cell surface markers is not fluorescent, neutravidin fluospheres were selected as a suitable fluorescent analogue to visualise the streptavidin-biotin labelling system. The neutravidin fluospheres are comparable in size to the streptavidin linked iron oxide nanoparticles (Fluospheres = 40 nm, SPIONs = 30 nm) and offer selective binding to biotin labels.

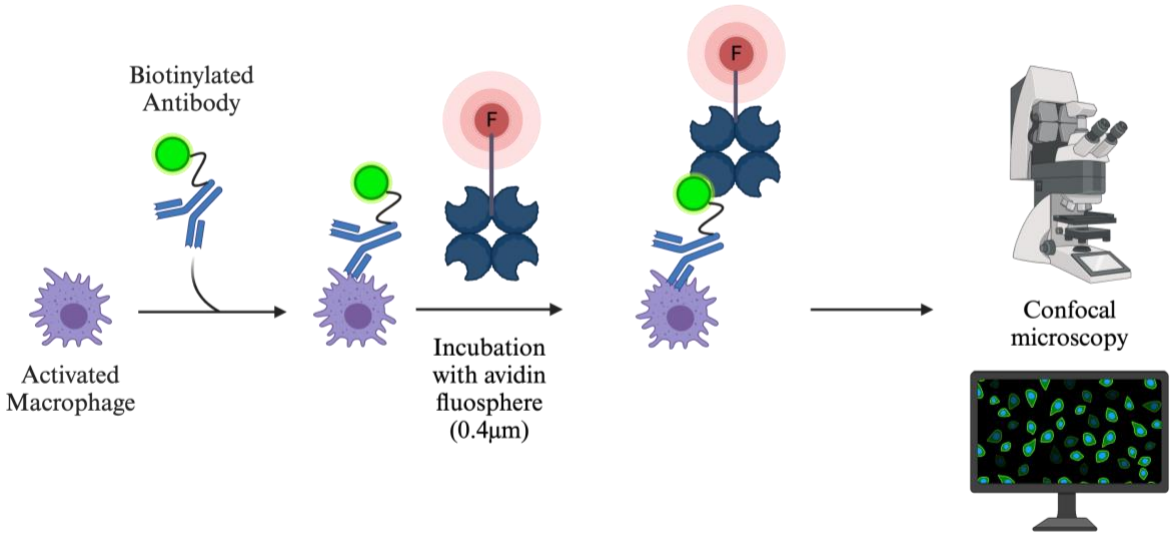

Figure 3.4 - Schematic depicting the streptavidin-biotin labelling system, as applied to labelling macrophages with neutravidin fluospheres. The biotinylated antibody will selectively bind to the macrophage surface marker. The neutravidin binding site will form an extremely strong non-covalent interaction ($K_d \sim 10^{-14}$ mol.L^{-1}) with the biotin link of the antibody. The fluospheres are red fluorescent labels, with excitation/emission of 580/605 nm, and can be visualised by both confocal and widefield fluorescent microscopy.

Having established M1 cells with high relative expression of the HLADR cell surface receptor, the streptavidin biotin system, depicted in *figure 3.4* was applied M1 cells. This fluorescent labelling experiment would provide a better understanding of how effective the streptavidin biotin system is at specifically binding to the target antigens relative to highly specific primary and

secondary antibody approaches. Using this labelling approach, screening was initially carried out on HLADR(+) THP1 under widefield fluorescent microscopy. This revealed a high degree of colocalization between the antibody and the red fluospheres (visualised in *figure 3.5*).

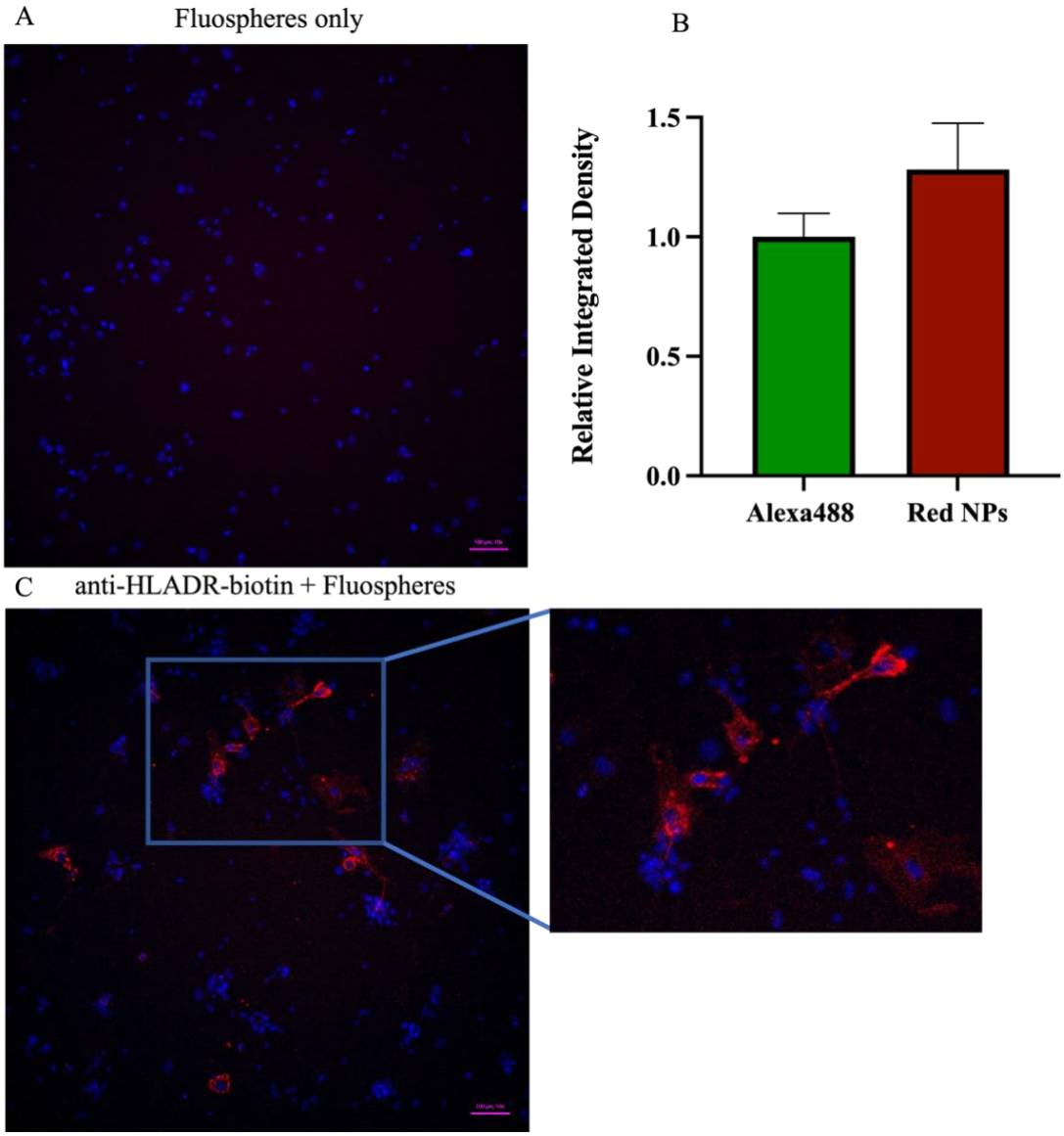

Figure 3.5 - M1 THP1 cells labelled with Neutravidin fluospheres**. A.** M1 THP1 cells, fixed and labelled with red neutravidin fluospheres, and counterstained with nuclear dye DAPI (blue) **B.** Relative integrated density measurement (normalised to cell count) for secondary antibody goat anti-mouse Alexa488 bound to M1 HLADR(+) cells vs relative integrated density measurement for red neutravidin fluospheres bound to the same M1 HLADR(+) cells **C.** M1 THP1 cells, fixed and labelled with anti-HLADR-biotin, red neutravidin fluospheres, and counterstained with nuclear dye DAPI (blue).

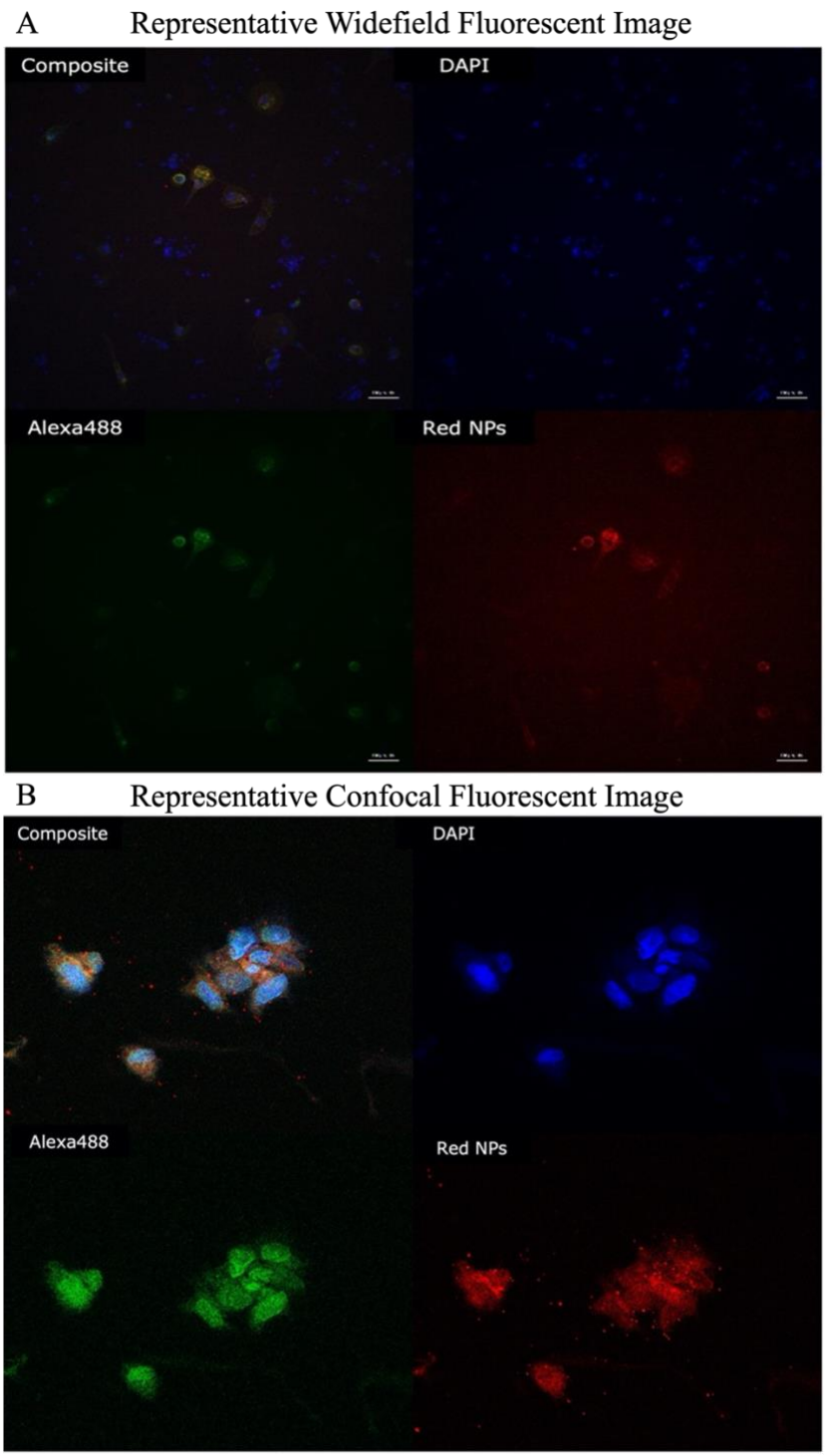

Figure 3.6 - **A.** Widefield montage image of M1 macrophages stained with anti-HLADR-biotin, Red neutravidin fluospheres and DAPI (blue), depicting colocalization between the red and green channels. **B.** Confocal montage image of M1 macrophages stained with anti-HLADR-biotin, red neutravidin fluospheres and DAPI.

3.3.2.2 Live Cell Staining – Preliminary Testing of Streptavidin-Biotin Labelling System Using SPIONs

Live cell staining was a first step in an effort to directly label M1 cells with the streptavidin-biotin system using anti-HLADR-biotin and streptavidin-SPIONs. Cells were cultured and polarised to M0 and M1 and stained with both anti-HLADR-biotin and streptavidin-SPIONs. Cells were then washed, detached and fixed. Cells were then pelleted and imaged using 7 T MRI. *Figure 3.7a* describes the labelling procedure applied during this experiments.

Live incubation of anti-HLADR-biotin antibody and THP1 M0/M1 subpopulations showed a significant increase in R_2 versus conditions with either without SPIONs and non-targeted SPIONs. M0 with HLADR targeted SPIONs displayed the highest R_2 values, with an average $R_2 = 2.99\ s^{-1}$ versus unlabelled M0 cells ($R_2 = 1.45\ s^{-1}$), across six axial slices. Whereas M1 cells targeted with HLADR targeted SPIONs ($R_2 = 2.59\ s^{-1}$,****$p<0.0001$) displayed a significant difference between relaxation rates of M1 cells with non-targeted SPIONs ($R_2 = 1.53\ s^{-1}$), demonstrating that the inclusion of the antibody does increase the R_2 relaxation rate, likely due to increased binding of streptavidin from the SPION binding to the biotin of the labelled antibody. The increased R_2 observed for M0 labelling with antibody is inconsistent with the findings from the fluorescent screen, where negligible HLADR expression was observed. This could be due to interactions between either the antibody, the SPION or both components stimulating increased phagocytosis by M0 or indeed these compounds may stimulate these cells to polarise to an activated state with increased expression of HLADR.

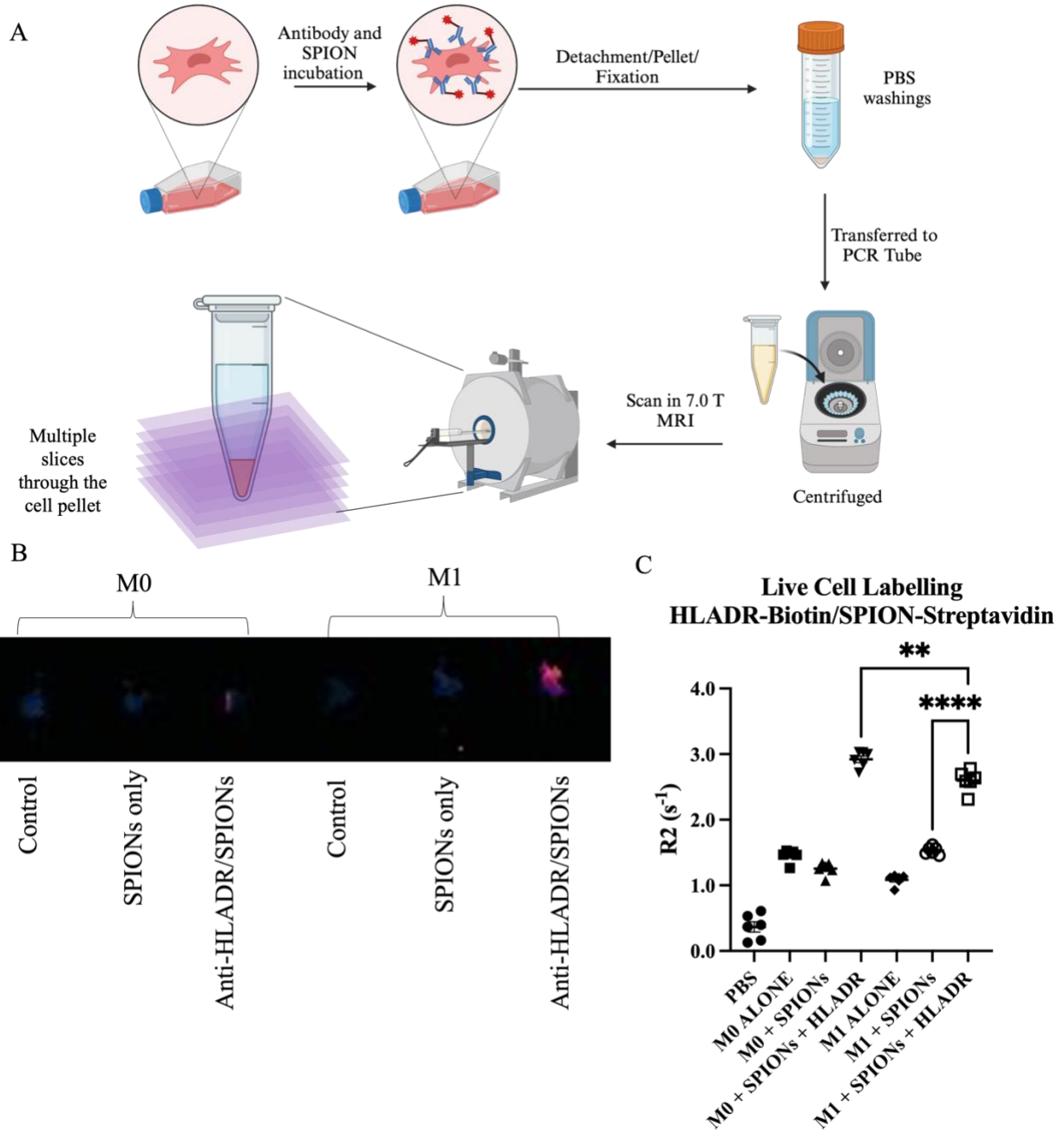

Figure 3.7 - Live cell staining M0 and M1 THP1 subpopulation with HLADR-biotin and streptavidin SPIONs. **A.** R_2 maps of 6 slices of PCR tubes containing cell pellets of M0 and M1 THP1 subpopulations. Slice 1 represents the bottom of the tube. **B.** The R_2 values for labelling THP1 M0 and M1 subpopulations. All data shown is form one measurement, with one technical replicate. *p<0.05, **p<0.01, ***p<0.001, ****p<0.0001

3.3.2.3 Cell Pellet Phantom Imaging Anti-HLADR-Biotin Labelled Neutral and Pro-Inflammatory THP1

The inconsistency between low HLADR (+) cells within the M0 subpopulation at the fluorescent level and high R_2 value for αHLADR/SPIONs M0 cells suggests that potentially nonspecific binding of the antibody occurred during the live staining approach. To address this issue, THP1 cells were instead first detached and fixed in 4% PFA. Cells were then subjected to the same non-specific protein blocking steps as immunofluorescent approaches. *Figure 3.8a* highlights the overall procedure for this approach. Following staining with αHLADR/SPIONs, the labelled cells were resuspended in PBS and pelleted by centrifugation (160 g, 5 mins). The PCR tubes containing the cells were then imaged in the 7 T MRI. For cell pellet phantoms, αHLADR/IONPs incubated with M1 cells displayed the largest $R_2 = 26.52\ s^{-1}$. This was significantly (**p<0.01) higher than the R_2 observed in M0 cells with the same labelling conditions. M0 cells incubated with αHLADR/IONPs showed a relative increase versus control groups, this difference in R_2 was non-significant, with an $R_2 = 12.14\ s^{-1}$ versus average R_2 value for non-targeted M0 cells with a displayed $R_2 = 9.581\ s^{-1}$.

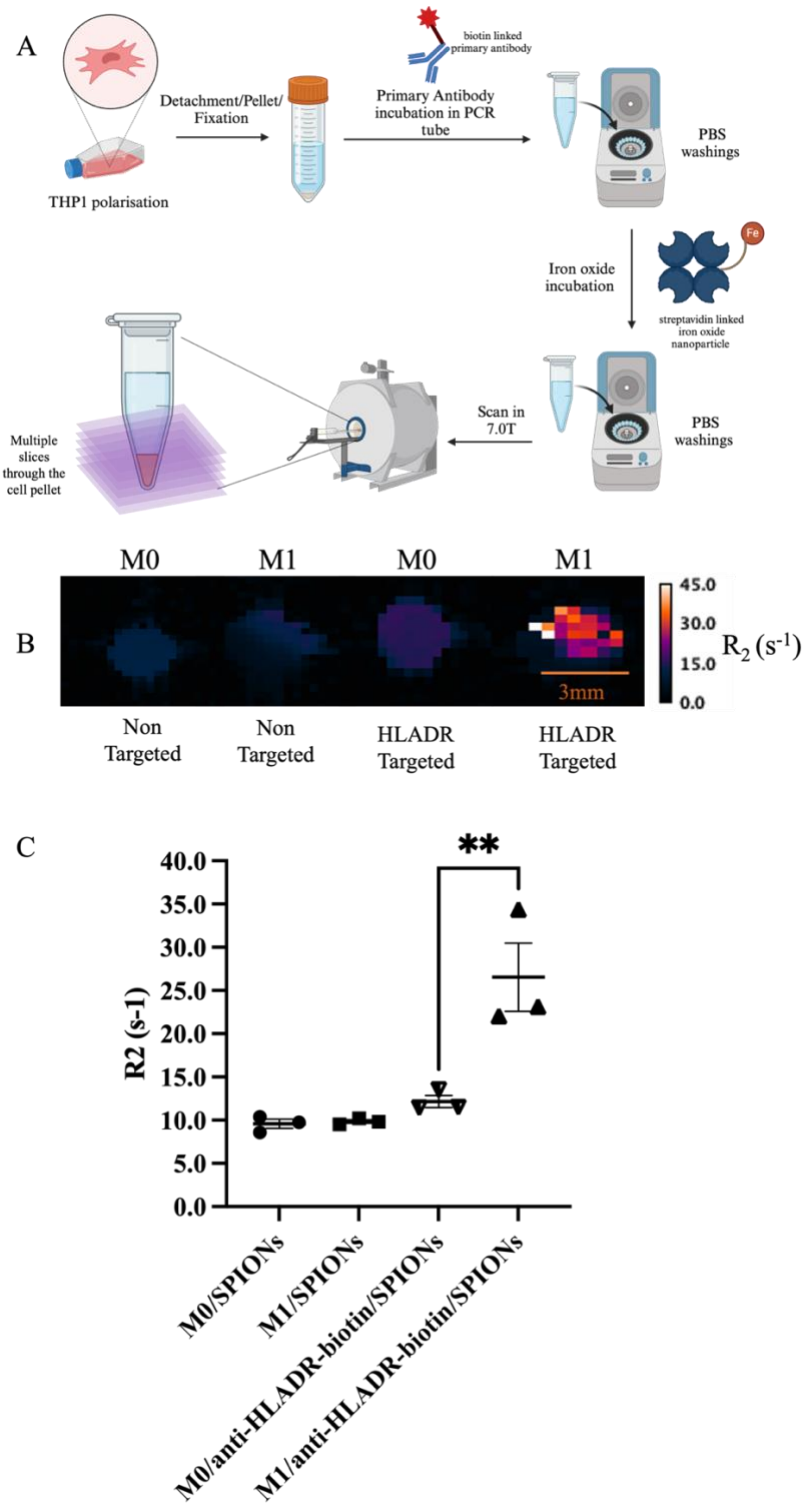

Figure 3.8 Cell Pellet Phantom of M0/M1 THP1 with/without targeted SPIONs. **A.** Schematic of cell pellet labelling and preparation. **B**. Representative slice of R_2 map showing axial cross section of PCR tubes containing cell pellet phantoms. **C.** R_2 values for cell pellet phantoms. All data shown is from one measurement with three technical replicates. *p<0.05, **p<0.01, ***p<0.001, ****p<0.0001

3.3.2.4 Agarose Phantoms of THP1 Monocytes and Macrophages

Imaging a cell pellet is technically challenging and required a significant number of slices in order to capture the exact part of the phantom containing the highest density of cells. To improve imaging capabilities, 3-dimensional agarose suspensions were fabricated using fixed cells. This approach allowed for a reduction in slice number (increasing scan efficiency), and allowed for multiple measurements to be taken through a sample, allowing for signal average to be calculated through a given sample. In addition to HLADR, CD14 also served as a target for optimisation experiments. CD14 is a marker for monocytes and is moderately expressed as a surface marker in THP1 monocytes. Fixed monocytes were labelled with anti-CD14/SPION to investigate the effective labelling using the streptavidin biotin system in an agarose phantom.

Figure 3.9a shows a schematic for the preparation of these agarose phantoms. Of the phantoms, anti-CD14/SPION labelled THP1 displayed the largest relaxation rate, (R_2 = 19.84 s^{-1}), which is a significantly higher (****p<0.0001) R_2 versus both non-targeted SPIONs (R_2 = 12.64 s^{-1}) and control THP1 alone (R_2 = 6.833 s^{-1}). Interestingly, there was still an increase in R_2 for the non-targeted SPIONs versus the control condition, suggesting that there might be non-specific labelling of the SPION to the monocytes.

Initial use of monocytes allowed for facile fabrication of phantoms, eliminating the both the requirement for a 3-day polarisation step and enzymatic detachment of adherent THP1 macrophages. This also highlights that the modular streptavidin biotin system works for targeted imaging of other cell types.

Figure 3.9d-e shows both the R_2 relaxation maps and graph of calculated R_2 rates from those maps for anti-HLADR/SPIONs labelled M0 and M1 THP1s. anti-HLADR/SPIONs displayed far superior labelling in the M1 with a significantly higher R_2 (R_2 = 51.47 s^{-1},****p<0.0001)

subpopulation of THP1 versus M0 (R_2 = 7.757 s^{-1}). There were minimal differences in R_2 observed between the non-targeted labelling groups and the control groups.

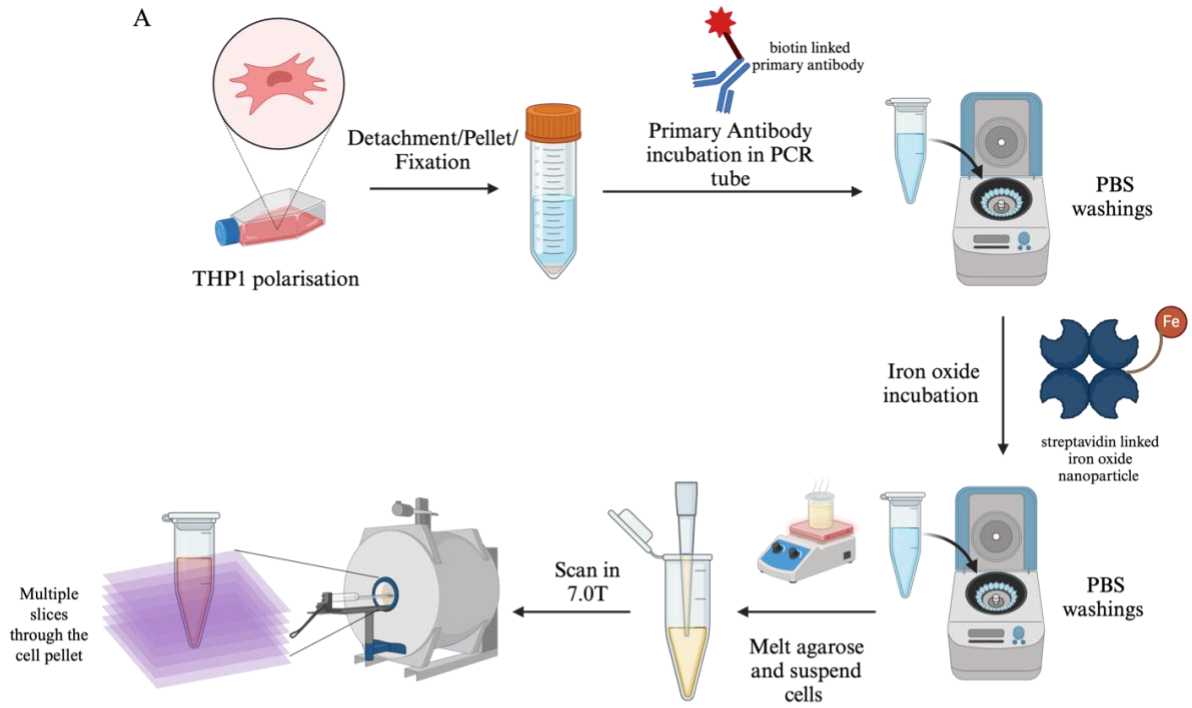

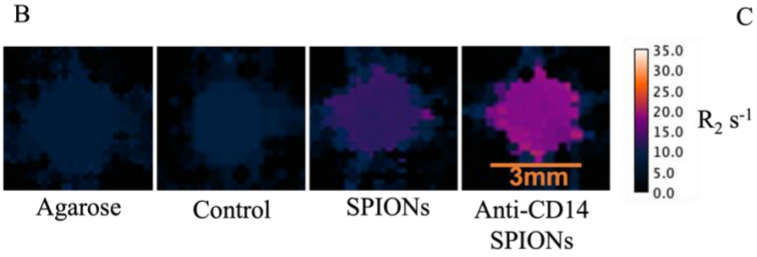

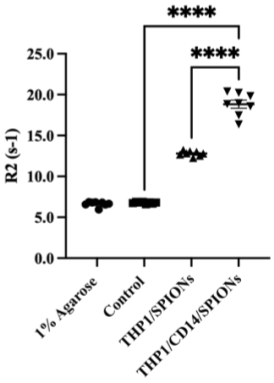

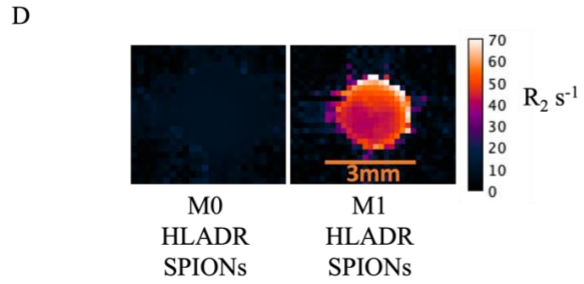

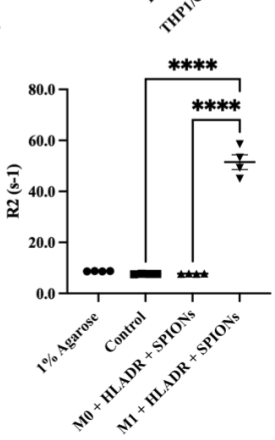

Figure 3.9 A. Schematic depicting the fabrication of agarose based THP1 phantoms. THP1 cells were cultured and polarised if required, detached and fixed. The cells were then stained sequentially with biotinylated primary antibodies and then streptavidin-SPIONS. Labelled cells were then suspended in melted agarose solution for imaging. **B**. Representative axial slice R_2 map of the PCR tube phantom containing agarose alone, THP1 in agarose suspension, non-targeted SPIONs with THP1 in agarose, and CD14 targeted SPIONs with THP1 in agarose. **C.** Graph of calculated R_2 values for anti-CD14/SPIONs/THP1 experiments. All data show is from two independent measurements with three technical repeats across four axial slices. *p<0.05, **p<0.01, ***p<0.001, ****p<0.0001. **D.** Representative axial slice R_2 map of agarose PCR tube phantom containing THP1 M1 and M0 cells stained with anti-HLADR-biotin and streptavidin-SPIONs. **E.** Graph of calculated R_2 values for anti-HLADR/SPIONs with M0 and M1 experiments. All data show is from one measurements with three technical repeats across four axial slices. . *p<0.05, **p<0.01, ***p<0.001, ****p<0.0001.

3.3.2.5 Agarose Droplet Phantoms

The agarose PCR tube agarose phantom displayed highly favourable R_2 rates for distinction between labelled and non-labelled cells. Understanding of contrast agent detection limits is incredibly important for translation to the *in vivo* level. An initial inflammatory response may only involve a small number of cells, meaning highly sensitive detection of these events is incredibly important to early detection. Therefore a phantom system that allows for 3D imaging of multiple labelling conditions within a finite area provides for better insight into the minimum number of contrast agent labelled cells required for detection. An agarose based droplet phantom was developed to allow for encapsulation of cells within 3D space whilst maintaining a relatively small footprint. These droplets were then further suspended in agarose, allowing for the droplet phantoms to be completely surrounded by a homogenous agarose with high water content. This minimised the impact of susceptibility effects that could be observed in a system surrounded by air, such as the PCR tube phantom.

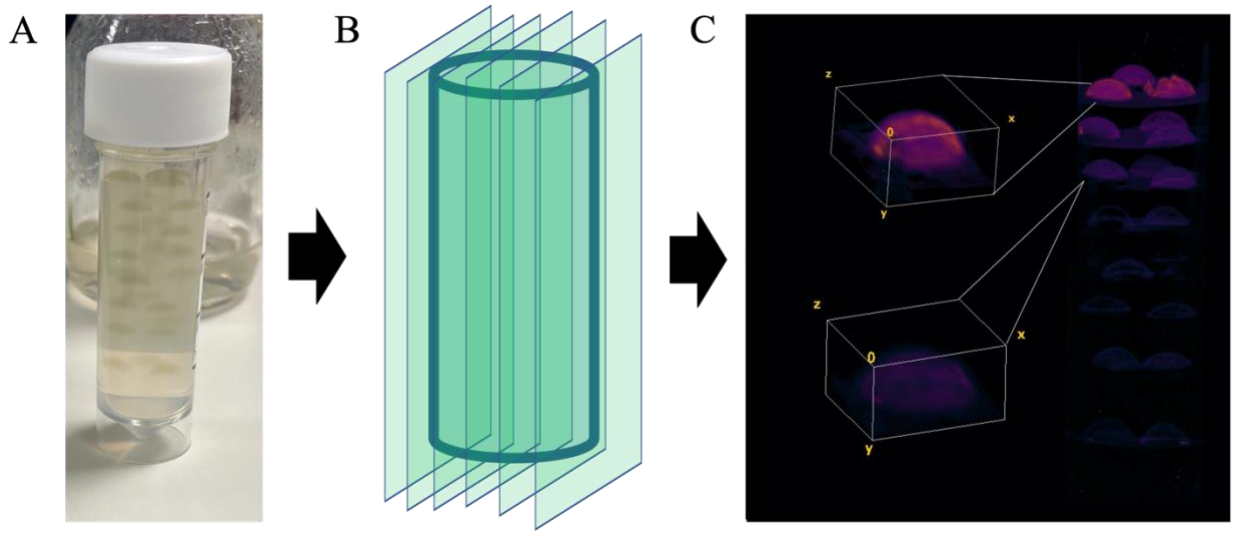

Figure 3.10 Overall Schematic for agarose phantom and MRI imaging**. A**. Image of a 30 mL universal holder containing agarose droplet phantoms, expanding on the use of 3-dimensional phantoms, an alternative approach is to resuspend cells within a droplet of agarose. Once set, these droplets can be easily manipulated and further suspended in agarose. **B.** Diagram illustrating the direction of slices taken in the sagittal plane during MR acquisition. **C.** 3-D volumetric reconstruction of the droplet phantom using a stack of R_2 maps.

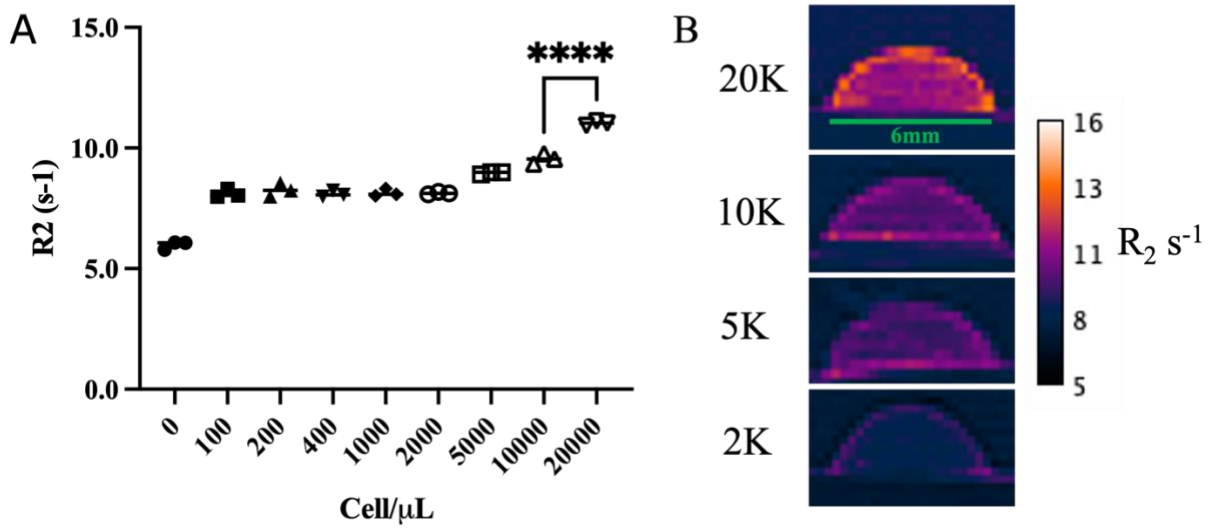

Figure 3.11 R_2 data for Agarose phantom containing agarose droplets of anti-CD14-biotin/IONP-streptavidin stained THP1 at varying cell density. **A**. Graph plotting the R_2 values of the phantoms at increasing THP1 cell density, each data point represents the R_2 value recorded for the respective agarose droplet. **B.** Representative axial R_2 map images of individual agarose phantoms. . *p<0.05, **p<0.01, ***p<0.001, ****p<0.0001.

Given that previous results from PCR tube agarose phantoms indicate that anti-CD14/SPIONs provide R_2 enhancement versus control, this provided a useful basis of which to develop droplet phantoms. Agarose droplet phantoms were prepared with different densities of THP1 monocytes stained with anti-CD14/SPIONs. Given the facile fabrication of THP1 monocytes versus the 6-day macrophage polarisation, it also allowed for much faster workflow. Agarose phantoms stained with anti-CD14/SPIONs increased moderately for cell densities between 100-2000 cells.μL^{-1} versus 1% agarose. Densities above 2000 cells.μL^{-1} displayed iterative significant increases in R_2 relaxation rate. The largest relaxation rate enhancement was recorded for the highest density phantom 20000 cells.μL^{-1} (R_2 = 11.03 s^{-1}) display a highly significant (****$p<0.0001$) increase in relaxation rate relative to 10000 cells.μL^{-1}.

3.3.2.6 Coverslip MRI – An Approach for Visualising Monolayers of Macrophages

To even further stretch the boundaries of cellular detection limits, another cell phantom approach was developed. One major application for molecular MRI would be investigating immune response to implanted materials, presenting a unique challenge for imaging. Adverse immune response to foreign bodies, such as an implant, will drive immune cell recruitment towards the device/tissue interface.[178] Typically, macrophage infiltration and response to implanted materials represents one of the earliest events, adhering to device material interfaces and participating in downstream foreign body response and would healing.[174,178,197] The coverslip phantom was designed replicate early stages of immune cell recruitment and adherence to the interface of an implanted material. This approach is unique in that it allows for correlative imaging between fluorescent and MRI. M1 and M0 coverslips were cultured on to glass coverslips, which were then fixed and labelled with anti-HLADR-biotin and streptavidin-SPIONs.

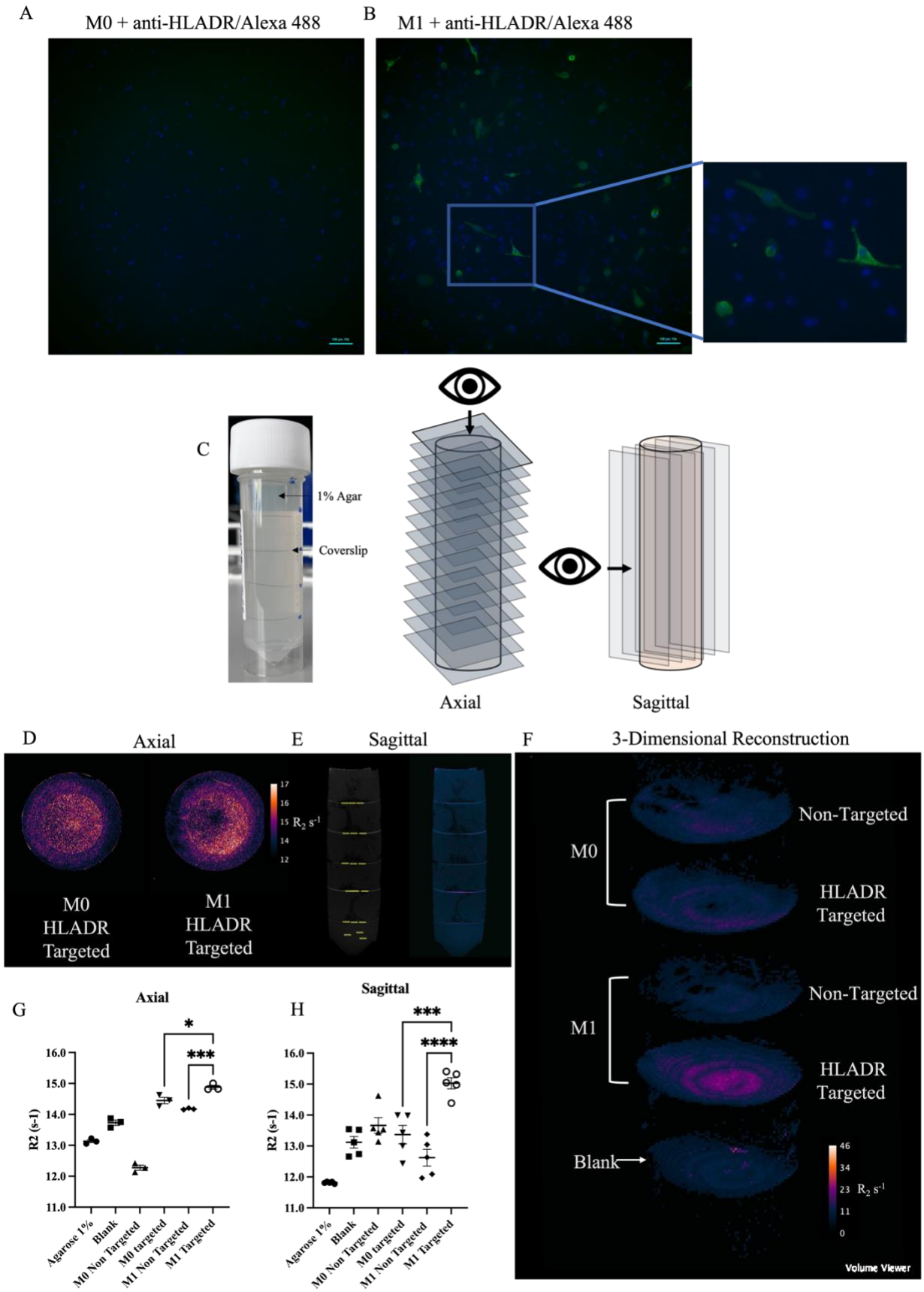
A
M0 + anti-HLADR/Alexa 488
B
M1 + anti-HLADR/Alexa 488
C
1% Agar
Coverslip
Axial
Sagittal
D
Axial
E
Sagittal
F
3-Dimensional Reconstruction
M0
HLADR
Targeted
M1
HLADR
Targeted
17
16
15 R2 s-1
14
12
Non-Targeted
HLADR
Targeted
M0
Non-Targeted
M1
HLADR
Targeted
Blank
46
34
23 R2 s-1
11
0
Volume Viewer
G
Axial
H
Sagittal
R2 (s-1)
16.0
15.0
14.0
13.0
12.0
11.0
*
***
***
****
Agarose 1%
Blank
M0 Non Targeted
M0 targeted
M1 Non Targeted
M1 Targeted

Figure 3.12 Top to Bottom: Coverslip Imaging representative widefield fluorescent image of coverslips with M0 (A) and M1 (B) THP1 stained with anti-HLADR (green, alexa488) and DAPI. (C) Photograph of coverslip phantom containing coverslips suspended in 1% agarose. (D) Visual representation of MR axial slice acquisition through the coverslip phantom. (E) visual representation of the MR sagittal slice acquisition through the coverslip phantom. (F) 3D volumetric representation of 21-slice stack of sagittal R_2 maps. (G) Graph of R_2 values from axial 5 slices. Individual data points represent average of triplicate measurement across a single slice for a given coverslip. (H). R_2 values from sagittal containing coverslip. Individual data points represent triplicate measurement across a single coverslip. *p<0.05, **p<0.01, ***p<0.001, ****p<0.0001.

Figure 3.12A-B depicts widefield fluorescent imaging of anti-HLADR-biotin labelling of M0 and M1 THP1 on glass coverslips, again confirming the presence of HLADR(+) cells within the M1 samples. *Figure 3.12C* depicts how labelled coverslips were arranged within the universal holder. Coverslips were suspended in 1% agarose layers allowing for coverslips to be equally spaced. This meant that multiple surfaces could be imaged in one acquisition. The coverslip phantoms were then imaged taking multiple slices through the phantom in both the axial and sagittal plane. Following image processing R_2 relaxation rates were calculated for each coverslip from both the axial and sagittal perspective. *Figure 3.12D-E* show representative R_2 maps of the coverslips; this revealed a non-uniform distribution of R_2 signal across the coverslips. The coverslip imaging approach revealed similar results to previous attempts to distinguish between M1 and M0, with M1 anti-HLADR/SPION labelled coverslips displaying the highest R_2 relaxation rates, significantly higher than both unlabelled M1 and anti-HLADR/SPION M0.

3.3.2.7 Fluorescent screening for PBMC derived macrophages.

THP1 facilitates cell labelling optimisation experiments as it offers moderate control over the expression of surface markers such as HLADR. However, surface markers of THP1 are not necessarily representative of macrophage polarisation markers in patients. It is therefore important to identify markers that are clinically relevant and have the highest potential to be carried through to clinic. Peripheral blood mononuclear cells (PBMCs) were isolated by CD14+ MACs microbeads, which were then differentiated and polarised to M0, M1 and M2 macrophages in 96 well plates using cytokine stimulation over a 6-day period. Several surface markers were selected

from literature to further develop a panel of immune targeted contrast agents which could visualise the multiple different polarisation states of macrophages.[198–200] HLADR, CD86, CD163, and CD206 were all screened via immunofluorescence as markers for the various cell polarisation states. HLADR expression was evident in all polarisation states. Interestingly, M2 subpopulation displayed the highest relative fluorescent intensity (RFI) for HLADR, this was significantly higher than M1 (*p<0.05) and M0 (***p<0.001). CD86 showed relatively selective expression in M1 subpopulations. M0 macrophages displayed high RFI for CD163, this was highly significantly different (****p<0.0001) to the relative negligible RFI in both M1 and M2 macrophages. CD206 (mannose receptor) displayed a high level of RFI in M2 macrophages, relative to both M0 and M1 macrophages. Between these results, distinct markers could be selected for each polarisation state

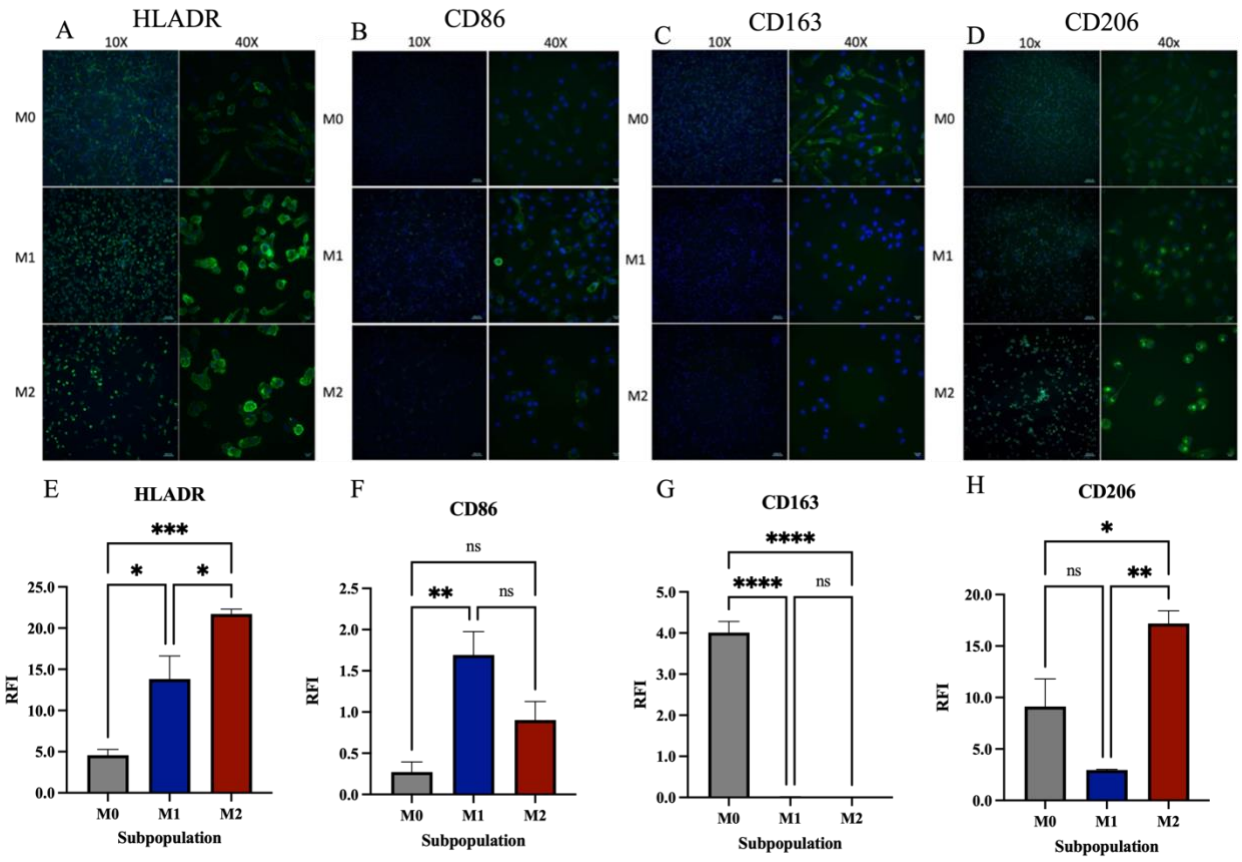

Figure 3.13 **-** Representative widefield fluorescent images of 6-day cultured primary derived macrophage subpopulations. 10x/40x representative fluorescent images of M0/M1/M2 macrophage subpopulations stained with DAPI (Blue) and **A.** anti-HLADR (Green, Alexa fluor 488) **B**. anti-CD86 (Green, Alexa fluor 488) **C.** anti-CD163 (Green, Alexa fluor 488) **D**. anti-CD206 (Green, Alexa fluor 488). **E**. RFI of HLADR in M0/M1/M2 primary derived, RFI was quantified by measuring the integrated density of HLADR(+) cells, normalised to the total cell count. **F.** RFI of HLADR in M0/M1/M2 primary derived, RFI was quantified by measuring the integrated density of CD86(+) cells, normalised to the total cell count. **G**. RFI of CD163 in M0/M1/M2 primary derived, RFI was quantified by measuring the integrated density of CD163(+) cells, normalised to the total cell count. **H.** RFI of CD206 in M0/M1/M2 primary derived, RFI was quantified by measuring the integrated density of CD206(+) cells, normalised to the total cell count. . *p<0.05, **p<0.01, ***p<0.001, ****p<0.0001.

This fluorescent panel provides some future targets that could be used to further developed targeted probes. Critically, an understanding of the surface marker expression of macrophage phenotypes in primary cells provides a much more representative platform for developing translational imaging tools.

3.4 Discussion

Cell tracking, especially by MRI, represents and incredible useful, yet underdeveloped strategy for non-invasive detection and mapping of unique cells types in real time. Cell tracking has the potential to aid detection of diseased cell types, track the delivery of therapeutics cells or monitor the immune response to foreign implanted materials. Traditionally an understanding of these processes would be limited to invasive biopsy. The main focus of this chapter was to investigate the application of a modular antibody-biotin/streptavidin-SPION system for visualising and distinguishing between macrophage polarisation states.

3.4.1 Platform Design

Iron oxide nanoparticles are particularly attractive for cell tracking applications as they can be generated in a range of sizes, shapes and can be surface modified with various coatings including dextran, PEG and silica.[201] Iron oxide nanoparticles have previously been used to visualise macrophage behaviour in real time.[90,100,185,186,202] For macrophages, the predominant strategy for labelling is to target uptake of iron oxide nanoparticles either by phagocytosis (for nanoparticles

>100 nm), pinocytosis, in the case of SPIONs (~10-100 nm) or passive diffusion for ultrasmall iron oxide nanoparticles (<10 nm).[203–206] Interestingly, macrophages labelled with SPIONS have remained viable and can be visualised migrating to the site of inflammation.[207]

An alternative approach, as employed in this chapter is to target the unique surface markers of cells. Surface marker expression is specific to cell type and status (such as activation), and is routinely used as a strategy for identifying cell populations in techniques such as flow cytometry.[208] This approach has been applied before to imaging immune cells, Khurana and others used commercially available CD25 cell sorting microbeads (50 nm SPIONs modified with anti-CD25) to selectively label T-cells.[43] This demonstrated the initial capabilities of SPIONs to label and visualise immune cells via MRI. However, the SPIONs used within the study were 50 nm in size which does have some downstream limitations for imaging, such as decreased blood brain barrier permeability.[209,210] The ideal SPION size to remain at the cell surface is a sweet spot between being small enough to evade phagocytosis/pinocytosis and large enough to avoid passive diffusion. The nanoparticles used in this chapter were 30 nm. Previous studies into silica based nanoparticles demonstrated that murine macrophages did not internalise nanoparticles of 35 nm.[211] Equally, SPIONs of 10 nm were taken up by tumour cells at a higher rate than 30 nm SPIONs.[212] This highlights that 30-35 nm is within the right size to slow the rate of internalisation, whilst maintaining superparamagnetic properties required for MRI detection.

The streptavidin biotin system is inherently modular, meaning that contrast agents and targeting moieties can easily be substitute to suit the application. Whilst this chapter focuses on imaging specific macrophage cell types, this system could be applied to imaging a number of cell types with unique surface marker expression.

To develop an imaging system capable of distinguishing between different cell types, a suitable marker at the cell surface had to be validated. Whilst the overall aim of the project was to discriminate between macrophage polarisation states, the fundamental concept is using MRI to distinguish between positively labelled cells and regions with no labelling.

THP1 was selected as a cell line to generate macrophage the polarisation states. THP1 allowed for facile fabrication of M0, M1 and M2 as well as CD14(+) monocytes, giving rise to subpopulations with differential expression of established cell surface markers. LPS/IFN-γ stimulation of PMA differentiated THP1 (M1) has been previously documented as eliciting a large upregulation of the cell surface receptor HLADR.[194,196] Whilst, HLADR expression remains relatively low in M0 and M2 THP1 subpopulations.

3.4.2 Fluorescent Labelling Experiments

The first step was to distinguish between two different cell types. Consistent with the literature immunofluorescent staining of M0,M1 and M2 THP1 in this chapter revealed high HLADR expression in M1 phenotype. Fundamentally, this provided two populations of cells, HLADR(+) cells (M1, LPS/IFN-γ stimulated) and HLADR(-) cells (M0, PMA only; M2, IL4), which could then be used for downstream optimisation of experiments. Between both the marker selection and the fluorescent screening approach presented in this chapter, there some limitations to address.

Firstly, the markers selected were selected on the basis of expression in a controlled THP1 system. Where realistically, markers that are reliably expressed by THP1 may not be expressed in primary macrophages. There are a number of factors to consider, including donor to donor variability.

A limitation of THP1, as mentioned earlier, is that it does not reliably produce M2 surface markers.[183] Equally, markers such as HLADR may be expressed by other cells, including dendritic cells and B-cells.[213,214] Fluorescent screening was carried out in monocultures only, where only a

fraction of cells were positively labelled for HLADR. Interestingly, fluorescent screening of primary derived macrophages revealed a more homogenous expression of surface markers. Nonetheless, the development of a modular, proof of concept platform that can distinguish between positive and negative labelled cells is immensely powerful.

Once a suitable marker had been identified, the next step was to validate that the modular streptavidin biotin system was capable of selectively labelling HLADR(+) M1 cells with a fluorescent analogue for SPION, a neutravidin fluospheres. This approach allowed for efficient screening and optimisation of the labelling system. A similar labelling approach had been employed by Ayer and colleagues, where T-lymphocytes were biotinylated and subsequently labelled with neutravidin fluospheres, demonstrating the cell tracking capability of these nanoparticles.[215] Colocalisation of the neutravidin fluospheres was confirmed by both widefield and confocal microscopy, with minimal off target labelling. This approach could be improved, to ascertain the subcellular location of the fluospheres, which is not apparent without a membrane or cytoplasm dye. Equally this labelling approach could be applied to flow cytometry, which could quantify the number of positively labelled cells. Absolute quantification of the receptors expressed is complex, however there are techniques such as quantitative flow cytometry and quantitative single molecule microscopy which could provide a better insight into exact surface marker cocentrations.[216,217]

3.4.3 Early Strategies to Visualise HLADR+ THP1 via MRI

Following on from fluorescent validation of the streptavidin biotin system, the next objective was investigate MRI imaging phantoms using this platform. Early strategies for selectively labelling HLADR(+) subpopulations, such as displayed in *figure 3.7* by the live cell staining of M0 and M1 THP1, showed a high level of non-specific binding of the iron-oxide nanoparticle. The comparably

high R_2 values displayed by M0 cells live incubated with αHLADR/IONPs, relative to that of M1, were inconsistent with the previous findings at the immunofluorescent level. There are several potential reasons why this non-specificity might occur in live cell culture. The primary difference between the immunofluorescent protocol and live cell staining protocol is that the immunofluorescent protocol involved several non-specific protein blocking steps with 5% goat serum. The lack of non-specific protein blocking likely contributes to the off-target binding of the primary antibody to the cell surface receptors. The nanoparticle itself may be inducing HLADR expression in the M0 subpopulation, as has previously been reported for silica nanoparticles in dendritic cells.[218] To address this issue in future phantoms, THP1 cells were detached and fixed prior to staining, allowing for inclusion of non-specific blocking to the cell labelling.

Fixed pellets of HLADR(-) (M0) and HLADR(+)(M1) cells were labelled with anti-HLADR/SPIONs were visualised by MRI. This method allowed for the positive identification of M1 labelled cells from M0, with lower non-specific labelling. This was consistent with the fluorescent labelling findings. This was likely due to the inclusion of a non-specific blocking step. MRI of cell pellets is a fairly common strategy to visualise labelled cell populations.[219,220] This approach facilitated easy testing although there were limitations to its application. Generation of cell pellets required a large number of macrophage cells per condition (1.5 million), to be sufficiently large enough for MRI.

3.4.4 3D Agarose Phantoms for Imaging HLADR+ Populations

1% Agarose suspensions were used to address the limitations of the cell pellet phantoms. Agarose and agar gels display T_2 relaxation rates that are similar to that of human tissue (40-150 ms).[221] 1% Agarose suspensions of cells allowed homogenous distribution of cells through 3D space, allowing for multiple slices to be taken. This also allows for 3D reconstruction of phantom, through

z-stacking of R_2 maps (see *figure 3.11* and *3.12)*. CD14(+) THP1 monocytes were also visualised using this method, which further demonstrated the transferrable capabilities of this imaging platform. There were two obvious weaknesses to the agarose based system described in this chapter. The first being, that the agarose used required heating (95 ºC) which could cause cell damage or contrast agent degradation. This could be addressed by using a more biocompatible hydrogel based system such as collagen, fibrin or alginate.[222] The second, was that PCR tube phantoms are more likely to display susceptibly artifacts, due to the proximity of the tube wall to air. This limitation was addressed, in the subsequent agarose droplet phantom, where agarose cell droplet suspensions were further encapsulated by 1% agarose.

Correlative, multimodal imaging can provide holistic information facilitating creation of a composite perspective of tissues. Combining two or more modalities such as optical (fluorescent) and MR imaging, allows for multiscale complementary data collection on the same sample.[223]

3.5 Conclusion

The agarose based phantom approach, combined with the streptavidin-biotin labelling system could serve as powerful strategy to screen multiple targeted contrast agents, with high throughput. Interestingly, agarose based systems have been used as a surrogate for brain tissue to study contrast agent diffusion.[224] An interesting future experiment could involve the perfusion of targeted vs non-targeted contrast agents through an agarose system with immobilised cells. In such, it would be possible to compare behaviour of the contrast agents selective binding.

The two approaches employed could allow for multimodal correlative imaging. The optical properties of agarose may allow for further potential 3D correlative fluorescent imaging, with several approaches such as light sheet fluorescence microscopy and structured illumination microscopy capable of imaging and reconstructing fluorescently labelled 3D structures. Equally,

the coverslip imaging (seen in *figure 3.12*) approach demonstrate that fluorescent imaging and MR imaging could be carried out on the same sample. It is conceivable that the coverslip could be recovered, following MR imaging and used for mass spectrometry analysis. This approach could be used to model various disease states, especially those involving small monolayers of cells, such as immune cell recruitment to the interface of an implanted biomaterial.

To summarise, the antibody-biotin streptavidin-SPION system was successfully applied to discriminate between different macrophage surface markers, with labelling visible via fluorescent and MR imaging. The initial aims as set out at the beginning of this chapter state a requirement to find a suitably distinct marker for positively identifying one macrophage polarisation state from the other. HLADR was identified as a suitable marker for distinction between M0 and M1 THP1, with HLADR positive macrophage being visualised through multiple 3D phantoms. In conclusion, the streptavidin-biotin system serves as a powerful modular approach for contrast agent screening for cell tracking applications.

Chapter 4 - Using Deuterium Magnetic Resonance Spectroscopy to Positively Identify Macrophage Polarisation States

4.1 Introduction

4.1.1 Metabolic Imaging for Cell Identification

Changes to cellular metabolism represent some of the most distinctive biomarkers for a wide range of pathologies, including inflammation and cancer. Dysregulation of metabolic processes are heavily implicated in multiple disease states including obesity, diabetes and cancer.[4,225,226] In their 2011 review, Hanahan and Weinberg described reprograming of energy metabolism as an emerging hallmark of cancer.[227] Accurate fingerprinting of metabolism within tissue can pinpoint the timescale of a given pathology. Metabolic reprogramming in tissues is present before the occurrence of visible inflammation and tissue damage, making metabolic shifts an attractive target for diagnostic imaging.[228] Current imaging modalities are predominantly optimised for resolving the structural and functional parts of a tissue. Of equal importance is the transport and movement of those metabolites within space and time that can reveal disease progression and response.[229]

4.1.2 Aerobic Glycolysis

One of the most distinctive, well documented metabolic shifts, with high clinical significance, is aerobic glycolysis.[230–233] It is implicated in cancer metabolism, glucokinase deficiency, pyruvate kinase deficiency and conditions resulting in low oxygen availability.[234] Otto Warburg initially discovered this metabolic shift in cancer metabolism, such that tumour cells produce lactate irrespective of tissue oxygenation.[235] Under physiological conditions, glycolysis is the core metabolic pathway by which cells generate adenosine triphosphate (ATP) from glucose. Differentiated tissue displays oxygen-dependent glucose metabolism, where the presence of oxygen determines the fate of downstream pyruvate, as demonstrated in *figure 4.1*. In proliferative and tumour tissue, downstream glucose metabolism occurs in an oxygen independent manner, whereby 85% of glucose is metabolised to lactate.[236,237] In both proliferative tissue and tumour

tissue, a number of factors drive increased glucose uptake, including upregulation of phosphoinositide 3-kinase (PI3K) signalling pathway and stabilisation of hypoxia inducible factors (HIFs).[237]

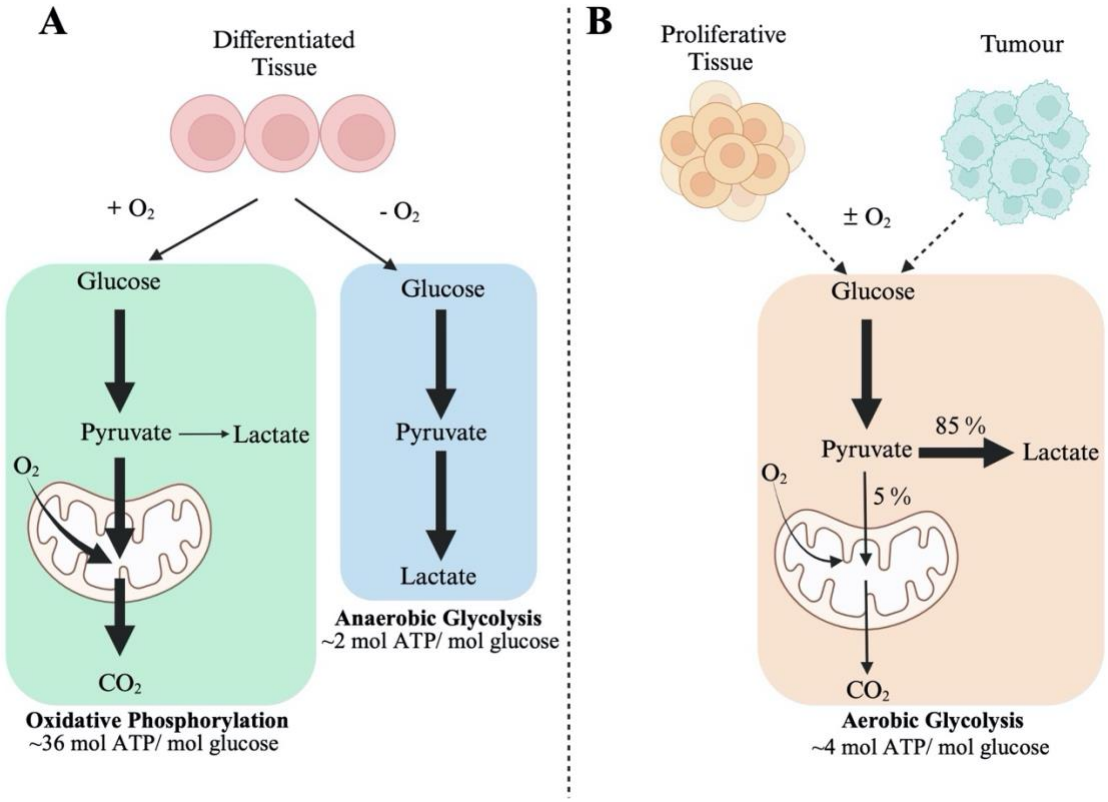

Figure 4.1 - Schematic displaying differences in glucose metabolism in differentiated, proliferative and tumour tissue. A Under aerobic conditions, differentiated tissue converts glucose to pyruvate via glycolysis, and generates large quantities of ATP via oxidative phosphorylation. Under anaerobic conditions, differentiated tissues undergo ATP inefficient anaerobic glycolysis. B. Independent of oxygen presence, proliferative tissue and tumour tissue undergo 'Warburg effect' or aerobic glycolysis, whereby pyruvate is catalysed to lactate. Lactate production facilitates the oxidation of coenzyme NADH to NAD+, which can be used to aid ATP production. Figure adapted from Van der Heiden et al. [237]

Aerobic glycolysis is a highly inefficient pathway for ATP production, with 18x lower ATP production versus oxidative phosphorylation. The metabolic switch observed in cancer towards aerobic glycolysis is paired with upregulation of glucose transporters, leading to increased cytosolic glucose availability.[238–240] Metabolic shifts represent some of the earliest manifesting changes to physiology and response to injury and disease.[241–244] Dysregulation of metabolic

processes, make the metabolic niche an attractive target for diagnostics. Warburg-like metabolism is also observed in many inflammatory processes, including in M1 macrophages and activated T-cells.[51,245–248] Therefore, this metabolic profile is an attractive imaging modality to identify local inflammatory processes. Pre-existing metabolic imaging approaches to explore this area include techniques such as FDG-PET and magnetic resonance spectroscopy (MRS).[249]

4.1.3 Inflammation as a Target for Metabolic Imaging

Macrophages serve as a central hub for the immune response. They are critical for maintaining tissue homeostasis in response to physiological insult, injury and disease.[171,172,250] Macrophages are specialised immune cells and display high contextual plasticity.[9,251,252] The unique attribute of macrophage biology is the ability of macrophages to adapt to their surroundings. Macrophages have long been a focal point for diagnosis of inflammation. Activated macrophages can be generally categorised into three groups: the naïve-like (M0), the pro-inflammatory (M1) and the anti-inflammatory (M2) subtype.[13] M1 and M2 activated macrophages are present in heterogenous populations of immune cells.[178,253] The ratio of M0/M1/M2 macrophages is a useful prognostic parameter and is indicatives of the phase of inflammation.[254,255] M0 macrophages are uncommitted, resting macrophages which are precursors to polarised macrophages.[256,257] M1 macrophages are associated with acute phase of inflammation, characterised by immune cell recruitment, endothelial cell activation and release of pro-inflammatory cytokines.[155] In contrast, M2 macrophages are associated with inflammatory resolution, wound healing and tissue repair.[9,13] Along with their distinct functions, macrophages subtypes display both distinct morphology, surface markers and metabolic profiles.[13,155,194] The metabolic niche of macrophages represents one of the most distinctive aspects of macrophage polarisation. *Figure 4.2* depicts a generalised

overview of M1 and M2 macrophage metabolism. M1 macrophages are characterised by a glycolytic-like metabolism, owed in part to the oxygen independent stabilisation of HIF1a.[246] IFN-γ/LPS stimulated M1 macrophages demonstrate the highest rate of glycolysis and the highest glycolytic capacity, in comparison to M0 and M2 macrophages.[199] As M1 macrophages represent one of the primary responses to physiological insult, coupled with their metabolic shift being dependent on aerobic glycolysis, they provide an excellent target for molecular imaging and potential to detect disease at an early stage. In contrast to M1 macrophages, M2 macrophages display an increased dependence on oxidative phosphorylation (OXPHOS) to fuel their role in wound healing and inflammatory resolution.[155,245,258] The capability to target macrophages, in particular the metabolic fingerprints they exhibit, could pinpoint inflammatory timescales. There is enormous potential to develop upon pre-existing metabolic imaging approaches, to target inflammation in real time.

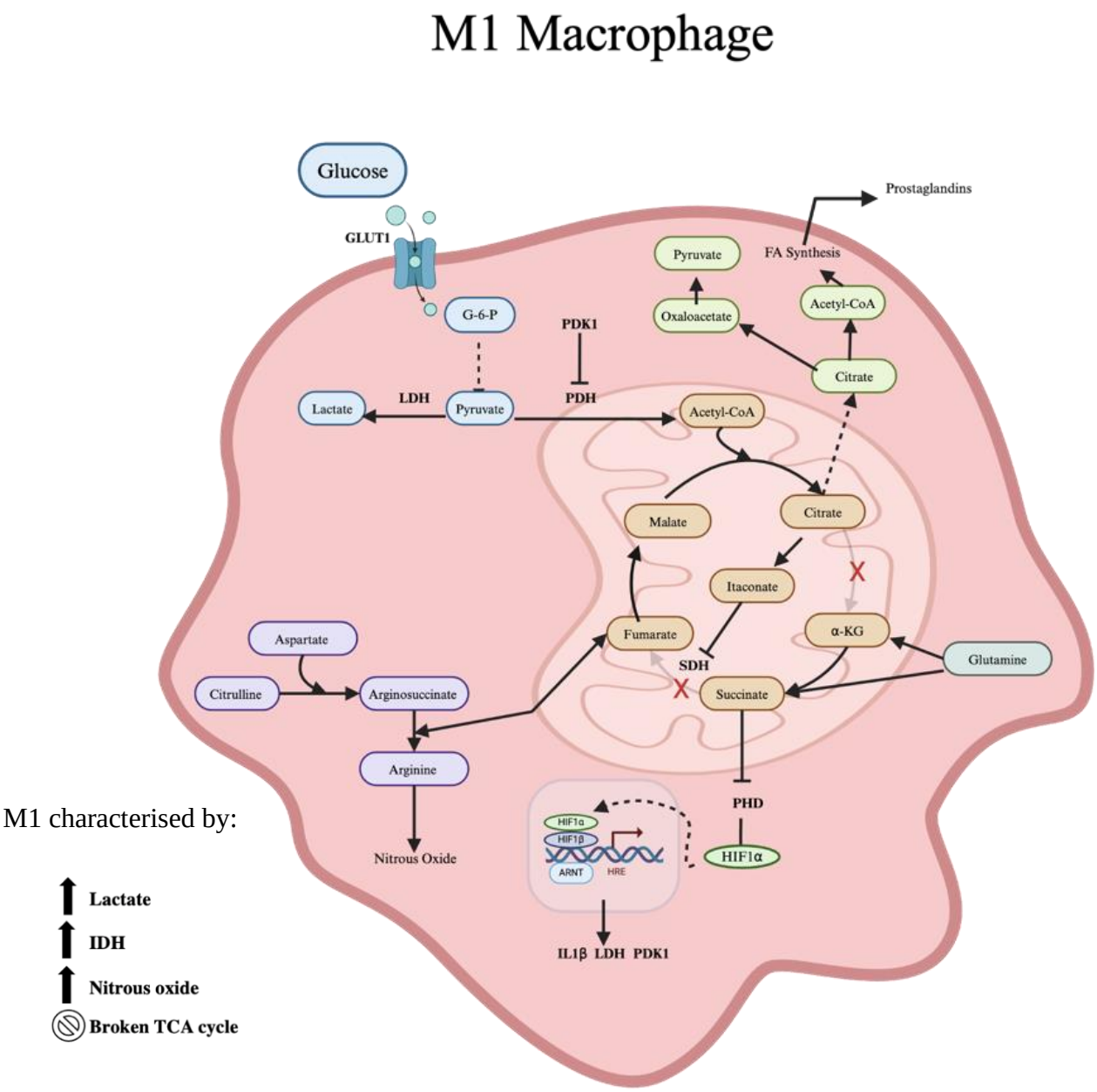

Figure 4.2 - Metabolic pathway of M1 macrophages. **A**. M1 macrophages exhibit a disrupted Krebs cycle, with two breakages at the citrate conversion to alpha-ketoglutarate. The expression of isocitrate dehydrogenase, responsible for catalysing this conversion displays a 7-fold lower expression versus M0 macrophages. This first breakage, leads to accumulation of citrate, which is redirected to both itaconate and fatty acid synthesis. Itaconate, an antimicrobial compound, inhibits succinate dehydrogenase (SDH), leading to the second break within the Krebs cycle of M1 macrophages. Build-up of succinate inhibits prolyl hydroxylase domain (PHD) enzymes, which regulates hypoxia inducible factor 1 alpha (HIF1a). Inhibition by succinate of the PHD enzymes leads to the stabilisation of HIF1a, in an oxygen independent manner, leading to the transcription of glycolytic genes including lactate dehydrogenase (LDH) and pyruvate dehydrogenase kinase 1 (PDK1). In tandem, LDH

and PDK1 upregulation by HIF1a mediated transcription leads to an increase in glycolytic-like metabolism associated with M1 macrophages. Figure adapted from Liu et al.[245]

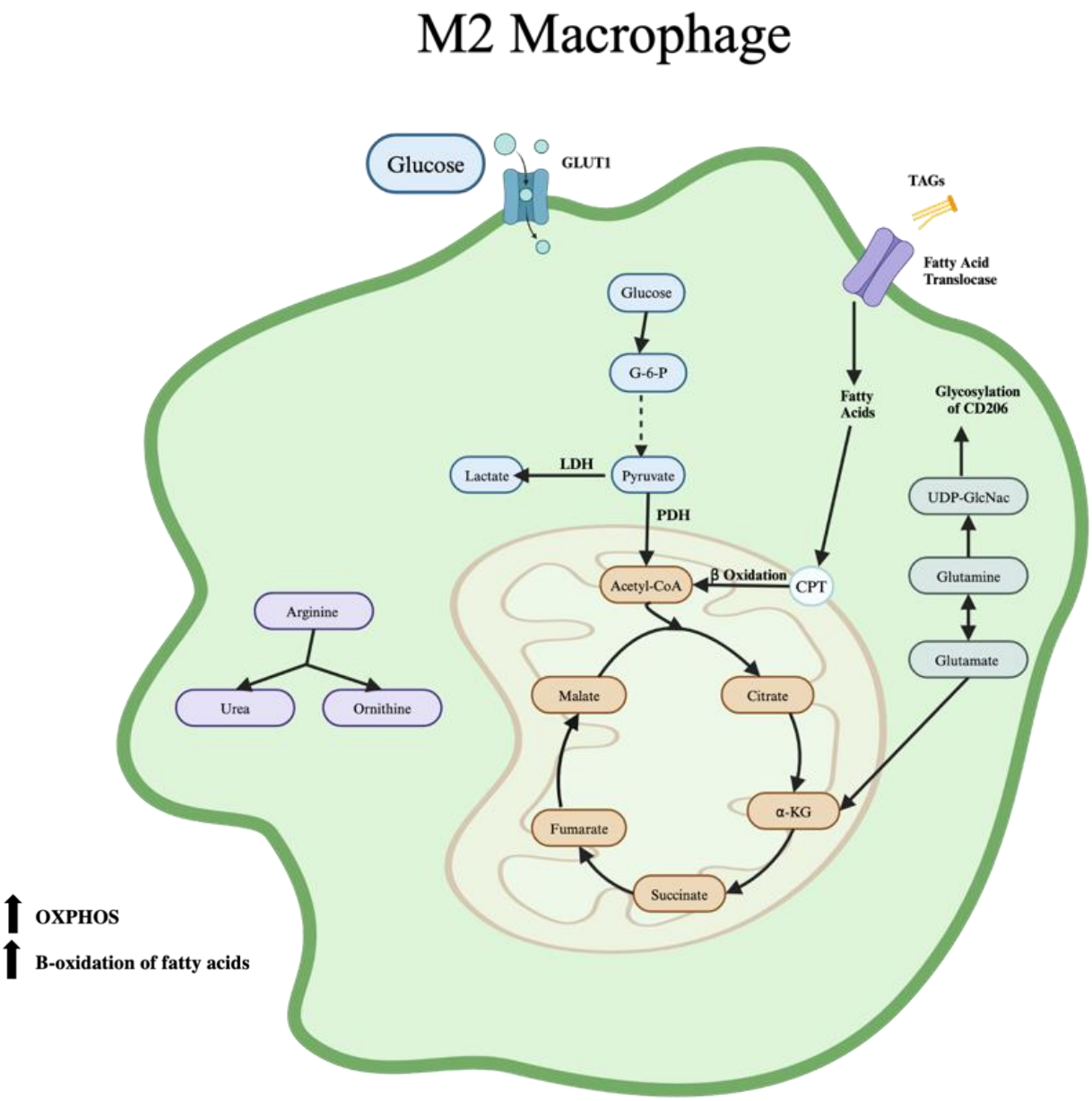

Figure 4.3. Metabolic pathways of M2 macrophages. M2 macrophages unlike M1 macrophages, exhibit an intact Krebs cycle. M2 macrophages are dependent on oxidative phosphorylation (OXPHOS) to generate significant quantities of ATP. Beta oxidation of fatty acids is another hallmark of M2 metabolism. Figure adapted from Liu et al.[245]

4.1.4 What are the Current clinical options available?

For high specificity, mass spectrometry is the gold standard for determining metabolite presence within a given sample. However, metabolite tracking using mass spectrometry based techniques is destructive and lacks temporal resolution. ^{18}F-fluorodeoxyglucose positron emission tomography (FDG-PET) remains the only current metabolic imaging technique that is routinely used at a clinical level.[259–261] In FDG-PET imaging, contrast is generated by the accumulation of FDG, a fluorinated glucose analogue, where high signal correlates high glucose uptake.[262,263] A highly sensitive imaging modality, FDG-PET works by detecting two 511 KeV photons from positron emission from an ^{18}F isotope. FDG-PET was initially developed as a research tool to visualise glucose utilisation in rodents, however it is now used widely in the clinic to visualise and identify tumours by their relative increase rate of glucose uptake[264]

FDG-PET has also been applied to studies of tumour associated macrophages (TAMs).[27,265] FDG-PET/CT revealed that increased glucose uptake in head and neck squamous cell carcinoma was correlated with increased M2 macrophage polarisation.[266] However, M2 macrophage presence could not be directly detected by PET/CT. Interestingly, PET imaging has been used to target bacterial infection using both FDG and ^{18}F-fluordeoxysorbitol as probes.[267] However, it is impossible to distinguish the metabolic niche of bacteria from host inflammatory processes with this technique. Certainly, PET imaging serves as a potential platform for metabolic assessment of immune state, however there are several limitations to its application in practice. The primary limitation of FDG-PET with respect to metabolic imaging is that it can only visualise one aspect of metabolism – glucose uptake. An overview schematic of FDG-PET metabolism is detailed in *figure 4.3*. FDG is a deoxyglucose, with an ^{18}F moiety on the second carbon.

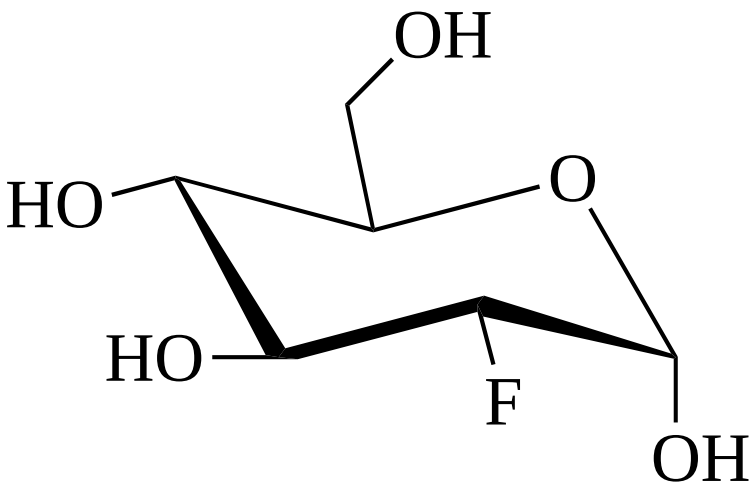

Figure 4.4: Chemical structure of 18F-Fluorodeoxyglucose

Under normal glycolysis, the rate of glucose uptake is limited by presence of glucose-6-phosphate, where it inhibits the hexokinase enzyme. Turnover of glucose-6-phosphate is then catalysed by an aldose-ketone isomeration via glucose-6-phosphate isomerase, resulting in fructose-6-phosphate. The isomeration of the C-1 carbonyl to C-2 facilitates the progression of the glycolytic pathway. However, in 2-deoxyglucose compounds, such as FDG, the hexokinase phosphorylates the deoxyglucose to 2-deoxglucose-6-phosphate which cannot be metabolised further due to the lack of hydroxyl group on the C2 position. The phosphorylated form of deoxyglucose remains entrapped within the cell.[268]

False negative results for tumours with low glycolytic activity, and false positive results for bacterial infections can limit the reliability of FDG-PET.[269] Being entirely reliant on one parameter, glucose uptake, prevents the detection of downstream and potentially clinically significant metabolic biomarkers. Crucially, many of these cancers that fall below the FDG-PET detection limit may not have glycolytic metabolic rate at a sufficiently high level to be detected by PET, or they may utilise a different carbon source to glucose.[262] In either circumstance, a metabolic

imaging modality that can visualise metabolic pathways beyond glucose uptake alone could prove extremely valuable.[262,270]

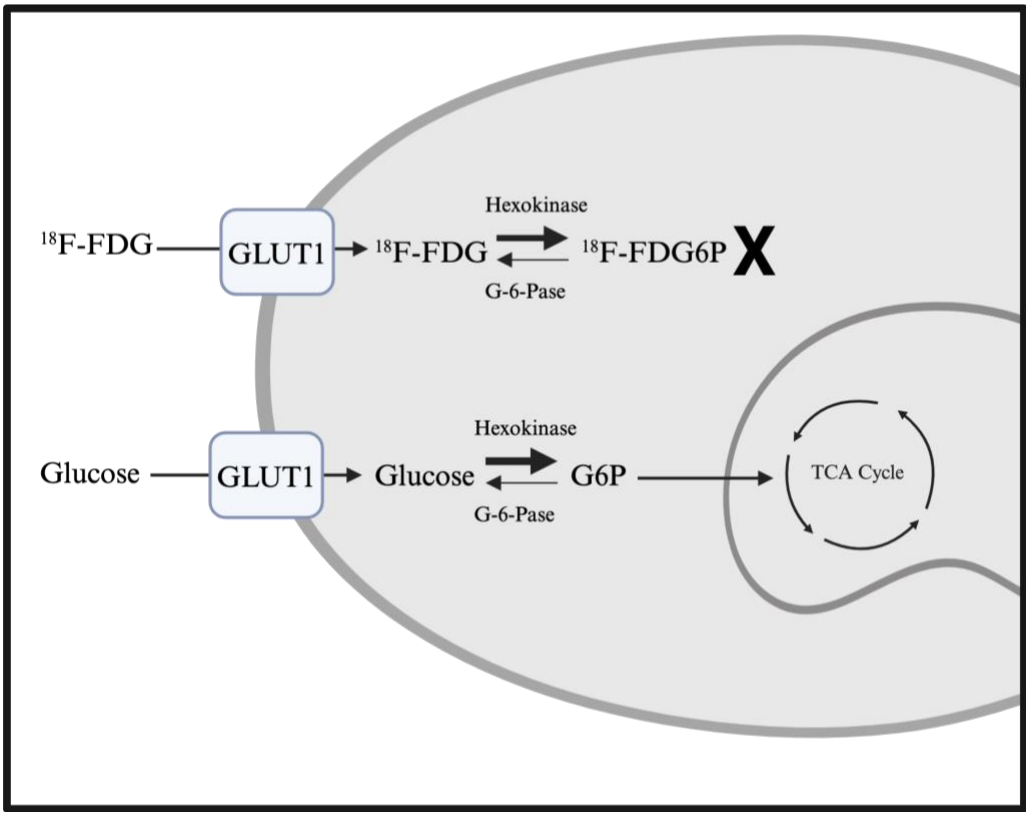

Figure 4.5 - FDG Glucose terminal entrapment following hexokinase phosphorylation to FDG-6-P. Figure adapted from Rahman *et al*.,2019[271]

Another diagnostic option is to use magnetic resonance spectroscopy (MRS), which employs conventional MR scanners to execute voxel by voxel NMR spectroscopy. In essence, NMR and MRS are interchangeable terms, in that the distinct chemical environments of spin active nuclei can be visualised by spectral readouts. Proton MRS is fundamentally identical in its detection approach to MRI. However, where MRI relies on water and fat proton signal to generate image contrast, MRS suppresses water and fat to better visualise resonances of clinically relevant metabolites.[166] These include N-acetyl-aspartate, choline, creatine, glutamate, glutamine, γ-aminobutyric acid (GABA) and lactate. Generally, natural abundance proton MRS can only provide static information in relation to metabolite concentration, and cannot provide insight into

metabolic flux in tissue.[166,272–274] This is because ^{1}H MRS measures the equilibrium state of ^{1}H environments, which may stem from numerous processes.[274]

The most prominent strategy for measuring metabolic flux by MRS is to target alternative spin active nuclei, such as ^{13}C and ^{2}H. In recent years, MR-based spectroscopic methods utilising metabolic substrates labelled by spin active stable isotopes including ^{13}C or ^{2}H have been carried through to the clinic.[259] Unlike FDG, the downstream metabolites of ^{13}C and ^{2}H labelled substrates do not become terminally entrapped, such is the metabolic fate for FDG-6P. This advancement means that it is possible to track metabolism beyond the initial stages of glucose uptake and hexokinase phosphorylation.[275] ^{13}C MRS has been the most extensively studied approach, where ^{13}C labelled substrates such as glucose and pyruvate have been employed at both *in vitro* and *in vivo* level. Furthermore, the advent of hyperpolarised dynamic nuclear polarisation (DNP) has afforded a 10,000x signal boost for ^{13}C based MRS.[141] The process of hyperpolarisation involves the significant increase in population of nuclear spin states beyond the thermal equilibrium. This leads to an signal enhancement by several orders of magnitude. DNP one of several techniques used to achieve hyperpolarisation, exploiting microwave irradiation to transfer the magnetic moment of electrons to nuclear spins. Macrophage polarisation states have been previously targeted using ^{13}C MRS using hyperpolarised ^{13}C-pyruvate and ^{13}C-dehydroascorbic acid.[48] Hyperpolarised ^{13}C-pyruvate was also used as means of detecting inflammatory arthritis in mouse models.[161] The study found a significant increase in lactate-pyruvate ratio in the arthritic mouse paws versus control. Steady state proton NMR and hyperpolarised-^{13}C pyruvate has also been used to monitor lactate production in M1 phenotypes only.[276] However, in general ^{13}C MRS has a limited clinical future. ^{13}C MRS-DNP has a very short application window of 20-30 seconds for

in vivo applications[277,278] ^{13}C MRS-DNP requires modifications to MRI hardware, and additional highly technical equipment and staff to achieve hyperpolarisation.[164]

4.1.5 Why Deuterium MRS?

Polvoy., et al summarised some key requirements for metabolic imaging successful at the in vivo level.[163] These were:

1. Turnover of labelled substrate to analyte occurs within an appropriate clinical timeframe.
2. Distinct labelled environments are capable of being resolved from bulk signal.
3. That analytes are detected by NMR spectroscopy
4. Analytes are produced at a sufficient concentration to be detected.

Deuterium (^{2}H) is a stable, spin active (S.= 1) isotope of hydrogen that can serve as an effective alternative to ^{13}C based MRS. ^{2}H MRS has recently regained a large amount of interest for clinical applications.[162,259,279] Deuterium was initially investigated at the *in vivo* level in the 1980s, where D_2O administration to rodents was used to visualise deuterium enrichment in triglycerides.[280] By comparison to ^{13}C MRS, signal acquisition in ^{2}H MRS is relatively simple, using basic pulse-acquire MR sequences.[164] Deuterium also benefits from a low natural abundance, meaning that ^{2}H MRS has minimal background and limits the spectral crowding caused by lipids and water resonances.[164] Deuterium MRS has gained particular interest in neuroimaging applications, where FDG-PET and ^{13}C MRS have particularly limited scope.

There have been numerous advances in deuterium probe development with deuterium enriched analogues of glucose, pyruvate, fumarate, acetate and choline all being investigated *in vivo*.[168–170,281,282] *Figure 4.6* provides an overview of downstream processing of deuterated glucose through glycolysis and TCA cycle, highlighting intermediates that could give rise to potential signals.

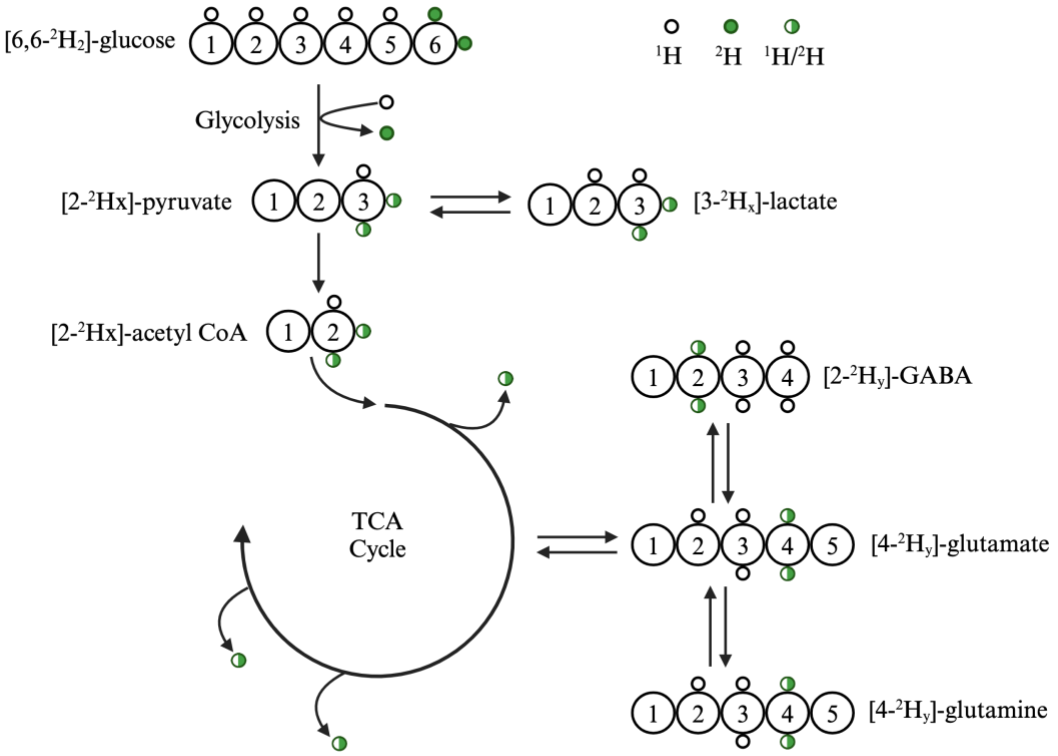

Figure 4.6 - Overview of metabolic processing of [6,6'-$^2H_2$]-glucose. Figure adapted from Low et al.[138]

To date, there have been no attempts to use deuterium MRS to visualise and distinguish macrophage polarisation states. In this chapter, a deuterium glucose probe [6,6'-$^2H_2$]-glucose is investigated as a potential substrate for ^{2}H MRS assessment of macrophage polarisation state and the following hypothesis was tested.

I hypothesise that the M1 macrophage metabolic fingerprint will be sufficiently glycolytic to be distinguished from M2 and M0 polarisation state, via ^{2}H MRS approaches. I will test this hypothesis using the following aims:

a. Investigate the spectroscopic detection limits of conventional NMR spectroscopy for detecting deuterium glucose and downstream metabolites in extracellular media of both GBM and macrophage *in vitro* samples.

b. Investigate the use of high resolution NMR spectroscopy, in conjugation with deuterated internal concentration reference to determine concentration of downstream metabolites.
c. Investigate if deuterium lactate production is a robust biomarker for M1 polarisation.
d. Investigate live cell ^{2}H NMR spectroscopy of deuterium glucose with macrophage polarisation states.
e. Validate lactate secretion in macrophage phenotypes by luminescent assay.

The feasibility of deuterium metabolic imaging to positively identify different macrophage subpopulations will be achieved through screening *in vitro* models of macrophages with deuterium labelled compounds, namely [6,6' $^{2}H_2$] glucose. The metabolic profile of macrophages will initially be assessed by sampling extracellular media containing deuterium probes at conventional NMR field strengths (400 MHz). This will be achieved using simple pulse/acquire NMR acquisition protocols. Once it has been determined that unique metabolic fingerprints can distinguish macrophage subpopulations, spectroscopic assessment will be scaled up to higher field strengths (800 MHz) in order to resolve metabolites of low concentrations. Beyond this, real time turnover of deuterium labelled probes will be assessed with *in vitro* ^{2}H-NMR.

4.2 Methods and Materials

4.2.1 Cell Culture

4.2.1.1 Culture of Glioblastoma Multiforme (GBM) Cell Lines

Glioblastoma multiforme (U251, ATCC) cells were cultured in high glucose Dulbecco's modified Eagles medium (DMEM), supplemented with 10% FBS (v/v), 1% penicillin-streptomycin (v/v) and 1% L-glutamine (v/v) in adherent T175 flasks under sterile conditions (37º C, 5% CO_2, relative humidity). **G**lioblastoma **IN**vasive margin (GIN31) cells were cultured in DMEM supplemented with 10% FBS and incubated under sterile conditions (37º C, 5% CO_2, relative humidity).

4.2.1.2 Subculturing of Cells

For cell passage, TrypLE express (Gibco) was used to detach cells. At 80% cell confluency, spent cell culture media was aspirated from the cell culture flask and cells were subsequently washed using warm PBS (37ºC, sterile). PBS was then removed, and prewarmed TryPLE was added directly to cells. Cells were then left to incubate (37ºC, 5% CO2, 10 minutes). The cell culture flask was then gently tapped to aid detachment. Visible cell detachment was confirmed by light microscopy. The cell/TrypLE solution was then removed from the flask, where cells were resuspended into a fresh 50mL falcon tube containing complete DMEM media. The cell containing falcon tube was then centrifuged (5 mins, 350 G, r.t) to pellet the live cells. Following centrifugation, supernatant was discarded and cell pellet was resuspended in complete media for cell counting.

4.2.1.3 Culture of Primary Derived Macrophages

Blood was obtained from healthy donors (National Blood Service, Sheffield, UK) after informed written consent and following ethics committee approval (Research Ethics Committee, School of Medicine, University of Nottingham). Peripheral blood mononuclear cells (PBMCs) were separated via density gradient centrifugation with histopaque, and CD14+ monocytes were positively selected using MACS CD14 isolation kit (Miltenyi Biotec, UK). PBMCs were twice washed with MACS buffer (2mM EDTA with 0.5% FBS in PBS) and then incubated with CD14+ targeted magnetic beads (15mins, 4ºC). Following incubation, labelled cells were then selected using LS columns. CD14+ bound cells were washed using MACS buffer, three times and then eluted. CD14+ monocytes were then cultured in RPMI-1640 media supplemented with 10% fetal bovine serum (FBS) 1% penicillin/streptomycin (v/v) and 1% L-glutamine (v/v). Cells were cultured at a density of 500,000 viable cells per ml.

4.2.1.4 Preparation of Macrophages from PBMCs

To generate naïve-like monocytes (M0), RPMI-1640 media was further supplemented with macrophage colony stimulating factor (M-CSF, 10 ng/mL). To generate proinflammatory macrophages (M1) RPMI-1640 media was further supplemented with interferon gamma (IFN-y, 20ng/mL) and (GM-CSF, 50ng/mL). To generate anti-inflammatory macrophages, RPMI-1640 media was further supplemented with interlukin-4 (IL4, 20ng/mL) and macrophage colony stimulating factor (M-CSF, 50ng/mL). Cells were cultured under sterile conditions (37ºC, 5% CO2, relative humidity) for 6 days, with media changes at day 3 of the polarisation procedure.

4.2.1.5 Culture with (6,6' $^{2}H_2$) Glucose

Following macrophage polarisation, cells were washed using sterile PBS. RPMI-1640 doped with (6,6'-$^{2}H_2$) glucose (1 g/L) (Sigma Aldrich) was added to the cells. After 24 hrs incubation with deuterium glucose, supernatant was collected and frozen at -80ºC.

4.2.2 ^{2}H-NMR spectroscopy of Extracellular Media on 400 MHz NMR

4.2.2.1 Initial 2H NMR Spectroscopy Optimisation Experiments on Extracellular Media Sample Preparation

Optimisation experiments were carried out with both GIN31 cells and patient derived M1 and M0 macrophages. For macrophages, monocytes were isolated, counted and seeded in T75 flask at a density of 8 mn/mL. Cells were polarised to M0 and M1 subpopulations, as previously described. On day 6, spent media was removed and cells were washed with PBS. RPMI containing 1 g/L (6,6-$^{2}H_2$)-glucose was added to cells. 1mL aliquots of extracellular media were removed at 1, 2 and 24hrs and stored at -80º C until NMR acquisitions. For GIN31 cells were seeded into a T75 flask and grown until high (90-100%) confluency. Cell culture media was then removed and cells were washed with PBS. DMEM media containing 1 g/L (6,6-$^{2}H_2$)-glucose was then added to the

1mL aliquots of extracellular media were removed at 1, 2 and 24hrs and stored at -80º C until NMR acquisitions.

4.2.2.2 NMR Acquisition Using 400 MHz Spectrometer

^{2}H NMR spectra of extracellular macrophage media solutions were acquired at 298 K using an 400 MHz (9.4 T) Bruker BioSpin equipped with a 5mm BBFO multinuclear probe. All spectra were acquired in both lock off and sweep mode. The spectrometer frequency was set to the lamour frequency of deuterium of 61.41 MHz [6.55 MHz per Tesla]. A 1 s relaxation delay (d1), 3.3 s acquisition time (AQ) with a 90º pulse was used to acquire spectra. The data acquisition size (TD) was 4096 data points with a spectral width of 1225.5 Hz, and was post processed using zero filling to 8192 datapoints giving a digital resolution of 0.15 Hz/pt. Spectral data acquired was the product of either 64 or 1000 scans. Then 1.0 Hz exponential window function line broadening was applied followed by baseline and phase corrections.

4.2.3 800 MHz NMR Spectroscopy

4.2.3.1 Sample Preparation

For macrophages, monocytes were isolated, counted and seeded in 12-well plate at a density of 500K/mL. Cells were polarised to M0 and M1 subpopulations, as previously described. On day 6, spent media was removed and cells were washed with PBS. RPMI containing 1 g/L (6,6-$^{2}H_{2}$)-glucose was added to cells. 1mL aliquots of extracellular media were removed at 24 hrs and stored at -80º C until NMR acquisitions.

4.2.3.2 1D ^{2}H-NMR Spectroscopy

^{2}H NMR spectra of extracellular macrophage media solutions were acquired at 298 K using an 800 MHz (18.8 T) Bruker BioSpin Avance Neo spectrometer equipped with a 5-mm QCI helium cryoprobe. All spectra were acquired in both lock off and sweep mode. The spectrometer frequency

was set to the lamour frequency of deuterium of 122 MHz [6.55 MHz per Tesla] and manually matched and tuned to the correct frequency. 1-dimensional automatic gradient shimming was carried out on each sample. The spectrometer was configured to deliver RF signal via a 150W deuterium transmitter and deuterium pre-amplifer. A 1 s relaxation delay (d1) and 2.2 s acquisition time (AQ) with a 90º pulse at 150 µs. The data acquisition size (TD) was 4096 data points with a spectral width of 1851.9 Hz, and was post processed using zero filling to 8192 datapoints giving a digital resolution of 0.23 Hz/pt. Then 1.0 Hz exponential window function line broadening was applied followed by baseline and phase corrections. NMR data was processed using both Bruker TopSpin 4.1.4 and MestreNova (version 14.4.0-30573).

4.2.3.3 The Longitudinal Relaxation Time T_1 Inversion Recovery Measurements for Compounds

The T_1 inversion recovery pulse sequence was used to calculate the longitudinal relaxation times (T_1) of the internal concentration standard pyrazine-d4 (Sigma Aldrich), HDO, (6,6-$^2H_2$)-glucose and (3,3-$^2H_2$)-lactate. All NMR experiments were carried out at 298 K with a relaxation delay (d1) of 5 s and 21 inversion recovery delays (τ) of 0.0005, 0.001, 0.002, 0.005, 0.010, 0.02, 0.03, 0.05, 0.07, 0.1, 0.2, 0.3, 0.4, 0.5, 0.7, 0.9, 1.0, 1.5, 2.0, 2.5, 5.0, 10.0 s was used to determine the T_1 of metabolites per sample.

4.2.4 Real Time NMR Spectroscopy

4.2.4.1 Sample Preparation

For real time NMR, primary macrophages were fabricated using the 6-day polarisation procedure described above. Cells were cultured in a T75 flask at a density of 1mn/mL. On day 6 cells were initially washed with warm PBS (37ºC) and detached using TrypLE (37º C). Cells were then centrifuged (350 g, 5mins, r.t) to generate a cell pellet. Cells were then counted using an automated

cytometer. 5 mn cells were then resuspended in 600 µL of deuterium-glucose containing media and transferred to a sterile NMR tube. The NMR tube sealed with a cap and was placed within a styrofoam holder for transport to the NMR facility.

4.2.4.2 Sample Acquisition

^{2}H NMR spectra of live macrophage cell solutions were acquired at 310.1 K using an 800 MHz (18.8 T) Bruker BioSpin Avance Neo spectrometer equipped with a 5-mm QCI cryoprobe. All spectra were acquired in both lock off and sweep mode. The spectrometer frequency was set to the Lamour frequency of deuterium of 122 MHz [6.55 MHz per Tesla] and manually matched and tuned to the correct frequency. 1-dimensional automatic gradient shimming was carried out on each sample. (Spectra were acquired using a relaxation delay (d1) of 0.5 s and an acquisition time (Aq) of 0.901s and a 90º pulse. The spectrometer was configured to deliver RF signal via a 150W deuterium transmitter and deuterium pre-amplifer. Each spectra were acquired with 1024 data points, a spectral width of 1136.4 Hz (9.25 ppm) and a recycling time (Tr) of 1.8 s [3 x 624 ms (T1 of internal standard)] and were the product of 234 scans.

4.2.4.3 Data Analysis

Spectra were analysed using TopSpin 4.1.4 NMR software**.** Spectra were zero filled to 4096 data points. Spectra were processed with an exponential window function with 1 Hz of line broadening, phase and baseline corrected ahead of analysis. Resonance peaks and integrals were manually selected. Spectra was reference aligned to HDO resonance at 4.7 ppm and the metabolite integrals were normalised to HDO. Negative integral values were replaced using the following affine transformation of negative values (ATNV)[283]:

$$value = \frac{value + maxTMP - minTMP}{(maxTMP - minTMP) * maxTMP * 0.99} + maxTMP * 0.01 \quad (3)$$

minTMP = lowest negative data point, maxTMP = lowest positive data point

Following the deuterium timecourse, 5 mM pyrazine was doped into the NMR tube to provide relative quantification. Assuming the HDO integral remains unchanged, relative concentrations were then extrapolated from the known pyrazine-d4 resonance integral.

Spectra were then visualised using MestreNova NMR software, displaying a decimated spectra stack of the deuterium timecourse. All data acquired from live cell spectroscopy is expressed as a mean ± the column standard deviation. One-way ANOVA and Tukey's post hoc analysis was used to calculate statistical significance, where $p < 0.05$ is considered to be statistically significant.

4.2.5 Lactate Glo Assay

Extracellular lactate presence was validated through the luciferin-based bioluminescent assay Lactate-Glo (Promega). Donor derived CD14+ monocytes were seeded onto a 96 well plate at a density of $5x10^3$ per mL and polarised into M0, M1 and M2 macrophages (as previously described). Following, the 6 day polarisation period, cells were then washed using PBS (sterile, 37º C). Deuterium glucose media (1 g/L) was then added to each well and left to incubate (24hrs, 37º C, 5% CO_2, relative humidity). After 24hrs, the extracellular media was removed and plated into a fresh 96 well plate. Each polarisation condition was plated in triplicate. Each media sample was then diluted 40-fold in PBS, giving a final working volume of 100 µL. 50 µL of each of the triplicate samples was then transferred to a fresh plate where the an equivalent volume of the detection reagent was added. The 96-well plate was then transferred to a GloMax Explorer plate reader (Promega) and luminescent readings were taken using a 0.5 second integration time. All data acquired from lactate Glo is expressed as a mean ± the column standard deviation. One-way ANOVA and Tukey's post hoc analysis was used to calculate statistical significance, where $p < 0.05$ is considered to be statistically significant.

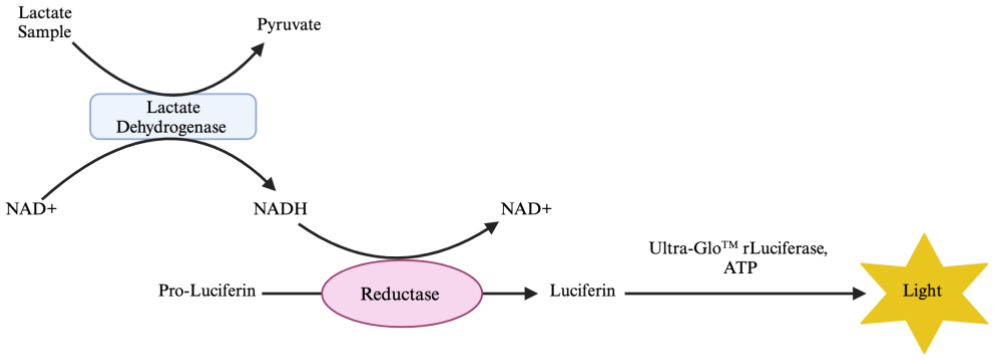

Figure 4.7 - Lactate-Glo assay. The assay involves incubation with lactate dehydrogenase to catalyse the conversion of lactate within the sample the pyruvate, leading to the concomitant reduction of NAD+ to NADH. In presences of NADH, Pro-luciferin, is then converted to luciferin which is further catalysed by rLuciferase, producing a stable light signal. The intensity of light signal is proportional to the l-lactate concentration of a given sample.

4.2.6 Live Dead Toxicity Assay

LIVE/DEAD assay was used to determine toxicity of deuterated compounds towards target cells. The general procedure for the LIVE/DEAD assay is described in the 'General Methods' chapter. For primary macrophages, primary CD14+ selected monocytes were seeded into a 96 well plate with 50,000 cells per well. Monocytes were then polarised to macrophages using the 6-day procedure. Cells were then incubated with 0, 0.25, 0.5 and 1.0 g/L of [6,6'-$^{2}H_2$]-glucose doped RPMI media for 24 hours. Following incubation cells were washed with PBS and treated with the calcien/EthD1 working solution and were left to incubate (30 mins, r.t). Cells were visualised using a GloMax® Explorer fluorescent plate reader using 475/550 nm excitation and emission filters for calcien readouts and 520/580 nm excitation and emission filters for EthD1. All data acquired from LIVE/DEAD assay is expressed as a mean ± the column standard deviation. One- or two- way ANOVA and Tukey's post hoc analysis was used to calculate statistical significance, where $p < 0.05$ is considered to be statistically significant.

4.3 Results

4.3.1 ^{2}H NMR Spectroscopy in Conventional 400 MHz Spectrometer

The first aim was to ascertain if downstream metabolites from macrophage culture with a deuterium labelled substrate could be detected by routine conventional NMR hardware. [6,6'-$^{2}H_2$]-glucose (deuterium glucose) was used as a substrate for all ^{2}H NMR experiments. The first optimisation experiments focused on visualising the metabolic profile of extracellular media from GBM cell lines. We selected two GBM cell lines, **G**lioma **IN**vasive margin 31 (GIN31) and U251. Detection at a clinical level using deuterium spectroscopy has shown glioblastoma to have a sufficient glycolytic metabolism to resolve deuterium labelled metabolites such as lactate.[162,170] Therefore, glioma cell lines are a rational starting point for optimisation experiments. Initial acquisitions were carried out using a conventional 400 MHz spectrometer using a 64-scan acquisition parameter. Extracellular media samples were taken from confluent GIN31 cells cultured in [6,6'-$^{2}H_2$]-glucose after 2 hours and 24 hours and visualised using ^{2}H-NMR spectroscopy. *Figure 4.8* below displays the initial ^{2}H spectra. Evidently, the expected [3,3'$^{2}H_2$]-lactate peak at 1.3 ppm is not distinguishable from background noise, suggesting that either there is not sufficient lactate within the sample or that a 64 scan acquisition does not offer sufficient signal to noise (SNR). SNR increases in proportion to the square root of number of scans. Therefore, increasing the number of scans from 64 to 1000 should increase the signal intensity by four-fold. However, there is an intrinsic trade of with increased signal averaging that scan time increases. To address lack of deuterium lactate signal within the GBM sample, cell samples were collected after 72 hours, to ensure highest concentration of lactate within spent media sample.

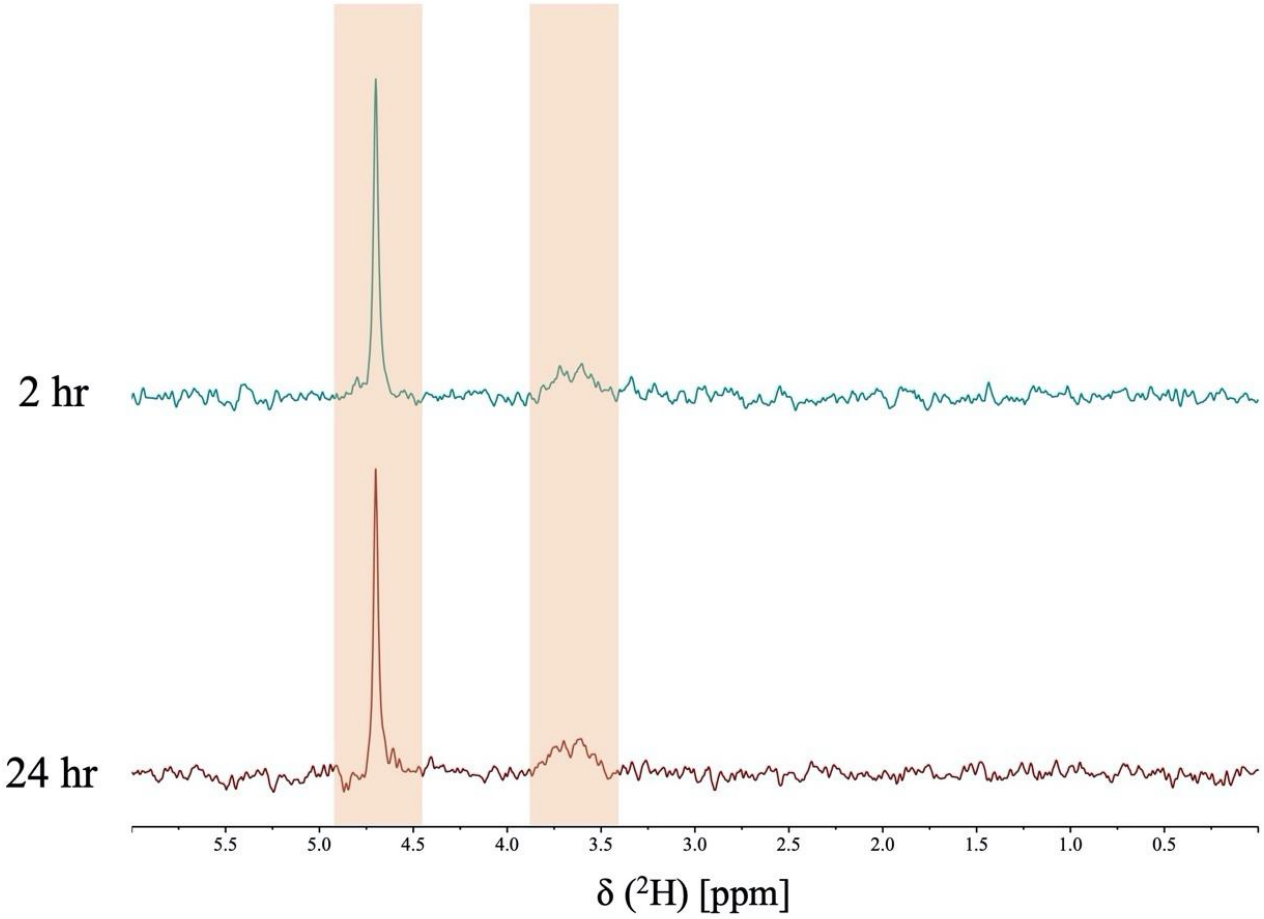

Figure 4.8 - Stacked 64-scan ^{2}H-NMR spectra of two GIN31 extracellular media samples at short (2 hrs, cyan) and long (24 hrs, red) time points. HDO resonance is highlighted at 4.7 ppm and [6,6'-$^{2}H_2$]-glucose at 3.7ppm. For both spectra there is no visible [3,3'$^{2}H_2$]-lactate peak visible above noise.

Following a 72 hour incubation period [6,6'-$^{2}H_2$]-glucose, extracellular media was extracted from GIN31 and visualised using ^{2}H-NMR spectroscopy. The [3,3'$^{2}H_2$]-lactate resonance at 1.3 ppm was visible within the extracellular sample. Equally, the broad [6,6'-$^{2}H_2$]-glucose resonance at 3.7 ppm was diminished, suggesting depletion of glucose by the GIN31 cells. *Figure 4.9* depicts the ^{2}H-NMR spectra of the GIN31 extracellular media with the single lactate resonance clearly visible above the noise at 1.3 ppm. Increasing both incubation time and the scan number to from 64 scans to 1000 scans at 400 MHz evidently improves signal to noise within the media samples, especially for the lactate resonance. The absence of an internal concentration reference in these experiments

makes absolute quantification of the [3,3'-$^2H_2$]-lactate sample challenging, but provides promising results for further studies.

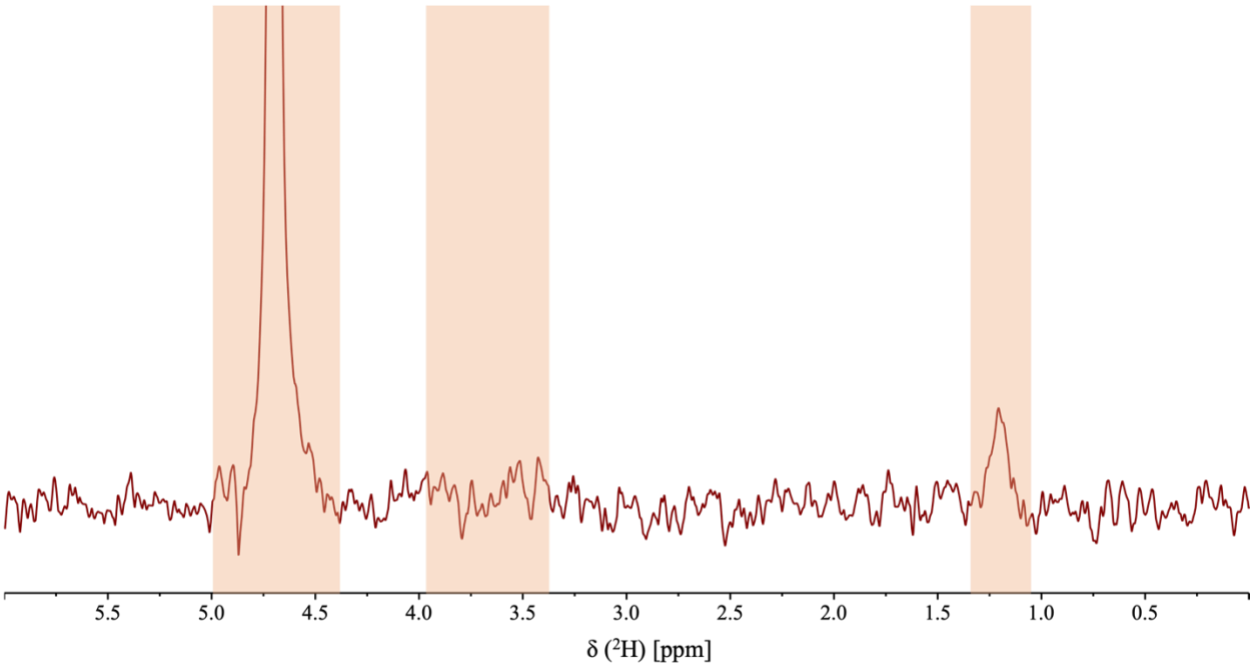

Figure 4.9 - 1000-scan 1D ^{2}H-NMR spectra of one GIN31 extracellular media samples at long (24 hrs) timepoint. HDO resonance is highlighted at 4.7 ppm and [6,6'-$^2H_2$]-glucose at 3.7 ppm and visible [3,3'-$^2H_2$] lactate peak at 1.3 ppm.

Optimisation with a glycolytic, cancer-based sample provided some key insights. Increased number of scans would allow for the best opportunity to detect the lactate resonance using the available 400 MHz NMR equipment. Carrying this understanding forward the next step was to test extracellular media samples from macrophage phenotypes. Given the acquisition time of a 1000 scan NMR is over 1 hour, 4 samples were generated and tested. M0 and M1 macrophages were generated from donor whole blood samples by magnetic activated cell sorting (MACS) positive selection of CD14 monocytes, followed by a 6-day polarisation procedure with cytokine stimulation. Following the six day polarisation procedure to M1 and M2 macrophages, spent media was replaced with [6,6'-$^2H_2$]-glucose containing RPMI media. Macrophages were left to incubate,

with extracellular media samples being collected at 2 and 24 hours. *Figure 4.10* depicts the spectral fingerprint of the M0 and M1 extracellular media samples collected at 2 and 24 hours. In line with the working hypothesis, the M1 phenotype displays a lactate resonance in the 24 hour sample.

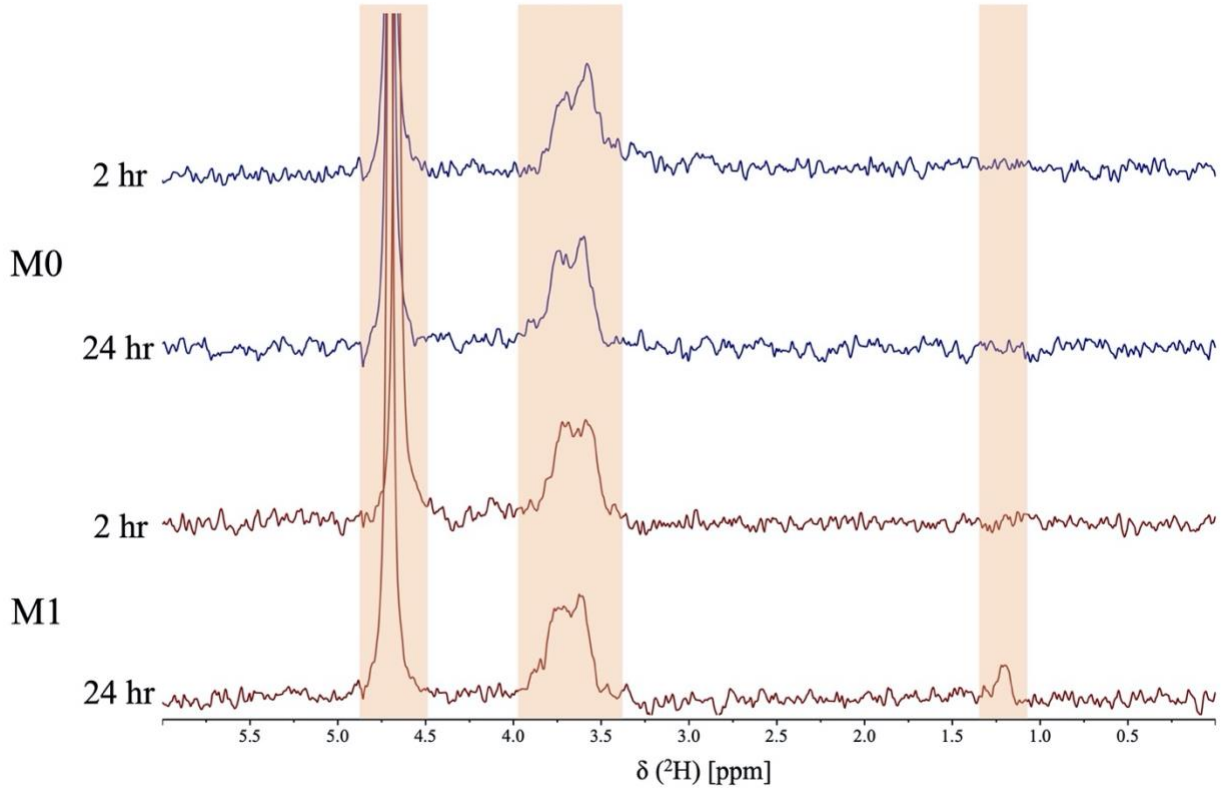

Figure 410 **–** Optimisation experiments with deuterium NMR, spectra were acquired using 1000 scans. Preliminary deuterium NMR time course for M0 (blue) and M1 (red) extracellular media samples with deuterium glucose. HDO resonance (4.7ppm), [6,6'-$^{2}H_2$]-glucose resonance (ppm) and [3,3'$^{2}H_2$] lactate (ppm) are highlighted in orange.

Figure 4.11 shows one representative data set from a total of 3 donors. Presence of extracellular lactate was consistently visible in the M1 subpopulation across 3 donors, further validating the potential of [3,3'$^{2}H_2$] lactate as an imaging marker for early stage proinflammatory M1 macrophages.

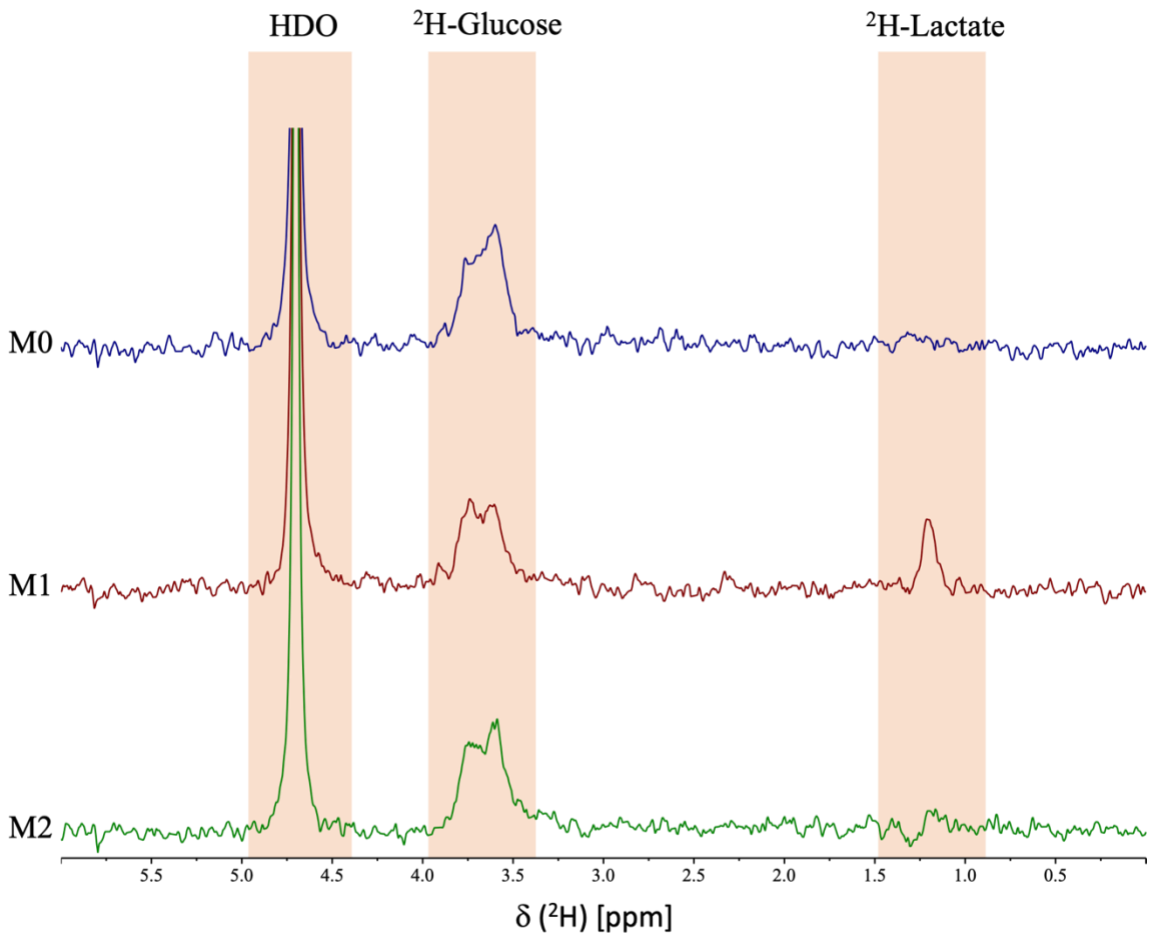

Figure 4.11 - Sample stacked spectra of initial NMR of extracellular media from macrophage phenotypes at 400 MHz acquired using 1000 scans. M0 (blue), M1 (green) and M2 (red) cell extracellular media samples were taken after 24 hrs incubation with [6,6'-$^2H_2$]-glucose. HDO resonance (4.7ppm), [6,6'-$^2H_2$]-glucose resonance (ppm) and [3,3'$^2H_2$] lactate (ppm) are highlighted in orange.

4.3.2 High Resolution ^{2}H-NMR of Macrophage Extracellular Media

Increasing magnetic field can greatly increase both sensitivity and resolution. 400 MHz translates to a 9.4 T MRI scanner. For reference, most clinical scanners are between 1.5 to 3 T, where MRI scanners rated at 7 T and above are denoted as "ultra-high field" and most common in preclinical studies, though human imaging systems are becoming more widespread. Notably, the University of Nottingham has recently been awarded the largest ever funding award to establish the United Kingdom's first 11.7 T human MRI scanner. Realistically, the field strengths achieved in conventional NMR hardware far exceed that of conventional MRI. SNR is influenced by numerous

factors, however fundamentally the largest improvement to SNR are found by either increasing signal intensity or reducing noise.

Considering the expression (1) below, the applied magnetic field (B_0) and number of scans are two variables that can be feasibly increased to improve SNR:

$$SNR \propto N\, A\, T_s^{-1}\, B_0^{\frac{3}{2}}\, \gamma^{\frac{5}{2}}\, T_{2*}\, (NS)^{\frac{1}{2}} \quad (1)$$

N number of molecules, **A** abundance of nuclide, **Ts** temperature of sample, $\boldsymbol{B_0}$ is applied magnetic field, **γ** is gyromagnetic ratio, $\mathbf{T_2^*}$ is transverse relaxation time and **NS** is number of scans.[284]

Following the same procedure as 400 MHz experiments, extracellular media from [6,6'-$^2H_2$]-glucose incubated M0, M1 and M2 macrophages was placed within an NMR tube and deuterium spectra was observed using 800 MHz ^{2}H NMR spectroscopy. To accurately quantify [3,3'$^2H_2$]-lactate concentration, pyrazine-d4 was used as an internal concentration and chemical shift reference. Pyrazine-d4 was added to each NMR experiment to give a final concentration of 5 mM. In order to acquire accurate quantitative data on deuterium metabolite concentrations, T_1 rates for each species should be determined. In general, the repetition time (TR) between successive excitation pulses should be at least 5 x T_1 to allow for sufficient relaxation time and avoid suppression of signal. The T_1 was determined by a T_1-inversion recovery experiment (see supplementary *figure 4.22*). 21 data points were taken and T_1 was determined by fitting magnetisation curve to equation 2:

$$M_z = M_0(1 - e^{-\frac{1}{T_1}}) \quad (2)$$

M_z is the longitudinal relaxation, M_0 is the equilibrium magnetisation, and T_1 is the longitudinal relaxation time.

Table 4.1 summarises the deuterium T_1 relaxation times for each of the molecules of interest.

Table 4.1 - Observed deuterium T1 relaxation times for different molecules of interest.

Species	^{2}H T_1 relaxation time (in seconds)
Pyrazine-d4	0.624
HDO	0.499
[6,6'$^2H_2$]-glucose	0.066
[3,3'$^2H_2$]-lactate	0.294

The quadrupolar moment of deuterium results in a relatively short T_1 relaxation times, which allow for higher rate of signal averaging leading to an increase in SNR. Consistent with the observed results with 400 MHz experiments, extracellular lactate was highest in the M1 samples. *Figure 4.12* shows a representative stacked spectra of macrophage subpopulation 24 hour extracellular ^{2}H NMR fingerprints, with the lactate resonance clearly visible in the red M1 spectrum.

When lactate abundance was quantified from each spectra, M1 macrophages displayed an average lactate concentration of 1.00 mM across three donors. This level was a statistically significant difference from M0 (0.00 mM, $p<0.001$) and M2 (0.37 mM, $P<0.01$) polarisation states. It is important to recognise that these values are calculated from extracellular media samples, meaning only lactate has been exported into extracellular space is being detected. Additionally, an additional caveat of note is that the lactate value for M0 does not imply that no lactate was present within the M0 sample, that rather an insufficient concentration of deuterated lactate was available to be detected within the sensitivity limits of high resolution ^{2}H NMR spectroscopy.

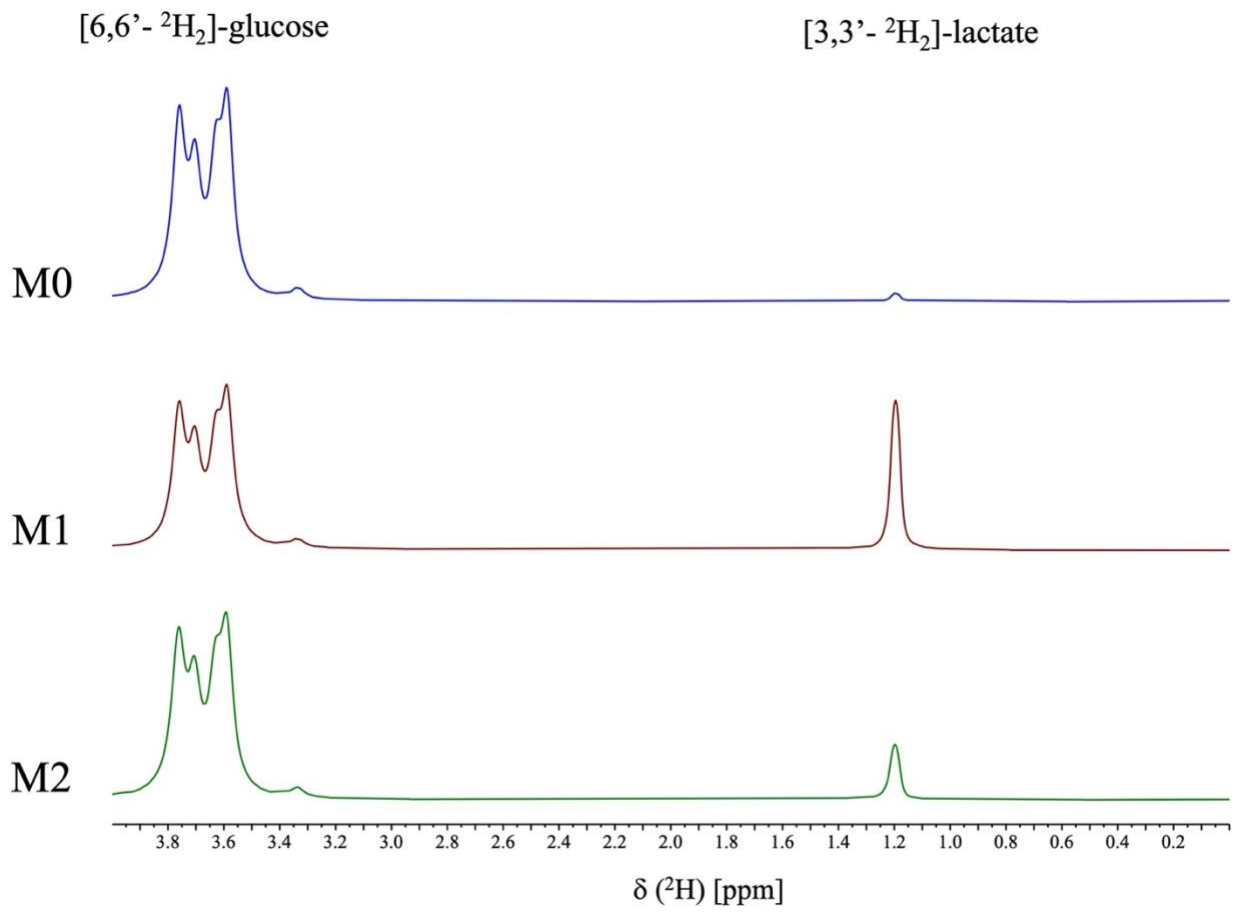

Figure 4.12 - Overview schematic of 800 MHz ^{2}H NMR spectroscopy with 8192 scans at 25 ºC of extracellular media with 5 mM pyrazine-d4. [3,3'-2H2]-lactate is visible in all samples at 1.19 ppm. The M1 sample (red) displayed the highest signal intensity for lactate.

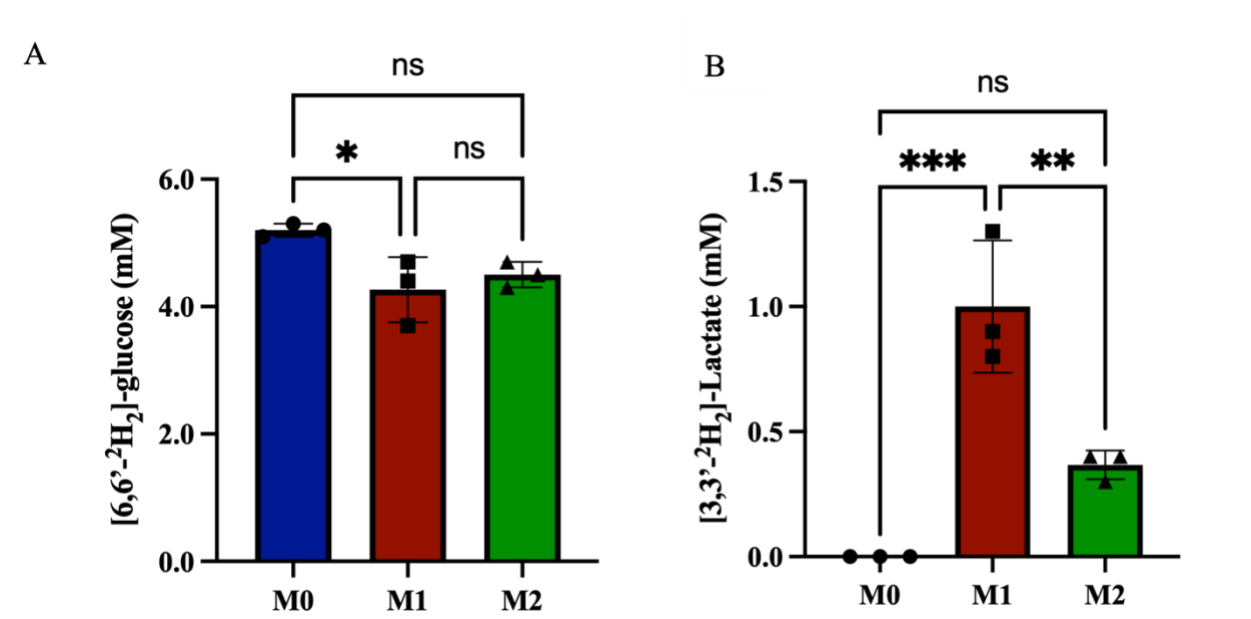

Figure 4.13 - A. Graph depicting deuterium glucose concentration in extracellular media of M0,M1 and M2 macrophages as determined by ^{2}H NMR spectroscopy. **B.** Graph depicting calculated deuterium lactate concentrations calculated from ^{2}H-NMR spectroscopy of macrophage extracellular media after 24 hours incubation with deuterium glucose from 3 donors. *p<0.05, **p<0.01, ***p<0.001, ***p<0.0001

Across three donors, the extracellular deuterium labelled lactate was consistently highest in the M1 extracellular media sample after a 24 hour incubation period with 1g/L deuterium glucose (5.5 mM). Deuterium lactate was increased in the M2 sample versus M0, although not significantly so. The mean concentrations of deuterium labelled compounds in extracellular media calculated from high resolution ^{2}H NMR is summarised in *table 4.2*. The concentration of deuterium labelled extracellular lactate present in M1 displayed a statistically significant difference from M0 and M2 subpopulations. The concentration of M1 extracellular lactate across 3 donors was, on average, 1.0 mM. M0 macrophages from the same donors showed no quantifiable concentration of deuterium lactate.

Table 4.2 **-** Mean concentration and standard deviation of molecules of interest in macrophage extracellular media after 24 hrs with deuterium glucose. Concentrations calculated from ^{2}H NMR experiments using 5mM pyrazine-d4 as an internal concentration reference. Spectra were processed and peaks were manually integrated. Integrals were then normalised to the pyrazine-d4 integral.

Macrophage	HDO (mM)	[6,6'$^{2}H_2$]-glucose (mM)	[3,3'$^{2}H_2$]-lactate (mM)
M0	16.73 (± 0.23)	5.20 (± 0.10)	0.0004
M1	17.53 (± 0.42)	4.27 (± 0.51)	1.00 (± 0.27)
M2	16.60 (± 0.40)	4.50 (± 0.20)	0.37 (± 0.06)

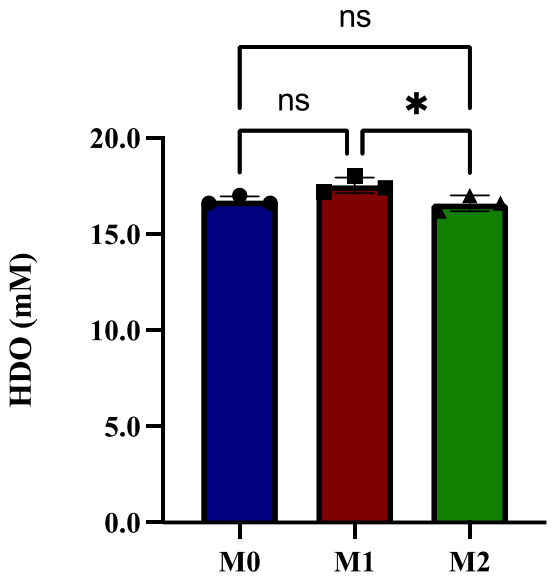

Figure 4.14 **-** HDO concentrations per macrophage subpopulation calculated from 2H NMR. *p<0.05, **p<0.01, ***p<0.001, ****p<0.0001

All subpopulations displayed relatively consistent HDO concentration within each sample. The highest HDO concentration was reported in the M1 subpopulations with a mean of 17.5 mM, whilst the lowest HDO concentration was from the M2 subpopulation with a mean of 16.6 mM. The difference in HDO concentration between M1 and M2 was statically significant, whereas the concentration HDO concentration between both M0 and M1 and M0 and M2 was non-significant. M2 macrophages display a metabolic shift towards fatty acid oxidation. Beta-oxidation, the metabolic process by which fatty acids are metabolised to generate ATP, is highly prevalent in M2 macrophages. The second step of beta-oxidation involves the enzyme enoyl-CoA hydratase, which

hydrates the double bond of enoyl-CoA isomers, resulting in turnover of water. This pathway could possibly account for lower HDO readouts in the M2 sample.

4.3.3 Real Time ^{2}H NMR Spectroscopy of Macrophage Polarisation States

Consistent with aim 'd' of the hypothesis, cell spectroscopy provides a better understanding of how deuterium glucose is processed and metabolised in real time. This is a far more representative approach than static sampling and has the potential to reveal clinically significant, albeit transient metabolites. In order to observe metabolism of deuterium glucose in real time, macrophage phenotypes were fabricated and polarised using a 6-day polarisation protocol. Cells were then detached via non-enzymatic detachment using TrypLE and washed. Deuterium glucose containing media was then added to cells and suspended within a sterilised NMR tube. The cell containing NMR tube was then transported to the 800 MHz NMR for analysis. Spectra were acquired using a continuous time course procedure for 22 hours at 37 ºC. *Figures 4.15, 4.16* and *4.17* display the results for live cell ^{2}H NMR spectroscopy for M0, M1 and M2 macrophages incubated with 1g/L deuterium glucose. M0 macrophages displayed a relatively slow rate of [6,6'-$^{2}H_2$]-glucose turnover towards [3,3'-$^{2}H_2$]-lactate. After 22 hours, M0 macrophages produced 1.50 mM of [3,3'-$^{2}H_2$]-lactate. Live ^{2}H NMR spectroscopy of M1 macrophages, visualised in *figure 4.14*, revealed a relatively rapid rate of glucose turnover, coupled with a high rate of lactate production. After 22 hrs, M1 macrophages produced 3.25 mM of [3,3'-$^{2}H_2$]-lactate and consumed 3.69 mM of [6,6'-$^{2}H_2$]-glucose.

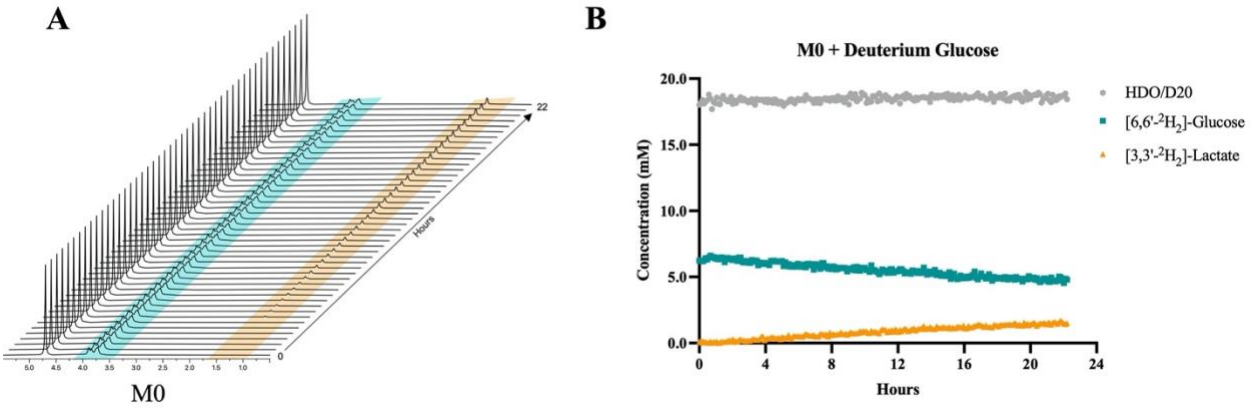

Figure 4.15 - Real-time deuterium NMR spectroscopy time-course of 5 million M0 macrophages incubated with [6,6'-$^2H_2$]-glucose. **A.** stacked decimated spectra displaying every 5th deuterium spectrum. Data was acquired over a 22 hour period at 37ºC at 5min intervals, giving a total of 232 spectra. Blue highlighted region corresponds to the [6,6'-$^2H_2$]-glucose resonance. Orange highlighted region corresponds to the [3,3'-$^2H_2$]-lactate resonance. **B.** Graph depicting concentrations of deuterium resonances over 22 hour time-course. Concentrations were calculated using internal concentration standard, pyrazine-d4. Grey plotted datapoints correspond to HDO/D_2O relative concentration, Blue plotted values correspond to [6,6'-$^2H_2$]-glucose relative concentration and orange plotted values correspond to [3,3'-$^2H_2$]-lactate relative concentration.

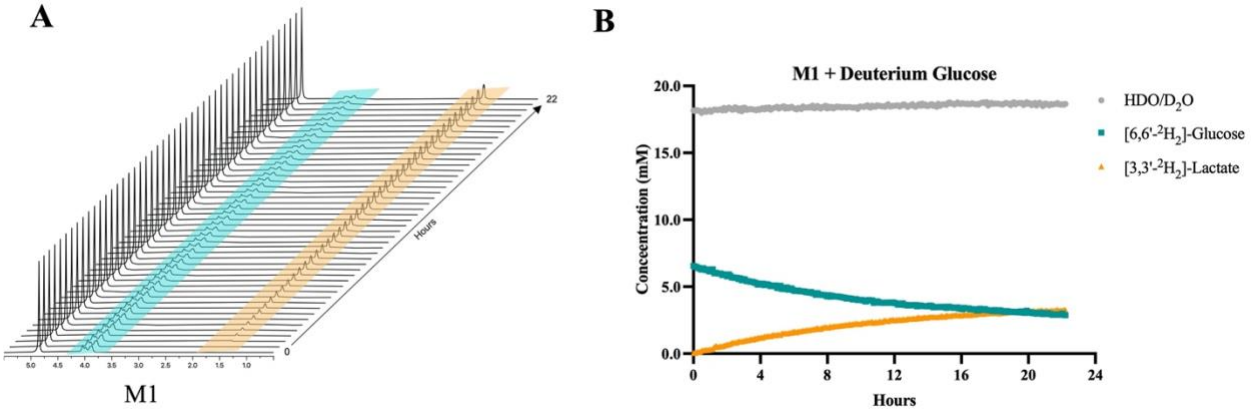

Figure 4.16 - Real-time deuterium NMR spectroscopy time-course of 5 million M1 macrophages incubated with [6,6'-$^2H_2$]-glucose. **A.** stacked decimated spectra displaying every 5th deuterium spectrum. Data was acquired over a 22 hour period at 37ºC at 5min intervals, giving a total of 232 spectra. Blue highlighted region corresponds to the [6,6'-$^2H_2$]-glucose resonance. Orange highlighted region corresponds to the [3,3'-$^2H_2$]-lactate resonance. **B.** Graph depicting concentrations of deuterium resonances over 22 hour time-course. Concentrations were calculated using internal concentration standard, pyrazine-d4. Grey plotted datapoints correspond to HDO/D2O relative concentration, Blue plotted values correspond to [6,6'-$^2H_2$]-glucose relative concentration and orange plotted values correspond to [3,3'-$^2H_2$]-lactate relative concentration.

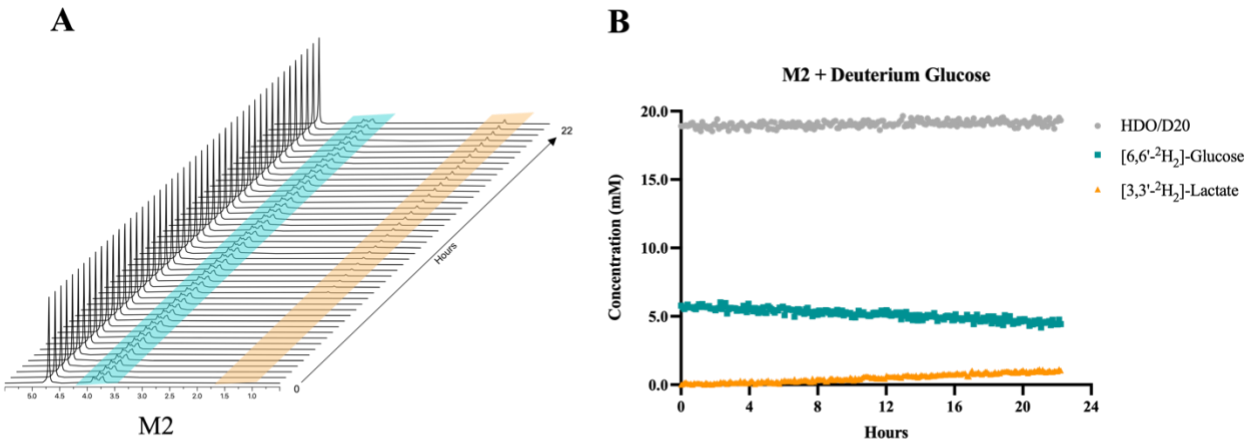

Figure 4.17 - Real-time deuterium NMR spectroscopy time-course of 5 million M2 macrophages incubated with [6,6'-$^2H_2$]-glucose. **A.** stacked decimated spectra displaying every 5th deuterium spectrum. Data was acquired over a 22 hour period at 37^{o}C at 5min intervals, giving a total of 232 spectra. Blue highlighted region corresponds to the [6,6'-$^2H_2$]-glucose resonance. Orange highlighted region corresponds to the [3,3'-$^2H_2$]-lactate resonance. **B.** Graph depicting concentrations of deuterium resonances over 22 hour time-course. Concentrations were calculated using internal concentration standard, pyrazine-d4. Grey plotted datapoints correspond to HDO/D2O relative concentration, Blue plotted values correspond to [6,6'-$^2H_2$]-glucose relative concentration and orange plotted values correspond to [3,3'-$^2H_2$]-lactate relative concentration.

The M2 subpopulation showed a decreased rate of [3,3-$^2H_2$]-lactate production, by comparison to the M1 subpopulation over 22 hours. Equally glucose turnover was diminished. The subpopulation with the fastest rate of glucose turnover was M1. The subpopulation with the fastest rate of lactate production was M1, followed by M2.

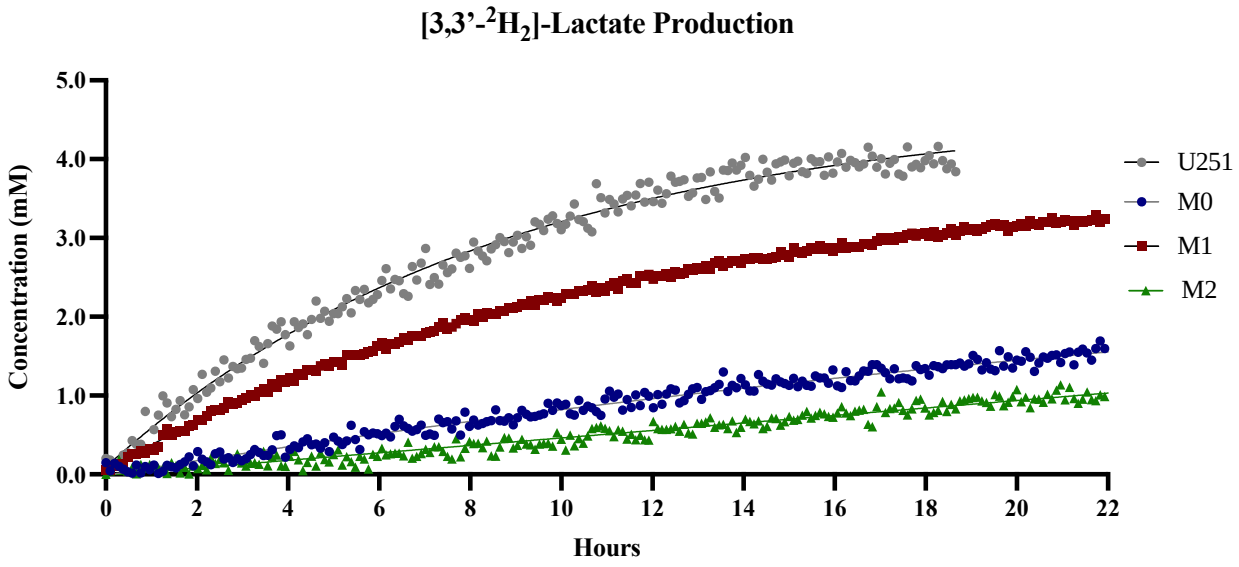

Figure 4.18 **-** Graph depicting production of deuterium lactate in glioblastoma and macrophage polarisation states. Grey plotted datapoints correspond to U251 (glioblastoma), blue plotted data points to M0, red plotted datapoints to M1 and green plotted datapoints to M2 macrophages. Curves were fit by a one phase association non-linear regression model.

Given that most deuterium based approaches at *in vivo* level are focused on visualising brain tumour metabolism such as glioblastoma, U251 makes for a useful comparison. *Figure 4.18* displays the overall production of [3,3-$^2H_2$]-lactate over 4 cell time courses, for the three macrophage polarisation states and U251. Unfortunately, due to spectrometer malfunction, the entirety of the U251 time course could not be collected beyond 18 hours. However, as expected, U251 displays the fastest rate of lactate production.

4.3.4 Luminescent confirmation of lactate presence in extracellular media samples.

Following detection of deuterium-lactate in extracellular media samples using ^{2}H-NMR spectroscopy, extracellular lactate presence was further confirmed using an *in vitro* luminescent lactate assay. The Lactate-Glo assay is a luminescence based assay used to cross validate lactate production in blood derived macrophage subpopulations. A total of three donors were used to generate macrophage subpopulations and investigate lactate production. Cells were seeded at a concentration of 1mn/cells per mL and polarised over a 6 day period. After day 6, cells were

incubated with deuterium glucose media and left to incubate for 24 hours. The Lactate-Glo assay was then used to verify relative lactate production in different macrophage subpopulations. Across three different donors, the M1 subpopulation consistently displayed the highest lactate concentration in extracellular media relative to other macrophage polarisation states. *Figure 4.19* depicts the results for the lactate glo assay for three donors. For each donor an ordinary one-way ANOVA test with a post-hoc Tukey's multiple comparison test was carried out. Across three donors, two exhibited an increase lactate concentration for the M1 polarisation state versus M0 and M2. 'Donor 2' exhibited no significant difference between lactate in samples for M0, M1 and M2. Overall donor 1 displayed the highest lactate secretion for the M1 subpopulation, with an average of 60,900 RL, corresponding to 1.86 µM lactate per 5000 cells. Similar trends were observed in donor 3, both displaying relatively increased lactate secretion relative to the M0 and M2 subpopulations from the same donor. Donor 2 displayed no significant differences in lactate secretion between any of the subpopulations. Differences observed could be accounted for by donor-to-donor variability.

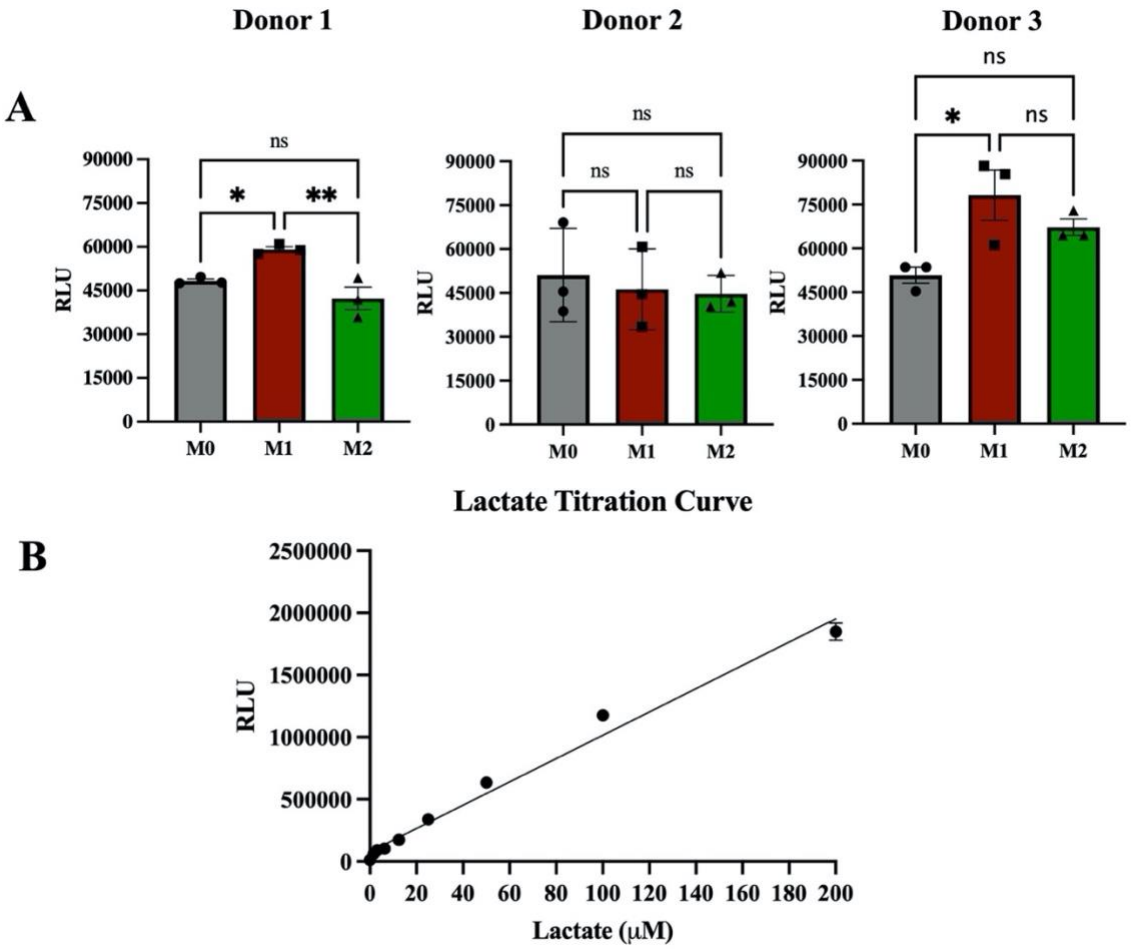

Figure 4.19 - Lactate Glo assay data from 3 donors. **A**. Graphs depicting relative intensity of lactate luminescent readouts. **B**. Standard curve for known lactate concentrations using the Lactate-Glo assay. Known lactate concentrations were plated in triplicate and incubated with lactate glo working solution. A simple linear regression test was used to determine the line of best fit, giving the equation y=(9369)x + 78292. *p<0.05, **p<0.01, ***p<0.001, ****p<0.0001

4.3.5 Deuterium Glucose Toxicity Towards Macrophages

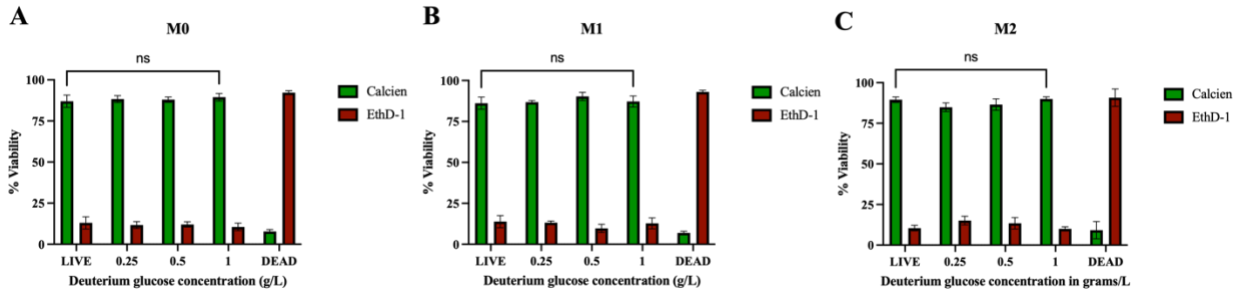

Figure 4.20 - Toxicity data for deuterium glucose dosing of macrophage polarisations states after 24 hrs incubation. Bar chart depicting a live control, 0.25, 0.5, 1.0 g/L glucose and dead control (100% EthOH), Green corresponds to live cell population calculated from calcien-AM staining. Red corresponds to dead cell populations calculated from ethidium-dimer staining. **A.** M0 macrophages **B.** M1 macrophages **C**. M2 macrophages ns>0.05, *p<0.05, **p<0.01, ***p<0.001, ****p<0.0001

Deuterium oxide is lethal when total body water is enriched by 30-40%.[163,285]This highlights some concerns for its safe application to clinical study. In order to test toxicity of deuterium glucose towards macrophage polarisations states, a LIVE/DEAD assay was used. LIVE/DEAD assay revealed no significant differences in cell viability across all labelling concentrations with deuterium glucose for all macrophage polarisation states. Dead controls were treated with 100% ethanol for 30 mins at room temperature 92.2, 93.0 and 90.81% average dead cells for M0, M1 and M2 subpopulations respectively. The percentage of dead cells for each of labelling conditions showed no significant difference between live control and conditions with deuterium glucose up to 1.0 g/L.

4.4 Discussion

There are a limited number of metabolic imaging approaches available that can visualise metabolism non-invasively in real time. There are even fewer metabolic imaging approaches that specifically target inflammatory processes and, to date, only one has employed deuterium as a labelling probe.[286] The present chapter has demonstrated a proof-of-concept platform for assessing macrophage polarisation state via ^{2}H NMR spectroscopy. Metabolism of [6,6' $^{2}H_2$]-glucose substrate by both GBM and macrophages was successfully visualised using a combination of conventional and high resolution NMR systems. ^{2}H NMR data from this chapter demonstrates that deuterium-labelled compounds can serve as powerful, translational tools for inflammatory imaging applications. This work provides a basis of understanding for further translation of these approaches to *in vivo* level applications.

Lactate represents one of the most common biomarkers for injury and dysregulated metabolism and, being heavily implicated in many disease types, makes it a highly attractive imaging target for metabolic imaging. Previous studies have demonstrated that lactate can reliably be detected in using stable isotope metabolic imaging approaches including ^{13}C, ^{15}N and ^{2}H MRS.[48,162,259] Evidently, Qiao *et al* demonstrate the use of hyperpolarised ^{13}C-pyruvate MRS to distinguish between macrophage populations, where [1-^{13}C]-lactate was produced at greater concentrations in the M1 polarisations state.[48] However there are several limitations to this study, chiefly the use of hyperpolarisation to achieve sufficient SNR. Practically, dynamic nuclear polarisation has limited clinical scope due to the technically demanding procedures to achieve hyperpolarisation of substrates. In addition, hyperpolarised substrates have an extremely short window in which they remain hyperpolarised, and therefore suitable for detection. This means that introduction of

substrates to cells and then spectrum acquisition occurs within a 5 minute timeframe. Furthermore, metabolic activity following a rapid media change could potentially misrepresent overall cell metabolism. The same study also used a high density of cells, 100,000 cells per µL, which could potentially contribute to increased glycolytic environment within the sample. Whilst the results from the Qiao *et al* study are promising to suggest that ^{13}C DNP MRS can be used to distinguish between macrophage phenotypes, they do also highlight the challenging aspects of developing metabolic imaging approaches, especially when targeting macrophages. A once overlooked approach, in recent years deuterium metabolic imaging has been rapidly developed. Deuterium metabolic imaging offers a multifaceted alternative to PET and ^{13}C MRS.

4.4.1 Deuterium Glucose MRS Could Serve as a Potential Diagnostic Tool for Identifying Macrophage Polarisation States

Aim 'a' of the hypothesis testing was to investigate the spectroscopic detection limits of conventional NMR systems for carrying out deuterium NMR spectroscopy on cell based samples. Using conventional 400 MHz NMR spectroscopy, we successfully detected deuterium labelled lactate in both glioblastoma and M1 macrophage extracellular media samples. There are a few technical limitations to detecting deuterium labelled metabolites via NMR spectroscopy. Firstly deuterium NMR spectroscopy has several inherent limitations with respect to sensitivity when compared to proton NMR spectroscopy, which makes signal acquisition challenging. Sensitivity of deuterium NMR spectroscopy is severely dampened by the gyromagnetic ratio of deuterium, which is roughly 6.5 fold less than hydrogen. This is marginally compensated by deuterium's larger spin quantum number of 1 to the ½ of hydrogen.[163] Another technical limitation of deuterium NMR spectroscopy is that deuterium has extremely short T_1 and T_2 relaxation times. The short T_2 relaxation time contributes to the broader resonances observed in deuterium spectra. However,

short T_1 times can be advantageous, especially at a clinical level. A shorter T_1 relaxation time, relative to hydrogen, allows for an increased rate of radiofrequency pulse, improving scan efficiency. Most of these sensitivity issues a can be dealt with through using increased magnetic fields.[129,287]

These sensitivity limitations meant that there were acquisition parameter compromises in order to detect deuterium labelled metabolites with appropriate SNR. The first system tested was the conventional NMR spectroscopy system at 400 MHz, where static extracellular media samples were analysed. Poor SNR on the 64 scan acquisitions meant an increase in scan number and therefore acquisition time was required to achieve sufficient SNR. Increasing the number of scans to 1000 per sample achieved appropriate SNR, with a compromise on acquisition time. This made experimentation using the 400 MHz NMR spectrometer inefficient, especially given most experimental findings would feed into process optimisation. Beyond acquisition time, there were additional experimental limitations to testing using conventional NMR spectroscopy. The initial samples tested were extracellular media samples from discrete time points. This limitation meant that total lactate from a sample was not being tested, such as intracellular lactate. Determining an appropriate sampling timepoint was especially technically challenging, as acquisition constraints to achieve sufficient SNR meant precious equipment time had to be used as efficiently as possible. Furthermore, these initial samples lacked an internal concentration reference, which makes absolute quantification not possible. Equally, dynamic real time information could not be generated, as the time to achieve appropriate transients was too high to justify real time acquisition. All of the requirements described by Polvoy *et al* are addressed through assessment with conventional NMR spectroscopy, however increasing the field strength, allows for much better SNR, and shorter acquisition times.

Thus, carrying sample testing forward to an 800 MHz NMR spectrometer system meant that there was no longer acquisition scan number compromise to achieve sufficient SNR.

4.4.2 High Resolution NMR Spectroscopy on Extracellular Samples

Testing of discrete time points using an 800 MHz NMR spectrometer facilitated quantification via use of an internal concentration reference, pyrazine-d4. Again, consistent with findings at lower field, M1 was the sample with the highest lactate concentration after 24 hour incubation with [6,6'-$^{2}H_{2}$]-glucose. The studies also revealed that lactate was present at detectable levels in the M2 sample. Quantitative NMR spectrometry could also reveal differences in HDO concentration between samples. HDO labelling concentration has previously been used as a marker for quantifying Warburg-like metabolism.[288] ^{2}H NMR spectroscopy data revealed a significant difference between HDO concentration in M1 and M2 extracellular samples. The M2 samples displayed a lower HDO concentration relative to the M1 subpopulation, which could potentially indicate turnover. This would be consistent with M2 being more dependent on OXPHOS for ATP generation, a process which involves uptake of water in enoyl-CoA hydratase catalysed reactions. Conversely, HDO may be higher in M1 samples due to an increased rate of glucose turnover as the deuterium label of downstream deuterium-pyruvate and deuterium-lactate are more likely to exchange with protons from solvent water.[289] This further indicates three different parameters, glucose consumption, lactate production and HDO turnover could be monitored to facilitate distinction of macrophage polarisation states.

4.4.3 Live Cell ^{2}H NMR Spectroscopy

Aim 'd' of the hypothesis testing was to investigate application of deuterium glucose - ^{2}H NMR spectroscopy with live cell spectroscopy. The rationale for investigating live cell spectroscopy is twofold. It allows for the detection of short-lived metabolic intermediates, potentially not visible

in discrete ‘static’ samples. As most metabolic imaging in patients is time sensitive, live cell NMR spectroscopy also allows for determination of potentially clinically significant timescales for imaging and provides a better understanding of how quickly substrates are turned over, informing probe administration.

Developing a better understanding of imaging timescales can help improve imaging efficiency. Understanding of imaging individual cell populations helps to build a better picture of the individual cell-based dynamics. For the most part, the work carried out in this chapter is designed to test proof of concept for further metabolic imaging questions. It provides a testing platform to interrogate the application of novel deuterium labelled probes to inflammatory imaging applications. Ever increasing hardware developments with high magnetic field scanners, such as those seen at Nottingham, opens the door to high resolution spectroscopy being available at clinical level. Thus, testing probes at high resolution is important for future clinical development. Live cell spectroscopy revealed metabolic turnover of deuterium glucose in real time for both U251 GBM and macrophage polarisation states.

There are certainly limitations to the experimental approaches employed within this thesis with respect to live cell spectroscopy. The first obvious limitation is that the NMR tube is not continuously oxygen perfused throughout the experiment, meaning that oxygen availability is limited to the head space within the NMR tube. This could be addressed by using an oxygen perfusion line directly into the NMR tube, which appropriately cycles oxygen and waste gases through the sample. Another limitation is sedimentation rate of cells. Macrophages are highly adherent cells and over a period of hours, they begin to sediment and form a pellet within their environment. Over time, the physical characteristics of the sample change from a relatively homogenous colloidal-like sample to a biphasic sample. Additionally, there was a time gap

between sample preparation and data acquisition due to sample transport between buildings. In an idealised set up, the sample would be perfused with deuterated glucose *in situ* to avoid data loss. Additionally, the sample size for each cell populations presented in the live cell study is 1. More live cell samples from different donors would be required in order to achieve more representative data. One further consideration is the effect that deuteration has on cell metabolism. Deuterium has twice the mass of hydrogen, meaning that the C-D has a far smaller zero-point energy and frequency vibration than that of a C-H bond. The C-D bond, as a result, displays a greater bond dissociation energy than C-H bond. From a kinetics perspective, deuterium labelled compounds aid detection of rate limiting steps and reaction transition states.[290] However, in general the kinetic isotope effect leads to a reduction in metabolic activity of deuterated compounds. In turn, this could mean uptake and turnover of deuterium substrates is not necessarily representative of metabolism within a given tissue.

4.4.4 What are the Potential Applications of Glucose Metabolic Imaging Especially Within the Context of Inflammation?

An additional concern is probe delivery. Delivering sufficient amount of probe to a region of interest is not a unique problem to metabolic probes, however systematic delivery will result in a high level of non-specific uptake, especially in glucose privileged organs such as brain and cardiac tissue.

Considering that the vast majority of applications for deuterium metabolic imaging are likely cancer related, it is foreseeable that distinction between glycolytic immune cells and cancer cells would be challenging. However, deuterium metabolic imaging using glucose probes is not limited to cancer alone. The current standard for evaluating post-transplant complications, including host graft rejection is tissue biopsy and ultrasound doppler.[291] Renal imaging could serve as an imaging

target for deuterium based probes such as [6,6'-$^{2}H_2$]-glucose, especially given the implication of proinflammatory macrophage response to foreign bodies including transplants. Gadolinium-based contrast agent approaches are contraindicated in patients with renal impairment, limiting the available options for contrast-enhanced MRI. Another application could see the incorporation of deuterium labelled endogenous compound into biomaterial implant coatings, to map surface degradation.

4.4.5 Alternative Probes?

This study exclusively focused on using [6,6'-$^{2}H_2$]-glucose as a probe for visualising macrophage polarisation. Although [6,6'-$^{2}H_2$]-glucose is the most extensively studied probe at a clinical level, there are numerous commercially available deuterated exogenous compounds available that could be appropriate substrates for targeting the metabolic niche. [$^{2}H_3$] acetate has been used to target the TCA cycle and lipogenesis in glioblastoma patients.[259,273] [$^{2}H_9$] choline is another such probe that has been investigated, with applications for renal metabolic studies.[292–294] Choline is an essential nutrient for macrophages, and IL-4 stimulation of macrophages upregulates the expression of choline transporter-like protein 1.[295] Interestingly, inhibition of choline receptors M1 like macrophage polarisations state. This makes [$^{2}H_9$] choline an interesting substrate for deuterium NMR spectroscopy.

4.4.6 Multimodal Probes

Glucose analogues have been previously demonstrated as viable targeting moieties for M1-selective macrophage fluorescent imaging. Cho *et al*., designed a panel of glucosamine based luminescent probes, designed to exploit increased carbohydrate uptake in GLUT1+ M1 macrophages.[44] Similar probes have been designed for tumour targeting applications.[296] Given that the glucosamine backbone, is related to glucose, with the exception of an amide on the 2nd carbon,

probes such as these could potentially be deuterated to achieve a fluorescent/MRI active probe. Equally fluorescent deoxyglucose analogues, such as 2-NBDG have been developed in an attempt to target GLUT1 transporters in E.coli.[297] Interestingly, unlike other deoxyglucose probes, 2-NBDG undergoes further downstream metabolism, until being decomposed into non-fluorescent analogues.

In summary, macrophage polarisation states were identified as having distinct metabolic profiles that could be targeted for distinction by metabolic imaging. Deuterium metabolic imaging was selected as a metabolic imaging approach capable of resolving the downstream glycolytic metabolites that characterise M1 metabolism. Through *in vitro* ^{2}H NMR experiments carried out throughout this chapter, deuterium MRS with deuterium labelled glucose, can identify the high glycolytic niche of M1 macrophages. To conclude, deuterium glucose has been demonstrated to be a suitable probe at a proof of concept level for distinguishing macrophage polarisation states using both conventional and high resolution NMR spectroscopy. The work carried out in this chapter lays the foundations for future deuterium metabolic investigations of inflammation to be carried out at *in vivo* level.

4.5 Supplementary

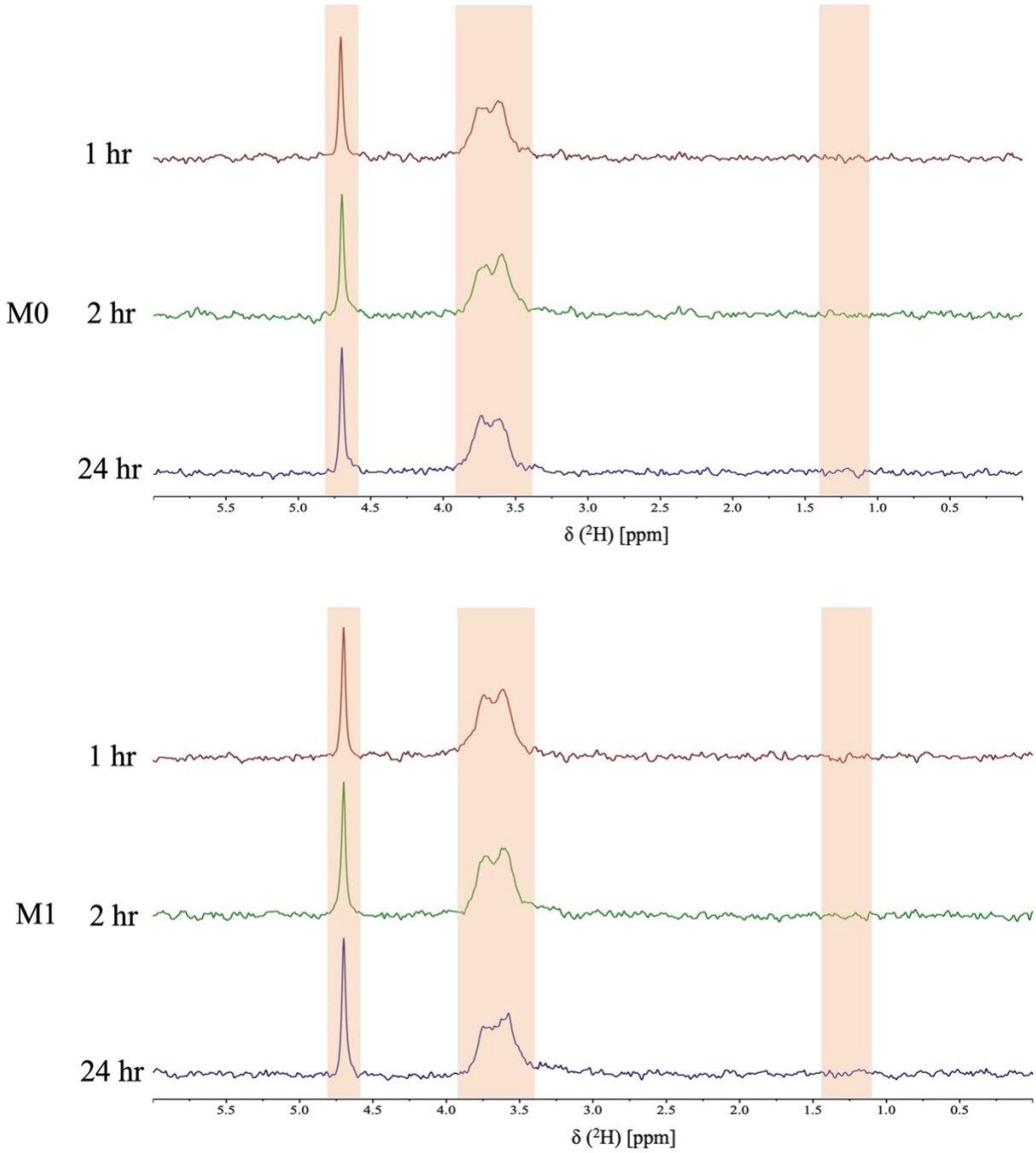

Figure 4.21 **-** Optimisation experiments with deuterium NMR, spectra were acquired using 64 scans. Preliminary deuterium NMR time course for M0 and M1 macrophage extracellular media with deuterium glucose at 1 hrs (red), 2 hrs (green) and 24 hrs (blue) . HDO resonance (4.7ppm), [6,6'-$^{2}H_2$]-glucose resonance (ppm) and [3,3'$^{2}H_2$] lactate (ppm) are highlighted in orange.

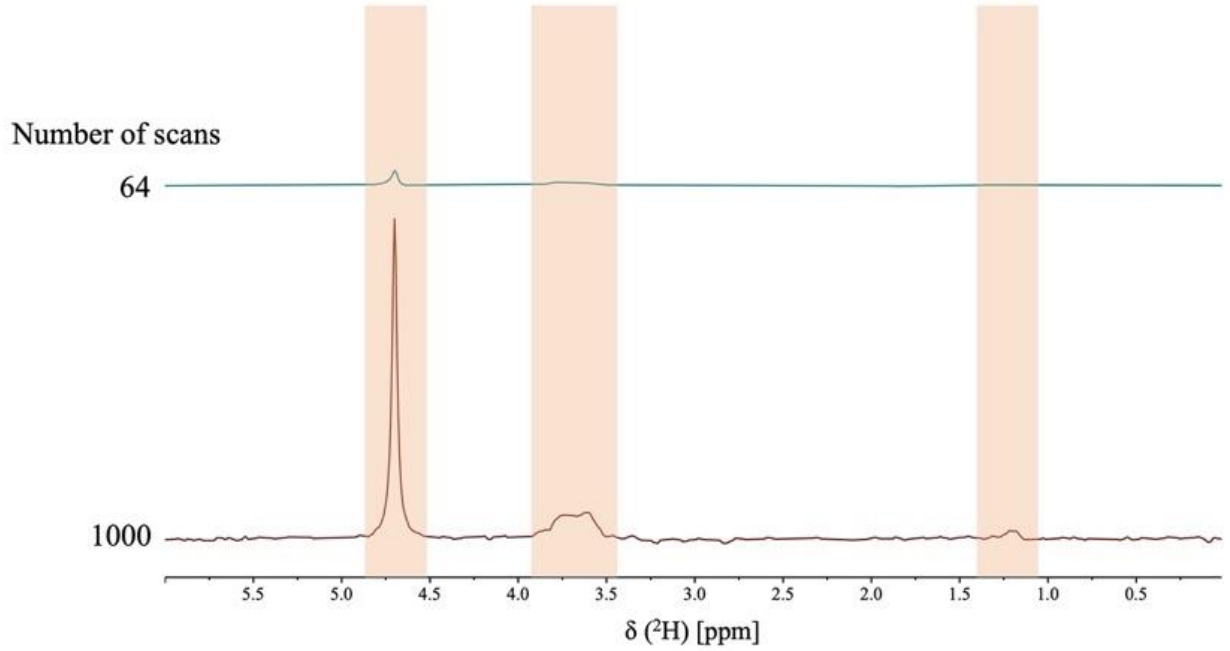

Figure 4.22- Stacked spectra of 64 scan vs 1000 scans ^{2}H NMR at 400 MHz.

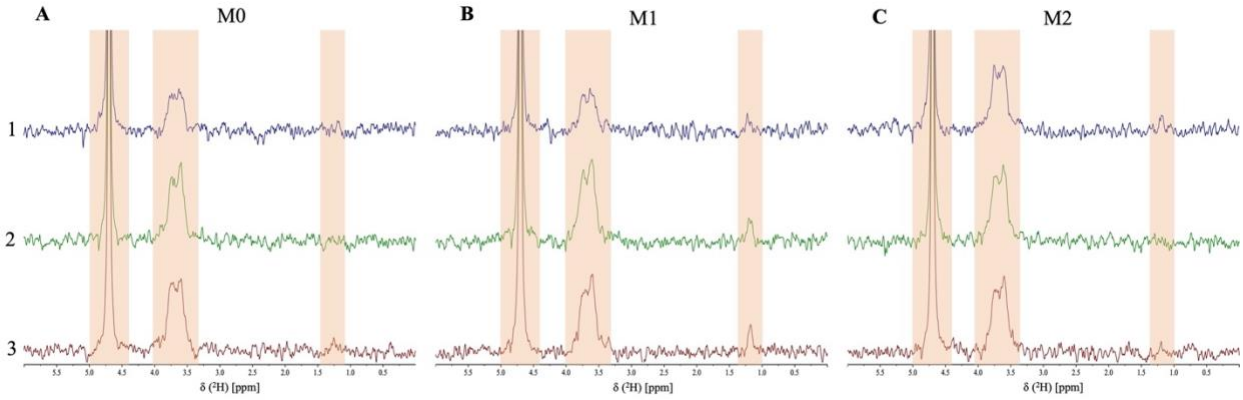

***Figure 4.2*3 -** Sample stacked spectra of initial NMR of extracellular media from macrophage phenotypes at 400 MHz acquired using 1000 scans) cell extracellular media samples were taken after 24 hrs incubation with [6,6'-$^{2}H_2$]-glucose. HDO resonance (4.7ppm), [6,6'-$^{2}H_2$]-glucose resonance (ppm) and [3,3'$^{2}H_2$] lactate (ppm) are highlighted in orange. **A.** M0 extracellular media sample from 3 separate donors at 24 hr post [6,6'-$^{2}H_2$]-glucose incubation. **B.** M1 extracellular media sample from 3 separate donors at 24 hr post [6,6'-$^{2}H_2$]-glucose incubation. **C.** M2 extracellular media sample from 3 separate donors at 24 hr post [6,6'-$^{2}H_2$]-glucose incubation.

Longitudinal Relaxation Time (T_1) Measurements

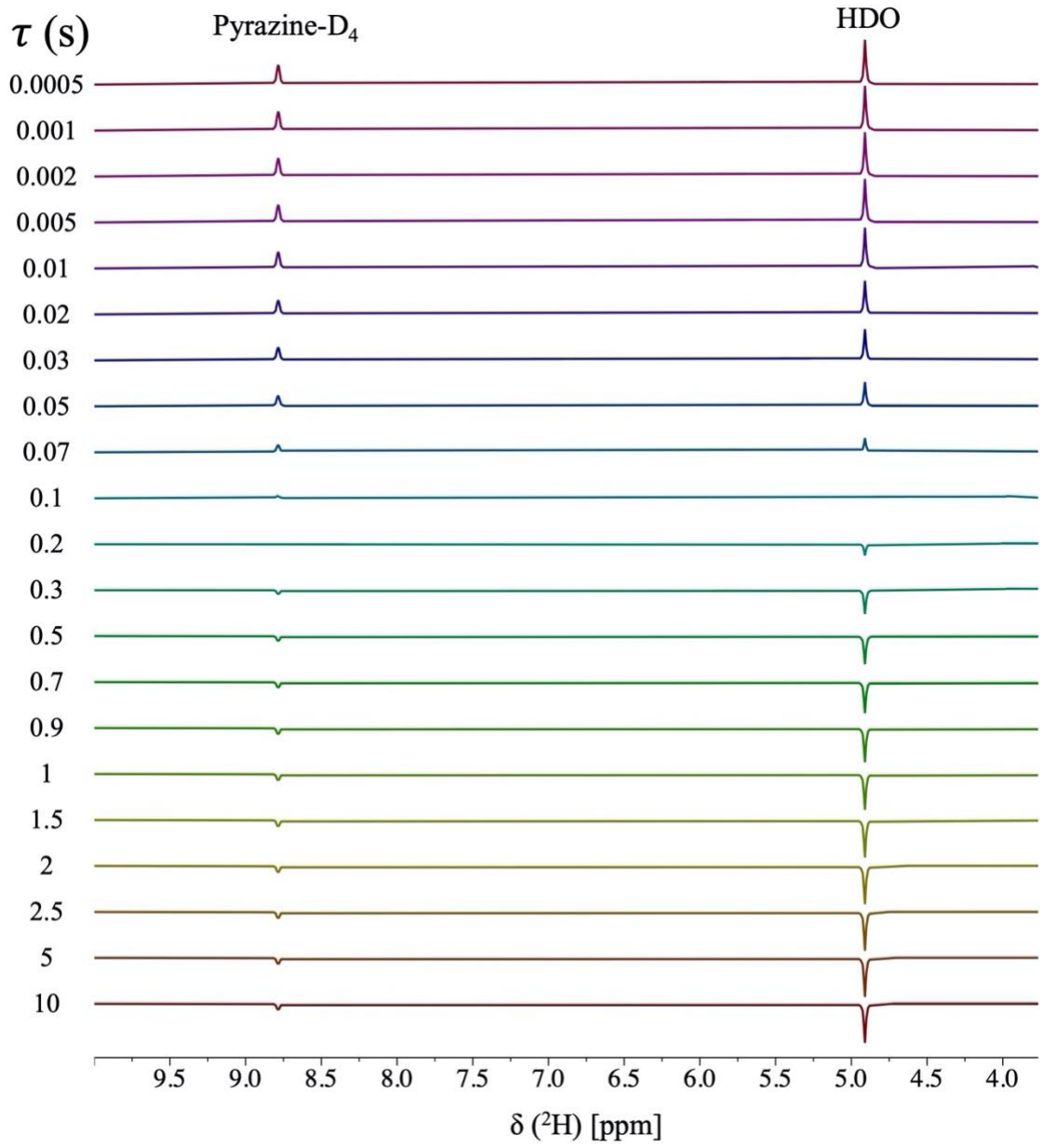

Figure 4.24 - Stacked spectra plot of ^{2}H-NMR T1 inversion recovery visualising both the pyrazine-D_4 and HDO resonance peaks. The T1 relaxation time for HDO was calculated as 0.499s. For pyrazine-D4 the T1 time was calculated as 0.624s. 21 inversion recovery delays (τ) were used carry out the T1 inversion recovery experiments, are denoted next to their respective spectra.

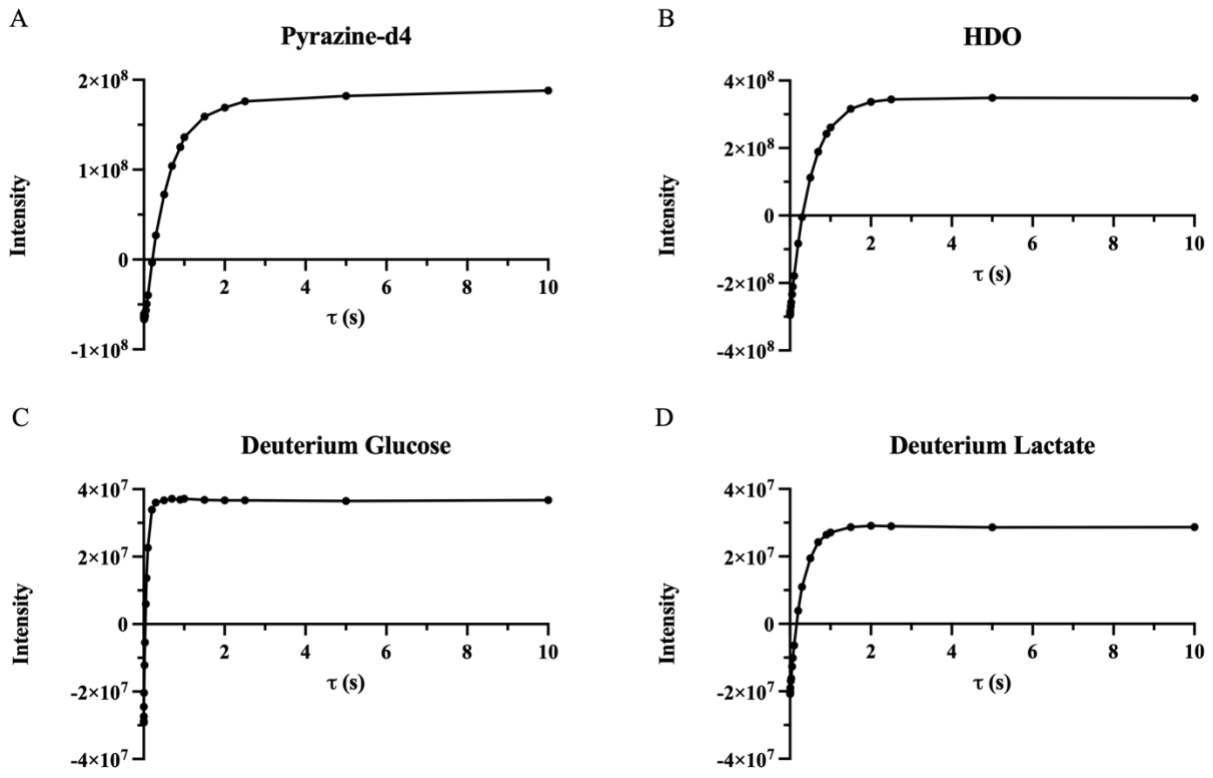

Figure 4.25 – T_1 inversion recovery plots for peaks of interest. **A.** T_1 inversion recovery plot for pyrazine-d4 **B.** T_1 inversion recovery plot for HDO **C.** T_1 inversion recovery plots for deuterium glucose **D.** T_1 inversion recovery plots for deuterium lactate

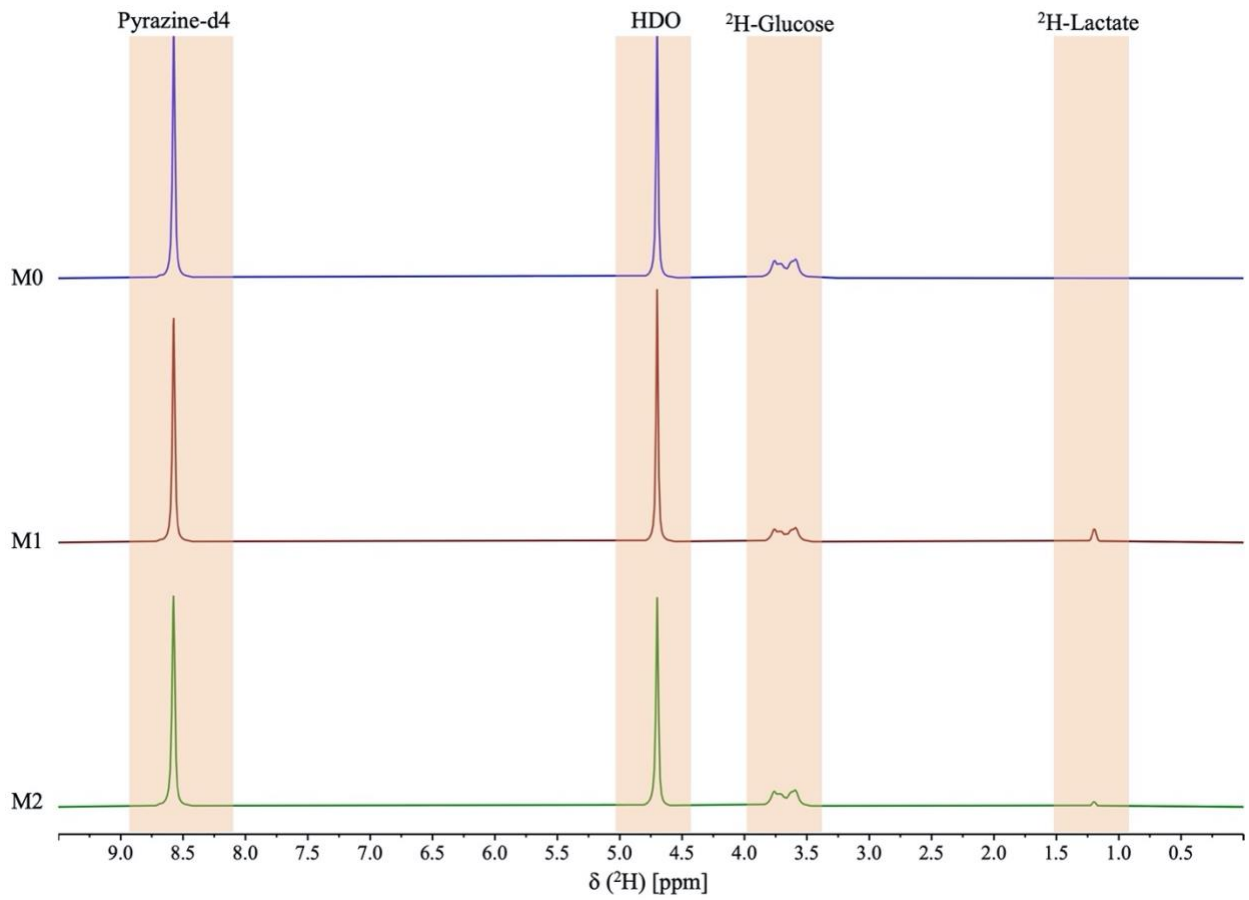

Figure 4.26 Sample stacked spectra of initial NMR of extracellular media from macrophage phenotypes at 800 MHz acquired using scan. cell extracellular media samples were taken after 24 hrs incubation with [6,6'-$^{2}H_2$]-glucose. HDO resonance (4.7 ppm), [6,6'-$^{2}H_2$]-glucose resonance (ppm) and [3,3'$^{2}H_2$] lactate (1.19 ppm) are highlighted in orange. **A**. M0 extracellular media sample from 3 separate donors at 24hr post [6,6'-$^{2}H_2$]-glucose incubation. **B**. M1 extracellular media sample from 3 separate donors at 24hr post [6,6'-$^{2}H_2$]-glucose incubation. **C.** M2 extracellular media sample from 3 separate donors at 24hr post [6,6'-$^{2}H_2$]-glucose incubation.

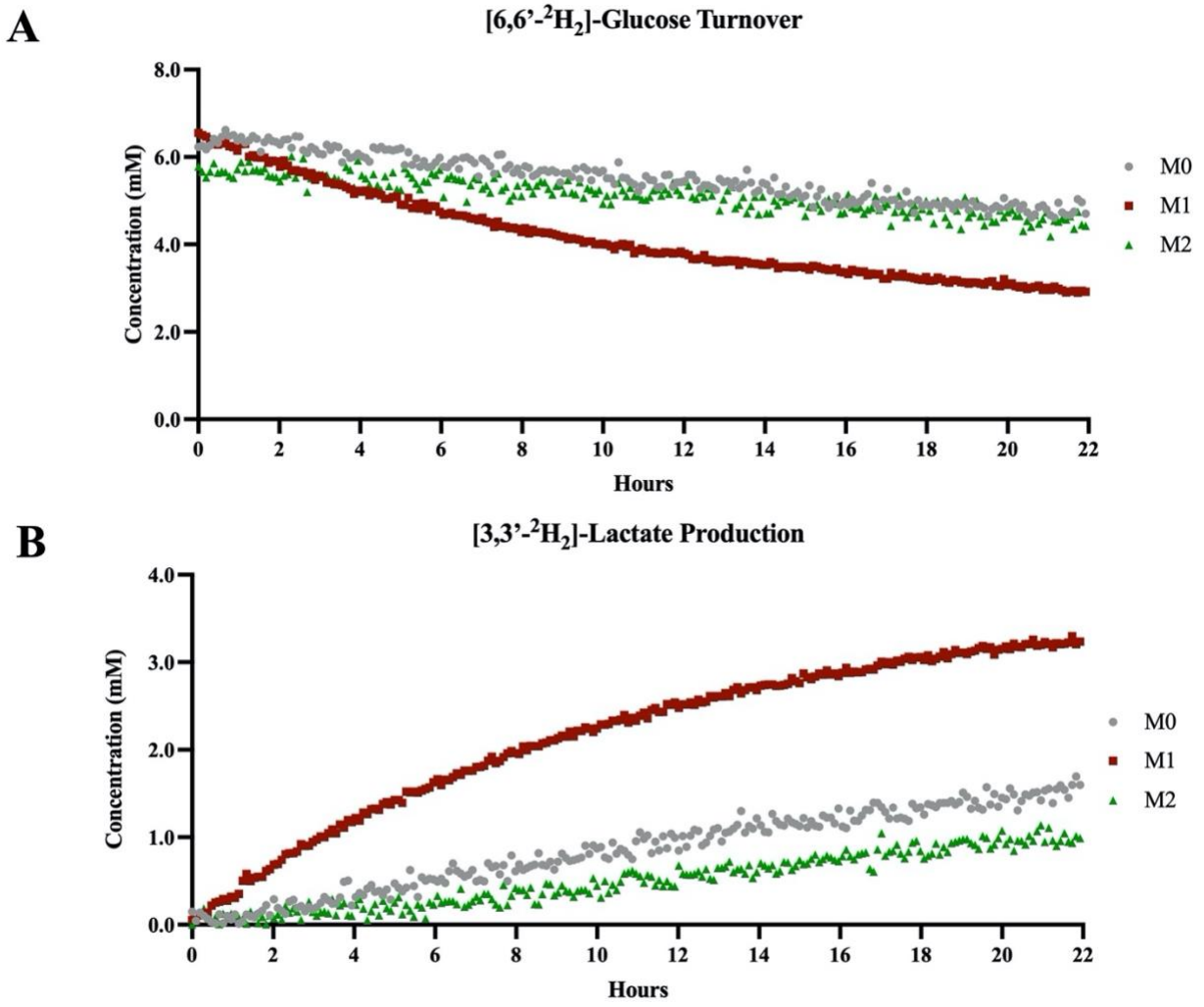

Figure 4.27 - Graphs depicting turnover of deuterium glucose and deuterium lactate in different macrophage phenotypes. Grey plotted datapoints correspond to M0, red plotted datapoints to M1 and green plotted datapoints to M2 macrophages. **A.** Graph plotting [6,6'-$^2H_2$]-glucose turnover in M0,M1, M2 macrophage phenotypes. **B.** Graph plotting [3,3'-$^2H_2$]-lactate turnover in M0,M1,M2 macrophage phenotypes.

Chapter 5 - Theranostic Platforms for Visualising Cytotoxic Drug Uptake in Glioblastoma Multiforme

5.1 Introduction

Brain tumours present a significant clinical challenge for both diagnosis and treatment. The most prevalent primary brain tumour is glioblastoma multiforme (GBM).[298–301] It is also one of the most

lethal and possesses a dismal prognosis, with a median overall survival of 12.1 to 14.6 months from diagnosis.[298,302] GBM is of astrocytic origin and is characterised by its highly aggressive diffuse infiltrative growth into surrounding brain parenchyma, and progression coupled to high treatment resistance with recurrence.[299,303,304] The most widely accepted approach for treatment of GBM is the Stupp protocol, which involves maximal surgical resection, irradiation and treatment with the blockbuster drug temozolomide (TMZ).[305] Treatment by this method only offers an average survival benefit of 2 months.[306] There have been numerous developments in targeted therapies to treat GBM, however none have yet significantly improved median survival.[307]

5.1.1 Barriers to Successful Treatment

5.1.1.1 Heterogeneity in GBM

There are a number of factors that limit the success of GBM treatments, including heterogeneity, immune cell evasion, tumour hypoxia and hypermutation.[308–310] One of the attributes that interferes with both chemotherapy and radiotherapy in GBM is heterogeneity.[307,311] Interpatient, intratumoral, functional and molecular heterogeneity all contribute to the diverse presentations of GBM.[299,311] Not unlike other cancers, this can be explained by clonal evolution and presence of glioma stem cells. [299,312] GBM is highly heterogenous, where a single tumour can constitute multi-subclones.[313]

5.1.1.2 Physical Complications Caused by Blood Brain Barrier and Blood Tumour Barrier

A major physical barrier to therapeutic access to the brain is the blood brain barrier (BBB). The BBB is a network of microvascular endothelial cells, which provides a physical barrier between blood and brain interstitial fluid.[314] The BBB is characterised by tight and adherens junctions, formed between adjacent endothelial cells, forming extremely small pores (1.4-1.8 nm), meaning only particles of a certain size can successfully pass through via passive transcytosis.[315] For an

intact BBB, there is a 150 Da exclusion limit for hydrophilic compounds and 400-600 Da exclusion limit for highly hydrophobic compounds.[316,317]

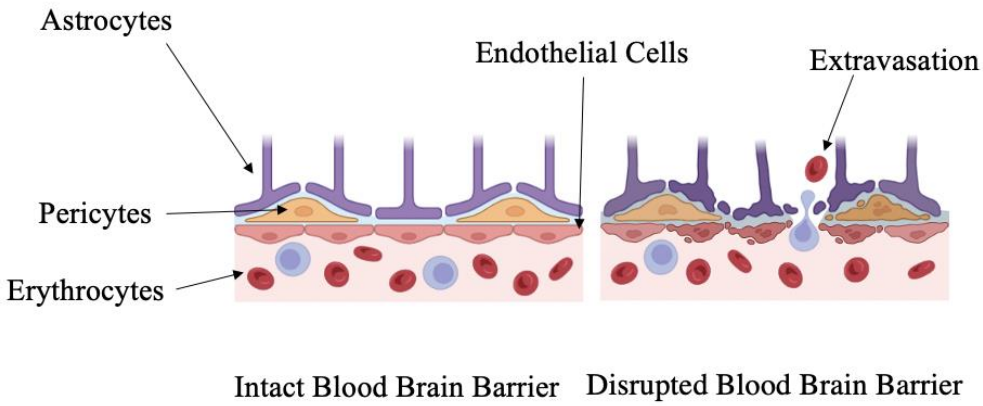

Figure 5.1- Visual of simplified structure of the blood brain barrier. The functional unit of the blood brain barrier includes a matrix of endothelial cells, astrocytes and pericytes, where blood brain barrier serves as a physical exclusion barrier. In diseased states the blood brain barrier is often disrupted , allowing for previously excluded species to traverse into the parenchyma.

This further complicates GBM treatment, where there are very limited opportunities to access a tumour or tumour resection cavity. BBB disruption using ultrasound waves and microbubbles is one method that has demonstrated promising results for therapeutic delivery at clinical trials.[318] Equally, implantable drug delivery devices, such as gliadel wafers, have been developed with the aim of providing sustained release of therapeutic agents.[319–321] However, in general, drug delivery is limited to either systemic or intratumoral delivery. [322,323]

5.1.2 Why Imaging is Important?

Medical imaging is a cornerstone for GBM diagnosis and forms part of the longitudinal assessment of treatment.[324] There have been attempts to try and visualise GBM using imaging, including PET, MRI, CT and fluorescent labelling.[210,325–330] T_2-weighted, fluid attenuated inversion recovery (FLAIR) and gadolinium T_1-weighted MRI are all commonly used for diagnosis, monitoring and treatment evaluation in GBM.[331] GBM is normally identified as a heterogenous mass with a necrotic core, with surrounding peritumoral oedema.[325]

5.1.3 Maximal Safe Resection with Imaging

Gross-total surgical resection is positively correlated with improved median survival by comparison to subtotal resection.[332,333] Given the high tumour burden, and diffuse nature of GBM, complete clearance is likely impossible via surgical means, where residual populations in the tumour margin possess tumorigenic potential, leading to recurrence.[310] Fluorescent pro-agent probes such as the 5-aminolevulinic acid (5-ALA) have been used as intraoperative agents.[328,329,334] 5-ALA is taken up by malignant glioma cells and is metabolised to protoporphyrin IX (PpIX), which emits red fluorescence following excitation by 405 nm light.[328,329,335] Contemporary approaches for determination of gross-total resection are routinely carried out using post-operative T_1 contrast enhanced MRI, where previously this would have been done via surgical assessment.[326]

5.1.4 Molecular Imaging for GBM

Molecular imaging can serve as tool to address the limitations that routine diagnostics encounter. Advanced molecular imaging approaches can provide superior spatiotemporal resolution of tumour marker status, over a prolonged observational period.[330] Groups have developed targeted molecular imaging approaches for visualising GBM using targeted PET, CT and MRI/MRS, which have been extensively reviewed.[210,330] Targeted molecular imaging of GBM throughout treatment can provide useful clinical insights into invasiveness, therapeutic resistance and tumour volume.[330] Equally important is an understanding of how these cytotoxic agents behave, including their propensity for drug uptake within tumours versus normal tissue. There is a distinct requirement for multifunctional imaging agents capable of monitoring delivery of necessary cytotoxic drugs but also capable of monitoring tumour response.[336–339] To date there are very few examples of MRI contrast agents that have been directly conjugated to chemotherapeutics, and none that have been carried through to clinical trials. Current therapy regimes employ stepwise, discrete imaging

protocols that do not convey real time spatial temporal information relating to therapy uptake in GBM. Monitoring of drug uptake in brain tumours is incredibly important, theranostic agents could serve as a tool for the non-invasive monitoring of drug dynamics *in vivo*.

5.1.5 Imaging the Dynamics of Cytotoxic Small Molecules in GBM using MRI

There are several considerations for brain imaging, as previously mentioned. Blood brain barrier, targeting specificity, concentration and clearance should be considered as part of the rational design of contrast agents. Contrast agents enhance both the longitudinal (T_1) and/or transverse relaxation (T_2) rates of local water molecules, resulting in enhanced signal contrast between distinct biological tissues.[340–342] Gadolinium based contrast agents are the most common contrast agents used for contrast enhancement in MRI, thanks to the large magnetic moment and electronic relaxation time of the Gd^{3+} ion.[343] To date, nine gadolinium based contrast agents have been approved by the FDA, which include a number of linear and macrocyclic based ligand systems.[344] There are, however, concerns over the *in vivo* stability of linear gadolinium based contrast agents such as [GdDTPA], which are contraindicated for patients with acute nephrogenic systemic fibrosis.[345] Increasing concern around the use of linear GBCAs is highlighted in several studies that have documented gadolinium ion deposition in brains of healthy patients.[346–348] In general, macrocyclic contrast agents, such as [GdDOTA], display greater stability with respect to ion leaching.[349] Gadolinium is one of many paramagnetic metals that are capable of producing favourable MR contrast enhancement for GBM. Manganese is one example which has also previously been used for MRI applications, with a plethora of ligand systems being developed.[350,351] Most MR contrast agents are polar and incapable of permeating cell membranes, making it challenging to target intracellular compartments. Critically, some manganese based

contrast agents have shown to be cell membrane permeable, which is an ideal characteristic for imaging the intracellular uptake of cytotoxic drugs.[352]

5.1.6 Olaparib as a Potential Contrast Agent Labelled Drug

Olaparib ('Lynparza', AstraZeneca, Cambridge, UK) is a poly(ADP-ribose) polymerase (PARP) inhibitor, which has been clinically approved for use in a number of cancers, including advanced ovarian cancer.[353] PARP inhibitors are designed to serve as competitive inhibitors of NAD+, acting at the catalytic sites of PARP1 and PARP2 enzymes.[354,355] PARP1 enzymes are highly conserved and comprise of several functional domains including an N-terminal double zinc finger DNA binding domain, nuclear localisation signal, central auto-modification domain and a C-terminal catalytic domain.[356] Olaparib is designed with nicotinamide moiety that competitively inhibits NAD+.[354] Both PARP1 and PARP2 enzymes function as essential part base excision repair pathway (BER) which acts upon repair mechanisms for DNA single-strand breaks.[357,358]

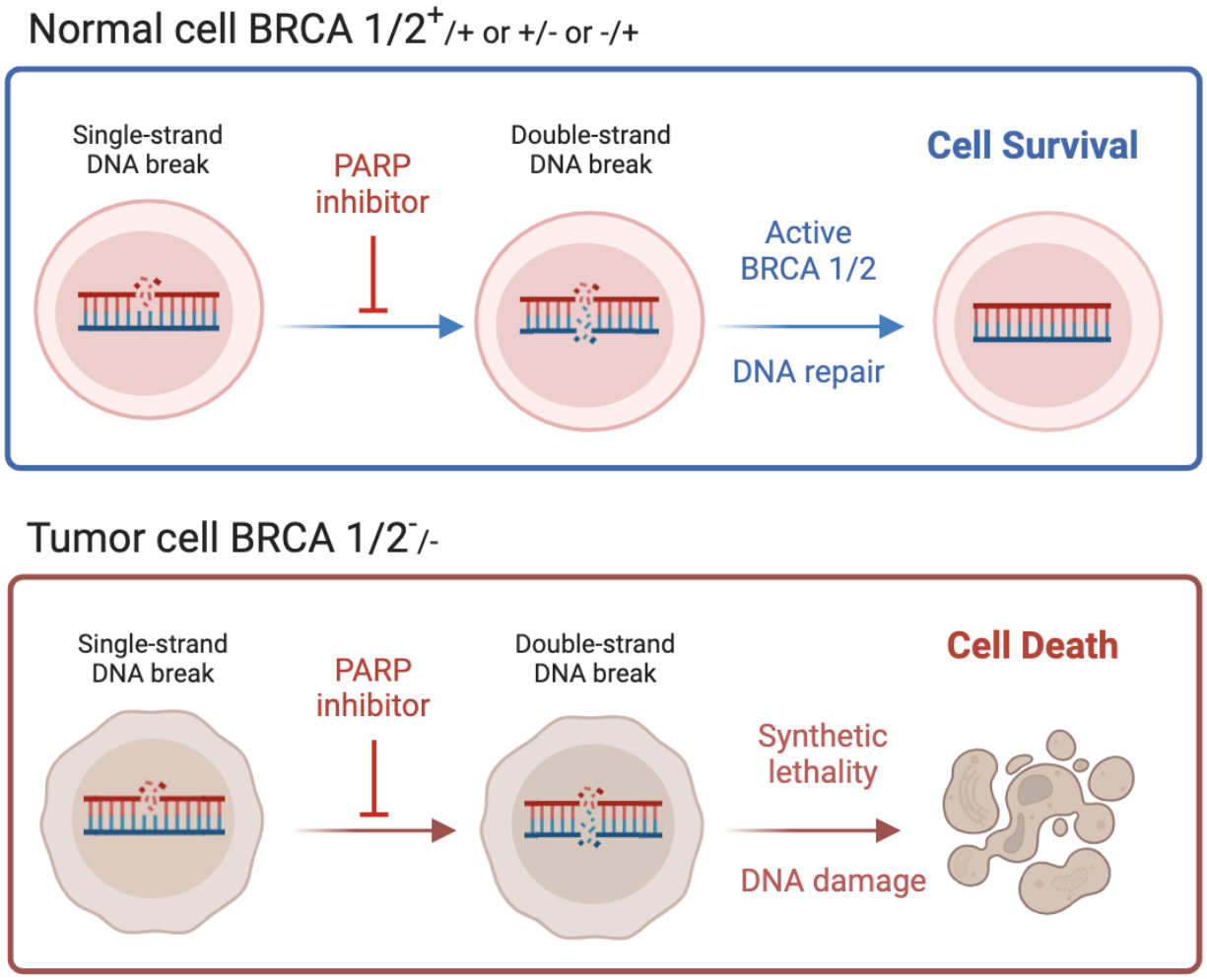

Figure 5.2 - Schematic of PARP inhibition in healthy and tumour cells. In healthy cells with active BRCA, double strand breaks are successfully repaired. However in tumour cells with impaired BRCA function, double strand breaks lead to cell death. Figure adapted from Polyak et al.,2011[359]

Following DNA damage, PARP1 is recruited to sites of DNA damage, where its catalytic activity increased between 10-500 fold.[360] Activated DNA-bound PARP1 synthesizes negatively charged ADP-ribose polymers (PARs) from donor NAD+ molecules. [356] Single strand breaks are normally repaired by BER, however PARP inhibition leads to single strand breaks being converted into double strand break. Double strand breaks are a highly cytotoxic form of DNA damage, which potentiates genomic rearrangements and cell death if unrepaired.[361] Some tumours present with an impaired homologous repair (HR) pathway, such as those with deficient in BRCA1 or BRCA2.

Cells with BRCA1 and BRCA2 deficiency display a high level of chromosome instability, which can manifest as chromosome breakages.[362] PARP inhibitors implementation as anti-cancer therapeutics is driven by hypersensitivity of homologous recombination (HR) deficient cells.[363] In HR functional cells, double strand breaks are repaired , however in HR deficient cells double strand breaks remain unrepaired. [355,364] PARP inhibitors have demonstrated massive therapeutic potential, with many PARP1 inhibitors being approved for clinical practice including Olaparib, Rucaparib and Niraparib.[365] PARP inhibitor efficacy are being explored as both monotherapies and or in conjugation with other chemotherapeutic agents.[366] Moreover, PARP inhibitors display a synergistic relationship with DNA damaging agents such as temozolomide, platins and ionising radiation.[363,367] Olaparib is capable of crossing the BBB, given its small size, and has been investigated for therapeutic application in GBM patients via both the 'OPARATIC' and 'Paradigm 2' phase 1 clinical trials.[368,369] A few olaparib based contrast agents have been developed, mostly focused on PET applications including ^{68}Ga-DOTA-olaparib, ^{64}Cu-DOTA-olaparib and ^{18}F-Olaparib derivatives.[370–372] Equally, fluorescent compounds have been developed, such as the well the documented fluorescent Olaparib analogue PARPi-FL.[327,365] To date there have been no published Olaparib based contrast agents for MRI.

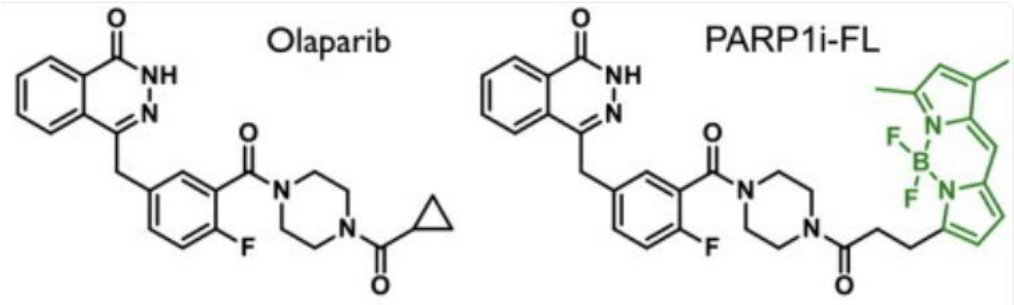

Figure 5.3 - Chemical structure of Olaparib and fluorescent labelled derivative of Olaparib PARP1i-FL. (Image adapted from Irwin et al., 2014).[327]

5.1.7 Doxorubicin as a Potential Contrast Agent Labelled Drug

Doxorubicin (DOX) is another drug that is frequently used in anti-cancer treatment regimens.[373–375] DOX is a topoisomerase I inhibitor, which induce DNA strand breaks and impede the function of topoisomerases which are heavily involved in DNA replication and transcription.[376] Mechanistically, DOX acts to damage DNA by formation of an DNA adduct, induction of double strand breaks and through intercalation where DOX binds to DNA through hydrogen bonding with guanines on DNA base pairs.[377] Conveniently, DOX also has fluorescent properties (480/590 nm excitation/emission), which allows for multimodal drug tracking.[378,379]

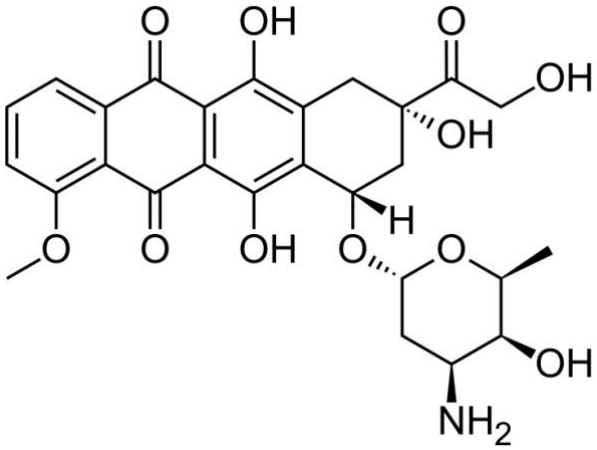

Figure 5.4- Chemical structure of Doxorubicin.

DOX has previously been used to optically visualise drug uptake using liposomes and hydrogel platforms.[378–380] As a multimodal MRI agent, DOX has been covalently conjugated to nitroxides, as metal-free organic radical contrast agents. [381] Nanoparticle based approaches have also been used in an attempt to track DOX delivery to tumours.[382–384]

To screen the multimodal contrast agents, an appropriate 3D cell culture phantom model would be required, One option is to use alginate hydrogels as an approach to encapsulate cells in a media perfusable matrix .The rationale behind designing an alginate-based phantom is driven by increased biocompatibility. Firstly, alternative agarose-based cell phantom systems require heating

above 90 ºC in order to achieve polymerisation. This heating step is incompatible for any live cell work. Alginate systems benefit from gelification at physiologically acceptable temperatures. The second is that alginate based hydrogels have well established use as scaffolds for 3D-cell culture, allowing for nutrient and gas exchange.[385] Encapsulation and recovery of cells is facile, which is an added benefit for downstream processing.

I hypothesise that Olaparib and DOX based contrast agents will be able to serve as a companion diagnostic tool for monitoring drug uptake and efficacy in GBM at an *in vitro* level and will be visible via MRI.

I will test the hypothesis using the following aims:

a. To investigate 3-dimensional phantoms systems capable of monitoring drug diffusion and cell uptake.
b. To investigate the use of alginate based hydrogels to encapsulate labelled U251 GBM cells.
c. To investigate imaging of hydrogels using high resolution MRI.
d. To investigate toxicity of theranostic compounds using a LIVE/DEAD assay.

The efficacy and feasibility of drug-contrast agent for monitoring drug diffusion and uptake will be assess initially using 2D fluorescent imaging. Using Mn-Salen-DOX as a platform probe, Doxorubicin is a fluorescent molecule (480/590 nm excitation/emission) and co-localisation of Doxorubicin labelled compounds should be easily identifiable by red channel fluorescent imaging. Beyond positive identification of agent uptake, MR imaging feasibility will be assessed using perusable 3D imaging phantoms, such as alginate hydrogels. Performance of the drug-contrast agent will be assessed via both R_1 and R_2 relaxation rates.

5.2 Materials and Methods

Throughout this chapter, four therapeutic imaging compounds, synthesised within the group, were used to label U251 cells. Two compounds were designed using a salen ligand: manganese-salen-DOX and iron-salen-olaparib (detailed in *figure 5.5*). Two further compounds were designed using a DOTA-olaparib ligand: gadolinium-DOTA-olaparib and terbium-DOTA-olaparib (detailed in *figure 5.5*). It is envisioned that, based on the fluorescent properties of DOX, the manganese-salen-DOX agent could be used for multimodal fluorescent and MRI investigations into drug tracking and uptake. Furthermore, terbium-DOTA-olaparib could be used for luminescence based approaches. [386,387] Compounds and samples were provided by Patricia Jensen and Dr. Charlotte Gidman.

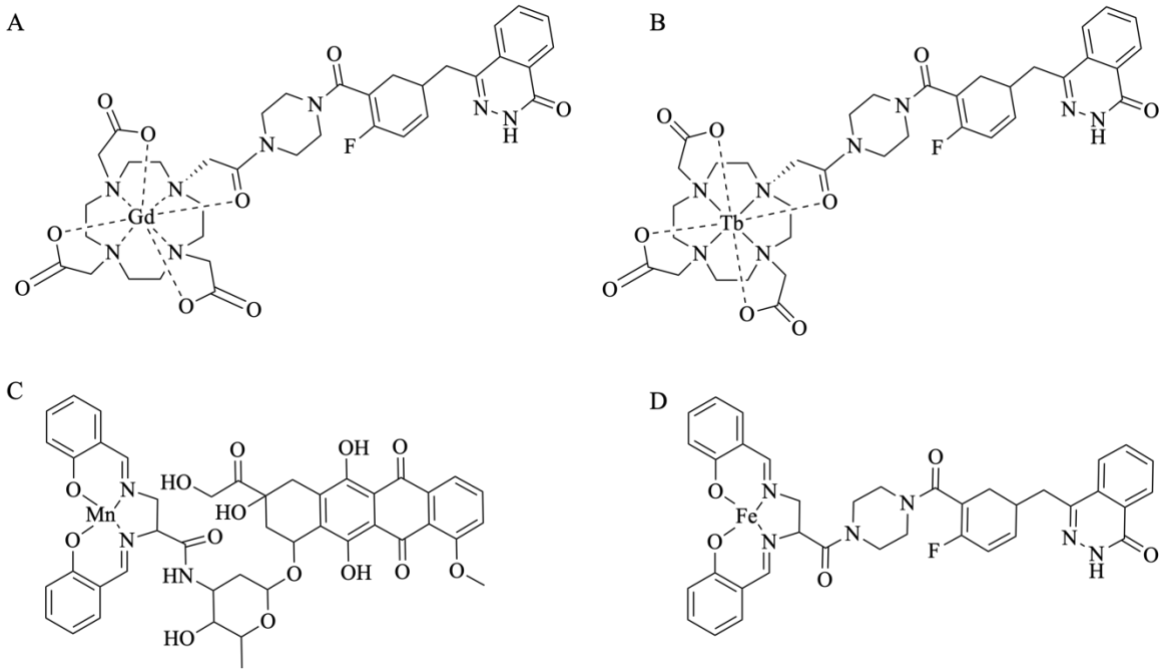

Figure 5.5 - Salen based compounds used in this chapter. **A.** Gadolinium-DOTA-olaparib **B.** Terbium-DOTA-olaparib **C.** Manganese-salen-doxorubicin **D.** Iron-salen-olaparib

Table 5.1 - Relaxivity (r_1 and r_2) values for theranostic compounds at 7T. Calculations were carried out by Dr. Charlotte Gidman and Patricia Jensen and have not been corrected by ICP-MS

Compound	$r_1(mM^{-1}s^{-1})$	$r_2(mM^{-1}s^{-1})$
Mn-salen-DOX	6.20	90.40
Fe-salen-olaparib	0.81	3.53
Gd-DOTA-olaparib	1.65	2.31
Tb-DOTA-olaparib	0.06	2.82
Gd-DOTA	4.20	-

5.2.1 Cell Culture

Glioblastoma multiforme (U251, ATCC) cells were cultured in high glucose Dulbecco's modified Eagles medium (DMEM), supplemented with 10% FBS (v/v), 1% penicillin-streptomycin (v/v) and 1% L-glutamine (v/v), under sterile conditions within a class II biosafety cabinet.

5.2.1.1 Subculturing of Cells

For cell passage, TrypLE express was used to detach cells. At 80% cell confluency, spent cell culture media was aspirated from the cell culture flask and cells were subsequently washed using warm PBS (37 ºC, 3x times, sterile). PBS was then removed and TryPLE was added directly to cells. Cells were then left to incubate (37 ºC, 5% CO_2, 10 minutes). The cell culture flask was then gently tapped to aid detachment. Visible cell detachment was confirmed by light microscopy. The cell/TrypLE solution was then removed from the flask, cells were then counted using trypan blue staining with an automated haemocytometer. Cells were then resuspended into a fresh 50 mL Falcon tube containing complete DMEM media. The cell containing Falcon tube was then centrifuged (5 mins, 350 g, r.t) to pellet the live cells. Following centrifugation, supernatant was discarded and the cell pellet was resuspended in complete media for cell counting.

5.2.2 Cell Labelling with Theranostic Contrast Agents

Theranostic contrast agents were weighed and suspended into cell grade DMSO to give 20 mM stock solutions of each compound. The small molecule solutions were then sterile filtered using a 0.22 µm syringe filter. 20 mM small molecule/DMSO stock solutions were then diluted into complete cell media at concentrations of 0.1, 0.25 and 0.5 mM and cells were labelled at high confluency (>80% surface coverage). 8 million (1.0 mn/mL) cells were incubated with small molecules for 24 hours at standard incubation conditions (37º C, 5% CO2, relative humidity). Following the incubation period, the staining media was removed and cells were washed using PBS (3x times , 37º C), and fresh DMEM media was then added directly to the cells.

5.2.3 Fluorescent Screening of Mn-salen-DOX on U251

U251 cells were seeded into 96 well plates at a density of 50,000 cells per well. Cells were then left to adhere in an incubator (37 ºC, 5% CO_2, relative humidity). Cells were then incubated with 0.5 mM of Mn-salen-DOX doped into DMEM media for 24 hours. The following day, media was removed from cells and cells were washed with PBS. Media was removed from cells and 4% PFA was added to each well for 10 minutes. PFA was removed and cells were stored in PBS. Cells were then imaged using an EttaLuma widefield fluorescent microscope with 10x and 40x objectives.

5.2.4 Alginate Hydrogel Fabrication

For alginate hydrogel fabrication, labelled cells were washed with PBS and detached using warmed TrypLE (37 ºC, 10 mins). The cell suspension was then removed from the flask and centrifuged (5 mins, 350 G). Following centrifugation, the supernatant was discarded and the cells were resuspended in 4% PFA in PBS (10 mins, r.t). Following fixation the cells were centrifuged again, and supernatant containing PFA was discarded. The cells were then washed using sterile distilled water (3 times, rt). Cells were then counted as described above. To fabricate alginate

hydrogels, sodium alginate powder (Sigma) was weighed and suspended in complete DMEM media to give a 1% (w/v) solution. Calcium chloride (Sigma) (100 mM) was dissolved into sterile filtered, distilled water. Fixed cells were resuspended in 1% alginate DMEM at density of 1500 cells per µL alginate hydrogels formed by droplet of 1% alginate/cell solution into 100 mM calcium chloride solution. The 1% alginate solution polymerises instantly, forming a spherical hydrogel with encapsulated U251 cells.

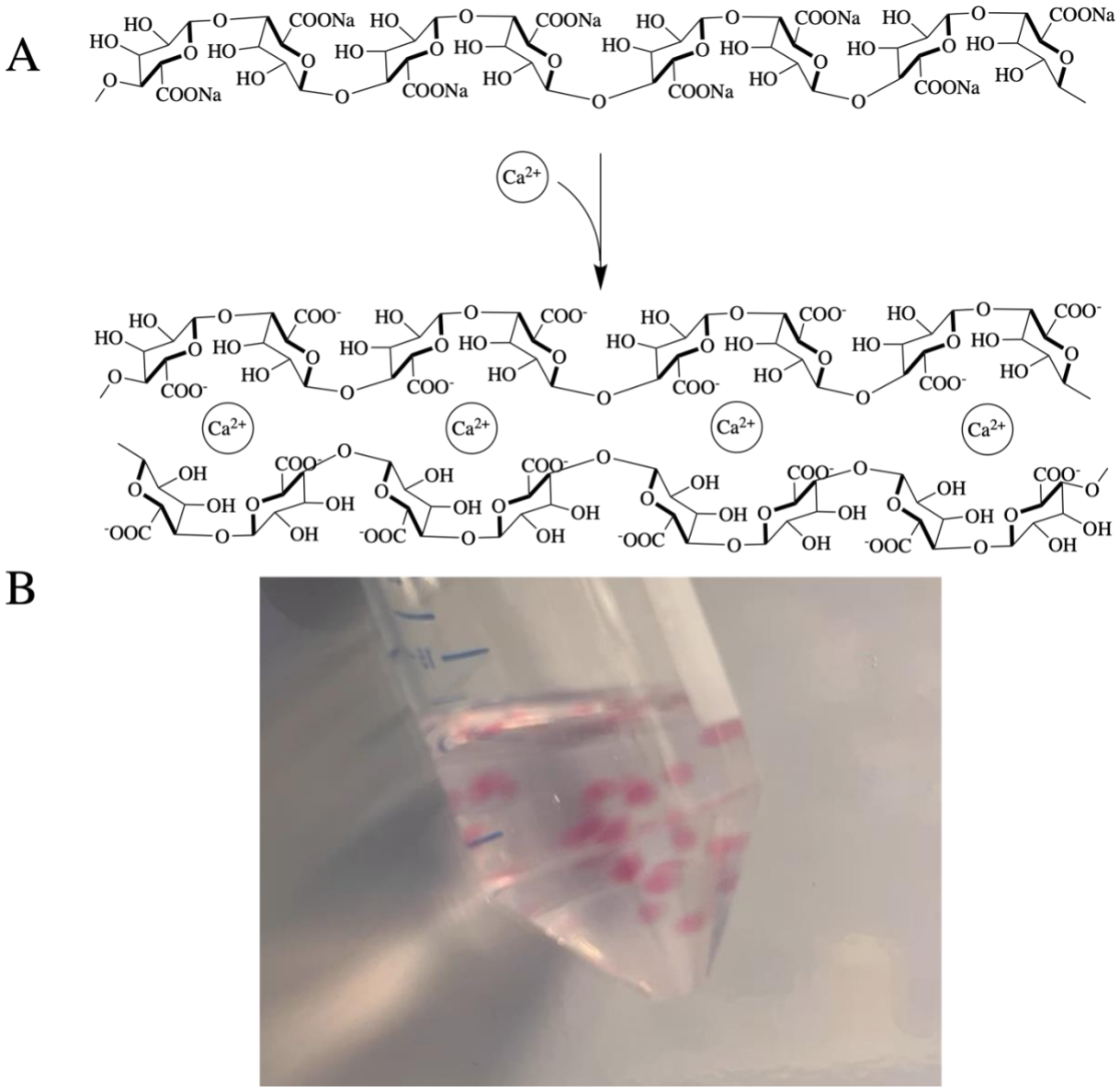

Figure 5.6 **- A.** The "egg-box" model for ion induced alginate gelation. Formation of calcium alginate gel from sodium alginate. **B.** Alginate hydrogels (pink) in a 50 mL Falcon tube.

5.2.5 MR Imaging of Alginate-U251 Phantoms with Small Molecules

Alginate hydrogels were transferred to a 100 µL PCR tube. Each PCR tube contained 5 hydrogels. PCR tubes were then arranged within a Styrofoam tube holder and placed within a 30 cm bore Bruker Biospec 70/30 7 T MR scanner with a Bruker Avance III Console (Bruker BioSpin, Ettlingen, Germany).

For the first optimisation scan using Mn-Salen-Dox: 4 x 1 mm slices were imaged in a coronal orientation through the centre of each PCR tube with data matrices of 256 x 192 with a field of view of 7.7 x 5.8 cm. The T_1 relaxation times were calculated using a RARE VTR sequence (flip angle = 90º) with 6 TRs ranging between 93.1 and 10,000 ms. T_2 relaxation times were calculated with a MSME pulse sequence (flip angle = 90 º) with 16 TEs ranging from 7.8 to 125.9 ms.

For the second acquisition using all small molecules compounds: A 4 x 1 mm slice was imaged in a coronal orientation through the centre of each PCR tube with data matrices of 192 x 180 with a field of view of 5.4 x 5.8 cm. The T_1 relaxation times were calculated using a RARE VTR sequence (flip angle = 90º) with 6 TRs ranging between 93.1 and 10,000 ms. T_2 relaxation times were calculated with a MSME pulse sequence (flip angle = 90 º) with 20 TEs ranging from 7.8 to 157.4 ms.

For concentration gradient plate map: A 4 mm slice was imaged in a coronal orientation through the centre of each PCR tube with data matrices of 256 x 256 with a field of view of 5.0 x 5.0 cm. The T_1 relaxation times were calculated using a RARE VTR sequence (flip angle = 90º) with 6 TRs ranging between 53.59 and 10,000 ms. T_2 relaxation times were calculated with a MSME pulse sequence (flip angle = 90 º) with 16 TEs ranging from 7.8 to 123.65 ms.

Image J (FIJI) was used to reconstruct slices and the relaxation times were calculated by fitting the image intensity data to the exponential decay curves using the MRI Analysis Calculator plugin

(Karl Schmidt). Relaxation times (T_1/T_2) were converted to relaxation rates (R_1/R_2) for presentation, where $R_1 = 1/T_1$ and $R_2 = 1/T_2$.

5.2.6 Live Dead Toxicity Assay

A LIVE/DEAD viability/cytotoxicity kit (ThermoFisher) was used to determine toxicity of small molecule compounds towards target cells. The general procedure for the LIVE/DEAD assay is described in the 'General Methods' chapter. For theranostic molecule toxicity towards GBM, U251 cells were seeded into a 96 well plate with 50,000 cells per well. Cells were then left to adhere in an incubator (37 ºC, 5% CO_2, relative humidity). The following day, media was removed from cells and cells were washed with PBS. Cells were then incubated with 0, 0.25, or 0.5 mM of each theranostic compound doped into DMEM media for 24 hours. Following incubation cells were washed with PBS and treated with the calcien/EthD1 working solution and were left to incubate (30 mins, rt). Cells were visualised using a GloMax® Explorer (Promega) fluorescent plate reader using 475/550 nm excitation and emission filters for calcien readouts and 520/580 nm excitation and emission filters for EthD1.

5.3 Results

5.3.1 Fluorescent Labelling of U251 with Mn-salen-DOX

The fluorescent properties and DNA intercalation properties of DOX make it an attractive compound to use for cell labelling experiments. Following optimisation experiments using various concentrations, Mn-salen-DOX was successfully visualised via fluorescent microscopy. From optimisation, Mn-salen-DOX accumulated intracellularly in sufficient concentrations for fluorescent visualisation following 24 hours incubation. *Figure 5.7* below depicts a representative selection of images from the fluorescent screen using Mn-salen-DOX on U251. Curiously, DAPI, the nuclear dye, appears to only label some of the nuclei. It is also difficult to determine the location

of the dye within the cell, which could be improved by using a cytoplasm or membrane co-stain. Equally, a higher resolution imaging technique, such as confocal microscopy, could provide a better spatial resolution with respect to subcellular location of dyes.

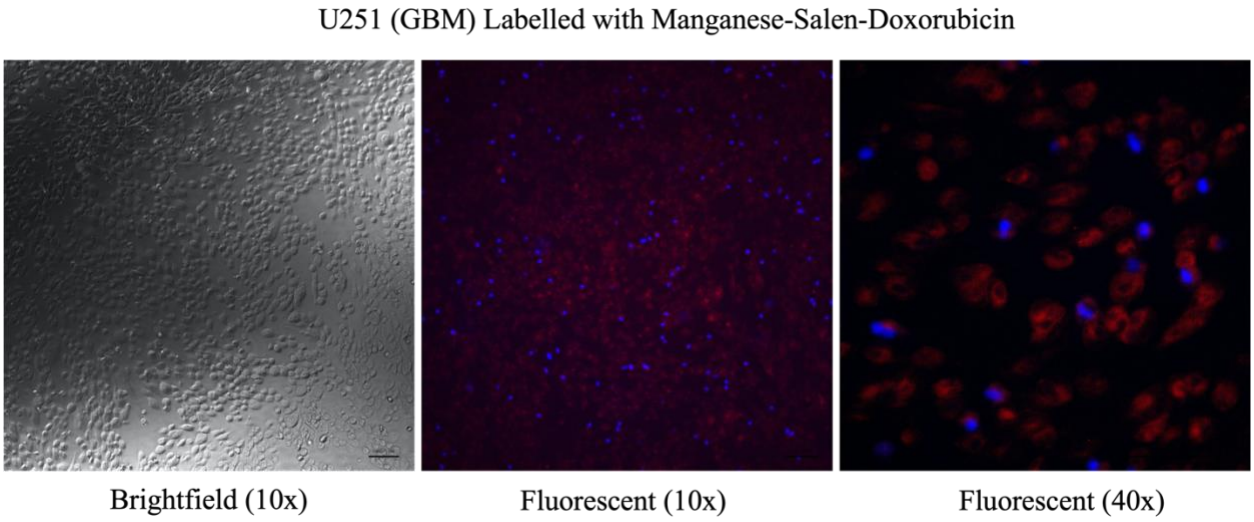

Figure 5.7 **-** Representative brightfield and fluorescent images of U251 labelled with Mn-salen-DOX (red, 480/590 nm excitation/emission). Cells were live incubated with 0.5 mM Mn-salen-DOX for 24 hours following optimisation. Cells were counterstained with nuclear dye DAPI (blue). Cells were then imaged with brightfield and fluorescent channels using 10x and 40x objectives. Brightness of images have been enhanced using ImageJ.

5.3.2 MRI of Theranostic Compound Labelled Alginate Hydrogel Encapsulated Glioblastoma

Formation of hydrogels was carried out by droplet dispersion of alginate (1% w/v) media into a calcium chloride bath, leading to instant formation of spherical hydrogels. Several approaches were tested during optimisation, including using different tip and needle sizes in order to fabricate both large and spherically uniform hydrogels. Once fabricated hydrogels were imaged using brightfield microscopy. *Figure 5.8a* shows a representative image of a hydrogel made by dispersion from a p1000 tip.

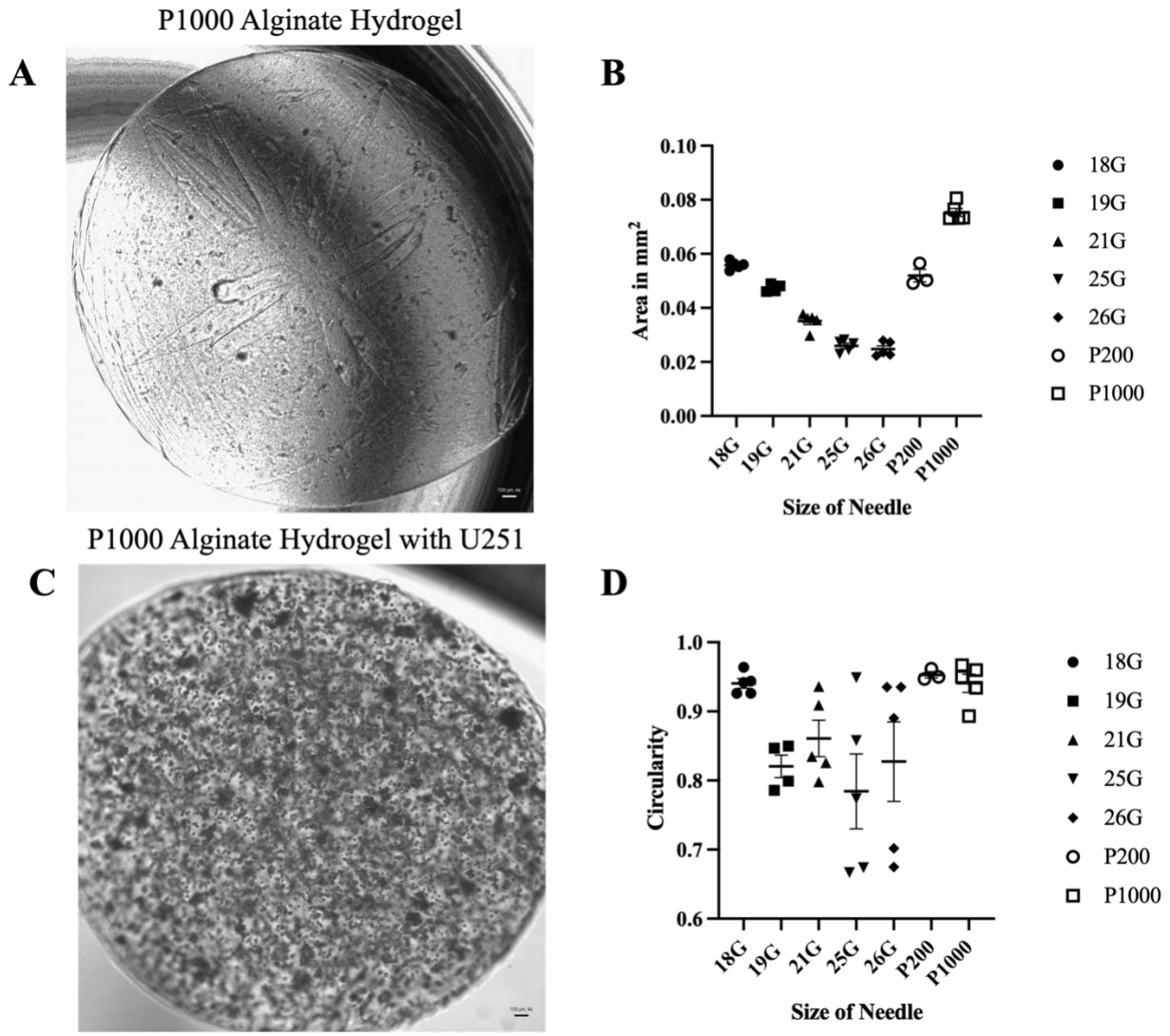

Figure 5.8 **-** Alginate optimisation experiments. **A.** Representative image of an alginate hydrogel made using a p1000 tip. **B.** Area measurements of cross sections of alginate hydrogels. **C.** Alginate hydrogel with encapsulated U251. **D.** Circularity measurements of alginate hydrogels calculated by (4π*area)/perimeter^2. A value of 1.0 indicated a perfect circle, where a value approaching 0.0 indicates an elongated shape.

Alginate hydrogels formed using a P1000 tip offered good consistency with respect to size and uniformity (circularity = 0.94). However, these findings are based off a couple assumptions. The measurement of hydrogels are imperfect, and were taken using a circle selection tool, approximating the centre of the hydrogel from the point with the largest diameter.

5.3.3 Concentration Optimisation

Here, alginate was used to encapsulate U251 cells, which were stained with increasing concentrations of Mn-salen-Dox. Following labelling, alginate hydrogels were imaged using 7.0 T MRI. R_1 and R_2 maps were generated and depicted in *figure 5.5* below. Expectedly, U251 alginate hydrogels incubated with the highest concentration of Mn-salen-DOX (0.5 mM) displayed the most favourable contrast enhancement. 5 alginate hydrogels were loaded into each PCR tube per condition and this data only represents one biological repeat. *Figure 5.9* includes graphs of R_1 and R_2 data calculated from the R_1 and R_2 maps. Data from MRI indicate that 0.5 mM labelled hydrogels display the highest R_1 (0.67 s^{-1}) and R_2 (7.57 s^{-1}) as expected. The increase in R_1 first became significantly different from the control (0.35 s^{-1}) at 0.1 mM (0.46 s^{-1}, **$p<0.01$). For R_2, the first significant difference relative to control (4.79 s^{-1}) was for the 0.25 mM sample (7.08 s^{-1}, *$p<0.05$). *Figure 5.10* depicts a 3D reconstruction of an R_2 maps through a single u251 alginate hydrogel labelled with 0.5 mM Mn-salen-DOX.

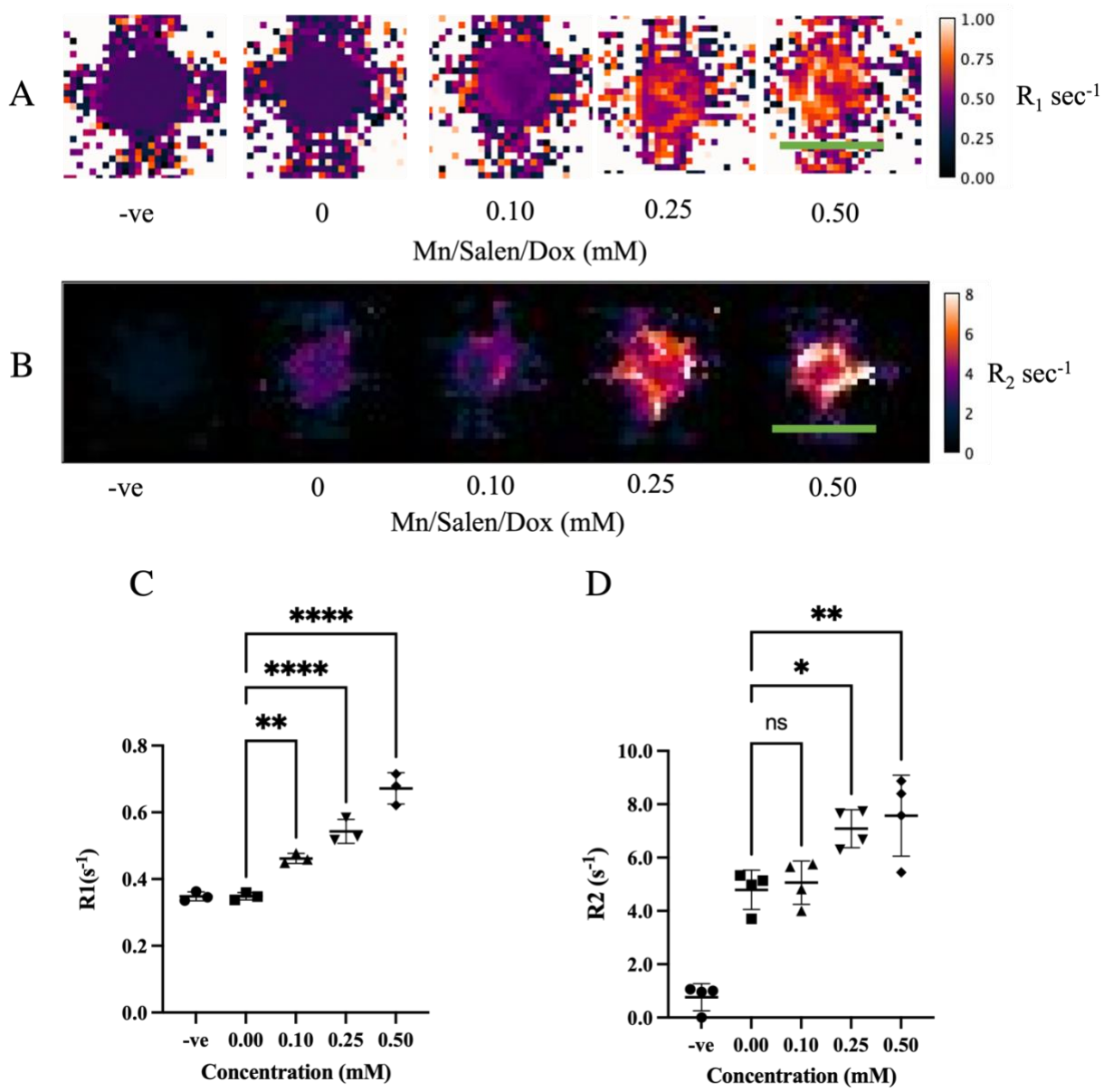

Figure 5.9 - Mn-salen-DOX labelling optimisation experiments. **A.** Representative slice of R_1 maps of U251 encapsulated alginate hydrogels, containing different labelling concentrations of Mn-salen-Dox.**B**. Representative slice of R_2 maps of U251 encapsulated alginate hydrogels, containing different labelling concentrations of Mn-salen-dox. '-ve' denotes a blank PCR tube containing water only. Maps are false coloured using the 'GEM' lookup table within ImageJ. Green scale bar = 3 mm. Graphs depicting relaxation rate data from U251 alginate labelled with increasing concentrations of Mn-salen-DOX. **C.** R_1 relaxation rate data from a RAREVTR acquisition. 1mm coronal slice of PCR tube with U251 alginate hydrogels labelled with 0.0, 0.1, 0.25 and 0.50 mM of Mn-salen-DOX. Each data point corresponds to a region of interest selection from one slice. **D.** R_2 relaxivity data calculated from MSME acquisition. 1 mm coronal slice of PCR tube with U251 alginate hydrogels labelled with 0.0, 0.1, 0.25 and 0.50 mM of Mn-salen-DOX. Each data point corresponds to a region of interest selection from one slice. *p<0.05, **p<0.01, ***p<0.001, ****p<0.0001

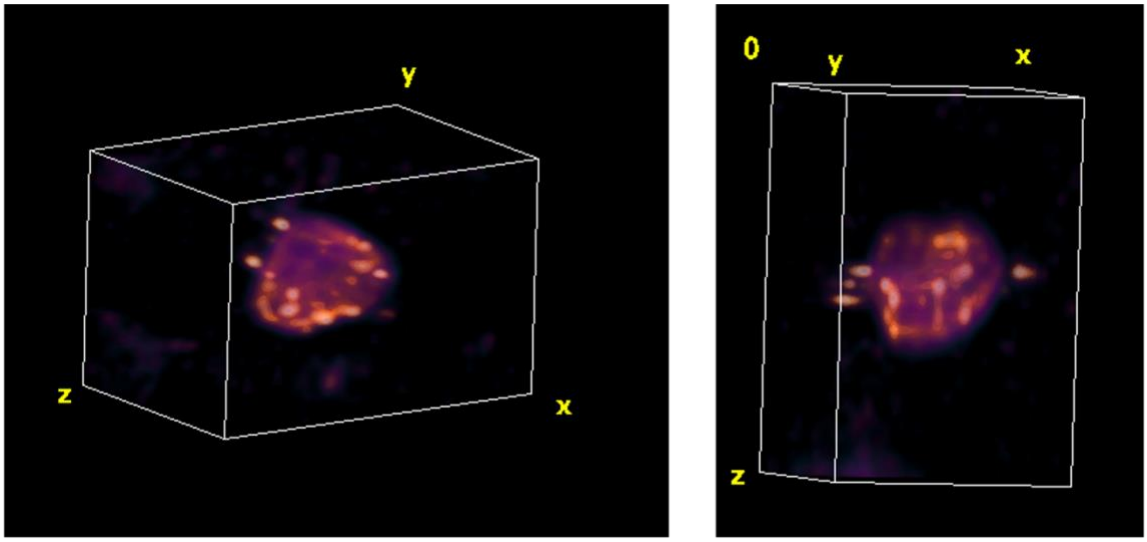

Figure 5.10 – R_2 map reconstruction of an individual U251 alginate hydrogel labelled with 0.5 mM Mn-salen-DOX.

5.3.4 R_1 maps of small molecule labelling of U251 hydrogels

Figure 5.11 displays T_1 data from MRI imaging of alginate encapsulated U251 hydrogels labelled with an array of DOX and olaparib based small molecules compounds. Gd-DOTA-olaparib displayed the highest observed R_1 value for any of the tested compounds with an average of 0.77 s^{-1} across 4 slices, followed by Mn-salen-DOX (0.65 s^{-1}) and Fe-salen-olaparib (0.44 s^{-1}). Tb-DOTA-olaparib showed very little difference in R_1 between PBS and control samples.

5.3.5 R2 maps of small molecule labelling of U251 hydrogels

T_2 weighted imaging was carried out on the same sample as for T_1 imaging. R_2 values across four representative slices of the tube displayed consistent signal trend and is visualised in *figure 5.11* below. Mn-salen-DOX displayed the highest R_2 values across all slices with an average of 9.15 s^{-1} across all 4 slices. Gd-DOTA-olaparib showed the second largest R_2 (4.50 s^{-1}) relative to the control measurement (2.49 s^{-1}). Both Tb-DOTA-olaparib (2.77 s^{-1}) and Fe-salen-olaparib (2.93 s^{-1}) showed a moderate increase in R_2 relative to control alginate sample.

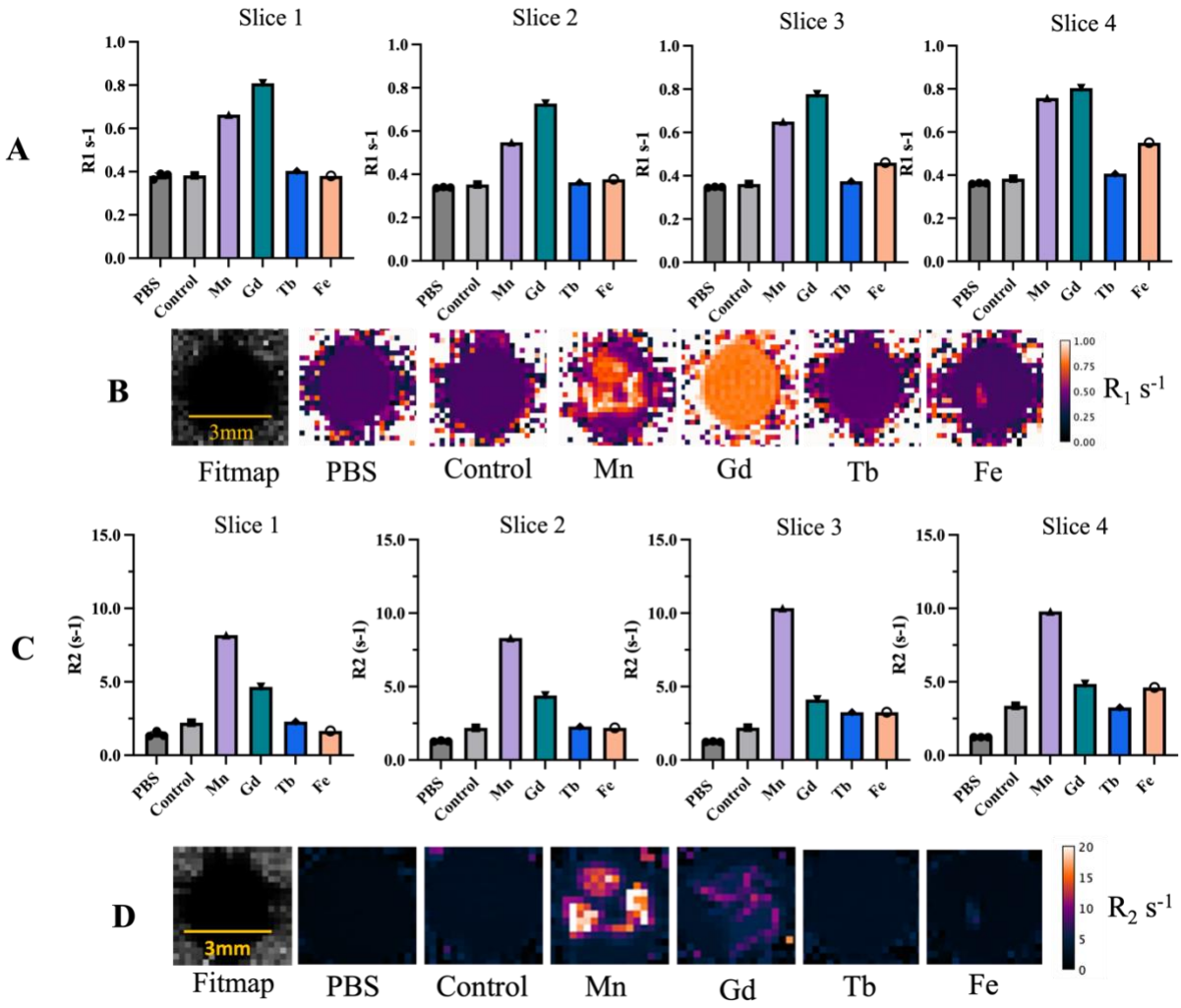

Figure 5.11 - *R_1* data from small molecule labelling of U251 cells encapsulated in alginate hydrogels**. A.** Graphs for *R_1* values calculated from ROI selection of *R_1* map. Graphs depicting the *R_1* values per image slice through the PCR tube, with a single value plotted per condition. **B.** Representative *R_1* maps (slice 1) of each labelling condition. "Fitmap' denotes a representative image from an *T_1* fit quality map. 'PBS" sample contains only PBS. The 'Control' sample contained 5 U251/alginate hydrogels. The 'Mn' sample contained U251/alginate hydrogels labelled with Mn-salen-DOX. The 'Gd' sample contained U251/alginate hydrogels labelled with Gd-DOTA-olaparib. The 'Tb' sample contained U251/alginate hydrogels labelled with Tb-DOTA-olaparib. The 'Fe' sample contained U251/alginate hydrogels labelled with Fe-salen-olaparib. *R_2* Data for small molecule labelling of U251 glioblastoma cells encapsulated in alginate hydrogels. **C**. Graphs for *R_2* values calculated from ROI selection of *R_2* map. PCR tubes containing alginate hydrogels were acquired in 4x1 mm slices. The 'control' sample contained 5 U251/alginate hydrogels. The 'Mn' sample contained U251/alginate hydrogels labelled with Mn-salen-DOX. The 'Gd' sample contained U251/alginate hydrogels labelled with Gd-DOTA-olaparib. The 'Tb' sample contained U251/alginate hydrogels labelled with Tb-DOTA-olaparib. The 'Fe' sample contained U251/alginate hydrogels labelled with Fe-salen-olaparib. **D.** Representative *R_2* maps of PCR tube containing labelled alginate hydrogels.

5.3.6 Toxicity of Theranostic Molecules Toward Cultured GBM Cells

Detailed earlier in this chapter, compounds such as olaparib and doxorubicin have a cytotoxic effect on cancer cells. A LIVE/DEAD assay was used to determine the toxicity of the small molecule compounds towards cultured glioblastoma cells. High calcien signal correlates to increased cell viability, whereas high ethidium dimer signal correlates to high cell death. All compounds displayed a decrease in calcien signal with increasing label concentration, with 0.5 mM labelling conditions displaying the lowest calcien signals (with the exception of the dead control).

For **Mn-salen-DOX:** a large significant decrease in calcien signal was observed between the live control (101.57%) and 0.1 mM (78.93%) labelling amounting to a 22.2% decrease in observed calcien signal. The largest decrease relative to the control was observed in the 0.5 mM (66.16 a.u) labelling condition (33.9% decrease, ****$p<0.0001$). For **Gd-DOTA-olaparib**, there was no significant change to calcien signal between the control and the 0.1 mM labelling condition, however there was an overall decrease. Significant decrease in calcien signal was observed at the 0.25 mM (86.57%, ***$p<0.001$) and 0. 5mM (76.30%, ****$p<0.0001$) representing a 14.8% and 24.9% respective decrease relative to the live control. Similarly, for **Tb-DOTA-olaparib**, there was no significant change to calcien signal between the control and the 0.1 mM labelling condition, however there was an overall decrease. Significant decrease in calcien signal was observed at the 0.25 mM (90.52% *$p<0.05$) and 0.5 mM (79.85%, ****$p<0.0001$) representing a 10.9% and 21.4% respective decrease relative to the live control. For **Fe-salen-olaparib,** significant decreases in calcien signal were observed for all labelling concentrations. 0.1 mM (95.36%, *$p<0.05$), 0.25 mM (85.64%, ****$p<0.0001$) and 0.5 (80.68%, ****$p<0.0001$) displayed a respective 6.1%, 15.7% and 20.6% decrease relative to the live control.

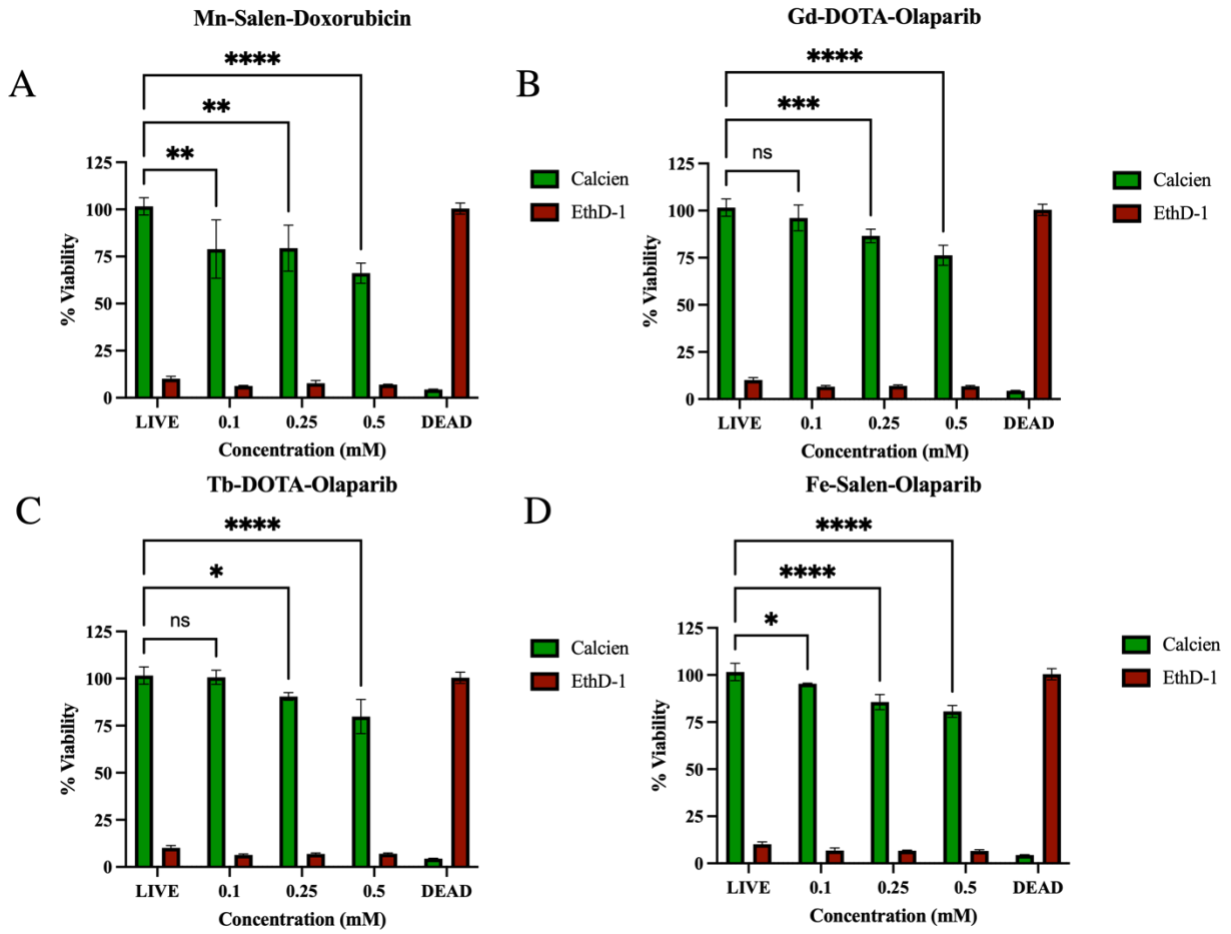

Figure 5.12 **-** LIVE/DEAD toxicity stain for selected small molecule compounds. For graphs A-D U251 cells were stained with respective compounds at 0.0 , 0.1, 0.25 and 0.5 mM. Live marker (calcien) is green and dead marker (EthD1) is red. *p<0.05, **p<0.01, ***p<0.001, ****p<0.0001 **A.** Graph displaying toxicity results for Mn-salen-DOX against U251 cells**. B.** Graph displaying toxicity results for Gd-DOTA-olaparib **C.** Graph displaying toxicity results for Tb-DOTA-olaparib **D.** Graph displaying toxicity results for Fe-salen-olaparib **E**. Representative fluorescent images for calcien staining was visualised using the green channel, where increased green signal correlates to an increase in esterase activity owing to increased cellular viability. The EthD-1 staining was visualised through the red channel, where increased red signal corresponds to decreased cell viability as a result of EthD1 permeating the cell membrane and intercalating with cellular DNA.

5.4 Discussion

Understanding of drug dynamics is limited to very few techniques. Pharmacokinetic (PK) and pharmacodynamic (PD) studies on drug behaviour in the brain have mostly been limited to ex-vivo mass spectrometry analysis, immunohistochemistry or PET-based detection of radiolabelled ligands.[388,389] Albeit, there are distinct challenges to recording drug dynamics in real time, especially when the drug of interest is conjugated to a radio-label or contrast agent. An imaging

technique with sufficient spatial resolution and sensitivity is required. Additionally conjugated drugs may not behave in the same way as non-conjugated drugs. Moreover, understanding of therapy response in conditions such as GBM is mostly limited to non-targeted imaging, where progression pseudoprogression are notoriously challenging to differentiate.[390,391] Precise understanding of therapeutic uptake is incredibly important in diseases such as GBM, especially given the limited success of available drug regimens.

Developing a toolkit of targeted, drug conjugated contrast agents can serve multiple purposes, including as research tools to better understand real time physiological processes, with potential for future translation to clinical practice. The hypothesis, at the beginning of this chapter, put forward that olaparib and DOX based contrast agents could serve as companion tool for monitoring drug uptake. From this, the main objectives of this chapter were to establish the proof of concept application of novel theranostic contrast agents to GBM with visualisation via MRI. Whilst not designed to completely replace conventional therapies, these theranostic platforms could act as a companion tool to help inform research into drug dynamics and efficacy.

In this chapter, four theranostic imaging complexes were investigated as agents for both imaging and exerting cytotoxic activity towards the GBM derived line, U251. These were: Mn-salen-DOX, Gd-DOTA-olaparib, Tb-DOTA-olaparib and Fe-salen-olaparib (see *figure 5.5*). These probes were selected as they offered a variety of different paramagnetic ion/ligand/cytotoxic drug combinations, which could be used for assessment of cellular drug uptake at a proof of concept level. This chapter has demonstrated the initial capabilities of these theranostic contrast agents for tracking cell uptake *in vitro*. On initial inspection, from the results described in this chapter, Mn-salen-DOX displayed several ideal properties for tracking cellular drug uptake, including

fluorescence, and favourable R_1 and R_2 relaxation rates. Furthermore, Mn-salen-DOX, amongst the other theranostic agents tested, displayed elevated cytotoxicity towards U251.

Previously mentioned in the introduction of this chapter, there are numerous challenges which make both imaging and treating brain tumours extremely challenging endeavours. Access to the brain is a challenge complicated by the BBB. There are also concerns of clearance and bioaccumulation of contrast agents following imaging, meaning there is an inherent risk/benefit trade-off associated with neuroimaging. A contrast agent platform that could track drug delivery, whilst maintaining expected drug behaviour and efficacy is highly desirable. In such, proof-of-concept testing of chelator-drug complexes such as those described within this chapter, can provide a basic platform for which promising drug complexes can be tested at an *in vivo* level, providing better insights into the delivery and efficacy of a given drug. Evidently, more optimisation around drug conjugation, delivery and safety will be required to translate these compounds, yet a preliminary understanding of which systems work well provides a stepping stone for the development of more effective, more biocompatible drugs.

5.4.1 Alginate Hydrogel Optimisation

Aim 'a' of the hypothesis testing was to generate a representative, 3-dimensional imaging phantom, that could allow for drug diffusion, provide a scaffold for imaging and allow for visualisation of cellular uptake. In order to address these aims, the first objective was to design an imaging medium that could both serve as an appropriate phantom for tissue, maintain appropriate cell culture conditions with good biocompatibility and allow for the appropriate diffusion of nutrients and compounds of interest. Alginate was selected as a hydrogel medium for the purpose of encapsulating U251. Previous studies have reported that cells maintain expected characteristic behaviours whilst suspended in alginate.[222,392–394] Importantly, alginate fabrication avoids heating,

which could cause damage to both cells and compounds. Fabrication of alginate hydrogel also allows for good control of gel elasticity, which can be modified to user requirements. It has also displayed T_1 & T_2 relaxation times close to that of human tissue.[221] Furthermore, whilst not applied in this study, alginate further benefits from optical transparency, which could allow for correlative optical imaging.[395,396] Alginate hydrogels also allows users to easily recover cells, which facilitates downstream testing applications.

In this chapter, alginate hydrogels were fabricated using multiple different needle and pipette tip sizes. Alginate hydrogels were formed by dispersion of alginate/media droplets into a calcium chloride bath, resulting in instant gel formation. From optimisation experiments, hydrogels formed using a p1000 tip offer an ideal combination of hydrogel size and circularity. Other needle/tip sizes tested in this chapter (*figure 5.8*) resulted in smaller hydrogels, less uniform hydrogels as visualised by brightfield microscopy. Subsequent experiments used the p1000 method for hydrogel fabrication, which allowed for facile, rapid encapsulation of U251 cells. Using this method, cells could be encapsulated either live or post-fixation. This approach also allows for live cell staining, making it an immensely beneficial tool for imaging applications. The alginate hydrogel approach allows for both 3-dimensional drug delivery and imaging of cells which allows for more representative modelling. Alginate hydrogels do have some limitations, however. There is limited control over how cells are distributed within the 3-dimensional space of a hydrogel system (see *figure 5.8c*), although control of size and shape of alginate hydrogels have been improved by use of microfluidics.[397] Additionally, inherent to the design of an alginate hydrogel, is the central calcium ion bound to hydroxyl groups of the polymeric α-L-guluronate units (see *figure 5.6a*). This Ca-OH binding means that alginate can rapidly disintegrate in the presence of phosphate buffers, forming calcium phosphate. Interestingly, whilst these properties are not ideal for the

present application, they have been exploited for drug release applications.[398–400] Potentially, alginate bound to MRI-active transition metal compounds could serve as useful tools for visualising hydrogel degradation in real time. Arguably, there are better options for forming uniform 3-dimensional cells models, such as spheroids, however the enhanced accessibility of the alginate technique remains highly attractive for imaging applications.

5.4.2 Theranostic Agent for Monitoring Cell Uptake of Drug

DOX and olaparib were selected as two drugs that could target GBM, and have the potential to enhance therapeutic outcomes.[401,402] DOX and olaparib based systems were designed with the intention of delivering a drug small enough to cross the BBB. DOTA and salen were selected as chelators that bind either lanthanide or transition metal ions while possessing sites that allow for conjugation of drug moieties, such as DOX and olaparib. DOTA-olaparib based systems have already been developed for PET applications, as previously mentioned in the introduction of this chapter.[370,371]

5.4.3 Fluorescent Screening of Mn-salen-DOX and U251

DOX has the added benefit of being a fluorescently active probe, which allows for optical detection. Mn-salen-DOX was screened for fluorescent activity following incubation with U251 cells. These fluorescent screens revealed high cellular uptake of Mn-salen-DOX. Fluorescent imaging of this chapter revealed DOX labelling of cells, and apparent absence of DAPI+ nuclear labelling. This could be due to intercalation competition between DAPI and DOX, which has previously been reported in with Hoechst dyes.[403] Clearly, more investigation is required into the activity of DOX and other nuclear dyes. However, the initial fluorescent results from this study suggest that there is uptake of Mn-salen-DOX by U251.

A potentially useful further experiment would involve correlative fluorescent/MR imaging of DOX distribution through alginate hydrogels to better understand molecular dynamics within the phantoms. Equally, DOX was not tested independently on U251, which could provide some insight into the behaviour of conjugated versus un-conjugated DOX.

Fluorescent validation of other olaparib based compounds were not be addressed in the same way as Mn-salen-DOX. One potential solution could be to use a conjugated fluorescent label for these compounds. However, fluorescent imaging does provide good insight into drug localisation, and provides substantive evidence that a given compound is behaving as expected. Initial insights from this study clearly suggest that the salen-DOX complex makes for an attractive ligand for other potential transition metals, given its small size and fluorescent activity.

5.4.4 MRI of Theranostic Drug Uptake in Alginate Hydrogels

MRI was then used to visualise these alginate phantoms, labelled with the panel of theranostic agents. Due time constraints, priority was given to optimising labelling for Mn-salen-DOX. Cells stained with Mn-salen-DOX at increasing concentrations were detached and encapsulated into an alginate hydrogel. These alginate hydrogels were then imaged via MRI, generating R_1 and R_2 relaxation rate maps (visualised in *figure 5.11*). These R_1 and R_2 maps revealed that 0.5 mM labelling provided a significant enhancement of R_1 and R_2 relaxation rates relative to the control.

Following on from this initial experiment, Mn-salen-DOX and the further three olaparib based compounds were used to label U251 cells for a further MRI screen. R_1 and R_2 maps were generated for each theranostic compound. Arguably, Mn-salen-DOX was the best performing compound, displaying favourable R_2 (9.15 s^{-1}), nearly a 2-fold enhancement relative to Gd-DOTA-olaparib. Mn-salen-DOX also displayed good T_1 properties relative to other compounds tested, with Gd-

DOTA-olaparib only outperforming Mn-salen-DOX in R_1 rate enhancement. This highlights the suitability of the manganese as an alternative paramagnetic ion to gadolinium. Alginate gels labelled with Mn-salen-DOX were visible on R_1 and R_2 maps in good detail.

5.4.5 Cytotoxicity of Theranostic Compounds Towards U251

Given that these theranostic agents are designed to map drug behaviour, it is important to understand if they can maintain cytotoxic effects. A LIVE/DEAD assay was used to assess both cell viability and agent cytotoxicity following 24 hours incubation with the theranostic agents. All compounds demonstrated significant changes to cell viability with increasing labelling concentration with 0.5 mM Mn-salen-DOX displaying the lowest cell viability.

5.5 Conclusion

The hypothesis stated at the beginning of this chapter was that olaparib and DOX based contrast agents could serve as a companion tool for monitoring cytotoxic drug uptake in tumour cells. In this proof of concept work, one theranostic platform, Mn-salen-DOX displayed especially favourable characteristics for monitoring cell uptake of cytotoxic drugs. The combined fluorescent and MR characteristics makes Mn-salen-DOX and attractive MR active analogue to DOX and certainly warrants further investigation.

5.6 Supplementary

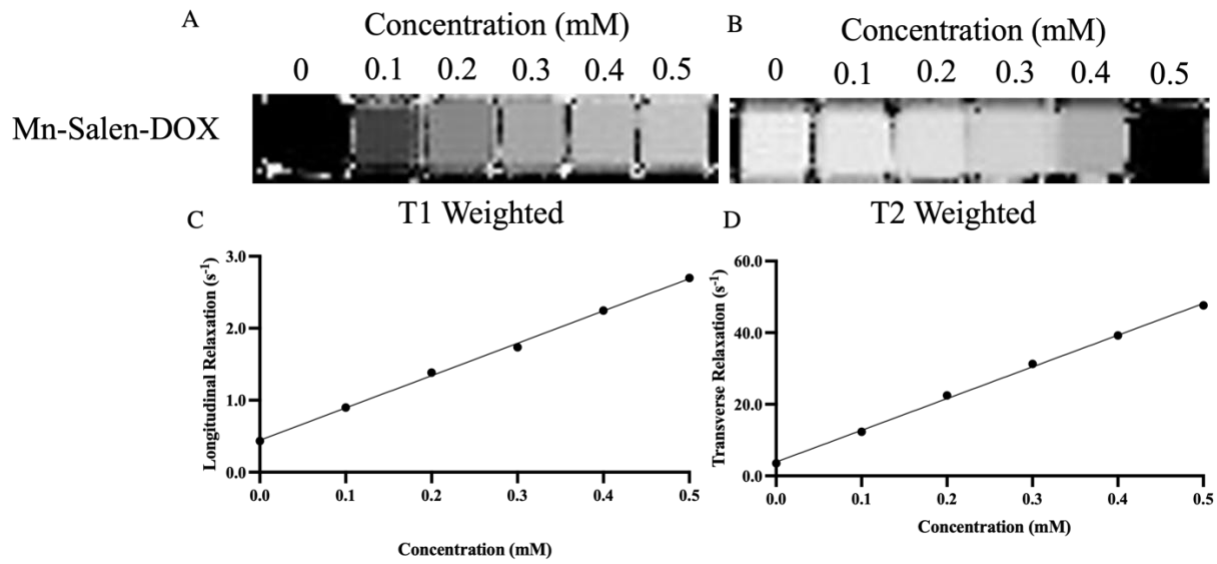

Figure 5.9 – Concentration dependent effects of Mn-salen-DOX on T_1 and T_2 relaxation times. **A.** T_1 weighted plate map of Mn-salen-DOX in increasing concentrations. **B.** T_2 weighted plate map of Mn-salen-DOX in increasing concentrations. **C.** T_1 relaxation of Mn-salen-DOX as a function concentration. **D.** T_2 relaxation of Mn-salen-DOX as a function concentration.

Chapter 6 - General Conclusion

6.1 Three Distinct Imaging Strategies

Throughout this thesis, three distinct magnetic resonance based imaging approaches for cell tracking were designed, developed and tested, each addressing key challenges for contrast agent development.

Chapter 3 explored the application of superparamagnetic iron oxide nanoparticles (SPIONs) to macrophage cell labelling applications. Central to this body of work is the modular streptavidin biotin system, which was used to selectively co-localise MR active streptavidin SPIONs to the cell surface of HLADR(+) M1 THP1. The demonstratable success of this labelling system, confirmed by both fluorescent and MR imaging, signifies an approach that could be used for labelling distinct immune cell types but also any cell type with a unique surface marker. The flexibility and modularity of the system means that direct conjugation methods are no longer required to achieve targeted imaging of a particular cell type. This massively simplifies target screening for downstream imaging applications. Equally the targeting moiety is not limited to antibodies; targeting peptidomimetics, small molecules or affibodies could all feasibly be used, so long as they have been appropriately biotinylated (or streptavidin linked, in the case of a biotin-linked contrast agent). From a contrast agent perspective, SPIONs were selected to delineate cell subpopulations as they offer the lowest minimum detection for any contrast agent. However, other imaging agents including those from other modalities may also be applied to this system.

Chapter 3 also documented the development of several imaging phantoms for visualising macrophage polarisation states. Latter development of 3D phantoms, described in this chapter allowed for 3D imaging of labelled cells via MRI. It is foreseeable that this style of imaging phantom could be used for live cell, real time MR experiments, given they satisfy the necessary biocompatibility requirements for cell culture. Further experiments achievable in the near term

might include co-culture imaging experiments, to visualise macrophages in concert with other distinct cell types. Beyond *in vitro* experiments, pre-clinical *in vivo* models of macrophage polarisation could be used to assess the performance of the streptavidin-biotin labelling system, in a complex organism.

Deuterium metabolic imaging is a rapidly developing field, with a core focus on non-invasive imaging of brain tumours. *Chapter 4* questioned the suitability of deuterium metabolic imaging approaches to delineate macrophage polarisations states. [6,6' $^{2}H_2$]-glucose based ^{2}H MRS was successful in positively identifying the glycolytic fingerprint of M1 macrophages. The downstream applications of imaging macrophage populations in this way are numerous. One application could be transplant rejection monitoring, where proinflammatory responses may occur over a prolonged period, where the alternative is biopsy. Whilst M1 macrophages and glycolytic tumours share similar metabolic fingerprints, screening of metabolic processes using clinically translatable probes such as [6,6' $^{2}H_2$]glucose may help identify any intermediate metabolites unique to cells of interest. Developing workflows and procedures for testing labelled substrates, as done here, can provide a useful framework for testing of further compounds. A potentially interesting avenue for probe development may be to develop deuterated arginine probes, given the differential metabolism of arginine in macrophage polarisation. Further experiments to be carried out in the medium term include screening of glioblastoma cell lines (including U251, GIN27,GIN31) with various deuterated compounds including [d^2]glucose and [d^7]-glucose. Ultimately, an overarching aim is to establish a screening approach that could be used alongside clinical level assessment of patients. The metabolic profile of patient derived samples could be visualised alongside clinical spectroscopy, providing a detailed fingerprint. Another approach that should be investigated is to

use mass spectrometry based techniques to visualise a metabolites that may not have sufficient concentration to be detected via NMR.

Chapter 5 explored the application of theranostic cytotoxic compounds for tracking drug dynamics. Salen and DOTA based compounds are extremely useful platforms for imaging, both in MRI and PET, allowing for direct conjugation of drug and/or diagnostic moieties. Two salen and two DOTA theranostic compounds were tested for their drug tracking capabilities against U251 glioblastoma (GBM). One of the theranostic compounds, Manganese-salen-DOX demonstrated promising characteristics for drug tracking and cell uptake at this initial stage of testing, with favourable R_1 and R_2 relaxation rates reported. This highlighted the potential of alternative non-gadolinium based theranostic compounds to study drug dynamics. Further understanding of drug dynamics is required, especially within the context of subcellular location of Mn-Salen-Dox. Therefore a useful experiment would be to apply a cytoplasm co-stain to identify the subcellular location of the compound. Further experiments to stratify the existing understanding of these theranostic compounds should involve longitudinal tracking of the compounds through an *in vivo* model.

6.2 A Combined Strategy?

In isolation, each of the strategies described in *Chapters 3-5* have obvious benefits for cell tracking and drug uptake. However, if combined into a multi-agent approach, these strategies have the potential to illuminate complex physiological processes, such as those taking place in GBM. Given GBM is a highly heterogenous disease, a MR approaches that could identify characteristics between many different cell populations would be especially useful for understanding intratumoral cell dynamics. *Figure 6.1* highlights a theoretical combined strategy to image different characteristics of tumour biology.

Interestingly, chemotherapeutic application of DOX may lead to increased immune cell infiltration to tumour lesions, including recruitment of CD8+ T cells and NK cells and differentiation of monocytes.[376] Furthermore work carried out by Taglang *et al* demonstrated that treatment of IDH(mut) positive astrocytomas with PARP inhibitors could be positively identified using deuterium MRS with [6,6'-^{2}H]-glucose at 14.1T. Further highlighting the exciting potential of combining these strategies.

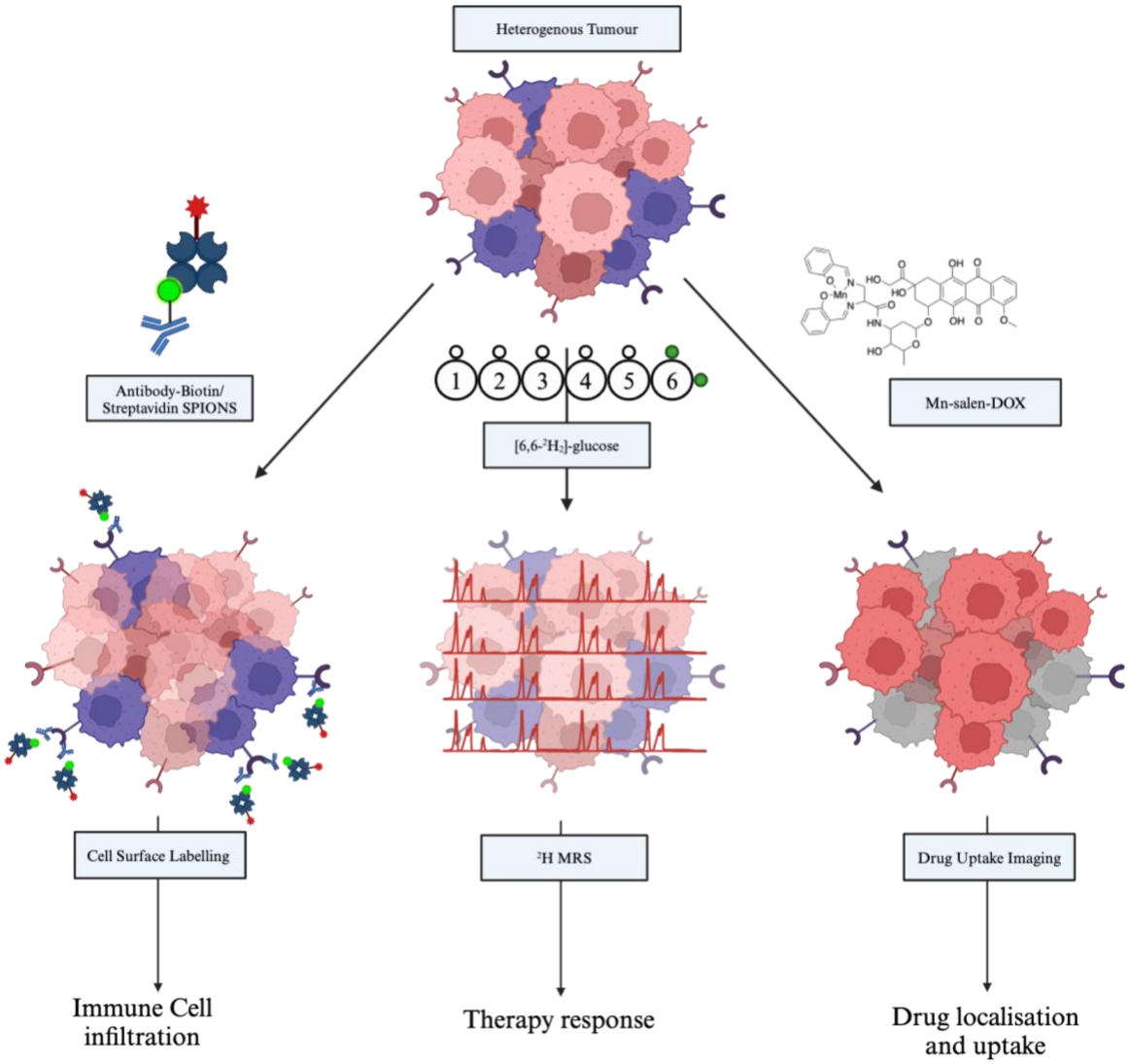

Figure 6.1 **-** Schematic illustrating multi-strategy approach to imaging a heterogenous tumour, such as GBM. In isolation, each strategy provides useful information relating to different aspects of the tumour. Used together, the imaging outputs could provide dynamic information relating to immune cell infiltration, therapy response and drug uptake. (Drawn using Biorender.com)

Chapter 7 - References

1. Ahrens, E. T. & Bulte, J. W. M. Tracking immune cells in vivo using magnetic resonance imaging. *Nat. Rev. Immunol.* **13**, 755–763 (2013).
2. Cheng, H.-L. M. A primer on in vivo cell tracking using MRI. *Front. Med.* **10**, 1193459 (2023).
3. Hoehn, M. *et al.* Cell tracking using magnetic resonance imaging. *J. Physiol.* **584**, 25–30 (2007).
4. Greten, F. R. & Grivennikov, S. I. Inflammation and Cancer: Triggers, Mechanisms, and Consequences. *Immunity* **51**, 27–41 (2019).
5. Amor, S., Puentes, F., Baker, D. & van der Valk, P. Inflammation in neurodegenerative diseases. *Immunology* **129**, 154–169 (2010).
6. Duan, L., Rao, X. & Sigdel, K. R. Regulation of Inflammation in Autoimmune Disease. *J. Immunol. Res.* **2019**, 7403796 (2019).
7. Chen, L. *et al.* Inflammatory responses and inflammation-associated diseases in organs. *Oncotarget* **9**, 7204–7218 (2018).
8. Mori, T., Asano, T. & Town, T. Targeting S100B in Cerebral Ischemia and in Alzheimer's Disease. *Cardiovasc. Psychiatry Neurol.* **2010**, 1–14 (2010).
9. Kim, S. Y. & Nair, M. G. Macrophages in wound healing: activation and plasticity. *Immunol. Cell Biol.* **97**, 258–267 (2019).
10. Wynn, T. A., Chawla, A. & Pollard, J. W. Macrophage biology in development, homeostasis and disease. *Nature* **496**, 445–455 (2013).

11. Albina, J. E., Mills, C. D., Henry, W. L. & Caldwell, M. D. Temporal expression of different pathways of 1-arginine metabolism in healing wounds. *J. Immunol. Baltim. Md 1950* **144**, 3877–3880 (1990).
12. Mills, C. D., Kincaid, K., Alt, J. M., Heilman, M. J. & Hill, A. M. M-1/M-2 Macrophages and the Th1/Th2 Paradigm. *J. Immunol.* **164**, 6166–6173 (2000).
13. Mills, C. D. Anatomy of a discovery: m1 and m2 macrophages. *Front. Immunol.* **6**, 212 (2015).
14. Orecchioni, M., Ghosheh, Y., Pramod, A. B. & Ley, K. Macrophage Polarization: Different Gene Signatures in M1(LPS+) vs. Classically and M2(LPS–) vs. Alternatively Activated Macrophages. *Front. Immunol.* **10**, 1084 (2019).
15. Martinez, F. O. & Gordon, S. The M1 and M2 paradigm of macrophage activation: time for reassessment. *F1000Prime Rep.* **6**, (2014).
16. Rőszer, T. Understanding the Mysterious M2 Macrophage through Activation Markers and Effector Mechanisms. *Mediators Inflamm.* **2015**, 1–16 (2015).
17. Wynn, T. A. & Vannella, K. M. Macrophages in Tissue Repair, Regeneration, and Fibrosis. *Immunity* **44**, 450–462 (2016).
18. Strizova, Z. *et al.* M1/M2 macrophages and their overlaps – myth or reality? *Clin. Sci. Lond. Engl. 1979* **137**, 1067–1093 (2023).
19. Yunna, C., Mengru, H., Lei, W. & Weidong, C. Macrophage M1/M2 polarization. *Eur. J. Pharmacol.* **877**, 173090 (2020).
20. Das, A. *et al.* Monocyte and Macrophage Plasticity in Tissue Repair and Regeneration. *Am. J. Pathol.* **185**, 2596–2606 (2015).

21. Gajanayaka, N. *et al.* TLR-4 Agonist Induces IFN-γ Production Selectively in Proinflammatory Human M1 Macrophages through the PI3K-mTOR– and JNK-MAPK–Activated p70S6K Pathway. *J. Immunol.* **207**, 2310–2324 (2021).
22. Thomas, L. *et al.* Selective upregulation of TNFα expression in classically-activated human monocyte-derived macrophages (M1) through pharmacological interference with V-ATPase. *Biochem. Pharmacol.* **130**, 71–82 (2017).
23. Munawara, U. *et al.* Hyperactivation of monocytes and macrophages in MCI patients contributes to the progression of Alzheimer's disease. *Immun. Ageing* **18**, 29 (2021).
24. Di Gregoli, K. *et al.* MicroRNA-24 regulates macrophage behavior and retards atherosclerosis. *Arterioscler. Thromb. Vasc. Biol.* **34**, 1990–2000 (2014).
25. Cao, Q. *et al.* Macrophages as a potential tumor-microenvironment target for noninvasive imaging of early response to anticancer therapy. *Biomaterials* **152**, 63–76 (2018).
26. Gaglia, J. L. *et al.* Noninvasive mapping of pancreatic inflammation in recent-onset type-1 diabetes patients. *Proc. Natl. Acad. Sci. U. S. A.* **112**, 2139–2144 (2015).
27. Cencini, E. *et al.* Evaluation of the prognostic role of tumour-associated macrophages in newly diagnosed classical Hodgkin lymphoma and correlation with early FDG-PET assessment. *Hematol. Oncol.* **35**, 69–78 (2017).
28. Pan, Y., Yu, Y., Wang, X. & Zhang, T. Tumor-Associated Macrophages in Tumor Immunity. *Front. Immunol.* **11**, 583084 (2020).
29. Tong, N. *et al.* Tumor Associated Macrophages, as the Dominant Immune Cells, Are an Indispensable Target for Immunologically Cold Tumor-Glioma Therapy? *Front. Cell Dev. Biol.* **9**, 706286 (2021).

30. Riabov, V. *et al.* Role of tumor associated macrophages in tumor angiogenesis and lymphangiogenesis. *Front. Physiol.* **5**, 75 (2014).

31. Lin, Y., Xu, J. & Lan, H. Tumor-associated macrophages in tumor metastasis: biological roles and clinical therapeutic applications. *J. Hematol. Oncol.J Hematol Oncol* **12**, 76 (2019).

32. Shen, H. *et al.* Prognostic Value of Tumor-Associated Macrophages in Clear Cell Renal Cell Carcinoma: A Systematic Review and Meta-Analysis. *Front. Oncol.* **11**, 657318 (2021).

33. Wang, C. *et al.* The Prognostic and Clinical Value of Tumor-Associated Macrophages in Patients With Breast Cancer: A Systematic Review and Meta-Analysis. *Front. Oncol.* **12**, 905846 (2022).

34. Sigalov, A. B. Nature-inspired nanoformulations for contrast-enhanced *in vivo* MR imaging of macrophages: NANOFORMULATIONS FOR TARGETED MRI OF MACROPHAGES. *Contrast Media Mol. Imaging* **9**, 372–382 (2014).

35. Melancon, M. P. *et al.* Targeted imaging of tumor-associated M2 macrophages using a macromolecular contrast agent PG-Gd-NIR813. *Biomaterials* **31**, 6567–6573 (2010).

36. Bruckman, M. A., Randolph, L. N., Gulati, N. M., Stewart, P. L. & Steinmetz, N. F. Silica-coated Gd(DOTA)-loaded protein nanoparticles enable magnetic resonance imaging of macrophages. *J. Mater. Chem. B* **3**, 7503–7510 (2015).

37. Bendszus, M. & Stoll, G. Caught in the Act: *In Vivo* Mapping of Macrophage Infiltration in Nerve Injury by Magnetic Resonance Imaging. *J. Neurosci.* **23**, 10892–10896 (2003).

38. Cai, Q.-Y. *et al.* Magnetic resonance imaging of superparamagnetic iron oxide-labeled macrophage infiltrates in acute-phase renal ischemia-reperfusion mouse model. *Nanomedicine Nanotechnol. Biol. Med.* **8**, 365–373 (2012).

39. Montet-Abou, K. *et al.* In vivo labelling of resting monocytes in the reticuloendothelial system with fluorescent iron oxide nanoparticles prior to injury reveals that they are mobilized to infarcted myocardium. *Eur. Heart J.* **31**, 1410–1420 (2010).

40. Selt, M. *et al.* In Vivo Non-Invasive Tracking of Macrophage Recruitment to Experimental Stroke. *PLOS ONE* **11**, e0156626 (2016).

41. Bierry, G., Lefevre, S., Dietemann, J.-L. & Jehl, F. In vivo Macrophage Imaging Using MR Targeted Contrast Agent for Longitudinal Evaluation of Septic Arthritis. *J. Vis. Exp.* 50296 (2013) doi:10.3791/50296.

42. Temme, S., Bönner, F., Schrader, J. & Flögel, U. ^{19} F magnetic resonance imaging of endogenous macrophages in inflammation: ^{19} F MRI of endogenous macrophages in inflammation. *Wiley Interdiscip. Rev. Nanomed. Nanobiotechnol.* **4**, 329–343 (2012).

43. Khurana, A. *et al.* Visualization of macrophage recruitment in head and neck carcinoma model using fluorine-19 magnetic resonance imaging. *Magn. Reson. Med.* **79**, 1972–1980 (2018).

44. Cho, H. *et al.* Visualizing inflammation with an M1 macrophage selective probe via GLUT1 as the gating target. *Nat. Commun.* **13**, 5974 (2022).

45. Fernandez, A. *et al.* Chemical Modulation of in Vivo Macrophage Function with Subpopulation-Specific Fluorescent Prodrug Conjugates. *ACS Cent. Sci.* **3**, 995–1005 (2017).

46. Lee, C. *et al.* In vivo delineation of glioblastoma by targeting tumor-associated macrophages with near-infrared fluorescent silica coated iron oxide nanoparticles in orthotopic xenografts for surgical guidance. *Sci. Rep.* **8**, 11122 (2018).

47. Abdul-Hamid, N. A. *et al.* 1H-NMR-based metabolomics to investigate the effects of *Phoenix dactylifera* seed extracts in LPS-IFN-γ-induced RAW 264.7 cells. *Food Res. Int.* **125**, 108565 (2019).

48. Qiao, K., Le Page, L. M. & Chaumeil, M. M. Non-Invasive Differentiation of M1 and M2 Activation in Macrophages Using Hyperpolarized 13C MRS of Pyruvate and DHA at 1.47 Tesla. *Metabolites* **11**, 410 (2021).

49. Fuchs, A. L. *et al.* Quantitative 1H NMR Metabolomics Reveal Distinct Metabolic Adaptations in Human Macrophages Following Differential Activation. *Metabolites* **9**, (2019).

50. Bulte, J. W. M. Science to Practice: Can MR Imaging Cell Tracking of Macrophage Infiltration Be Used as a Predictive Imaging Biomarker for Transplanted Stem Cell Rejection? *Radiology* **284**, 307–309 (2017).

51. Abuawad, A., Mbadugha, C., Ghaemmaghami, A. M. & Kim, D.-H. Metabolic characterisation of THP-1 macrophage polarisation using LC–MS-based metabolite profiling. *Metabolomics* **16**, 33 (2020).

52. Suvannapruk, W. *et al.* Single-Cell Metabolic Profiling of Macrophages Using 3D OrbiSIMS: Correlations with Phenotype. *Anal. Chem.* **94**, 9389–9398 (2022).

53. Foss, C. A. *et al.* Biodistribution and Radiation Dosimetry of 124I-DPA-713, a PET Radiotracer for Macrophage-Associated Inflammation. *J. Nucl. Med.* **59**, 1751–1756 (2018).

54. Hellberg, S. *et al.* Positron Emission Tomography Imaging of Macrophages in Atherosclerosis with 18F-GE-180, a Radiotracer for Translocator Protein (TSPO). *Contrast Media Mol. Imaging* **2018**, 9186902 (2018).

55. Yoon, S. *et al.* Recent advances in optical imaging through deep tissue: imaging probes and techniques. *Biomater. Res.* **26**, 57 (2022).

56. Sprinz, C. *et al.* Effects of blood glucose level on 18F fluorodeoxyglucose (18F-FDG) uptake for PET/CT in normal organs: an analysis on 5623 patients. *Sci. Rep.* **8**, 2126 (2018).

57. So, P.-W., Ashraf, A., Durieux, A. M. S., Crum, W. R. & Bell, J. D. The Application of In Vivo MRI and MRS in Phenomic Studies of Murine Models of Disease. in *Modern Magnetic Resonance* (ed. Webb, G. A.) 19–62 (Springer International Publishing, Cham, 2018). doi:10.1007/978-3-319-28388-3_95.

58. Grover, V. P. B. *et al.* Magnetic Resonance Imaging: Principles and Techniques: Lessons for Clinicians. *J. Clin. Exp. Hepatol.* **5**, 246–255 (2015).

59. Bloch, F. Nuclear Induction. *Phys. Rev.* **70**, 460–474 (1946).

60. Purcell, E. M., Torrey, H. C. & Pound, R. V. Resonance Absorption by Nuclear Magnetic Moments in a Solid. *Phys. Rev.* **69**, 37–38 (1946).

61. Arnold, T. C., Freeman, C. W., Litt, B. & Stein, J. M. Low-field MRI: Clinical promise and challenges. *J. Magn. Reson. Imaging* **57**, 25–44 (2023).

62. Metzner, R. *et al.* Direct comparison of MRI and X-ray CT technologies for 3D imaging of root systems in soil: potential and challenges for root trait quantification. *Plant Methods* **11**, 17 (2015).

63. Boulant, N. & Quettier, L. Commissioning of the Iseult CEA 11.7 T whole-body MRI: current status, gradient–magnet interaction tests and first imaging experience. *Magma N. Y. N* **36**, 175–189 (2023).

64. Gold, G. E. *et al.* Musculoskeletal MRI at 3.0 T: Relaxation Times and Image Contrast. *Am. J. Roentgenol.* **183**, 343–351 (2004).

65. Alvares, R. D. A., Szulc, D. A. & Cheng, H.-L. M. A scale to measure MRI contrast agent sensitivity. *Sci. Rep.* **7**, 15493 (2017).

66. Marasini, R., Thanh Nguyen, T. D. & Aryal, S. Integration of gadolinium in nanostructure for contrast enhanced-magnetic resonance imaging. *WIREs Nanomedicine Nanobiotechnology* **12**, (2020).

67. Yang, R., Sarkar, S., Yong, V. W. & Dunn, J. F. In Vivo MR Imaging of Tumor-Associated Macrophages: The Next Frontier in Cancer Imaging. *Magn. Reson. Insights* **11**, (2018).

68. Dimelow, R. J., Burton, N. A. & Hillier, I. H. The dynamics of water exchange in gadolinium DOTA complexes studied by transition path sampling and potential of mean force methods. *Phys. Chem. Chem. Phys.* **9**, 1318–1323 (2007).

69. Rogosnitzky, M. & Branch, S. Gadolinium-based contrast agent toxicity: a review of known and proposed mechanisms. *BioMetals* **29**, 365–376 (2016).

70. Marckmann, P. *et al.* Nephrogenic Systemic Fibrosis: Suspected Causative Role of Gadodiamide Used for Contrast-Enhanced Magnetic Resonance Imaging. *J. Am. Soc. Nephrol.* **17**, 2359–2362 (2006).

71. Weng, T.-I. *et al.* Exposure of Macrophages to Low-Dose Gadolinium-Based Contrast Medium: Impact on Oxidative Stress and Cytokines Production. *Contrast Media Mol. Imaging* **2018**, 1–10 (2018).

72. Hao, D. *et al.* MRI contrast agents: Basic chemistry and safety. *J. Magn. Reson. Imaging* **36**, 1060–1071 (2012).

73. Ishiguchi, T. & Takahashi, S. Safety of Gadoterate Meglumine (Gd-DOTA) as a Contrast Agent for Magnetic Resonance Imaging: Results of a Post-Marketing Surveillance Study in Japan. *Drugs RD* **10**, 133–145 (2010).

74. Patel, S. K. & Janjic, J. M. Macrophage targeted theranostics as personalized nanomedicine strategies for inflammatory diseases. *Theranostics* **5**, 150–172 (2015).

75. Leung, A. H.-H., Jin, J., Wang, S., Lei, H. & Wong, W.-T. Inflammation Targeted Gd3+-Based MRI Contrast Agents Imaging Tumor and Rheumatoid Arthritis Models. *Bioconjug. Chem.* **25**, 1112–1123 (2014).

76. Narayan, N. *et al.* Translocator Protein as an Imaging Marker of Macrophage and Stromal Activation in Rheumatoid Arthritis Pannus. *J. Nucl. Med.* **59**, 1125–1132 (2018).

77. Hou, Z. *et al.* Gadolinium-conjugated CB86: a novel TSPO-targeting MRI contrast agent for imaging of rheumatoid arthritis. *J. Drug Target.* **28**, 398–407 (2020).

78. Kim, Y.-S. *et al.* Synthesis and characterization of gadolinium—Peptidomimetic complex as an αvβ3 integrin targeted MR contrast agent. *Bioorg. Med. Chem. Lett.* **25**, 2056–2059 (2015).

79. Sturzu, A. & Heckl, S. Magnetic Resonance Imaging of Human Glioma Cells by means of an Interleukin-6 Receptor-Targeted Contrast Agent. *Chem. Biol. Drug Des.* **75**, 369–374 (2010).

80. Ayat, N. R. *et al.* Effective MR Molecular Imaging of Triple Negative Breast Cancer With an EDB-Fibronectin-Specific Contrast Agent at Reduced Doses. *Front. Oncol.* **9**, 1351 (2019).

81. Xin, X. *et al.* Coupling Gd-DTPA with a bispecific, recombinant protein anti-EGFR-iRGD complex improves tumor targeting in MRI. *Oncol. Rep.* **35**, 3227–3235 (2016).

82. Jun, H. Y. *et al.* Visualization of Tumor Angiogenesis Using MR Imaging Contrast Agent Gd-DTPA-anti-VEGF Receptor 2 Antibody Conjugate in a Mouse Tumor Model. *Korean J. Radiol.* **11**, 449 (2010).

83. Maiseyeu, A. *et al.* Gadolinium-containing phosphatidylserine liposomes for molecular imaging of atherosclerosis. *J. Lipid Res.* **50**, 2157–2163 (2009).

84. Gao, L. *et al.* A Novel Gd-DTPA-conjugated Poly(L-γ-glutamyl-glutamine)-paclitaxel Polymeric Delivery System for Tumor Theranostics. *Sci. Rep.* **7**, 3799 (2017).

85. Jackson, E. F. *et al.* Magnetic resonance imaging of therapy-induced necrosis using gadolinium-chelated polyglutamic acids. *Int. J. Radiat. Oncol. Biol. Phys.* **68**, 830–838 (2007).

86. Wang, S. *et al.* Increased Retention of Gadolinium in the Inflamed Brain After Repeated Administration of Gadopentetate Dimeglumine: A Proof-of-Concept Study in Mice Combining ICP-MS and Micro– and Nano–SR-XRF. *Invest. Radiol.* **54**, 617–626 (2019).

87. Xiao, Y.-D. *et al.* MRI contrast agents: Classification and application (Review). *Int. J. Mol. Med.* **38**, 1319–1326 (2016).

88. Toth, G. B. *et al.* Current and potential imaging applications of ferumoxytol for magnetic resonance imaging. *Kidney Int.* **92**, 47–66 (2017).

89. Chavhan, G. B., Babyn, P. S., Thomas, B., Shroff, M. M. & Haacke, E. M. Principles, techniques, and applications of T2*-based MR imaging and its special applications. *Radiogr. Rev. Publ. Radiol. Soc. N. Am. Inc* **29**, 1433–1449 (2009).

90. Dadfar, S. M. *et al.* Iron oxide nanoparticles: Diagnostic, therapeutic and theranostic applications. *Adv. Drug Deliv. Rev.* **138**, 302–325 (2019).

91. Marcos-Contreras, O. A. *et al.* Selective targeting of nanomedicine to inflamed cerebral vasculature to enhance the blood-brain barrier. *Proc. Natl. Acad. Sci. U. S. A.* **117**, 3405–3414 (2020).

92. Husain, S. F. *et al.* Locating the Site of Neuropathic Pain *In Vivo* Using MMP-12-Targeted Magnetic Nanoparticles. *Pain Res. Manag.* **2019**, 1–11 (2019).

93. Khurana, A. *et al.* Cell sorting microbeads as novel contrast agent for magnetic resonance imaging. *Sci. Rep.* **12**, 17640 (2022).

94. Weise, G. & Stoll, G. Magnetic Resonance Imaging of Blood Brain/Nerve Barrier Dysfunction and Leukocyte Infiltration: Closely Related or Discordant? *Front. Neurol.* **3**, (2012).

95. Ye, Y.-X. *et al.* Monitoring of Monocyte Recruitment in Reperfused Myocardial Infarction With Intramyocardial Hemorrhage and Microvascular Obstruction by Combined Fluorine 19 and Proton Cardiac Magnetic Resonance Imaging. *Circulation* **128**, 1878–1888 (2013).

96. Yang, Y., Yang, Y., Yanasak, N., Schumacher, A. & Hu, T. C.-C. Temporal and noninvasive monitoring of inflammatory-cell infiltration to myocardial infarction sites using micrometer-sized iron oxide particles: MPIO-Enhanced Cardiac MRI. *Magn. Reson. Med.* **63**, 33–40 (2010).

97. Wu, Y. L. *et al.* Magnetic Resonance Imaging Investigation of Macrophages in Acute Cardiac Allograft Rejection After Heart Transplantation. *Circ. Cardiovasc. Imaging* **6**, 965–973 (2013).

98. Leftin, A., Ben-Chetrit, N., Joyce, J. A. & Koutcher, J. A. Imaging endogenous macrophage iron deposits reveals a metabolic biomarker of polarized tumor macrophage infiltration and response to CSF1R breast cancer immunotherapy. *Sci. Rep.* **9**, 857 (2019).

99. Leftin, A. *et al.* Iron deposition is associated with differential macrophage infiltration and therapeutic response to iron chelation in prostate cancer. *Sci. Rep.* **7**, 11632 (2017).

100. Kirschbaum, K. *et al.* In vivo nanoparticle imaging of innate immune cells can serve as a marker of disease severity in a model of multiple sclerosis. *Proc. Natl. Acad. Sci.* **113**, 13227–13232 (2016).

101. Shin, S. H., Park, S. H., Kim, S. W., Kim, M. & Kim, D. Fluorine MR Imaging Monitoring of Tumor Inflammation after High-Intensity Focused Ultrasound Ablation. *Radiology* **287**, 476–484 (2018).

102. Constantinides, C. *et al.* Improved cellular uptake of perfluorocarbon nanoparticles for in vivo murine cardiac 19F MRS/MRI and temporal tracking of progenitor cells. *Nanomedicine Nanotechnol. Biol. Med.* **18**, 391–401 (2019).

103. Jacoby, C. *et al.* Probing different perfluorocarbons for *in vivo* inflammation imaging by ^{19}F MRI: image reconstruction, biological half-lives and sensitivity: PERFLUOROCARBONS FOR *IN VIVO* INFLAMMATION IMAGING BY ^{19}F MRI. *NMR Biomed.* **27**, 261–271 (2014).

104. Janjic, J. M. & Ahrens, E. T. Fluorine-containing nanoemulsions for MRI cell tracking: Fluorine-containing nanoemulsions for MRI cell tracking. *Wiley Interdiscip. Rev. Nanomed. Nanobiotechnol.* **1**, 492–501 (2009).

105. Zhong, J., Mills, P. H., Hitchens, T. K. & Ahrens, E. T. Accelerated fluorine-19 MRI cell tracking using compressed sensing: ^{19} F Cell Tracking Using Compressed Sensing. *Magn. Reson. Med.* **69**, 1683–1690 (2013).

106. Zhong, J., Narsinh, K., Morel, P. A., Xu, H. & Ahrens, E. T. In Vivo Quantification of Inflammation in Experimental Autoimmune Encephalomyelitis Rats Using Fluorine-19 Magnetic Resonance Imaging Reveals Immune Cell Recruitment outside the Nervous System. *PLOS ONE* **10**, e0140238 (2015).

107. Bönner, F. *et al.* Monocyte imaging after myocardial infarction with 19F MRI at 3 T: a pilot study in explanted porcine hearts. *Eur. Heart J. - Cardiovasc. Imaging* **16**, 612–620 (2015).

108. Shin, S. H. *et al.* Fluorine-19 Magnetic Resonance Imaging and Positron Emission Tomography of Tumor-Associated Macrophages and Tumor Metabolism. *Contrast Media Mol. Imaging* **2017**, 1–8 (2017).

109. Chaussy, C. G. & Thüroff, S. High-Intensity Focused Ultrasound for the Treatment of Prostate Cancer: A Review. *J. Endourol.* **31**, S-30-S-37 (2017).

110. Ahrens, E. T., Helfer, B. M., O'Hanlon, C. F. & Schirda, C. Clinical cell therapy imaging using a perfluorocarbon tracer and fluorine-19 MRI. *Magn. Reson. Med.* **72**, 1696–1701 (2014).

111. Ribot, E., Gaudet, J., Chen, Y., Gilbert, K. & Foster, P. In vivo MR detection of fluorine-labeled human MSC using the bSSFP sequence. *Int. J. Nanomedicine* 1731 (2014) doi:10.2147/IJN.S59127.

112. Makela, A. V., Gaudet, J. M. & Foster, P. J. Quantifying tumor associated macrophages in breast cancer: a comparison of iron and fluorine-based MRI cell tracking. *Sci. Rep.* **7**, 42109 (2017).

113. Aoki, I. *et al.* Cell labeling for magnetic resonance imaging with the T1 agent manganese chloride. *NMR Biomed.* **19**, 50–59 (2006).

114. Dash, R. *et al.* Manganese-enhanced MRI enables longitudinal tracking of transplanted stem cell viability in the murine myocardium. *J. Cardiovasc. Magn. Reson.* **16**, O95 (2014).

115. Gupta, A., Caravan, P., Price, W. S., Platas-Iglesias, C. & Gale, E. M. Applications for Transition Metal Chemistry in Contrast Enhanced Magnetic Resonance Imaging. *Inorg. Chem.* **59**, 6648–6678 (2020).

116. Hancu, I. *et al.* CEST and PARACEST MR contrast agents. *Acta Radiol. Stockh. Swed. 1987* **51**, 910–923 (2010).

117. Aime, S., Carrera, C., Delli Castelli, D., Geninatti Crich, S. & Terreno, E. Tunable Imaging of Cells Labeled with MRI-PARACEST Agents. *Angew. Chem. Int. Ed.* **44**, 1813–1815 (2005).

118. Wu, B. *et al.* An overview of CEST MRI for non-MR physicists. *EJNMMI Phys.* **3**, 19 (2016).

119. Bie, C., van Zijl, P., Xu, J., Song, X. & Yadav, N. N. Radiofrequency (RF) Labeling Strategies in Chemical Exchange Saturation Transfer (CEST) MRI. *NMR Biomed.* **36**, e4944 (2023).

120. Vinogradov, E., Sherry, A. D. & Lenkinski, R. E. CEST: From basic principles to applications, challenges and opportunities. *J. Magn. Reson.* **229**, 155–172 (2013).

121. Ferrauto, G., Delli Castelli, D., Terreno, E. & Aime, S. In vivo MRI visualization of different cell populations labeled with PARACEST agents. *Magn. Reson. Med.* **69**, 1703–1711 (2013).

122. Faubert, B., Solmonson, A. & DeBerardinis, R. J. Metabolic reprogramming and cancer progression. *Science* **368**, eaaw5473 (2020).

123. Assmann, J. C. *et al.* Glycolytic metabolism of pathogenic T cells enables early detection of GVHD by 13C-MRI. *Blood* **137**, 126–137 (2021).

124. Brindle, K. New approaches for imaging tumour responses to treatment. *Nat. Rev. Cancer* **8**, 94–107 (2008).

125. Soares, D. P. & Law, M. Magnetic resonance spectroscopy of the brain: review of metabolites and clinical applications. *Clin. Radiol.* **64**, 12–21 (2009).

126. Chaumeil, M. M., Najac, C. & Ronen, S. M. Studies of Metabolism Using 13C MRS of Hyperpolarized Probes. in *Methods in Enzymology* (ed. Metallo, C. M.) vol. 561 1–71 (Academic Press, 2015).

127. Wilson, M. *et al.* Methodological consensus on clinical proton MRS of the brain: Review and recommendations. *Magn. Reson. Med.* **82**, 527–550 (2019).

128. Bonavita, S., Di Salle, F. & Tedeschi, G. Proton MRS in neurological disorders. *Eur. J. Radiol.* **30**, 125–131 (1999).

129. Ladd, M. E. *et al.* Pros and cons of ultra-high-field MRI/MRS for human application. *Prog. Nucl. Magn. Reson. Spectrosc.* **109**, 1–50 (2018).

130. Chang, L., Munsaka, S. M., Kraft-Terry, S. & Ernst, T. Magnetic Resonance Spectroscopy to Assess NeuroInflammation and Neuropathic Pain. *J. Neuroimmune Pharmacol.* **8**, 576–593 (2013).

131. Ashwal, S. *et al.* Proton Spectroscopy Detected Myoinositol in Children with Traumatic Brain Injury. *Pediatr. Res.* **56**, 630–638 (2004).

132. Kantarci, K. Magnetic Resonance Spectroscopy in Common Dementias. *Neuroimaging Clin. N. Am.* **23**, 393–406 (2013).

133. Kantarci, K. Proton MRS in Mild Cognitive Impairment. *J. Magn. Reson. Imaging JMRI* **37**, 770–777 (2013).

134. Castillo, M., Smith, J. K. & Kwock, L. Correlation of Myo-inositol Levels and Grading of Cerebral Astrocytomas. *AJNR Am. J. Neuroradiol.* **21**, 1645–1649 (2000).

135. Laino, M. E. *et al.* Magnetic resonance spectroscopic imaging in gliomas: clinical diagnosis and radiotherapy planning. *BJR Open* **2**, 20190026 (2020).

136. King, N. J. C., Ward, M. H. & Holmes, K. T. Magnetic resonance studies of murine macrophages: Proliferation is not a prerequisite for acquisition of an 'activated' high resolution spectrum. *FEBS Lett.* **287**, 97–101 (1991).

137. Mishra, S. K., Kumar, B. S. H., Khushu, S., Singh, A. K. & Gangenahalli, G. Early monitoring and quantitative evaluation of macrophage infiltration after experimental traumatic brain injury: A magnetic resonance imaging and flow cytometric analysis. *Mol. Cell. Neurosci.* **78**, 25–34 (2017).

138. Chen Ming Low, J., Wright, A. J., Hesse, F., Cao, J. & Brindle, K. M. Metabolic imaging with deuterium labeled substrates. *Prog. Nucl. Magn. Reson. Spectrosc.* **134–135**, 39–51 (2023).

139. Kurhanewicz, J., Bok, R., Nelson, S. J. & Vigneron, D. B. Current and Potential Applications of Clinical 13C MR Spectroscopy. *J. Nucl. Med.* **49**, 341–344 (2008).

140. Shulman, G. I. *et al.* Quantitation of muscle glycogen synthesis in normal subjects and subjects with non-insulin-dependent diabetes by 13C nuclear magnetic resonance spectroscopy. *N. Engl. J. Med.* **322**, 223–228 (1990).

141. Ardenkjær-Larsen, J. H. *et al.* Increase in signal-to-noise ratio of > 10,000 times in liquid-state NMR. *Proc. Natl. Acad. Sci.* **100**, 10158–10163 (2003).

142. Ardenkjaer-Larsen, J. H. On the present and future of dissolution-DNP. *J. Magn. Reson.* **264**, 3–12 (2016).

143. Boumezbeur, F. *et al.* The Contribution of Blood Lactate to Brain Energy Metabolism in Humans Measured by Dynamic 13C Nuclear Magnetic Resonance Spectroscopy. *J. Neurosci.* **30**, 13983–13991 (2010).

144. Miller, J. J. *et al.* 13C Pyruvate Transport Across the Blood-Brain Barrier in Preclinical Hyperpolarised MRI. *Sci. Rep.* **8**, 15082 (2018).

145. Anderson, S., Grist, J. T., Lewis, A. & Tyler, D. J. Hyperpolarized 13 C magnetic resonance imaging for noninvasive assessment of tissue inflammation. *NMR Biomed.* **34**, e4460 (2021).

146. Ursprung, S. *et al.* Hyperpolarized 13C-Pyruvate Metabolism as a Surrogate for Tumor Grade and Poor Outcome in Renal Cell Carcinoma-A Proof of Principle Study. *Cancers* **14**, 335 (2022).

147. Østergaard Mariager, C. *et al.* Can Hyperpolarized 13C-Urea be Used to Assess Glomerular Filtration Rate? A Retrospective Study. *Tomography* **3**, 146–152 (2017).

148. Friesen-Waldner, L. J. *et al.* Hyperpolarized choline as an MR imaging molecular probe: Feasibility of in vivo imaging in a rat model. *J. Magn. Reson. Imaging* **41**, 917–923 (2015).

149. Koellisch, U. *et al.* Metabolic imaging of hyperpolarized [1-(13) C]acetate and [1-(13) C]acetylcarnitine - investigation of the influence of dobutamine induced stress. *Magn. Reson. Med.* **74**, 1011–1018 (2015).

150. Najac, C. *et al.* Detection of inflammatory cell function using 13C magnetic resonance spectroscopy of hyperpolarized [6-13C]-arginine. *Sci. Rep.* **6**, 31397 (2016).

151. Larson, P. E. Z. *et al.* Current methods for hyperpolarized [1-13C]pyruvate MRI human studies. *Magn. Reson. Med.* **91**, 2204–2228 (2024).

152. Park, I. *et al.* Hyperpolarized 13C magnetic resonance metabolic imaging: application to brain tumors. *Neuro-Oncol.* **12**, 133–144 (2010).

153. Grist, J. T. *et al.* Quantifying normal human brain metabolism using hyperpolarized [1–13C]pyruvate and magnetic resonance imaging. *NeuroImage* **189**, 171–179 (2019).

154. Svyatova, A. *et al.* PHIP hyperpolarized [1-13C]pyruvate and [1-13C]acetate esters via PH-INEPT polarization transfer monitored by 13C NMR and MRI. *Sci. Rep.* **11**, 5646 (2021).

155. Viola, A., Munari, F., Sánchez-Rodríguez, R., Scolaro, T. & Castegna, A. The Metabolic Signature of Macrophage Responses. *Front. Immunol.* **10**, 1462 (2019).

156. Wang, T. *et al.* HIF1α-Induced Glycolysis Metabolism Is Essential to the Activation of Inflammatory Macrophages. *Mediators Inflamm.* **2017**, 9029327 (2017).

157. Sriram, R. *et al.* Molecular detection of inflammation in cell models using hyperpolarized 13C-pyruvate. *Theranostics* **8**, 3400–3407 (2018).

158. Can, E. *et al.* Noninvasive rapid detection of metabolic adaptation in activated human T lymphocytes by hyperpolarized 13C magnetic resonance. *Sci. Rep.* **10**, 200 (2020).

159. Lewis, A. J. M. *et al.* Noninvasive Immunometabolic Cardiac Inflammation Imaging Using Hyperpolarized Magnetic Resonance. *Circ. Res.* **122**, 1084–1093 (2018).

160. Mishkovsky, M. *et al.* Measuring glucose cerebral metabolism in the healthy mouse using hyperpolarized 13C magnetic resonance. *Sci. Rep.* **7**, 11719 (2017).

161. MacKenzie, J. D. *et al.* Detection of Inflammatory Arthritis by Using Hyperpolarized 13C-Pyruvate with MR Imaging and Spectroscopy. *Radiology* **259**, 414–420 (2011).

162. Kreis, F. *et al.* Measuring Tumor Glycolytic Flux in Vivo by Using Fast Deuterium MRI. *Radiology* **294**, 289–296 (2020).

163. Polvoy, I. *et al.* Deuterium Metabolic Imaging—Rediscovery of a Spectroscopic Tool. *Metabolites* **11**, 570 (2021).

164. De Feyter, H. M. & De Graaf, R. A. Deuterium metabolic imaging – Back to the future. *J. Magn. Reson.* **326**, 106932 (2021).

165. Cocking, D. *et al.* Deuterium brain imaging at 7T during D2O dosing. *Magn. Reson. Med.* **89**, 1514–1521 (2023).

166. Cember, A. T. J. *et al.* Integrating 1H MRS and deuterium labeled glucose for mapping the dynamics of neural metabolism in humans. *NeuroImage* **251**, 118977 (2022).

167. Ruhm, L. *et al.* Deuterium metabolic imaging in the human brain at 9.4 Tesla with high spatial and temporal resolution. *NeuroImage* **244**, 118639 (2021).

168. Hesse, F. *et al.* Monitoring tumor cell death in murine tumor models using deuterium magnetic resonance spectroscopy and spectroscopic imaging. *Proc. Natl. Acad. Sci.* **118**, e2014631118 (2021).

169. Ip, K. L., Thomas, M. A., Behar, K. L., de Graaf, R. A. & De Feyter, H. M. Mapping of exogenous choline uptake and metabolism in rat glioblastoma using deuterium metabolic imaging (DMI). *Front. Cell. Neurosci.* **17**, 1130816 (2023).

170. De Feyter, H. M. *et al.* Deuterium metabolic imaging (DMI) for MRI-based 3D mapping of metabolism in vivo. *Sci. Adv.* **4**, eaat7314 (2018).

171. Watanabe, S., Alexander, M., Misharin, A. V. & Budinger, G. R. S. The role of macrophages in the resolution of inflammation. *J. Clin. Invest.* **129**, 2619–2628.

172. Hirayama, D., Iida, T. & Nakase, H. The Phagocytic Function of Macrophage-Enforcing Innate Immunity and Tissue Homeostasis. *Int. J. Mol. Sci.* **19**, 92 (2017).

173. Butterfield, T. A., Best, T. M. & Merrick, M. A. The dual roles of neutrophils and macrophages in inflammation: a critical balance between tissue damage and repair. *J. Athl. Train.* **41**, 457–465 (2006).

174. Anderson, J. M., Rodriguez, A. & Chang, D. T. Foreign body reaction to biomaterials. *Semin. Immunol.* **20**, 86–100 (2008).

175. Aderem, A. & Underhill, D. M. Mechanisms of phagocytosis in macrophages. *Annu. Rev. Immunol.* **17**, 593–623 (1999).

176. Mantovani, A., Allavena, P., Marchesi, F. & Garlanda, C. Macrophages as tools and targets in cancer therapy. *Nat. Rev. Drug Discov.* **21**, 799–820 (2022).

177. Murray, P. J. Macrophage Polarization. *Annu. Rev. Physiol.* **79**, 541–566 (2017).

178. Rostam, H. M. *et al.* Immune-Instructive Polymers Control Macrophage Phenotype and Modulate the Foreign Body Response In Vivo. *Matter* **2**, 1564–1581 (2020).

179. Li, L. *et al.* Superparamagnetic Iron Oxide Nanoparticles as MRI contrast agents for Non-invasive Stem Cell Labeling and Tracking. *Theranostics* **3**, 595–615 (2013).

180. George, S., Georgouli, M. & Sanz-Moreno, V. Protocol to drive human monocyte-to-macrophage polarization in vitro using tumor conditioned media. *STAR Protoc.* **3**, 101666 (2022).

181. Zarif, J. C. *et al.* A phased strategy to differentiate human CD14+ monocytes into classically-activated, alternatively activated macrophages and dendritic cells. *BioTechniques* **61**, 33–41 (2016).

182. Genin, M., Clement, F., Fattaccioli, A., Raes, M. & Michiels, C. M1 and M2 macrophages derived from THP-1 cells differentially modulate the response of cancer cells to etoposide. *BMC Cancer* **15**, 577 (2015).

183. Tedesco, S. *et al.* Convenience versus Biological Significance: Are PMA-Differentiated THP-1 Cells a Reliable Substitute for Blood-Derived Macrophages When Studying in Vitro Polarization? *Front. Pharmacol.* **9**, 71 (2018).

184. Bates, D., Abraham, S., Campbell, M., Zehbe, I. & Curiel, L. Development and Characterization of an Antibody-Labeled Super-Paramagnetic Iron Oxide Contrast Agent Targeting Prostate Cancer Cells for Magnetic Resonance Imaging. *PLoS ONE* **9**, e97220 (2014).

185. Crețu, B. E.-B. *et al.* Imaging Constructs: The Rise of Iron Oxide Nanoparticles. *Molecules* **26**, 3437 (2021).

186. Korchinski, D. J., Taha, M., Yang, R., Nathoo, N. & Dunn, J. F. Iron Oxide as an MRI Contrast Agent for Cell Tracking. *Magn. Reson. Insights* **8**, 15–29 (2015).

187. Wahsner, J., Gale, E. M., Rodríguez-Rodríguez, A. & Caravan, P. Chemistry of MRI Contrast Agents: Current Challenges and New Frontiers. *Chem. Rev.* **119**, 957–1057 (2019).

188. Yang, C.-Y. *et al.* Labeling of human mesenchymal stem cell: Comparison between paramagnetic and superparamagnetic agents. *J. Appl. Phys.* **105**, 07B314 (2009).

189. Xie, J., Liu, G., Eden, H. S., Ai, H. & Chen, X. Surface-Engineered Magnetic Nanoparticle Platforms for Cancer Imaging and Therapy. *Acc. Chem. Res.* **44**, 883–892 (2011).

190. Kim, S. J. *et al.* Superparamagnetic Iron Oxide Nanoparticles for Direct Labeling of Stem Cells and In Vivo MRI Tracking. *Contrast Media Mol. Imaging* **11**, 55–64 (2016).

191. Naha, P. C. *et al.* Dextran-Coated Iron Oxide Nanoparticles as Biomimetic Catalysts for Localized and pH-Activated Biofilm Disruption. *ACS Nano* **13**, 4960–4971 (2019).

192. Mulens-Arias, V., Rojas, J. M. & Barber, D. F. The Use of Iron Oxide Nanoparticles to Reprogram Macrophage Responses and the Immunological Tumor Microenvironment. *Front. Immunol.* **12**, 693709 (2021).

193. Chanput, W., Mes, J. J., Savelkoul, H. F. J. & Wichers, H. J. Characterization of polarized THP-1 macrophages and polarizing ability of LPS and food compounds. *Food Funct* **4**, 266–276 (2013).

194. Forrester, M. A. *et al.* Similarities and differences in surface receptor expression by THP-1 monocytes and differentiated macrophages polarized using seven different conditioning regimens. *Cell. Immunol.* **332**, 58–76 (2018).

195. Yunna, C., Mengru, H., Lei, W. & Weidong, C. Macrophage M1/M2 polarization. *Eur. J. Pharmacol.* **877**, 173090 (2020).

196. Portillo, G., Turner, M., Chantry, D. & Feldmann, M. Effect of cytokines on HLA-DR and IL-1 production by a monocytic tumour, THP-1. *Immunology* **66**, 170–175 (1989).

197. Piatnitskaia, S. *et al.* Modelling of macrophage responses to biomaterials in vitro: state-of-the-art and the need for the improvement. *Front. Immunol.* **15**, 1349461 (2024).

198. Van Gorp, H., Delputte, P. L. & Nauwynck, H. J. Scavenger receptor CD163, a Jack-of-all-trades and potential target for cell-directed therapy. *Mol. Immunol.* **47**, 1650–1660 (2010).

199. Hickman, E. *et al.* Expanded characterization of in vitro polarized M0, M1, and M2 human monocyte-derived macrophages: Bioenergetic and secreted mediator profiles. *PLOS ONE* **18**, e0279037 (2023).

200. Wei, Q., Deng, Y., Yang, Q., Zhan, A. & Wang, L. The markers to delineate different phenotypes of macrophages related to metabolic disorders. *Front. Immunol.* **14**, 1084636 (2023).

201. Nelson, N. R., Port, J. D. & Pandey, M. K. Use of Superparamagnetic Iron Oxide Nanoparticles (SPIONs) via Multiple Imaging Modalities and Modifications to Reduce Cytotoxicity: An Educational Review. *J. Nanotheranostics* **1**, 105–135 (2020).

202. Daldrup-Link, H. E. *et al.* MRI of Tumor-Associated Macrophages with Clinically Applicable Iron Oxide Nanoparticles. *Clin. Cancer Res.* **17**, 5695–5704 (2011).

203. Sousa de Almeida, M. *et al.* Understanding nanoparticle endocytosis to improve targeting strategies in nanomedicine. *Chem. Soc. Rev.* **50**, 5397–5434.

204. Dulińska-Litewka, J. *et al.* Superparamagnetic Iron Oxide Nanoparticles—Current and Prospective Medical Applications. *Materials* **12**, 617 (2019).

205. Frantellizzi, V. *et al.* New Frontiers in Molecular Imaging with Superparamagnetic Iron Oxide Nanoparticles (SPIONs): Efficacy, Toxicity, and Future Applications. *Nucl. Med. Mol. Imaging* **54**, 65–80 (2020).

206. Polasky, C. *et al.* Impact of Superparamagnetic Iron Oxide Nanoparticles on THP-1 Monocytes and Monocyte-Derived Macrophages. *Front. Mol. Biosci.* **9**, 811116 (2022).

207. Matsushita, T. *et al.* Inflammatory imaging with ultrasmall superparamagnetic iron oxide. *Magn. Reson. Imaging* **29**, 173–178 (2011).

208. McKinnon, K. M. Flow Cytometry: An Overview. *Curr. Protoc. Immunol.* **120**, 5.1.1-5.1.11 (2018).

209. Hersh, A. M., Alomari, S. & Tyler, B. M. Crossing the Blood-Brain Barrier: Advances in Nanoparticle Technology for Drug Delivery in Neuro-Oncology. *Int. J. Mol. Sci.* **23**, 4153 (2022).

210. Wu, Z. *et al.* Advances in magnetic resonance imaging contrast agents for glioblastoma-targeting theranostics. *Regen. Biomater.* **8**, rbab062 (2021).

211. Petithory, T. *et al.* Size-Dependent Internalization Efficiency of Macrophages from Adsorbed Nanoparticle-Based Monolayers. *Nanomaterials* **11**, 1963 (2021).

212. Feng, Q. *et al.* Uptake, distribution, clearance, and toxicity of iron oxide nanoparticles with different sizes and coatings. *Sci. Rep.* **8**, 2082 (2018).

213. Katikaneni, D. S. & Jina, L. B cell MHC class II signaling: A story of life and death. *Hum. Immunol.* **80**, 37–43 (2019).

214. Collin, M. & Bigley, V. Human dendritic cell subsets: an update. *Immunology* **154**, 3–20 (2018).

215. Ayer, M. *et al.* Biotin–NeutrAvidin Mediated Immobilization of Polymer Micro- and Nanoparticles on T Lymphocytes. *Bioconjug. Chem.* **32**, 541–552 (2021).

216. Zhang, Y. P. *et al.* Improved Imaging Surface for Quantitative Single-Molecule Microscopy. *ACS Appl. Mater. Interfaces* **16**, 37255–37264 (2024).

217. Fang, Y., Malik, M., England, S. K. & Imoukhuede, P. I. Absolute Quantification of Plasma Membrane Receptors via Quantitative Flow Cytometry. *Methods Mol. Biol. Clifton NJ* **2475**, 61–77 (2022).

218. Feray, A. *et al.* How to Address the Adjuvant Effects of Nanoparticles on the Immune System. *Nanomaterials* **10**, 425 (2020).

219. Sehl, O. C. & Foster, P. J. The sensitivity of magnetic particle imaging and fluorine-19 magnetic resonance imaging for cell tracking. *Sci. Rep.* **11**, 22198 (2021).

220. Blahut, J. *et al.* Paramagnetic 19F Relaxation Enhancement in Nickel(II) Complexes of N-Trifluoroethyl Cyclam Derivatives and Cell Labeling for 19F MRI. *Inorg. Chem.* **56**, 13337–13348 (2017).

221. Hellerbach, A., Schuster, V., Jansen, A. & Sommer, J. MRI Phantoms – Are There Alternatives to Agar? *PLoS ONE* **8**, e70343 (2013).

222. Caliari, S. R. & Burdick, J. A. A practical guide to hydrogels for cell culture. *Nat. Methods* **13**, 405–414 (2016).

223. Walter, A. *et al.* Correlated Multimodal Imaging in Life Sciences: Expanding the Biomedical Horizon. *Front. Phys.* **8**, (2020).

224. Marty, B. *et al.* Hindered diffusion of MRI contrast agents in rat brain extracellular micro-environment assessed by acquisition of dynamic T1 and T2 maps. *Contrast Media Mol. Imaging* **8**, 12–19 (2013).

225. Rohm, T. V., Meier, D. T., Olefsky, J. M. & Donath, M. Y. Inflammation in obesity, diabetes, and related disorders. *Immunity* **55**, 31–55 (2022).

226. Grivennikov, S. I., Greten, F. R. & Karin, M. Immunity, inflammation, and cancer. *Cell* **140**, 883–899 (2010).

227. Hanahan, D. & Weinberg, R. A. Hallmarks of Cancer: The Next Generation. *Cell* **144**, 646–674 (2011).

228. Noversa De Sousa, R. *et al.* Metabolic and molecular imaging in inflammatory arthritis. *RMD Open* **10**, e003880 (2024).

229. Jang, C., Chen, L. & Rabinowitz, J. D. Metabolomics and Isotope Tracing. *Cell* **173**, 822–837 (2018).

230. Vaishnavi, S. N. *et al.* Regional aerobic glycolysis in the human brain. *Proc. Natl. Acad. Sci.* **107**, 17757–17762 (2010).

231. Ganapathy-Kanniappan, S. & Geschwind, J.-F. H. Tumor glycolysis as a target for cancer therapy: progress and prospects. *Mol. Cancer* **12**, 152 (2013).

232. Sawayama, H. *et al.* Clinical impact of the Warburg effect in gastrointestinal cancer (Review). *Int. J. Oncol.* **45**, 1345–1354 (2014).

233. Ma, S. *et al.* The Warburg effect in patients with brain tumors: a comprehensive analysis of clinical significance. *J. Neurooncol.* **165**, 219–226 (2023).

234. Naifeh, J., Dimri, M. & Varacallo, M. Biochemistry, Aerobic Glycolysis. in *StatPearls [Internet]* (StatPearls Publishing, 2023).

235. Warburg, O., Wind, F. & Negelein, E. THE METABOLISM OF TUMORS IN THE BODY. *J. Gen. Physiol.* **8**, 519–530 (1927).

236. Hay, N. Reprogramming glucose metabolism in cancer: can it be exploited for cancer therapy? *Nat. Rev. Cancer* **16**, 635–649 (2016).

237. Vander Heiden, M. G., Cantley, L. C. & Thompson, C. B. Understanding the Warburg Effect: The Metabolic Requirements of Cell Proliferation. *Science* **324**, 1029–1033 (2009).

238. Adekola, K., Rosen, S. T. & Shanmugam, M. Glucose transporters in cancer metabolism. *Curr. Opin. Oncol.* **24**, 650–654 (2012).

239. Szablewski, L. Expression of glucose transporters in cancers. *Biochim. Biophys. Acta BBA - Rev. Cancer* **1835**, 164–169 (2013).

240. Carvalho, K. C. *et al.* GLUT1 expression in malignant tumors and its use as an immunodiagnostic marker. *Clinics* **66**, 965–972 (2011).

241. Qiu, S. *et al.* Small molecule metabolites: discovery of biomarkers and therapeutic targets. *Signal Transduct. Target. Ther.* **8**, 1–37 (2023).

242. Nagana Gowda, G. A. *et al.* Metabolomics-Based Methods for Early Disease Diagnostics: A Review. *Expert Rev. Mol. Diagn.* **8**, 617–633 (2008).

243. Wang, W. *et al.* Cancer metabolites: promising biomarkers for cancer liquid biopsy. *Biomark. Res.* **11**, 66 (2023).

244. Wang, S. *et al.* Metabolomics study reveals systematic metabolic dysregulation and early detection markers associated with incident pancreatic cancer. *Int. J. Cancer* **150**, 1091–1100 (2022).

245. Liu, Y. *et al.* Metabolic reprogramming in macrophage responses. *Biomark. Res.* **9**, 1 (2021).

246. Corcoran, S. E. & O'Neill, L. A. J. HIF1α and metabolic reprogramming in inflammation. *J. Clin. Invest.* **126**, 3699–3707.

247. Blagih, J. & Jones, R. G. Polarizing Macrophages through Reprogramming of Glucose Metabolism. *Cell Metab.* **15**, 793–795 (2012).

248. Menk, A. V. *et al.* Early TCR Signaling Induces Rapid Aerobic Glycolysis Enabling Distinct Acute T Cell Effector Functions. *Cell Rep.* **22**, 1509–1521 (2018).

249. Pantel, A. R., Ackerman, D., Lee, S.-C., Mankoff, D. A. & Gade, T. P. Imaging Cancer Metabolism: Underlying Biology and Emerging Strategies. *J. Nucl. Med.* **59**, 1340–1349 (2018).

250. Koh, T. J. & DiPietro, L. A. Inflammation and wound healing: the role of the macrophage. *Expert Rev. Mol. Med.* **13**, e23 (2011).

251. Biswas, S. K. & Mantovani, A. Macrophage plasticity and interaction with lymphocyte subsets: cancer as a paradigm. *Nat. Immunol.* **11**, 889–896 (2010).

252. Vishwakarma, A. *et al.* Engineering Immunomodulatory Biomaterials To Tune the Inflammatory Response. *Trends Biotechnol.* **34**, 470–482 (2016).

253. Rostam, H. M., Reynolds, P. M., Alexander, M. R., Gadegaard, N. & Ghaemmaghami, A. M. Image based Machine Learning for identification of macrophage subsets. *Sci. Rep.* **7**, 3521 (2017).

254. Jayasingam, S. D. *et al.* Evaluating the Polarization of Tumor-Associated Macrophages Into M1 and M2 Phenotypes in Human Cancer Tissue: Technicalities and Challenges in Routine Clinical Practice. *Front. Oncol.* **9**, 1512 (2020).

255. Fukui, S. *et al.* M1 and M2 Monocytes in Rheumatoid Arthritis: A Contribution of Imbalance of M1/M2 Monocytes to Osteoclastogenesis. *Front. Immunol.* **8**, 1958 (2018).

256. Mosser, D. M. & Edwards, J. P. Exploring the full spectrum of macrophage activation. *Nat. Rev. Immunol.* **8**, 958–969 (2008).

257. Zhang, Y., Zou, J. & Chen, R. An M0 macrophage-related prognostic model for hepatocellular carcinoma. *BMC Cancer* **22**, 791 (2022).

258. Yu, Q. *et al.* Regulations of Glycolytic Activities on Macrophages Functions in Tumor and Infectious Inflammation. *Front. Cell. Infect. Microbiol.* **10**, 287 (2020).

259. De Feyter, H. M. *et al.* Deuterium metabolic imaging (DMI) for MRI-based 3D mapping of metabolism in vivo. *Sci. Adv.* **4**, eaat7314.

260. Brindle, K. M. Imaging cancer metabolism using magnetic resonance. *Npj Imaging* **2**, 1–5 (2024).

261. Di Gialleonardo, V., Wilson, D. M. & Keshari, K. R. The Potential of Metabolic Imaging. *Semin. Nucl. Med.* **46**, 28–39 (2016).

262. Peppicelli, S., Andreucci, E., Ruzzolini, J., Bianchini, F. & Calorini, L. FDG uptake in cancer: a continuing debate. *Theranostics* **10**, 2944–2948 (2020).

263. Almuhaideb, A., Papathanasiou, N. & Bomanji, J. 18F-FDG PET/CT Imaging In Oncology. *Ann. Saudi Med.* **31**, 3–13 (2011).

264. Gallagher, B. M. *et al.* Metabolic trapping as a principle of oradiopharmaceutical design: some factors resposible for the biodistribution of [18F] 2-deoxy-2-fluoro-D-glucose. *J. Nucl. Med. Off. Publ. Soc. Nucl. Med.* **19**, 1154–1161 (1978).

265. Parker, C. C. & Lapi, S. E. Positron Emission Tomography Imaging of Macrophages in Cancer. *Cancers* **13**, 1921 (2021).

266. Ohashi, T. *et al.* The importance of FDG-PET/CT parameters for the assessment of the immune status in advanced HNSCC. *Auris. Nasus. Larynx* **47**, 658–667 (2020).

267. Li, J., Zheng, H., Fodah, R., Warawa, J. M. & Ng, C. K. Validation of 2-18F-Fluorodeoxysorbitol as a Potential Radiopharmaceutical for Imaging Bacterial Infection in the Lung. *J. Nucl. Med. Off. Publ. Soc. Nucl. Med.* **59**, 134–139 (2018).

268. Pauwels, E. K. *et al.* FDG accumulation and tumor biology. *Nucl. Med. Biol.* **25**, 317–322 (1998).

269. Chang, J. M. *et al.* False Positive and False Negative FDG-PET Scans in Various Thoracic Diseases. *Korean J. Radiol.* **7**, 57–69 (2006).

270. Jones, R. G. & Thompson, C. B. Tumor suppressors and cell metabolism: a recipe for cancer growth. *Genes Dev.* **23**, 537–548 (2009).

271. Rahman, W. T. *et al.* The impact of infection and inflammation in oncologic 18F-FDG PET/CT imaging. *Biomed. Pharmacother.* **117**, 109168 (2019).

272. Ruiz-Rodado, V., Brender, J. R., Cherukuri, M. K., Gilbert, M. R. & Larion, M. Magnetic resonance spectroscopy for the study of cns malignancies. *Prog. Nucl. Magn. Reson. Spectrosc.* **122**, 23–41 (2021).

273. Rich, L. J. *et al.* 1H magnetic resonance spectroscopy of 2H-to-1H exchange quantifies the dynamics of cellular metabolism in vivo. *Nat. Biomed. Eng.* **4**, 335–342 (2020).

274. Brender, J. R. *et al.* Dynamic Imaging of Glucose and Lactate Metabolism by 13C-MRS without Hyperpolarization. *Sci. Rep.* **9**, 3410 (2019).

275. Miceli, A. *et al.* 18F-Fluorodeoxyglucose Positron Emission Tomography Tracks the Heterogeneous Brain Susceptibility to the Hyperglycemia-Related Redox Stress. *Int. J. Mol. Sci.* **21**, (2020).

276. Sriram, R. *et al.* Molecular detection of inflammation in cell models using hyperpolarized ^{13}C-pyruvate. *Theranostics* **8**, 3400–3407 (2018).

277. Woitek, R. & Brindle, K. M. Hyperpolarized Carbon-13 MRI in Breast Cancer. *Diagnostics* **13**, 2311 (2023).

278. Lumata, L. *et al.* HYPERPOLARIZED 13C MAGNETIC RESONANCE AND ITS USE IN METABOLIC ASSESSMENT OF CULTURED CELLS AND PERFUSED ORGANS. *Methods Enzymol.* **561**, 73–106 (2015).

279. Khan, A. S. *et al.* Deuterium Metabolic Imaging of Alzheimer Disease at 3-T Magnetic Field Strength: A Pilot Case-Control Study. *Radiology* **312**, e232407 (2024).

280. Brereton, I. M., Doddrell, D. M., Oakenfull, S. M., Moss, D. & Irving, M. G. The use of in vivo 2H NMR spectroscopy to investigate the effects of obesity and diabetes mellitus upon lipid metabolism in mice. *NMR Biomed.* **2**, 55–60 (1989).

281. Batsios, G. *et al.* Deuterium Metabolic Imaging Reports on TERT Expression and Early Response to Therapy in Cancer. *Clin. Cancer Res.* **28**, 3526–3536 (2022).

282. Bitencourt, A. G. V. *et al.* Deuterium MR spectroscopy: potential applications in oncology research. *BJR|Open* **6**, tzae019 (2023).

283. Klein, M. S. Affine Transformation of Negative Values for NMR Metabolomics Using the mrbin R Package. *J. Proteome Res.* **20**, 1397–1404 (2021).

284. Claridge, T. D. W. Chapter 5 - Introducing Two-Dimensional and Pulsed Field Gradient NMR. in *High-Resolution NMR Techniques in Organic Chemistry (Third Edition)* (ed. Claridge, T. D. W.) 171–202 (Elsevier, Boston, 2016). doi:10.1016/B978-0-08-099986-9.00005-1.

285. Koletzko, B., Sauerwald, T. & Demmelmair, H. Safety of stable isotope use. *Eur. J. Pediatr.* **156 Suppl 1**, S12-17 (1997).

286. Flocke, V., Temme, S., Bouvain, P., Grandoch, M. & Flögel, U. Noninvasive assessment of metabolic turnover during inflammation by in vivo deuterium magnetic resonance spectroscopy. *Front. Immunol.* **14**, 1258027 (2023).

287. On the magnetic field dependence of deuterium metabolic imaging - Graaf - 2020 - NMR in Biomedicine - Wiley Online Library. https://analyticalsciencejournals.onlinelibrary.wiley.com/doi/abs/10.1002/nbm.4235?casa_t

oken=gzteJxvEI9oAAAAA:SP8LOlxwXoRy7kb5jW7LHQ7yvvALW50QNDTZWVBc1O9m8m378IhUCYd0x-J5miRAIj0uUaTFWsQchj8.

288. Mahar, R., Donabedian, P. L. & Merritt, M. E. HDO production from [2H7]glucose Quantitatively Identifies Warburg Metabolism. *Sci. Rep.* **10**, 8885 (2020).

289. Simpson, R. J., Brindle, K. M., Brown, F. F., Campbell, I. D. & Foxall, D. L. Studies of pyruvate-water isotope exchange catalysed by erythrocytes and proteins. *Biochem. J.* **193**, 401–406 (1981).

290. Wiberg, K. B. The Deuterium Isotope Effect. *Chem. Rev.* **55**, 713–743 (1955).

291. Ghonge, N. P., Goyal, N., Vohra, S. & Chowdhury, V. Renal transplant evaluation: multimodality imaging of post-transplant complications. *Br. J. Radiol.* **94**, 20201253 (2021).

292. Eng, J., Berkowitz, B. A. & Balaban, R. S. Renal distribution and metabolism of [2H9]choline. A 2H NMR and MRI study. *NMR Biomed.* **3**, 173–177 (1990).

293. Katz-Brull, R., Margalit, R., Bendel, P. & Degani, H. Choline metabolism in breast cancer; 2H-, 13C- and 31p-NMR studies of cells and tumors.

294. Okada, T., Muto, E., Yamanaka, T., Uchino, H. & Inazu, M. Functional Expression of Choline Transporters in Microglia and Their Regulation of Microglial M1/M2 Polarization. *Int. J. Mol. Sci.* **23**, 8924 (2022).

295. Ghorbani, P. *et al.* Choline metabolism underpins macrophage IL-4 polarization and RELMα up-regulation in helminth infection. 2022.09.30.510305 Preprint at https://doi.org/10.1101/2022.09.30.510305 (2023).

296. Korotcov, A. V. *et al.* Glucosamine-Linked Near-Infrared Fluorescent Probes for Imaging of Solid Tumor Xenografts. *Mol. Imaging Biol.* **14**, 443–451 (2012).

297. Yoshioka, K. *et al.* Intracellular Fate of 2-NBDG, a Fluorescent Probe for Glucose Uptake Activity, in Escherichia coli Cells. *Biosci. Biotechnol. Biochem.* **60**, 1899–1901 (1996).

298. Davis, M. Glioblastoma: Overview of Disease and Treatment. *Clin. J. Oncol. Nurs.* **20**, S2–S8 (2016).

299. Dymova, M. A., Kuligina, E. V. & Richter, V. A. Molecular Mechanisms of Drug Resistance in Glioblastoma. *Int. J. Mol. Sci.* **22**, 6385 (2021).

300. Monteiro, A., Hill, R., Pilkington, G. & Madureira, P. The Role of Hypoxia in Glioblastoma Invasion. *Cells* **6**, 45 (2017).

301. Rong, Y., Durden, D. L., Van Meir, E. G. & Brat, D. J. 'Pseudopalisading' Necrosis in Glioblastoma: A Familiar Morphologic Feature That Links Vascular Pathology, Hypoxia, and Angiogenesis. *J. Neuropathol. Exp. Neurol.* **65**, 529–539 (2006).

302. Koshy, M. *et al.* Improved survival time trends for glioblastoma using the SEER 17 population-based registries. *J. Neurooncol.* **107**, 207–212 (2012).

303. Sofroniew, M. V. & Vinters, H. V. Astrocytes: biology and pathology. *Acta Neuropathol. (Berl.)* **119**, 7–35 (2010).

304. Pekny, M., Wilhelmsson, U. & Pekna, M. The dual role of astrocyte activation and reactive gliosis. *Neurosci. Lett.* **565**, 30–38 (2014).

305. Stupp, R. *et al.* Radiotherapy plus Concomitant and Adjuvant Temozolomide for Glioblastoma. *N. Engl. J. Med.* **352**, 987–996 (2005).

306. Bjorland, L. S., Fluge, O., Gilje, B., Mahesparan, R. & Farbu, E. Treatment approach and survival from glioblastoma: results from a population-based retrospective cohort study from Western Norway. *BMJ Open* **11**, e043208 (2021).

307. Angom, R. S., Nakka, N. M. R. & Bhattacharya, S. Advances in Glioblastoma Therapy: An Update on Current Approaches. *Brain Sci.* **13**, 1536 (2023).

308. Patel, A. P. *et al.* Single-cell RNA-seq highlights intratumoral heterogeneity in primary glioblastoma. *Science* **344**, 1396–1401 (2014).

309. Cruz, J. V. R. *et al.* Obstacles to Glioblastoma Treatment Two Decades after Temozolomide. *Cancers* **14**, 3203 (2022).

310. Putavet, D. A. & de Keizer, P. L. J. Residual Disease in Glioma Recurrence: A Dangerous Liaison with Senescence. *Cancers* **13**, 1560 (2021).

311. Becker, A. P., Sells, B. E., Haque, S. J. & Chakravarti, A. Tumor Heterogeneity in Glioblastomas: From Light Microscopy to Molecular Pathology. *Cancers* **13**, 761 (2021).

312. Wu, W. *et al.* Glioblastoma multiforme (GBM): An overview of current therapies and mechanisms of resistance. *Pharmacol. Res.* **171**, 105780 (2021).

313. Sottoriva, A. *et al.* Intratumor heterogeneity in human glioblastoma reflects cancer evolutionary dynamics. *Proc. Natl. Acad. Sci. U. S. A.* **110**, 4009–4014 (2013).

314. Noorani, I. & de la Rosa, J. Breaking barriers for glioblastoma with a path to enhanced drug delivery. *Nat. Commun.* **14**, 5909 (2023).

315. Wu, D. *et al.* The blood–brain barrier: Structure, regulation and drug delivery. *Signal Transduct. Target. Ther.* **8**, 1–27 (2023).

316. Pardridge, W. M. CNS drug design based on principles of blood-brain barrier transport. *J. Neurochem.* **70**, 1781–1792 (1998).

317. Tsuji, A. & Tamai, I. Carrier-mediated or specialized transport of drugs across the blood-brain barrier. *Adv. Drug Deliv. Rev.* **36**, 277–290 (1999).

318. Hynynen, K., McDannold, N., Vykhodtseva, N. & Jolesz, F. A. Non-invasive opening of BBB by focused ultrasound. *Acta Neurochir. Suppl.* **86**, 555–558 (2003).

319. Iuchi, T. *et al.* Long-term effectiveness of Gliadel implant for malignant glioma and prognostic factors for survival: 3-year results of a postmarketing surveillance in Japan. *Neuro-Oncol. Adv.* **4**, vdab189 (2022).

320. Perry, J., Chambers, A., Spithoff, K. & Laperriere, N. Gliadel wafers in the treatment of malignant glioma: a systematic review. *Curr. Oncol.* **14**, 189–194 (2007).

321. Smith, S. J. *et al.* Overall Survival in Malignant Glioma Is Significantly Prolonged by Neurosurgical Delivery of Etoposide and Temozolomide from a Thermo-Responsive Biodegradable Paste. *Clin. Cancer Res. Off. J. Am. Assoc. Cancer Res.* **25**, 5094–5106 (2019).

322. Haumann, R., Videira, J. C., Kaspers, G. J. L., van Vuurden, D. G. & Hulleman, E. Overview of Current Drug Delivery Methods Across the Blood–Brain Barrier for the Treatment of Primary Brain Tumors. *CNS Drugs* **34**, 1121–1131 (2020).

323. Mathew, E. N., Berry, B. C., Yang, H. W., Carroll, R. S. & Johnson, M. D. Delivering Therapeutics to Glioblastoma: Overcoming Biological Constraints. *Int. J. Mol. Sci.* **23**, 1711 (2022).

324. Kessler, A. T. & Bhatt, A. A. Brain tumour post-treatment imaging and treatment-related complications. *Insights Imaging* **9**, 1057–1075 (2018).

325. Bernstock, J. D. *et al.* Standard clinical approaches and emerging modalities for glioblastoma imaging. *Neuro-Oncol. Adv.* **4**, vdac080 (2022).

326. Shukla, G. *et al.* Advanced magnetic resonance imaging in glioblastoma: a review. *Chin. Clin. Oncol.* **6**, 40–40 (2017).

327. Irwin, C. P. *et al.* PARPi-FL - a Fluorescent PARP1 Inhibitor for Glioblastoma Imaging. *Neoplasia N. Y. N* **16**, 432–440 (2014).

328. Gautheron, A. *et al.* 5-ALA induced PpIX fluorescence spectroscopy in neurosurgery: a review. *Front. Neurosci.* **18**, (2024).

329. Eatz, T. A. *et al.* Intraoperative 5-ALA fluorescence-guided resection of high-grade glioma leads to greater extent of resection with better outcomes: a systematic review. *J. Neurooncol.* **156**, 233–256 (2022).

330. Li, D. *et al.* Visualization of Diagnostic and Therapeutic Targets in Glioma With Molecular Imaging. *Front. Immunol.* **11**, 592389 (2020).

331. Ellingson, B. M. *et al.* Consensus recommendations for a standardized Brain Tumor Imaging Protocol in clinical trials. *Neuro-Oncol.* **17**, 1188–1198 (2015).

332. Brown, T. J. *et al.* Association of the Extent of Resection With Survival in Glioblastoma: A Systematic Review and Meta-analysis. *JAMA Oncol.* **2**, 1460–1469 (2016).

333. Kow, C. Y. *et al.* Extent of resection affects prognosis for patients with glioblastoma in non-eloquent regions. *J. Clin. Neurosci.* **80**, 242–249 (2020).

334. Hadjipanayis, C. G., Widhalm, G. & Stummer, W. What is the Surgical Benefit of Utilizing 5-ALA for Fluorescence-Guided Surgery of Malignant Gliomas? *Neurosurgery* **77**, 663–673 (2015).

335. McCracken, D. J. *et al.* Turning on the light for brain tumor surgery: A 5-aminolevulinic acid story. *Neuro-Oncol.* **24**, S52–S61 (2022).

336. Zhang, Z., Zhou, F.-L., Davies, G.-L. & Williams, G. R. Theranostics for MRI-guided therapy: Recent developments. *VIEW* **3**, 20200134 (2022).

337. Huang, J., Chen, Z., Park, S.-W., Lai, J. H. C. & Chan, K. W. Y. Molecular Imaging of Brain Tumors and Drug Delivery Using CEST MRI: Promises and Challenges. *Pharmaceutics* **14**, 451 (2022).

338. Huang, C.-H. *et al.* Tumor protease-activated theranostic nanoparticles for MRI-guided glioblastoma therapy. *Theranostics* **13**, 1745–1758 (2023).

339. Hapuarachchige, S. & Artemov, D. Theranostic Pretargeting Drug Delivery and Imaging Platforms in Cancer Precision Medicine. *Front. Oncol.* **10**, 1131 (2020).

340. Werner, E. J., Datta, A., Jocher, C. J. & Raymond, K. N. High-Relaxivity MRI Contrast Agents: Where Coordination Chemistry Meets Medical Imaging. *Angew. Chem. Int. Ed.* **47**, 8568–8580 (2008).

341. Caravan, P., Ellison, J. J., McMurry, T. J. & Lauffer, R. B. Gadolinium(III) Chelates as MRI Contrast Agents: Structure, Dynamics, and Applications. *Chem. Rev.* **99**, 2293–2352 (1999).

342. Caravan, P. Strategies for increasing the sensitivity of gadolinium based MRI contrast agents. *Chem. Soc. Rev.* **35**, 512–523 (2006).

343. Lauffer, R. B. Paramagnetic metal complexes as water proton relaxation agents for NMR imaging: theory and design. *Chem. Rev.* **87**, 901–927 (1987).

344. Ibrahim, M. A., Hazhirkarzar, B. & Dublin, A. B. Gadolinium Magnetic Resonance Imaging. in *StatPearls* (StatPearls Publishing, Treasure Island (FL), 2024).

345. Abraham, J. L., Chandra, S., Thakral, C. & Abraham, J. M. SIMS imaging of gadolinium isotopes in tissue from Nephrogenic Systemic Fibrosis patients: Release of free Gd from magnetic resonance imaging (MRI) contrast agents. *Appl. Surf. Sci.* **255**, 1181–1184 (2008).

346. Aime, S. & Caravan, P. Biodistribution of gadolinium-based contrast agents, including gadolinium deposition. *J. Magn. Reson. Imaging* **30**, 1259–1267 (2009).

347. Kanda, T., Oba, H., Toyoda, K., Kitajima, K. & Furui, S. Brain gadolinium deposition after administration of gadolinium-based contrast agents. *Jpn. J. Radiol.* **34**, 3–9 (2016).

348. McDonald, R. J. *et al.* Intracranial Gadolinium Deposition after Contrast-enhanced MR Imaging. *Radiology* **275**, 772–782 (2015).

349. Clough, T. J., Jiang, L., Wong, K.-L. & Long, N. J. Ligand design strategies to increase stability of gadolinium-based magnetic resonance imaging contrast agents. *Nat. Commun.* **10**, 1420 (2019).

350. Pan, D., Schmieder, A. H., Wickline, S. A. & Lanza, G. M. Manganese-based MRI contrast agents: past, present and future. *Tetrahedron* **67**, 8431–8444 (2011).

351. Miyasaka, H., Saitoh, A. & Abe, S. Magnetic assemblies based on Mn(III) salen analogues. *Coord. Chem. Rev.* **251**, 2622–2664 (2007).

352. Barandov, A. *et al.* Membrane-Permeable Mn(III) Complexes for Molecular Magnetic Resonance Imaging of Intracellular Targets. *J. Am. Chem. Soc.* **138**, 5483–5486 (2016).

353. Arora, S. *et al.* FDA Approval Summary: Olaparib Monotherapy or in Combination with Bevacizumab for the Maintenance Treatment of Patients with Advanced Ovarian Cancer. *The Oncologist* **26**, e164–e172 (2021).

354. Murai, J. *et al.* Trapping of PARP1 and PARP2 by Clinical PARP Inhibitors. *Cancer Res.* **72**, 5588–5599 (2012).

355. Yap, T. A., Sandhu, S. K., Carden, C. P. & de Bono, J. S. Poly(ADP-ribose) polymerase (PARP) inhibitors: Exploiting a synthetic lethal strategy in the clinic. *CA. Cancer J. Clin.* **61**, 31–49 (2011).

356. Kim, M. Y., Zhang, T. & Kraus, W. L. Poly(ADP-ribosyl)ation by PARP-1: 'PAR-laying' NAD+ into a nuclear signal. *Genes Dev.* **19**, 1951–1967 (2005).

357. De Vos, M., Schreiber, V. & Dantzer, F. The diverse roles and clinical relevance of PARPs in DNA damage repair: current state of the art. *Biochem. Pharmacol.* **84**, 137–146 (2012).

358. Dantzer, F. *et al.* Involvement of poly(ADP-ribose) polymerase in base excision repair. *Biochimie* **81**, 69–75 (1999).

359. Polyak, K. & Garber, J. Targeting the missing links for cancer therapy. *Nat. Med.* **17**, 283–284 (2011).

360. Hassa, P. O. & Hottiger, M. O. The diverse biological roles of mammalian PARPS, a small but powerful family of poly-ADP-ribose polymerases. *Front. Biosci. J. Virtual Libr.* **13**, 3046–3082 (2008).

361. Haince, J.-F. *et al.* Ataxia Telangiectasia Mutated (ATM) Signaling Network Is Modulated by a Novel Poly(ADP-ribose)-dependent Pathway in the Early Response to DNA-damaging Agents *. *J. Biol. Chem.* **282**, 16441–16453 (2007).

362. Patel, K. J. *et al.* Involvement of Brca2 in DNA Repair. *Mol. Cell* **1**, 347–357 (1998).

363. Murai, J. *et al.* Rationale for Poly(ADP-ribose) Polymerase (PARP) Inhibitors in Combination Therapy with Camptothecins or Temozolomide Based on PARP Trapping versus Catalytic Inhibition. *J. Pharmacol. Exp. Ther.* **349**, 408–416 (2014).

364. Iglehart, J. D. & Silver, D. P. Synthetic lethality--a new direction in cancer-drug development. *N. Engl. J. Med.* **361**, 189–191 (2009).

365. Carney, B., Kossatz, S. & Reiner, T. Molecular Imaging of PARP. *J. Nucl. Med.* **58**, 1025–1030 (2017).

366. Scott, C. L., Swisher, E. M. & Kaufmann, S. H. Poly (ADP-ribose) polymerase inhibitors: recent advances and future development. *J. Clin. Oncol. Off. J. Am. Soc. Clin. Oncol.* **33**, 1397–1406 (2015).

367. Rouleau, M., Patel, A., Hendzel, M. J., Kaufmann, S. H. & Poirier, G. G. PARP inhibition: PARP1 and beyond. *Nat. Rev. Cancer* **10**, 293–301 (2010).

368. Hanna, C. *et al.* Pharmacokinetics, safety, and tolerability of olaparib and temozolomide for recurrent glioblastoma: results of the phase I OPARATIC trial. *Neuro-Oncol.* **22**, 1840–1850 (2020).

369. Fulton, B. *et al.* PARADIGM-2: Two parallel phase I studies of olaparib and radiotherapy or olaparib and radiotherapy plus temozolomide in patients with newly diagnosed glioblastoma, with treatment stratified by MGMT status. *Clin. Transl. Radiat. Oncol.* **8**, 12–16 (2017).

370. Huang, T., Hu, P., Banizs, A. B. & He, J. Initial evaluation of Cu-64 labeled PARPi-DOTA PET imaging in mice with mesothelioma. *Bioorg. Med. Chem. Lett.* **27**, 3472–3476 (2017).

371. Wang, X. *et al.* PET imaging of PARP expression using 68Ga-labelled inhibitors. *Eur. J. Nucl. Med. Mol. Imaging* **50**, 2606–2620 (2023).

372. Wilson, T. C. *et al.* PET Imaging of PARP Expression Using 18F-Olaparib. *J. Nucl. Med.* **60**, 504–510 (2019).

373. Tacar, O., Sriamornsak, P. & Dass, C. R. Doxorubicin: an update on anticancer molecular action, toxicity and novel drug delivery systems. *J. Pharm. Pharmacol.* **65**, 157–170 (2013).

374. Argenziano, M. *et al.* Improvement in the Anti-Tumor Efficacy of Doxorubicin Nanosponges in In Vitro and in Mice Bearing Breast Tumor Models. *Cancers* **12**, 162 (2020).

375. Dubbelboer, I. R., Pavlovic, N., Heindryckx, F., Sjögren, E. & Lennernäs, H. Liver Cancer Cell Lines Treated with Doxorubicin under Normoxia and Hypoxia: Cell Viability and Oncologic Protein Profile. *Cancers* **11**, 1024 (2019).

376. Kciuk, M. *et al.* Doxorubicin—An Agent with Multiple Mechanisms of Anticancer Activity. *Cells* **12**, 659 (2023).

377. Lipscomb, L. A. *et al.* Water ring structure at DNA interfaces: hydration and dynamics of DNA-anthracycline complexes. *Biochemistry* **33**, 3649–3659 (1994).

378. Degerstedt, O. *et al.* Quantitative imaging of doxorubicin diffusion and cellular uptake in biomimetic gels with human liver tumor cells. *Drug Deliv. Transl. Res.* **14**, 970–983 (2024).

379. Motamarry, A. *et al.* Real-time fluorescence imaging for visualization and drug uptake prediction during drug delivery by thermosensitive liposomes. *Int. J. Hyperth. Off. J. Eur. Soc. Hyperthermic Oncol. North Am. Hyperth. Group* **36**, 817–826 (2019).

380. Dong, X. *et al.* Thermosensitive porphyrin-incorporated hydrogel with four-arm PEG-PCL copolymer (II): doxorubicin loaded hydrogel as a dual fluorescent drug delivery system for simultaneous imaging tracking in vivo. *Drug Deliv.* **24**, 641–650 (2017).

381. Nguyen, H. V.-T. *et al.* Pro-organic radical contrast agents (“pro-ORCAs”) for real-time MRI of pro-drug activation in biological systems. *Polym. Chem.* **11**, 4768–4779 (2020).

382. Zhu, J., Xiong, Z., Shen, M. & Shi, X. Encapsulation of doxorubicin within multifunctional gadolinium-loaded dendrimer nanocomplexes for targeted theranostics of cancer cells. *RSC Adv.* **5**, 30286–30296 (2015).

383. Khan, M. *et al.* Doxorubicin (DOX) Gadolinium–Gold-Complex: A New Way to Tune Hybrid Nanorods as Theranostic Agent. *Int. J. Nanomedicine* **16**, 2219–2236 (2021).

384. Norouzi, M. *et al.* Doxorubicin-loaded iron oxide nanoparticles for glioblastoma therapy: a combinational approach for enhanced delivery of nanoparticles. *Sci. Rep.* **10**, 11292 (2020).

385. Andersen, T., Auk-Emblem, P. & Dornish, M. 3D Cell Culture in Alginate Hydrogels. *Microarrays* **4**, 133–161 (2015).

386. Hasegawa, M., Ohmagari, H., Tanaka, H. & Machida, K. Luminescence of lanthanide complexes: From fundamental to prospective approaches related to water- and molecular-stimuli. *J. Photochem. Photobiol. C Photochem. Rev.* **50**, 100484 (2022).

387. Rajapakse, H. E., Reddy, D. R., Mohandessi, S., Butlin, N. G. & Miller, L. W. Luminescent Terbium Protein Labels for Time-Resolved Microscopy and Screening. *Angew. Chem. Int. Ed Engl.* **48**, 4990–4992 (2009).

388. Varnäs, K., Varrone, A. & Farde, L. Modeling of PET data in CNS drug discovery and development. *J. Pharmacokinet. Pharmacodyn.* **40**, 267–279 (2013).

389. Srinivas, N., Maffuid, K. & Kashuba, A. D. Clinical Pharmacokinetics and Pharmacodynamics of Drugs in the Central Nervous System. *Clin. Pharmacokinet.* **57**, 1059–1074 (2018).

390. Ma, Y., Wang, Q., Dong, Q., Zhan, L. & Zhang, J. How to differentiate pseudoprogression from true progression in cancer patients treated with immunotherapy. *Am. J. Cancer Res.* **9**, 1546–1553 (2019).

391. Thust, S. C., van den Bent, M. J. & Smits, M. Pseudoprogression of brain tumors. *J. Magn. Reson. Imaging* **48**, 571–589 (2018).

392. Tibbitt, M. W. & Anseth, K. S. Hydrogels as Extracellular Matrix Mimics for 3D Cell Culture. *Biotechnol. Bioeng.* **103**, 655–663 (2009).

393. Dragoj, M. *et al.* Development and Validation of a Long-Term 3D Glioblastoma Cell Culture in Alginate Microfibers as a Novel Bio-Mimicking Model System for Preclinical Drug Testing. *Brain Sci.* **11**, 1025 (2021).

394. Pangjantuk, A., Kaokaen, P., Kunhorm, P., Chaicharoenaudomrung, N. & Noisa, P. 3D culture of alginate-hyaluronic acid hydrogel supports the stemness of human mesenchymal stem cells. *Sci. Rep.* **14**, 4436 (2024).

395. Betz, J. F. *et al.* Optically clear alginate hydrogels for spatially controlled cell entrapment and culture at microfluidic electrode surfaces. *Lab. Chip* **13**, 1854–1858 (2013).

396. Liang, J. *et al.* Phthalocyanine incorporated alginate hydrogel with near infrared fluorescence for non-invasive imaging monitoring in vivo. *RSC Adv.* **7**, 6501–6510 (2017).

397. Zhang, C., Grossier, R., Candoni, N. & Veesler, S. Preparation of alginate hydrogel microparticles by gelation introducing cross-linkers using droplet-based microfluidics: a review of methods. *Biomater. Res.* **25**, 41 (2021).

398. Abourehab, M. A. S. *et al.* Alginate as a Promising Biopolymer in Drug Delivery and Wound Healing: A Review of the State-of-the-Art. *Int. J. Mol. Sci.* **23**, 9035 (2022).

399. Abasalizadeh, F. *et al.* Alginate-based hydrogels as drug delivery vehicles in cancer treatment and their applications in wound dressing and 3D bioprinting. *J. Biol. Eng.* **14**, 8 (2020).

400. Hu, Y. *et al.* A double-layer hydrogel based on alginate-carboxymethyl cellulose and synthetic polymer as sustained drug delivery system. *Sci. Rep.* **11**, 9142 (2021).

401. Oraiopoulou, M.-E. *et al.* The Temozolomide–Doxorubicin paradox in Glioblastoma in vitro–in silico preclinical drug-screening. *Sci. Rep.* **14**, 3759 (2024).

402. Lesueur, P. *et al.* Phase I/IIa study of concomitant radiotherapy with olaparib and temozolomide in unresectable or partially resectable glioblastoma: OLA-TMZ-RTE-01 trial protocol. *BMC Cancer* **19**, 198 (2019).

403. Hovorka, O. *et al.* Spectral analysis of doxorubicin accumulation and the indirect quantification of its DNA intercalation. *Eur. J. Pharm. Biopharm.* **76**, 514–524 (2010).

404. Taglang, C. *et al.* Deuterium magnetic resonance spectroscopy enables noninvasive metabolic imaging of tumor burden and response to therapy in low-grade gliomas. *Neuro-Oncol.* **24**, 1101–1112 (2022).